

LNS-278

Effect of Softness and Charges on the
Volume Phase Transition of Colloidal
Microgels and Macrogels

Dissertation

Boyang Zhou

Laboratory for Neutron Scattering and Imaging

Paul Scherrer Institut

CH-5232 Villigen PSI

2024

Diss. ETH No. 29967

Effect of Softness and Charges on the Volume Phase Transition of Colloidal Microgels and Macrogels

A thesis submitted to attain the degree of

DOCTOR OF SCIENCES

(Dr. sc. ETH Zurich)

presented by

Boyang Zhou

MSc Materials science and Engineering, Georgia Institute of Technology

born on 25.04.1995

accepted on the recommendation of

Prof. Dr. Lucio Isa, examiner

Prof. Dr. Peter Fischer, co-examiner

Prof. Dr. Alberto Fernandez-Nieves, co-examiner

PD. Dr. Urs Gasser, co-examiner

Abstract

Colloids are mesoscopic particles suspended in a solvent that exhibit Brownian motion with an energy scale of $k_B T$. They are of great significance and are ubiquitous in both our daily lives and our bodies, present in items such as blood, milk, paint, cosmetics, and various food products. In particular, colloids can be classified into two main categories: hard colloids and soft compressible colloids. As a result of their deformable structure, soft colloids have a higher degree of freedom, leading to an increasingly complex and poorly understood colloidal system compared to their hard-colloid counterparts, especially at high concentrations. The rich swelling behavior of soft colloids makes them interesting for both scientific research and industrial applications. They are commonly used in applications such as drug delivery [16], smart coating [81], adhesives [191], and sensor technologies [138]. In addition, due to their stimuli-sensitive nature, soft colloids are also used as model systems for statistical mechanics [20], phase transitions [188], and interaction forces [108]. In this work, poly(*N*-isopropylacrylamide) (pNIPAM) microgels are used as a model system to study soft colloids. The behavior of the pNIPAM microgel suspension is investigated in both the fluid and crystalline phases, and the goal is to relate the behavior observed for single particles to the suspensions.

When large hard colloids are added to a suspension of smaller but otherwise identical colloids at high concentrations, the suspension polydispersity increases and the larger particles act as point defects that suppress suspension crystallization [48]. In the case of hard colloids, crystallization is suppressed for polydispersities larger than 12%. However, in the case of microgels, larger particles can spontaneously deswell to a size comparable to that of smaller ones, which is a very special behavior not known from other types of particulate systems. This behavior reduces the polydispersity of the suspension and eliminates point defects, so that the suspension can crystallize regardless of the initially high polydispersity [80, 150, 149]. This

deswelling is triggered by an increased osmotic pressure due to ions in the suspension. pNIPAM is an uncharged polymer. However, it is difficult to synthesize totally uncharged pNIPAM particles because of the use of ionic initiators in microgel synthesis. Sulfate groups from the ammonium persulfate (APS) initiator with negative charges remain at the ends of the NIPAM polymer chains, and the associated ammonium counterions ensure charge neutrality. For electrostatic reasons, the sulfate groups are expected to locate at the periphery of the microgel and because of the fuzzy-sphere structure of the microgel, the ammonium counterions that surround the sulfate groups form a spherical-shell cloud. At sufficiently high concentrations, the counterion clouds begin to overlap, allowing counterions bound to the microgel with an energy scale $< k_B T$ to explore the suspension volume and contribute to the suspension osmotic pressure. When the osmotic pressure outside the particle is comparable or greater than the bulk modulus of the particle, the particle is isotropically compressed [54, 156, 150]. Furthermore, the presence of counterions can explain the significant increase in the osmotic pressure of the microgel suspension observed at high concentration [150, 102]. The ion density is low, yet it plays a crucial role in dictating the microgel swelling behavior, influencing the polydispersity and, consequently, the phase behavior of the suspension. Understanding the ion cloud is essential for understanding microgel suspensions, particularly at high concentrations. However, a direct characterization of counterion clouds of microgels was lacking.

In this thesis, the configuration of the microgel counterion cloud is studied by means of small-angle neutron scattering (SANS). Note that the form factor can be expanded as $P(q) = F_p^2(q) + 2F_p(q)F_c(q) + F_c^2(q)$, where $F_p(q)$ is the scattering amplitude of the pNIPAM polymer, including the crosslinkers and charged groups due to the initiator, and $F_c(q)$, is the scattering amplitude of the counterion cloud. We prepared two suspensions, one with Na^+ ions and the other with NH_4^+ ions. The difference in scattering length density of these ions is explored to obtain an augmented scattering signal that provides structural information about the ion cloud and the arrangement of charged groups in a microgel. It is demonstrated that the counterion cloud is indeed located at the particle periphery, as expected from particle synthesis. This result also supports the previously established theory for microgel deswelling at high concentrations, which relates particle softness and surface charges to phase behavior.

The following chapter further investigates the dependence of the counterion cloud configuration for microgels with different softness, as softness affects suspension phase behavior. Microgel softness is controlled by the amount of cross-linker used

in the synthesis. The softest microgels are known as ultra-low crosslinked (ULC), and are synthesized by atom abstraction reactions without cross-linkers. Previous works have reported that ULC microgels and microgels synthesized with crosslinkers can all spontaneously deswell below random close packing ϕ_{rcp} . Furthermore, microgels with a higher crosslinking density are observed to deswell less and are prone to deform or interpenetrate at higher concentrations [29, 155, 135]. The behavior mentioned here is dependent on the percolation of counterion clouds, implying that the configuration of the counterion clouds for microgels with different softness allows understanding the softness dependence of the microgel deswelling mechanism. In this work, the spherical shell model is proven to be valid for all microgels containing cross-linkers; however, the model becomes insufficient at higher generalized volume fraction ζ for the stiffest particles, as particle deformation may have occurred. For ULC microgels, the counterion cloud signal is less pronounced. The possible reason is that the internal structure of the ULC microgel can be more homogeneous with a less defined core-shell structure due to the lack of exogenous cross-linker.

The spontaneous deswelling behavior, the width of the counterion cloud, and their connection with the suspension polydispersity and suspension structure have been studied using SANS. In this work, microgels synthesized with 2wt.% crosslinker are prepared at different concentrations. The generalized volume fraction ζ is used to describe the suspension concentration, and reflects the hypothetical volume if the microgels retained their dilute size. Note that ζ can be larger than one, as microgels can deswell and/or interpenetrate. In our experiments, ζ ranged from $\zeta = 0.01$ to $\zeta > 1.0$. All microgels are found to remain swollen and begin to deswell at ζ_c , where $\zeta_c < \phi_{\text{rcp}}$. The deswelling that occurs below random close-packing provides further evidence that the deswelling behavior cannot be due to direct interaction between neighboring microgels. The effective particle radius is used, which is the radius of the microgel plus the thickness of the counterion cloud σ_{ic} , $R_{\text{eff}} = R_{\text{SANS}} + \sigma_{\text{ic}}$. With R_{eff} , we calculate the effective volume fractions of these microgel suspensions, ϕ_{eff} . At ζ_c , the particles are effectively in direct contact such that $\phi_{\text{eff}} = 1$. This allows calculating σ_{ic} . The results found are in good agreement with the results obtained from our SANS measurement and a prior estimate in bidisperse pNIPAM suspension [150, 54]. Furthermore, a consistent decrease in suspension polydispersity is observed with increasing ζ for all samples, illustrating the fact that the larger particles shrink to the size of smaller microgels, making the suspension more monodisperse. Polydispersity is important for the phase behavior of both hard and soft colloids. However, it plays a different role for soft colloids

because polydispersity can change with concentration, and as a result, swelling can affect the suspension phase behavior. Therefore, it is important to take into account polydispersity both in the form factor $P(q)$ and in the structure factor $S(q)$ to obtain reliable results.

The interactions between the atoms of a material are reflected in the material's macroscopic properties, including all elastic properties. Consequently, it is anticipated that the ion cloud that surrounds the microgel can influence the behavior of the suspension, especially for the crystalline state at sufficiently high concentrations, with microgels acting as the 'atoms' forming the crystal. Since microgels can be large enough to be directly observed with a light microscope, the behavior of a microgel crystal can be conveniently studied using light microscopy. To investigate the influence of the delocalized counterions on the microgel-microgel interaction, we studied the normal modes, basic lattice excitation in a crystal, of pNIPAM crystals with confocal microscopy. Microgels used in this work are pNIPAM copolymerized with acrylic acid (AAC) with a fluorescent core. Using confocal microscopy, it was discovered that the microgel crystals have face-centered cubic (fcc) structures. Normal modes can be obtained from time-series of microscopy images. The deviations of the microgel from its lattice site suggest that the microgel crystals behave essentially as harmonic crystals, indicating that the equipartition theorem can be applied to the measured normal modes. The interaction force between particle pairs is characterized by force constants that define normal modes, and, by comparing the force constants between the nearest and second-nearest neighbors, it can be concluded that the interaction force among microgels is non-central. Note that non-central interaction forces are also reported to be important in crystals consisting of charged hard colloids, where many-body interactions play a role [140]. From work presented here and previous studies, it has been shown that counterion clouds are at the microgel periphery and counterions are capable of exploring suspension volumes due to percolation of counterion clouds; hence, microgel crystals should be analogous to charged hard-sphere crystals [140] and even metals [111, 160]. The key difference is that, because of softness, the microgels in the crystalline state can change their size. The results suggest that the interaction of the microgel suspension in the crystalline state cannot be sufficiently described by pair potentials, such as the Derjaguin-Landau-Verwey-Overbeek (DLVO) potential, which is obtained by superimposing a radially symmetric pairwise interactions. Our work shows that many-body interactions and non-central forces are important in concentrated suspensions of soft and deformable microgels, and this is a direct consequence of the counterions at the

microgel periphery.

The temperature sensitivity of pNIPAM is important for both micro- and macrogels. In this work, we investigate the thermodynamic instability of pNIPAM macrogels. Macro gels are stimuli-sensitive materials that have great impact in the field of tissue regeneration[8], CO₂ capture [103], cosmetics [110], and water treatment [196]. Upon rapid heating above $T \approx 32^\circ\text{C}$, pNIPAM macrogels are observed to be trapped in a constrained equilibrium state, which can be characterized by a free energy with two minima, corresponding to swollen/deswollen coexistence. This results from the formation of a skin that constrains the gel volume and prevents the solvent from leaving the interior of the gel. The skin thus prevents the swollen interior from reaching the deswollen state, with phase coexistence corresponding to the free energy minimum at constant volume. This coexistence can lead to stresses that can cause buckling in toroidal gels. Note that the metastable state with skin and swollen interior also depends on the macroscopic shape of the gel, which makes the gel with skin an interesting material that is not well understood. Despite the significant role played by the skin, little is known about its properties. Here, we investigate the skin thickness of a cylindrical gel using neutron imaging, which captures the boundary between the gel surface and the gel interior, indicating the thickness of the skin is on the order of $40\ \mu\text{m}$. Furthermore, we apply a uniaxial strain to disk-shaped gels in the fully swollen, fully deswollen, and swollen-with-skin states. By monitoring the normal force response to the applied strain, we estimate the Young's modulus for the gels in these different states. We treat the skin-swollen gel as a three-layer composite material, where the thickness of the skin is estimated to be on the order of $49\ \mu\text{m}$, in good agreement with the neutron imaging results. We also investigate the internal structure of the skin via SANS, and find that correlation length of the skin is comparable to that of the deswollen gel, indicating that the structure of the skin is as dense as the deswollen gel phase. Additionally, by examining the asymptotic behavior at low momentum transfer q , we observe the formation of compact structures with rough surfaces. Our study is perhaps the first comprehensive investigation of polymer gel skin, further providing an estimate of the skin thickness.

This work demonstrates the connection between microscopic aspects, such as the ion cloud for microgels and the skin details for macrogels, and macroscopic material properties, including the elasticity of colloidal crystals for microgels and the size, elastic properties and permeability for macrogels, in various conditions. These linkages were not at all understood before our work. Realizing that most of the

so-called neutral microgels are peripherically charged, we have shown that any interaction model for microgels, must consider the spontaneous deswelling behavior and the presence of noncentral forces in some situations. Exploring whether the force non-centrality appears with microgel deswelling or whether it is also present at lower concentrations, in which the interactions are expected to be pairwise, would be a direction for future work. Furthermore, truly neutral microgel synthesized without ionic initiator should be investigated. In this case, the effect of microgel softness would be more rigorously isolated and explored. With respect to the macrogel work, additional imaging techniques such as microscopy, neutron tomography, and AFM could be used to analyze skin formation and thickness, as well as to better understand the phase coexistence inside the pNIPAM macrogel after rapid heating. Ultimately, the goal is to exploit thermodynamic instabilities in macrogels for both material design and to achieve macroscopic shape actuation, embodying the notion of extreme thermodynamics of macrogels.

Zusammenfassung

Kolloide sind mesoskopische Teilchen, die in einem Lösungsmittel suspendiert sind und Brownsche Bewegung mit einer Energieskala von $k_B T$ zeigen. Sie sind von großer Bedeutung und allgegenwärtig in unserem täglichen Leben, Beispiele sind das Blut in unseren Körpern oder Produkte wie Milch, Farbe, Kosmetika und verschiedene Lebensmittel. Insbesondere können Kolloide in zwei Hauptkategorien eingeteilt werden: harte Kolloide und weiche, komprimierbare Kolloide. Aufgrund ihrer verformbaren Struktur haben weiche Kolloide einen höheren Freiheitsgrad im Vergleich zu harten Kolloiden, was zu einem komplexeren und schlecht verstandenen kolloidalen Verhalten führt, insbesondere bei hohen Konzentrationen. Das reichhaltige Quellverhalten von weichen Kolloiden macht sie sowohl für die wissenschaftliche Forschung als auch für industrielle Anwendungen interessant. Sie werden häufig in Anwendungen wie der Arzneimittelabgabe [16], intelligenter Beschichtung [81], Klebstoffen [191] und Sensortechnologien [138] eingesetzt. Darüber hinaus werden aufgrund ihrer stimuliempfindlichen Eigenschaften weiche Kolloide auch als Modellsysteme für statistische Mechanik [20], Phasenübergänge [188] und die Wechselwirkung zwischen kolloidalen Teilchen verwendet [108]. In dieser Arbeit werden Poly(*N*-Isopropylacrylamid)-Mikrogele (pNIPAM) als Modellsystem für die Untersuchung weicher Kolloide verwendet. Das Verhalten der pNIPAM-Mikrogelsuspension wird sowohl in der flüssigen als auch in der kristallinen Phase untersucht, mit dem Ziel das Verhalten einzelner Partikel zu beobachten und die Auswirkung auf das Verhalten der Suspension zu übertragen.

Wenn große, harte Kolloide einer konzentrierten Suspension kleinerer aber ansonsten identischer Kolloide zugesetzt werden, nimmt die Polydispersität der Suspension zu, und die größeren Teilchen wirken als Punktdefekte, die die Kristallisation der Suspension unterdrücken. Im Fall harter Kolloide wird die Kristallisation bei einer Polydispersität von mehr als 12% unterdrückt. Bei Mikrogelen können größere Partikel jedoch spontan auf eine Größe anschwellen, die mit der der kleineren Partikel vergle-

ichbar ist, wodurch sich die Polydispersität der Suspension verringert und Punktdefekte beseitigt werden, so dass die Suspension unabhängig von der anfänglich hohen Polydispersität kristallisieren kann [80, 150, 149]. Diese Entquellung wird durch einen erhöhten osmotischen Druck aufgrund von Ionen in der Suspension ausgelöst. pNIPAM ist ein ungeladenes Polymer. Es ist jedoch schwierig, völlig ungeladene pNIPAM-Partikel zu synthetisieren, da bei der Mikrogelsynthese ionische Initiatoren verwendet werden. Die negativ geladenen Sulfatgruppen des Ammoniumpersulfat-Initiators (APS) verbleiben an den Enden der NIPAM-Polymerketten, und die zugehörigen Ammonium-Gegenionen sorgen für Ladungsneutralität. Aus elektrostatischen Gründen wird erwartet, dass sich die Sulfatgruppen an der Peripherie des Mikrogels befinden, und die Ammonium-Gegenionen, die Sulfatgruppen umgeben, eine Ionenwolke mit der Form einer Kugelschale bilden. Bei ausreichend hohen Konzentrationen beginnen sich die Gegenionenwolken zu überlappen, so dass auch Gegenionen, die mit einer Energie $> k_B T$ an das Mikrogel gebunden sind, das Suspensionsvolumen erkunden können und zum osmotischen Druck der Suspension beitragen. Wenn der osmotische Druck außerhalb des Partikels vergleichbar oder größer ist als der Kompressionsmodul des Partikels, wird das Partikel isotrop komprimiert [54, 156, 150]. Darüber hinaus kann das Vorhandensein von Gegenionen den signifikanten Anstieg des osmotischen Drucks der Mikrogelsuspension erklären, der bei hoher Konzentration beobachtet wird [150, 102]. Die Ionenkonzentration ist niedrig, spielt jedoch eine entscheidende Rolle fürs Schwellverhalten der Mikrogele, beeinflusst die Polydispersität und folglich das Phasenverhalten der Suspension. Das Verständnis der Ionenwolke ist für das Verständnis von Mikrogelsuspensionen, insbesondere bei hohen Konzentrationen, unerlässlich. Allerdings fehlte eine direkte Charakterisierung der Gegenionenwolken von Mikrogelen.

In dieser Arbeit wird die Konfiguration der Mikrogel-Gegenionenwolke mit Hilfe der Kleinwinkel-Neutronenstreuung (SANS) untersucht. Der Formfaktor eines Mikrogels kann als $P(q) = F_p^2(q) + 2 F_p(q) F_c(q) + F_c^2(q)$ geschrieben werden, wobei $F_p(q)$ die Streuamplitude des pNIPAM-Polymers, einschließlich Crosslinker und der geladenen Gruppen, und $F_c(q)$ die Streuamplitude der Gegenionenwolke ist. Wir haben zwei Suspensionen hergestellt, eine mit Na^+ und die andere mit NH_4^+ -Gegenionen. Die unterschiedliche Streulängendichte für Neutronenstrahlung dieser Ionen wird genutzt, um ein vergrößertes Streusignal zu erhalten, das strukturelle Informationen über die Ionenwolke und die Anordnung der geladenen Gruppen in einem Mikrogel liefert. Es wird gezeigt, dass sich die Gegenionenwolke tatsächlich an der Partikelperipherie befindet, wie von der Partikelsynthese erwartet. Dieses Ergeb-

nis stützt auch die zuvor aufgestellte Theorie für die Entquellung von Mikrogelele bei hohen Konzentrationen, die Weichheit der Partikel und die Oberflächenladungen mit dem Phasenverhalten in Verbindung bringt.

Ebenfalls wird die Abhängigkeit der Konfiguration der Gegenionenwolke für Mikrogele mit unterschiedlicher Weichheit untersucht, da die Weichheit das Phasenverhalten der Suspension beeinflusst. Die Weichheit von Mikrogelele wird durch die Menge des bei der Synthese verwendeten Crosslinkers gesteuert. Die weichsten Mikrogelele sind als ultra-low-crosslinked (ULC) bekannt und werden durch Atomabstraktionsreaktionen ohne Crosslinker synthetisiert. In früheren Arbeiten wurde berichtet, dass sowohl ULC-Mikrogelele als auch Mikrogelele, die mit Crosslinker synthetisiert wurden, bei einem Volumenbruch unterhalb der zufällig-dichtesten Packung, ϕ_{rcp} , spontan entquellen können. Darüber hinaus wird beobachtet, dass Mikrogelele mit einer höheren Crosslinker-Dichte weniger entquellen und bei höheren Konzentrationen zur Verformung oder Interpenetration neigen [29, 155, 135]. Das hier beschriebene Verhalten hängt von der Perkolation von Gegenionenwolken ab, was bedeutet, dass die Konfiguration der Gegenionenwolken von Mikrogelele mit unterschiedlicher Weichheit das Verständnis der Weichheitsabhängigkeit des Entquellungsmechanismus des Mikrogelels ermöglicht. In dieser Arbeit wird nachgewiesen, dass das Kugelschalenmodell der Gegenionenwolke für alle Mikrogelele, die Crosslinker enthalten, gültig ist; allerdings wird das Modell bei höheren verallgemeinerten Volumenbrüchen ζ für die steifsten Teilchen unzureichend, da es zu einer Teilchenverformung kommen kann. Bei ULC-Mikrogelele ist das Gegenionenwolken-signal weniger stark ausgeprägt. Der mögliche Grund dafür ist, dass die innere Struktur des ULC-Mikrogelels aufgrund des Fehlens von exogenem Crosslinker homogener sein kann und eine weniger definierte Kern-Schale-Struktur aufweist.

Das spontane Quellverhalten, die Ausdehnung der Gegenionenwolke und ihr Zusammenhang mit der Polydispersität der Suspension und der Suspensionsstruktur wurden mittels SANS untersucht. In dieser Arbeit wurden Mikrogelele, die mit 2wt.% Crosslinker synthetisiert wurden, in unterschiedlichen Konzentrationen hergestellt. Der verallgemeinerte Volumenbruch ζ wird verwendet, um die Konzentration der Suspension beschreiben. ζ ist der Volumenbruch, der von den Mikrogelele in ihrem vollständig geschwollenen Zustand eingenommen wird. Beachten Sie, dass ζ größer als eins sein kann, da Mikrogelele schrumpfen oder sich gegenseitig durchdringen können. Der effektive Volumenbruch der Suspensionen reichte von $\zeta = 0.01$ bis $\zeta > 1.0$. Alle Mikrogelele bleiben gequollen und beginnen bei ζ_c zu entquellen, wobei $\zeta_c < \phi_{\text{rcp}}$. Die Entquellung, die unterhalb der zufällig-dichtesten Packung auftritt,

ist ein weiterer Beweis dafür, dass das Entquellungsverhalten nicht auf eine direkte Wechselwirkung zwischen benachbarten Mikrogelen zurückzuführen ist. Es wird der effektive Teilchenradius verwendet, der sich aus dem Radius des Mikrogels und der Dicke der Gegenionenwolke ergibt: σ_{ic} , $R_{\text{eff}} = R_{\text{SANS}} + \sigma_{ic}$. Mit R_{eff} berechnen wir den effektiven Volumenbruch der Mikrogelsuspension, ϕ_{eff} . Bei ζ_c sind die effektiven Teilchen in direktem Kontakt, so dass $\phi_{\text{eff}} = 1$ ist. Dies ermöglicht die Bestimmung der Dicke der Gegenionenwolke, σ_{ic} . Die gefundenen Ergebnisse stehen in guter Übereinstimmung mit den Ergebnissen unserer SANS-Messung und einer früheren Schätzung in bidispersen pNIPAM-Suspensionen [150, 54]. Darüber hinaus ist bei allen Proben eine konsistente Abnahme der Polydispersität der Suspension mit zunehmendem ζ zu beobachten, was die Tatsache verdeutlicht, dass die größeren Partikel auf die Größe kleinerer Mikrogele schrumpfen und die Suspension dadurch monodisperser wird. Die Polydispersität ist für das Phasenverhalten sowohl harter als auch weicher Kolloide von Bedeutung. Bei weichen Kolloiden spielt sie jedoch eine ganz andere Rolle, da sich die Polydispersität mit der Konzentration ändern kann, was zur Folge hat, dass das Schwellverhalten das Phasenverhalten der Suspension beeinflussen kann. Daher ist es wichtig, die Polydispersität sowohl im Formfaktor $P(q)$ als auch im Strukturfaktor $S(q)$ zu berücksichtigen, um zuverlässige Ergebnisse zu erhalten.

Die Wechselwirkungen zwischen den Atomen eines Materials spiegeln sich in den makroskopischen Eigenschaften des Materials wider, einschließlich aller elastischen Eigenschaften. Folglich wird erwartet, dass die Ionenwolke, die das Mikrogel umgibt, das Verhalten der Suspension beeinflussen kann, insbesondere im kristallinen Zustand bei ausreichend hohen Konzentrationen, wobei die Mikrogele als "Atome" fungieren, die den Kristall bilden. Da Mikrogele groß genug sein können, um direkt mit einem Lichtmikroskop beobachtet zu werden, kann das Verhalten eines Mikrogelkristalls mittels Lichtmikroskopie untersucht werden. Die geladenen Gruppen und die Verformbarkeit der Mikrogele beeinflussen das Verhalten der Mikrogele im dicht gepackten Zustand, wie zum Beispiel im kristallinen Zustand. Um den Einfluss der delokalisierten Gegenionen auf die Mikrogel-Mikrogel-Wechselwirkung zu untersuchen, haben wir die Normalmoden, grundlegende Gitteranregungen in einem Kristall, von pNIPAM-Kristallen mit konfokaler Mikroskopie untersucht. Die in dieser Arbeit verwendeten Mikrogele bestehen aus pNIPAM, das mit Acrylsäure (AAC) kopolymerisiert ist und einen fluoreszierenden Kern enthält. Die mittels konfokaler Mikroskopie untersuchten Kristalle haben ein kubisch-flächenzentriertes (fcc) Gitter. Die Normalmoden können direkt aus einer Sequenz von Mikroskopiebildern

gewonnen werden. Die Abweichungen eines Mikrogels von seinem Gitterplatz legen nahe, dass sich die Mikrogel-Kristalle im Wesentlichen wie harmonische Kristalle verhalten, was darauf hinweist, dass das Äquipartitionstheorem auf die gemessenen Normalmoden angewendet werden kann. Die Wechselwirkungskraft zwischen Partikel-paaren wird durch Federkonstanten charakterisiert, die Normalmoden definieren. Aus den Federkonstanten zwischen nächsten und übernächsten Nachbarn kann geschlossen werden, dass die Wechselwirkungskraft zwischen Mikrogelen nicht zentral ist. Nicht-zentrale Wechselwirkungskräfte sind auch in Kristallen aus geladenen harten Kolloiden wichtig, bei denen Vielteilchenwechselwirkungen eine Rolle spielen [140]. Aus früheren Arbeiten geht hervor, dass sich die Gegenionen an der Mikrogel-Peripherie befinden und dass Gegenionen aufgrund der Perkolation von Gegenionenwolken in der Lage sind, das Suspensionsvolumen zu erkunden. Diesbezüglich verhalten sich Mikrogel-Kristalle analog zu geladenen harten Kolloiden [140] und sogar Metallen [111, 160]. Der entscheidende Unterschied besteht darin, dass die Mikrogele aufgrund ihrer Weichheit in einem kristallinen Zustand ihre Größe ändern können. Die Ergebnisse legen nahe, dass die Wechselwirkung der Mikrogel-Suspension im kristallinen Zustand nicht ausreichend durch Paarpotentiale beschrieben werden kann, wie zum Beispiel das Derjaguin-Landau-Verwey-Overbeek (DLVO)-Potential, das aus der Überlagerung von radial-symmetrischen Paarwechselwirkungen erhalten wird. Unsere Arbeit zeigt, dass weiche, dass Vielkörperwechselwirkungen und nicht-zentrale Kräfte in konzentrierten Suspensionen von weichen und deformierbaren Mikrogelen wichtig sind, und dies eine direkte Folge der Gegenionen an der Mikrogel-Peripherie ist.

Die Temperatursensitivität von pNIPAM ist sowohl für Mikro- als auch für Makrogele wichtig. In einem weiteren Teil der Arbeit untersuchen wir die thermodynamische Instabilität von pNIPAM-Makrogelen. Makrogele sind stimuliempfindliche Materialien, für Anwendungen im Bereich der Geweberegeneration [8], CO₂-Abscheidung [103], Kosmetik [110] und Wasseraufbereitung von grossem Interesse sind [196]. Bei schneller Erwärmung über $T \approx 32^\circ\text{C}$ beobachten wir, dass Makrogele in einem eingeschränkten Gleichgewichtszustand gefangen sind, der durch eine freie Energie mit zwei Minima charakterisiert werden kann, die einer Koexistenz von geschwellenem und entschwollenem Zustand entspricht. Dies resultiert aus der Bildung einer Haut, die das Gelvolumen begrenzt und verhindert, dass das Lösungsmittel aus dem Innern des Gels entweichen kann. Die Haut verhindert somit, dass das geschwollene Innere den entschwollenen Zustand erreicht, wobei die Phasenkoexistenz dem Freie-Energie-Minimum bei konstantem Volumen entspricht.

Diese Koexistenz kann zu Spannungen führen, die zu Buckelungen in toroidalen Gelen führen können. Trotz der bedeutenden Rolle, die Haut spielt, ist wenig über ihre Eigenschaften bekannt. Hier untersuchen wir die Hautdicke eines zylindrischen Gels mittels Neutronenradiographie, die Grenze zwischen der Geloberfläche und dem Gelinneren erfasst und darauf hinweist, dass die Hautdicke etwa $40 \mu\text{m}$ beträgt. Darüber hinaus applizieren wir einen uniaxialen Druck auf scheibenförmige Gele im vollständig geschwollenen, vollständig entschwollenen und im Koexistenz-Zustand. Durch Messung der Normalkraft und der angelegten Kompression schätzen wir den Elastizitätsmodul für die Gele in diesen verschiedenen Zuständen. Wir behandeln das Gel mit Haut als ein dreischichtiges Verbundmaterial, wobei die Hautdicke auf etwa $49 \mu\text{m}$ geschätzt wird, in guter Übereinstimmung mit den Ergebnissen der Neutronenradiographie. Wir untersuchen auch die innere Struktur der Haut mittels SANS und stellen fest, dass die Korrelationslänge der Haut vergleichbar mit der des entschwollenen Gels ist, was darauf hinweist, dass die Struktur der Haut so dicht ist wie die Phase des entschwollenen Gels. Zusätzlich beobachten wir durch Untersuchung des asymptotischen Verhaltens bei kleinem Impulsübertrag q , die Bildung von kompakten Strukturen mit rauen Oberflächen. Unsere Studie ist vielleicht die erste umfassende Untersuchung der Polymerschicht und liefert eine weitere Schätzung der Hautdicke.

Die Weiterentwicklung dieser Arbeit liegt in der Entwicklung eines Interaktionsmodells für Mikrogele, die in der Regel peripher geladen sind, sodass spontanes Entschwellungsverhalten und nicht-zentrale Kräfte berücksichtigt werden. Darüber hinaus wäre es interessant zu untersuchen, ob die Nichtzentralität der Kräfte mit der Mikrogele-Entschwellung auftritt oder ob sie auch bei niedrigeren Konzentrationen vorhanden ist, bei denen davon ausgegangen wird, dass die Wechselwirkung paarweise erfolgt. Des Weiteren sollten wirklich neutrale Mikrogele, die ohne ionischen Initiator synthetisiert werden, untersucht werden. In diesem Fall kann der Effekt der Mikrogele-Weichheit klarer isoliert werden. Hinsichtlich der Macrogele-Arbeit können zusätzliche Bildgebungstechniken wie Mikroskopie, Neutronentomographie und AFM angewendet werden, um die Hautbildung und -dicke zu analysieren und das Phasenverhalten des Macrogeles bei schneller Erwärmung besser zu verstehen. Die thermodynamische Instabilität des Macrogeles kann für die Materialgestaltung sowie für die Erzielung makroskopischer Formaktuationen genutzt werden und verkörpert das Konzept der extremen Thermodynamik von Macrogelen.

摘要

胶体是悬浮在溶剂中的中微观粒子，表现出具有 $k_B T$ 能量尺度的布朗运动。它们具有重要意义，并且在我们的日常生活和身体中无处不在，存在于血液、牛奶、油漆、化妆品和各种食品等物品中。特别是，胶体可以分为两大类：硬胶体和可压缩的软胶体。由于其可变形的结构，软胶体具有更高的自由度，相比起硬胶体，软胶体在高浓度下会形成一个更加复杂的胶体系统，因此它们在高粒子浓度的情况下的溶胀表现还没有完全被理解。软胶体的丰富膨胀行为使其在科学研究和工业应用中很有利用价值。它们常用于药物输送 [16]、智能涂层 [81]、粘合剂 [191] 和传感技术 [138] 等应用。此外，由于其对刺激敏感的特性，软胶体还被用作学习统计力学 [20]、相变 [188] 和相互作用力 [108] 的模型系统。在本研究中，聚 (*N*-异丙基丙烯酰胺) (pNIPAM) 微凝胶被用作研究软胶体的模型系统。研究了 pNIPAM 微凝胶悬浮液在流体和结晶相中的行为，目标是将观察到的单个粒子的行为与悬浮液联系起来。

当将大颗粒的硬胶体加入到高浓度的较小但在其他方面相同的胶体悬浮液中时，悬浮液的分散性增加，较大的颗粒充当点缺陷会抑制悬浮液的结晶过程 [48]。对于硬胶体，当分散度大于 12% 时，结晶会被抑制。不同的是，对于微凝胶而言，较大的颗粒可以自发地减小至与较小颗粒相当的尺寸，从而减小悬浮液的分散性并消除点缺陷，使得悬浮液能够结晶，而不受最初的高分散性的影响 [80, 150, 149]。这种减小尺寸的现象是由悬浮液中离子引起的渗透压增加触发的。pNIPAM 本是一种不带电的聚合物。然而，由于在微凝胶合成中使用了离子引发剂，要合成完全不带电的 pNIPAM 微凝胶是比较困难的。来自过硫酸铵 (APS) 引发剂的硫酸酯基团带有负电荷会保留在 NIPAM 聚合物链的末端，相关的铵盐确保了电荷中性。出于电荷静电原因，硫酸酯基团预计位于微凝胶的外围，并且由于微凝胶的模糊球结构，包围硫酸酯基团的铵离子形成一个球形壳层的离子云。在足够高的粒子浓度下，这些位于微凝胶表面的离子云开始重叠，使得能级低于 $k_B T$ 的氨离子可以突破静电力变成自由离子，从而增加了悬浮液溶剂的渗透压。当微凝胶外部的渗透压与粒子的体积模量相当或更大时，粒子会被各向同性地压缩 [54, 156, 150]。此外，离子云的存在可以解释在高浓度下观察到的微凝胶悬浮液渗透压显著增

[150, 102]。微凝胶外部离子密度虽然较低，但在决定微凝胶的溶胀行为中起着至关重要的作用；由于影响其多分散性，外部离子会直接决定悬浮液的相行为。影刺理解离子云对于理解微凝胶悬浮液至关重要，尤其是在高浓度下。然而，对微凝胶的对离子云进行直接表征是缺乏的。

在这篇论文中，通过小角中子散射 (SANS) 我们研究了微凝胶对离子云的构型。形状因子可以展开为 $P(q) = F_p^2(q) + 2F_p(q)F_c(q) + F_c^2(q)$ ，其中 $F_p(q)$ 是 pNIPAM 聚合物的散射振幅，包括由引发剂引发的交联剂和带电基团，而 $F_c(q)$ 是离子云的散射振幅。我们制备了两种悬浮液，一种含有 Na^+ 离子，另一种含有 NH_4^+ 离子。利用这些离子的散射长度密度的差异，以获得提供关于离子云结构和微凝胶中带电基团排列的结构信息的扩展散射信号。结果表明，离子云确实位于微凝胶的外围，符合粒子合成的预期。这一结果也支持先前建立的关于在高浓度下微凝胶减小尺寸的理论，该理论将粒子的柔软性和表面电荷与相行为联系起来。

因为柔软度会影响悬浮液的相行为，下一章进一步研究了不同柔软度的微凝胶对离子云配置的依赖性。微凝胶的柔软度由合成中使用的交联剂量控制。最柔软的微凝胶被称为超低交联 (ULC)，通过无交联剂的原子提取反应合成。先前的研究报告指出，ULC 微凝胶和使用交联剂合成的微凝胶都能在随机最密堆积 ϕ_{rcp} 以下自发减小尺寸。此外，观察到交联密度较高的微凝胶在高浓度下减小尺寸较少，并且更容易在更高浓度下变形或相互渗透 [29, 155, 135]。这里提到的行为取决于对离子云的渗透，暗示了对不同柔软度的微凝胶的离子云配置允许理解微凝胶减小尺寸机制的柔软度依赖性。在本研究中，球形壳模型被证明对所有含有交联剂的微凝胶都是有效的；然而，在广义体积分数 ζ 较高时，该模型已不足以描述最硬的颗粒的变形。对于 ULC 微凝胶来说，离子云的信号较不明显。可能的原因是由于缺乏外部交联剂，ULC 微凝胶的内部结构可能更均匀，因此核-壳结构定义较不明显。

通过小角中子散射 (SANS)，我们研究了微凝胶的自发消溶胀行为和对离子云的宽度以及它们与悬浮液的多分散性和结构的关系。在这项工作中，使用 2 wt.% 的交联剂合成了不同浓度的微凝胶。我们使用广义体积分数 ζ 来描述悬浮液浓度。 ζ 反映了完全膨胀的微凝胶所占的体积，并且由于微凝胶可以消溶胀或相互渗透， ζ 可以大于一。在此实验中，微凝胶样品的广义体积分数 ζ 范围从 $\zeta = 0.01$ 到 $\zeta > 1.0$ 。我们发现所有微凝胶在 ζ_c 处开始减小尺寸，其中 $\zeta_c < \phi_{\text{rcp}}$ 。由于是在随机最密堆积 ϕ_{rcp} 以下发生的减小尺寸行为，消溶胀因此不能归因于相邻微凝胶之间的直接相互作用。将微凝胶半径加上离子云的厚度 σ_{ic} ，我们可以计算有效微凝胶半径 $R_{\text{eff}} = R_{\text{SANS}} + \sigma_{\text{ic}}$ 。通过 R_{eff} ，我们进一步计算了这些微凝胶悬浮液的有效体积分数 ϕ_{eff} 。在 ζ_c 处，离子云直接接触和渗透，有效体积分数应 $\phi_{\text{eff}} = 1$ 。所以 $\phi_{\text{eff}} = 1$ 的限制条件下，我们反向计算了 σ_{ic} 。所得结果与我们的 SANS 测量和在双峰 pNIPAM 悬浮液中的先前估计结果 [150, 54] 吻合良好。此外，观察到在所

有样本中，随着 ζ 的增加，悬浮液的多分散性以及微凝胶半径一致减小，由此说明较大的颗粒缩小到与较小微凝胶相当的尺寸，进而导致悬浮液在高粒子浓度下变得更加单分散。分散性对硬胶体和软胶体的相行为都很重要。然而，对于软胶体，分散性的作用不同，因为分散性可能随着浓度的变化而改变，从而溶胀可能会影响悬浮液的相行为。因此，在形状因子 $P(q)$ 和结构因子 $S(q)$ 中都考虑分散性是获得可靠结果的重要因素。

材料中原子之间的相互作用会反映在材料的宏观性质上，包括所有的弹性性质。因此，预期微凝胶周围的离子云可能会影响悬浮液的行为，特别是在足够高浓度下微凝胶充当形成晶体的“原子”的晶态状态。由于微凝胶足够大，我们可以直接在光学显微镜下观察，从而更加直接的研究微凝胶晶体的行为。为了研究自由离子对微凝胶相互作用的影响，我们使用共焦显微镜研究了 pNIPAM 晶体的简正模式，即晶体中的基本晶格激发状态。本工作中使用的微凝胶是通过 pNIPAM 共聚丙烯酸 (AAC) 生成的并且含有荧光核心。通过共焦显微镜发现，微凝胶晶体具有面心立方 (fcc) 结构。在晶格中的微凝胶的简正模式可以从显微镜图像的时间序列中获得。微凝胶偏离其晶格位置的程度表明，微凝胶晶体基本上表现为谐振晶体，表明均分定理可以应用于测得的简正模式。粒子对之间的相互作用力由简正模式的力常数来表征，并通过比较最近邻和次近邻之间的力常数，可以得出微凝胶之间的相互作用力是非中心的。非中心的相互作用力在由带电硬胶体组成的晶体中也被报道为重要，其中多体相互作用也十分重要 [140]。从这里呈现的工作和先前的研究中，已经显示了离子云在微凝胶外围的存在，离子可以由于离子云的渗透而突破静电力进而探索悬浮体积；因此，微凝胶晶体应该类似于带电硬球晶体 [140] 甚至金属 [111, 160]。关键区别在于，由于柔软性，晶体状态下的微凝胶可以改变其尺寸。结果表明，在微凝胶浓缩悬浮液中，晶体状态下的微凝胶相互作用不能足够地通过成对势能（比如 Derjaguin-Landau-Verwey-Overbeek (DLVO) 势能，该势能通过叠加径向对称的两两相互作用得到）来描述。我们的工作表明，对软而可变形的微凝胶的高粒子浓度的悬浮液来说，多体相互作用和非中心力是重要的，而这是微凝胶外围的自由离子的带来的直接结果。

pNIPAM 的温度敏感性对于微观和宏观水凝胶也是同等重要的。在这项工作中，我们研究了 pNIPAM 水凝胶的热力学不稳定性。水凝胶同样也是一种对刺激敏感的材料，在组织再生 [8]、CO₂ 捕集 [103]、化妆品 [110] 和水处理 [196] 等领域都有很大的影响。当温度快速升至 $T \approx 32^\circ\text{C}$ 以上时，观察到水凝胶会相变到一个共存态，该状态可以用一个具有两个最小值的自由能来描述分别对应于溶胀态和消溶胀态。这是由于在凝胶表面形成了一个可以约束凝胶体积并防止溶剂离开凝胶内部的高分子链皮肤。这层皮肤阻止了溶胀的内部达到减小状态，并且此相共存态对应了在快速升温后水凝胶恒定体积下的自由能最小值。在这种共存态中，表面皮肤由于其结构不同于水晶胶依然溶胀的内部，因此会产生应力。由于不同形态

的水凝胶会在皮肤生成后产生不同的应力，因此具有皮肤和肿胀内部的水凝胶亚稳态还取决于凝胶的宏观形状，这使得在快速升温后的水凝胶成为一种十分有趣但尚未完全理解的材料。尽管皮肤起着重要作用，但关于其性质知之甚少。在这里，我们使用中子成像研究了柱状凝胶的皮肤厚度，该成像捕捉了凝胶表面与凝胶内部的边界，指示皮肤的厚度约为 $40\ \mu\text{m}$ 。此外，我们对完全溶胀、完全消溶胀和带有皮肤的溶胀盘状凝胶施加了单轴应变。通过监测对施加应变的正向力响应，我们估算了这些不同状态的凝胶的杨氏模量。我们将皮肤膨胀的凝胶视为三层复合材料，其中皮肤的厚度估计约为 $49\ \mu\text{m}$ ，与中子成像结果相吻合良好。我们还通过小角中子散射研究了皮肤的内部结构，并发现皮肤的相关长度尺寸与完全消溶胀的凝胶相当，表明皮肤的结构与失水的凝胶相一样致密。此外，通过检查在低动量转移 q 处的渐近行为，我们观察到了具有粗糙表面的紧凑结构的形成。我们的研究可能是对聚合物凝胶皮肤的首次全面调查，进一步提供了对皮肤厚度的估算。

这项工作揭示了微观性质（例如微凝胶的离子云和大型凝胶的皮肤结构）与宏观材料性质之间的联系，包括微凝胶胶体晶体的弹性和宏观水凝胶的形状和弹性性质。对于容易改变大小或形变的软材料，这种联系通常不太清楚。有必要进一步探索微观和宏观性质之间的相互作用。其中一部分将涉及为微凝胶开发一种包含了自发减小行为和非中心力的相互作用模型。此外，我们还要调查非中心作用力是否伴随着微凝胶的减小而出现，或者是否在较低浓度时也存在。研究使用电中性的引发剂合成的真正中性微凝胶将是一个有趣的方向，这可以更严谨地分离微凝胶柔软性的影响，并为了解自由离子在微凝胶相互作用中的作用提供更深入的理解。关于水凝胶方面的工作，我们可以采用显微镜、中子层析和原子力显微镜等成像技术来分析皮肤的形成和厚度，并更好地理解在快速升温下宏观凝胶的相共存行为。水凝胶的热力学不稳定性可以用于材料设计以及实现宏观形状驱动，体现了宏观凝胶的极端热力学概念。总的来说，实验研究和建模工作的结合将有助于更全面地理解微凝胶和宏观凝胶对外部刺激的复杂响应行为。

Contents

Abstract	ii
Zusammenfassung	viii
摘要	xiv
1 Microgels	2
1.1 Colloids	2
1.2 Microgels	3
1.3 Microgel synthesis	5
1.4 Swelling thermodynamics	8
1.4.1 Polymer/Solvent mixing	9
1.4.2 Chain elasticity	11
1.4.3 Ionic effects	15
1.4.4 Equation of state	16
1.5 Poisson-Boltzmann Calculations	17
1.6 Summary	19
2 Neutron scattering	20
2.1 Introduction	20
2.2 Elastic scattering from a single scatterer	21
2.3 Scattering from a collection of scatterers	22
2.4 The differential cross-section	26
2.5 Form factor and structure factor	27
2.6 Small-angle neutron scattering (SANS)	31
2.7 Experimental aspects of SANS	32
2.8 Summary	35

3	Experimental characterization	36
3.1	Introduction	36
3.2	Generalized Volume Fraction ζ	36
3.3	Viscosimetry	38
3.4	Dynamic light scattering	41
3.4.1	DLS data analysis	44
3.5	Summary	46
4	Spontaneous deswelling of microgels	48
4.1	Abstract	49
4.2	Introduction	49
4.3	Microgel suspensions	50
4.4	Small-angle neutron scattering (SANS)	53
4.5	Results and discussion	56
4.6	Conclusions	62
5	Measuring the counterion cloud of soft microgels using SANS with contrast variation	64
5.1	Abstract	65
5.2	Introduction	65
5.3	Method	67
5.4	Results	68
5.5	Discussion	75
5.6	Appendices	78
5.7	Particle softness dependence of counterion clouds	94
5.7.1	Summary	100
6	Lattice vibrations in microgel crystals studies using confocal microscopy	101
6.1	Introduction	101
6.2	Confocal microscopy	102
6.3	Fluorescent microgel	104
6.4	Data Acquisition	105
6.5	Particle finding method	106
6.5.1	Particle tracking	109
6.5.2	Local Bond-order parameters	111
6.6	The Harmonic Approximation	113

6.6.1	Force constants	115
6.6.2	Lattice vibrations	116
6.7	Measuring the dynamic matrix	118
6.7.1	Displacement modes with polarization perpendicular to the scan direction	119
6.7.2	Measurement of the eigenvalues of the dynamic matrix	124
6.8	Lattice Elasticity	125
6.8.1	Wave propagation	126
6.8.2	Strain and stress relation	128
6.8.3	Isotropic initial pressure	128
6.8.4	Elastic constants	130
6.9	Results and discussion	131
7	Rapid-heating-induced phase-coexistence of pNIPAM hydrogel	140
7.1	Introduction	140
7.2	Skin formation under rapid heating	142
7.3	Macrogel under an uni-axial compression	143
7.3.1	Fully swollen gel	145
7.3.2	Fully deswollen gel	146
7.3.3	Swollen gel with skin	148
7.3.4	Estimation of the skin thickness	149
7.4	SANS: Investigation of the polymer skin	151
7.4.1	Scattering model of polymer gels	153
7.4.2	Characterization of the hydrogel internal structure	154
7.5	Neutron imaging: direct visualization of the polymer skin	157
7.5.1	Data reduction	159
7.6	Summary	163
8	Conclusion and Outlook	164
	Curriculum Vitae	184
	List of Publications	186
	Acknowledgements	188

Chapter 1

Microgels

1.1 Colloids

Colloids are a type of mixture in which stable colloidal particles are homogeneously dispersed in a solvent and exhibit Brownian motion with energy scale $k_B T$. The particle size is generally between 1 and 1000 nm. Colloids are ubiquitous in our daily lives. Examples are paints (solid paint particles in liquid), milk (fat globules and protein particles dispersed in water), foams having Brownian bubbles and drops, etc. In addition, colloids are of great interest in scientific research, as they exhibit fascinating single-particle and collective behavior that is analogous to that of atomic or molecular systems at different concentrations, temperature, and pressure. This allows using them as a model systems for the study of Brownian motion, phase transitions, rheology, optical properties of matter, etc.

Broadly speaking, there are two categories of colloids, namely hard-incompressible colloids and soft-compressible colloids. Note that hard spheres are the most important model system for hard colloids. A suspension of hard spheres exhibits rich phase behavior when the volume fraction ϕ increases, where the liquid phase transition to the coexisting liquid-solid phases at $\phi \approx 0.49$ [137, 74], the freezing point of the system indicated by the hard-sphere model. When the volume fraction is further increased, the system undergoes crystallization and reaches the solid phase at the melting point at $\phi = 0.54$, [137, 74]. Depending on the history of the system and the suspension size polydispersity, the system may also undergo a glass transition at $0.58 < \phi < 0.63$. Due to the incompressibility of hard colloids, the theoretical limit of the highest volume fraction achievable is close packing, $\phi \approx 0.74$, which is difficult to reach in real experiments. If disordered, however, the limit is random close packing $\phi \approx 0.64$. In contrast, soft-compressible colloids can reach a higher

value of ϕ , since they are capable of deswelling, deforming, and/or interpenetrating with neighboring particles. Although soft colloids share certain similarities with their hard counterparts, they also exhibit distinct behavior. For example, while the crystallization of hard colloids is typically suppressed when the size polydispersity reaches 12%, some soft colloids can still crystallize with a 19% polydispersity in size [150]. Their softness induces extra degrees of freedom within the internal structure of the particles. This makes the behavior of soft colloids more complex and diverse, particularly at high-volume fractions where the deformability of the particles correlates with the suspension structure. As a result, there are many aspects of the phase behavior of soft particles that are still not well understood.

In this work, we use colloidal polymer gels, microgels, to study the phase behavior of soft colloids, especially at high concentrations. Since microgels can deswell and deform, the characterization of the microgel volume fraction relies on a generalized volume fraction ζ , defined in terms of the dilute microgel size. The derivation and details of ζ will be discussed later in Section 3.2.

1.2 Microgels

Microgels are one good example of soft colloids, they are dispersed in a solvent and swollen by the solvent, as is the case for hydrogels. Due to the particle synthesis protocol, microgels contain a polymer-dense core and a fuzzy shell formed by dangling chains and a network that is less cross-linked than the core, as illustrated in Fig.1.1. Unlike surfactant micelles, where the aggregation numbers changes under different conditions such as concentration and temperature [200], microgels are crosslinked and cannot fall apart. Hence, they are soft and flexible, but stable. The properties of a microgel are further determined by the swelling ratio of the microgel core and shell. Due to the limited degree of swelling, polymer or surfactant micelles, although having a similar internal structure, cannot be characterized as microgels. What makes microgels interesting is their ability to combine certain properties of macrogels with useful aspects of colloidal dispersions. Both macrogels and microgels can reversibly swell and deswell in response to changes in external stimuli, such as temperature [57, 83, 132], hydrostatic pressure [101, 99], pH [3, 26], solvent composition [177, 4], concentration [77], and electromagnetic fields [126, 179, 90]. Unlike macrogels, microgels have a much shorter response time to external stimuli, because of the large surface-to-volume ratio facilitating mass transport in and out of the microgel, ultimately making the equilibrium state of the microgels more easily approachable. Due

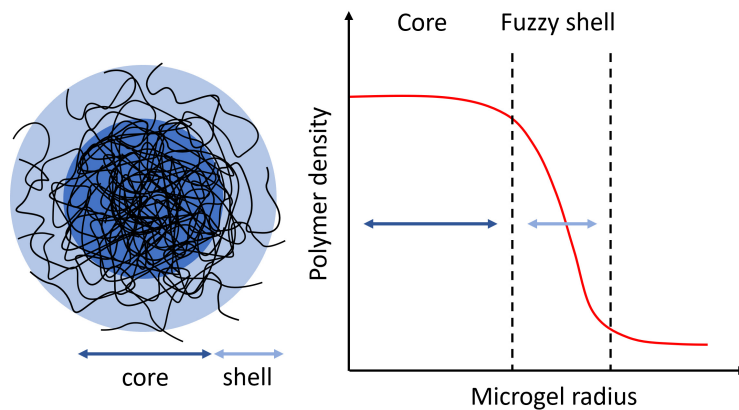


Figure 1.1: Sketch of a microgel (left): darker blue color highlights the polymer-dense core and lighter blue indicates the fuzzy shell. Sketch of polymer density as a function of microgel radius (right), highlighting the polymer-dense core and polymer-loose fuzzy corona.

to their deformability [148, 189], their stimuli-sensitive nature, responsiveness, and tunability, microgels are widely used in several technological areas, including drug delivery [120, 157], optical sensors [50], water purification [118], uses as absorbents [197], in the oil industry [12], and in cosmetics [172]. At the same time, microgels, along with other colloids, are of great interest in fundamental studies obtaining the behavior of soft colloids [88, 169, 127]. In the fully swollen state, the open internal structure makes microgels very soft and easy to deform. On the contrary, in the deswollen state, microgels approach the behavior of hard particles. Therefore, microgels are useful for studying the distinct behavior of soft spheres, as well as the transition from soft to hard-sphere behavior.

In this work, we focus on investigating the phase behavior of microgels at increasing concentration, reflecting the microgel number density. To determine the concentration, and then the number density of microgels, one has to know the mass of a single microgel, the mass of all particles, and the total volume. However, as a result of the fuzzy periphery of microgels, their volume is not straightforward to quantify. Furthermore, it has been reported that microgels deswell with increasing concentration. This makes the quantification of the microgel volume fraction ϕ very difficult. Therefore, an effective volume fraction, ζ , is used. ζ is calculated on the basis of the volume occupied by a microgel in the dilute state. If the solvent conditions are good for the microgel to be swollen, the microgel corresponds to the swollen radius, R_{sw} . Note that $\phi = \zeta$, if the microgels are fully swollen, and $\phi < \zeta$ when particles are forced to deswell, as they occupy less volume than the fully swollen

particles. As a result, microgel deswelling allows $\zeta > 1$, even if the true volume fraction is limited to $\phi \leq 1$.

1.3 Microgel synthesis

A good synthesis protocol should have good control over colloidal stability, microgel size distribution, and functional group distribution within the microgel network. There are typically three ways to synthesize microgels from macrogels, polymer chains, and monomers. First, it is possible to mechanically grind the macrogels to form microgels; however, this method tends to produce microgels with irregular sizes [60, 114]. Second, two solutions of oppositely charged polymer chains can be mixed together to allow the polymers to become chemically cross-linked to form microgels [97, 37]. The third method is the synthesis of microgels from monomers, which is based on mixing reagents in a solvent [65]. In our case, the solvent is distilled, deionized water, and the reagents include monomers, cross-linking agents, and water-soluble free radical initiators, such as ammonium persulfate, and surfactants. To ensure the formation of discrete microgels, it is the key that the polymers formed are under bad solvent condition because the soluble polymers will form macrogels instead. Additionally, surfactants are commonly utilized to control microgel size. We use a precipitation polymerization synthesis in the presence of surfactants [5]. The surfactant used is sodium dodecyl sulfate (SDS, $\text{CH}_3(\text{CH}_2)_{11}\text{OSO}_3\text{Na}$), and it is important to restrict the size of the microgels and prevent the formation of macrogels [5, 112]. Depending on the concentration of the cross-linker, microgels with different softness can be produced [159, 131]. The structural formulae of the key ingredients for microgel synthesis are shown in Fig.1.2.

For our synthesis, the reactor contains water. Water-soluble monomers are N-Isopropyl- acrylamide (NIPAM, $(\text{C}_6\text{H}_{11}\text{NO})_n$) and the cross-linking agent is N,N'-methylene bis (acrylamide) (BIS, $(\text{C}_7\text{H}_{10}\text{N}_2\text{O}_2)$). To ensure water insolubility of the reactant polymer and particles, the synthesis is carried out at 70°C , above the lowest critical solution temperature (LCST) of pNIPAM, where polymers are water-insoluble [67]. Therefore, this protocol is termed "precipitation polymerization". To obtain microgels, the persulfate of the initiator decomposes into sulfate radicals that initiate polymerization. The sulfate groups then connect at the polymer chain ends to terminate the polymerization and provide one charge group at the chain-end/water interface. As a result of the water insolubility, the polymer chain phase separates and forms precursor particles that are colloiddally unstable and are able to

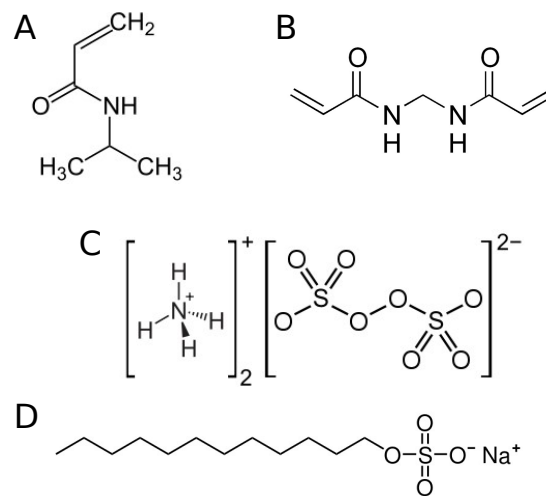


Figure 1.2: The image is taken from [154]. The chemical structure formulae of materials for SEP recipe: (A) N-Isopropylacrylamide (NIPAM, $(C_6H_{11}NO)_n$). (B) N,N'-methylene bis(acrylamide) (BIS, $(C_7H_{10}N_2O_2)$). (C) Ammonium persulfate (APS, $(NH_4)_2S_2O_8$). (D) Sodium dodecyl sulfate (SDS), $CH_3(CH_2)_{11}OSO_3Na$

coalesce with each other. Charge groups tend to concentrate at the particle/water interface due to electrostatic reasons [122]. As precursor particles grow larger, the surface charge density increases to the point that the particles are colloidally stable [133]. Stable particles are called primary particles. The newly formed precursor particles are then aggregated with the primary particles to form microgels containing surface charges from the initiators, similar to the primary particles, Fig.1.3. To control the microgel size and its size distribution, the addition of surfactants, such as SDS, is needed for the synthesis. SDS can stabilize the primary particles and moderate the further deposit of precursor particles. As a result, for the same amount of monomers, a larger number of primary particles with a smaller radius are synthesized compared to those prepared without SDS, Fig.1.4. The smaller primary particles also result in a more monodisperse suspension. Subsequently, we clean the microgel suspension to remove excess SDS surfactant and unreacted monomers at the end of the synthesis [43]. The recipe requires adding monomers, crosslinkers, and initiators all at once before the polymerization starts. As a result, polymer chains synthesized at the earlier stage contain more crosslinkers because of the initially high crosslinker concentration, which allows more polymers to be linked. Then, these polymers constitute the following primary particles. In the later stage, polymers that contain fewer cross-linkers as a result of the lower cross-linker concentration form precursor particles that are less cross-linked and more swollen. Subsequently, the precursor particles deposit on the primary particles. This gives the microgel a polymer-dense

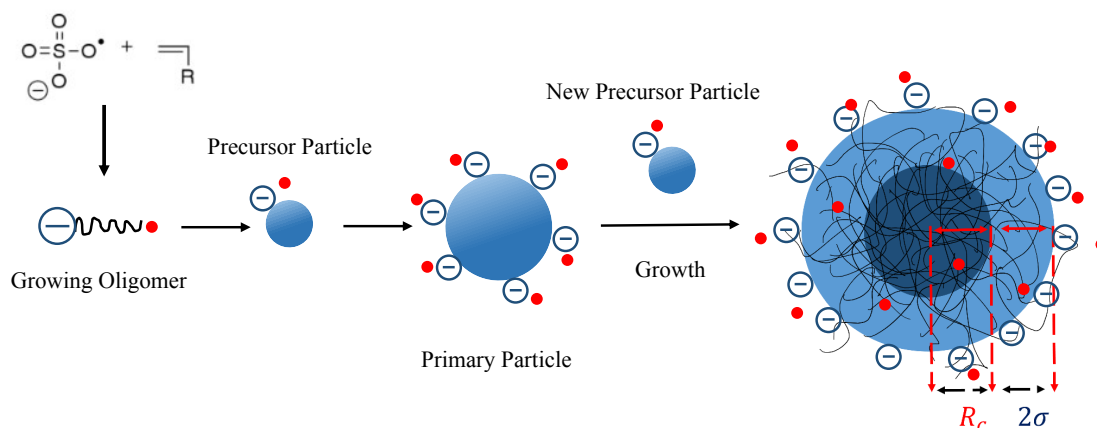


Figure 1.3: Microgel synthesized with surfactant-free emulsion polymerization (SEP). The growing oligomer (polymer chain) forms the precursor particle. The coalescence of the precursor particles forms the primary particle. The newly formed precursor particles are further deposited on the primary particle to form the microgel. Due to the reduction in crosslinker concentration, the microgel obtains the core-shell structure; the polymer-dense core with radius R_c and polymer-loose shell with width 2σ . For electrostatic reasons, the negative charge groups from the initiators concentrate in the periphery of the particles, along with the associated counterion (red dot).

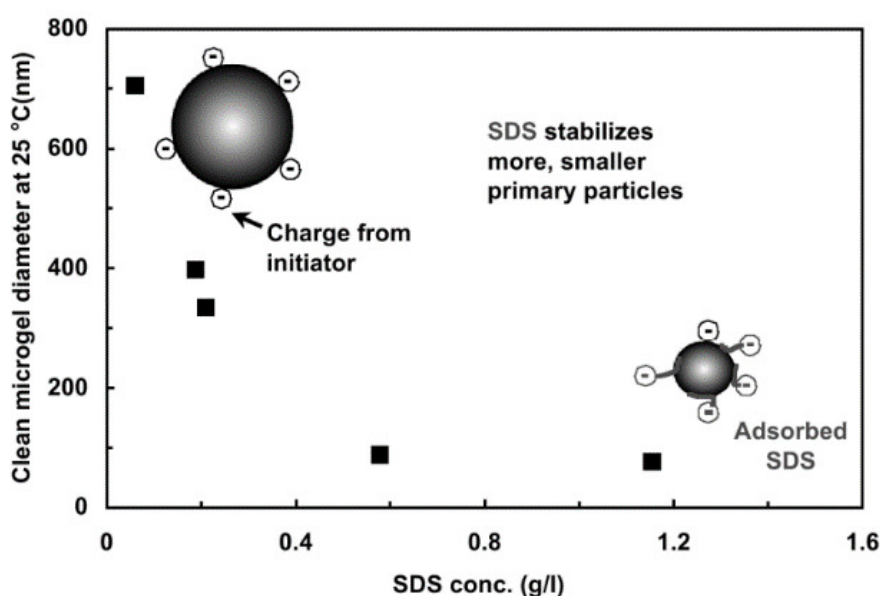


Figure 1.4: The figure is taken from [43]. Microgel sizes are regulated by the SDS concentration.

core and a polymer-loose shell, associated with two length scales, core radius R_c and shell width σ_s , shown in Fig.1.3.

1.4 Swelling thermodynamics

This section follows the derivation in previous works [154, 167, 151]. Microgels are colloids formed by cross-linked polymer networks. They are well known for their stimuli-sensitive nature and volume phase transition: Microgels can swell and deswell reversibly in response to external stimuli such as temperature, pH, ion, and polymer concentrations, factors that are able to alter the balance between repulsive and attractive interactions between polymers and solvent molecules and exert osmotic pressure [38, 178]. In microgel suspensions, four interactions control the swelling behavior of the microgel, namely the van der Waals interactions, hydrogen bonding, hydrophobic and electrostatic interactions [165]. The van der Waals interaction is most commonly attractive and results from the multipoles of molecules [79]. Hydrogen bonding is an attractive essential interaction that arises from the interaction between the polar group of the monomer and that of the solvent molecules. When a water molecule is close enough to polar groups, hydrogen bonds are formed with elements having high electronegativity, such as oxygen [79]. For this interaction, pNIPAM microgels swell when the solvent quality is good and deswell when the temperature increases, as hydrogen bonds break as a result of thermal agitation.

On the contrary, the hydrophobic interaction arises from the interaction between nonpolar groups. This interaction is strengthened at high temperatures when the solvent quality is low. It is intuitive to imagine that the polymer chains are more willing to interact with each other than with solvent molecules. As a result, solvent molecules are expelled from the polymer network and the particle deswells [79]. In addition, the fixed charge groups on the polymer backbone control the electrostatic interaction. Depending on the distribution of the charged groups in the polymer network and the presence of ions in the solvent, an imbalance between the distribution of ions inside and outside the microgel can be created, thereby inducing a change in the particle size; this will be explained in much more details in Chapters 4 and 5. Finally, the randomly distributed crosslinks result in a permanent elastic polymer network that help the microgel to recover its origin size and structure after being deformed. As a result, the chain elasticity should be considered along with the interaction forces resulting from the polymer-solvent mixing and charges. The interactions mentioned above are well described in terms of osmotic pressure and an

equation of state that can be written as: $\Pi_{\text{in}} = \Pi_{\text{mix}} + \Pi_{\text{elastic}} + \Pi_{\text{ionic}} = \Pi_{\text{out}}$. At equilibrium, assuming that the osmotic pressure outside the particle is 0, we have that $\Pi_{\text{in}} = 0$. Depending on external stimuli, Π_{in} could be positive or negative, causing the particle to swell or deswell until a new equilibrium balance is reestablished. In the following paragraphs, we will discuss each term in the equation of state from a thermodynamic point of view. The goal is to provide insight and a starting point for understanding the intrinsic nature of microgels.

1.4.1 Polymer/Solvent mixing

We can treat a microgel suspension as a binary mixture of polymer chains and solvent molecules. If the solvent quality is good, the polymer and solvent molecules are uniformly mixed, resulting in a homogeneous mixture. On the contrary, if the solvent quality is poor, the microgel suspension phase separates into a polymer-rich (deswollen microgels) and a solvent-rich phase, leading to a heterogeneous mixture. Moreover, depending on how fast the solvent quality changes, simulation work reported that microgels may experience an inhomogeneous phase transition, where polymer clusters form at the microgel periphery. As a result, the solvent is trapped inside and a change in particle size is prohibited [124].

To characterize the free energy associated with the configuration of the polymer and solvent molecules in the mixture, we need to calculate the change in energy ΔU_{mix} and the change in entropy ΔS_{mix} due to the polymer/solvent mixture. To do that, we can use the lattice model proposed by Flory [46], in which we consider the microgel suspension containing n_1 solvent molecules and n_2 polymer chains, each with x monomers. Therefore, the total number of lattice sites is $n_0 = n_1 + x n_2$. Using Boltzmann's entropy formula, we can write the entropy of the polymer solution as $S_{\text{mix}} = k_B \ln \Omega_{\text{mix}}$, where Ω_{mix} is the number of configurations of the monomers of polymers and solvent molecules occupying the lattice sites, calculated using the permutation formula. It is assumed that there is no spatial correlation for molecules, and microstates are equally probable. k_B is the Boltzmann constant. The reference state is the entropy of pure solvent molecules and pure polymer chains arranged in a crystalline state. By subtracting S_{mix} from the reference state, we can calculate the entropy change due to mixing [46, 143].

$$\Delta S_{\text{mix}} = -k_B(n_1 \ln \phi_1 + n_2 \ln \phi_2) \quad (1.1)$$

where $\phi_1 = n_1/n_0$ and $\phi_2 = x n_2/n_0$ are the volume fractions of the solvent and

polymer, respectively. The sum of ϕ_1 and ϕ_2 equals 1, due to the incompressibility assumption.

During the mixing process, polymer-polymer and solvent-solvent contacts break, while polymer-solvent contacts form. Since the interaction between species in the mixture is short-ranged, we consider only the breaking and forming of contacts between neighboring lattice sites. Thus, we describe this process with equality: $\frac{1}{2}(s-s) + \frac{1}{2}(p-p) \rightarrow (p-s)$, where ss, pp, and sp represent the contacts between two solvent molecules, two polymer monomers, and a solvent molecule and a polymer monomer, respectively. The energy associated with each bond is e_{ss} , e_{pp} , and e_{sp} . A given lattice site can have $z\phi_1$ solvent neighbors and $z\phi_2$ polymer neighbors, where z is the lattice coordination number. We can then calculate the energy change due to mixing by subtracting the energy of the pure solvent and pure polymer from the energy of the mixture.

$$\begin{aligned}\Delta U_{\text{mix}} &= \frac{z}{2}(\phi_1^2 e_{ss} + \phi_2^2 e_{pp} + 2\phi_1\phi_2 e_{ps}) - \frac{z}{2}(\phi_1 e_{ss} + \phi_2 e_{pp}) \\ &= \frac{z}{2}\phi_1\phi_2[2e_{ps} - (e_{ss} + e_{pp})]\end{aligned}\tag{1.2}$$

The energy change associated with the mixing per monomer-solvent contact is then given by $\Delta e = e_{ps} - \frac{1}{2}(e_{ss} + e_{pp})$. Importantly, the change in energy Δe is determined by the change of both the energetic part Δe_U and the entropic part Δe_S . Then, $\Delta e = \Delta e_U - T\Delta e_S$. To establish a connection with solvent quality, we introduce Flory's solvency parameter, defined as $\chi_1 = \frac{z\Delta e}{k_B T}$. Substituting Δe into χ_1 , we obtain $\chi_1 = z \frac{\Delta e}{k_B T} = \frac{ze_U}{k_B T} - \frac{z\Delta e_S}{k_B}$, which reflects both the energetic and entropic changes resulting from the breaking and formation of solvent-polymer contacts. Consequently, we can rewrite Equation 1.2 in terms of the Flory solvency parameter, χ_1 , as follows [46]:

$$\Delta U_{\text{mix}} = k_B T \chi_1 n_1 \phi_2\tag{1.3}$$

where $k_B T \chi_1 n_1 = \frac{z}{2}\phi_1[2e_{ps} - (e_{ss} + e_{pp})]$. During the mixing process, where the temperature and volume of the system are kept constant, the Helmholtz free energy change, ΔF_{mix} , can be expressed as follows [198]:

$$\Delta F_{\text{mix}} = \Delta U_{\text{mix}} - T\Delta S_{\text{mix}} = k_B T(n_1 \ln\phi_1 + n_2 \ln\phi_2 + \chi_1 n_1 \phi_2)\tag{1.4}$$

Additionally, since mixing occurs without change in pressure, the Helmholtz free energy change is equivalent to the change in the Gibbs free energy, $\Delta F_{\text{mix}} = \Delta G_{\text{mix}}$ [46, 143, 182]. Furthermore, the alteration in the composition of the pure solvent

resulting from the mixing process leads to a modification in the osmotic pressure. We can describe the osmotic pressure, Π , required to equilibrate the polymer-solvent mixture with the pure solvent using the excess chemical potential, $\Delta\mu_1$, as follows:

$$\mu_1^{\text{pure}}(P, T) = \mu_1^{\text{pure}}(P + \Pi, T) + \Delta\mu_1 \quad (1.5)$$

In this equation, $\mu_1^{\text{pure}}(P, T)$ represents the chemical potential in the pure solvent, while $\mu_1^{\text{pure}}(P + \Pi, T)$ corresponds to the chemical potential of the solvent molecules in the polymer/solvent mixture. At a constant temperature and volume, we can express $\mu_1^{\text{pure}}(P + \Pi, T)$ using the Gibbs-Duhem equation, $Nd\mu = -SdT + VdP$ as [182]:

$$\begin{aligned} \mu_1^{\text{pure}}(P, \Pi, T) &= \mu_1^{\text{pure}}(P, T) + \int_P^{P, \Pi} \frac{\partial \mu_1^{\text{pure}}}{\partial P'} dP' \\ &= \mu_1^{\text{pure}}(P, T) + \nu_1 \Pi \end{aligned} \quad (1.6)$$

By comparing Equation 1.5 and Equation 1.6, one can readily observe that

$$\Pi = \frac{-\Delta\mu_1}{\nu_1} \quad (1.7)$$

The negative sign indicates that a decrease in the chemical potential results in an increase in osmotic pressure. Utilizing the thermodynamic relationship between chemical potential and Gibbs free energy $\mu_1 = \left(\frac{\partial G}{\partial n_1}\right)_{T, P, n_2}$, we can express the osmotic pressure due to mixing as follows [46, 143]:

$$\begin{aligned} \Pi_{\text{mix}} &= -\frac{1}{\nu_1} \left(\frac{\partial \Delta G_{\text{mix}}}{\partial n_1}\right)_{T, P, n_2} \\ &= -\frac{k_b T}{\nu_s} [\phi_2 + \ln(1 - \phi_2) + \chi_1 \phi_2^2] \end{aligned} \quad (1.8)$$

1.4.2 Chain elasticity

A polymer chain is defined as a polymer strand between two cross-linkers. The cross-links present within the gel network contribute to its elasticity, and we need to consider the change in free energy associated with the restoring forces induced by chain deformation. Assuming that L represents the deformation and f represents the resulting restoring force, we can express the free energy as $dF = SdT + PdV + fdL$. The restoring force can be derived as $f = \left(\frac{\partial F}{\partial L}\right)_{T, V} = \left(\frac{\partial(U-TS)}{\partial L}\right)_{T, V} = \left(\frac{\partial U}{\partial L}\right)_{T, V} - \left(\frac{\partial S}{\partial L}\right)_{T, V}$, indicating that the restoring force comprises energetic and entropic contributions. However, the energetic contribution is much less dominant than the

entropic contribution, and polymer chains are taken as ideal and non-interacting [143, 141]. Therefore, we only consider the entropic contribution in this case. To determine the change in entropy due to deformation, we make a few assumptions. First, we assume that the deformation of a single chain is representative of the entire polymer network. Second, we assume that cross-linking during synthesis is random and that the distribution of the polymer's end-to-end distance vector ($\vec{r}_{c,i}$) follows the Gaussian distribution $G(x, y, z)$ [46]. The Gaussian probability density $G(x, y, z)$ is defined as:

$$G(x, y, z)dxdydz = G(x)G(y)G(z)dxdydz = \left(\frac{\beta}{\pi^{1/2}}\right)^3 e^{-\beta^2 r^2} dxdydz \quad (1.9)$$

where $r = |\vec{r}|$ is the amplitude of the chain-end position \vec{r} and $r^2 = x^2 + y^2 + z^2$. β is a constant determined by the chain segment length l and number of bonds n . Under a homogeneous stain, the change in the coordinates of the cross-linked site relative to the others must change due to the same factors. As a result, for a chain i with an end-to-end vector \vec{r}_i and components x_i , y_i , and z_i after deformation must have had coordinates $\frac{x_i}{\alpha_x}$, $\frac{y_i}{\alpha_y}$, and $\frac{z_i}{\alpha_z}$ before deformation, where α_x , α_y , and α_z are the deformation ratios in the x -, y -, and z -direction, respectively. In addition, it is assumed that the deformation is isotropic. The number v_i of chains with end-to-end components changing from $x \rightarrow x + \Delta x$, from $y \rightarrow y + \Delta y$, and from $z \rightarrow z + \Delta z$ after deformation can be expressed via the components of the undeformed state:

$$v_i(x_i, y_i, z_i) = N G\left(\frac{x_i}{\alpha_x}, \frac{y_i}{\alpha_y}, \frac{z_i}{\alpha_z}\right) \frac{\Delta x \Delta y \Delta z}{\alpha_x \alpha_y \alpha_z} \quad (1.10)$$

where N is the total number of chains and $\frac{\Delta x \Delta y \Delta z}{\alpha_x \alpha_y \alpha_z}$ represents the volume segment of the un-deformed chain-end. The configurational entropy of the deformed polymer network S_1 , where the homogeneous deformation is defined as $\vec{r}_{c,i}\left(\frac{x_{c,i}}{\alpha_x}, \frac{y_{c,i}}{\alpha_y}, \frac{z_{c,i}}{\alpha_z}\right)$ to $\vec{r}_{c,i}(x_{c,i}, y_{c,i}, z_{c,i})$, where α_i represents the deformation ratio in the i direction. The entropy in the undeformed state S_2 corresponds to $\alpha = 1$. The change in configurational entropy due to network deformation can be calculated as $\Delta S_{el} = S_1 - S_2$. Two conditions are needed to define a valid deformed network: (1) The chain vector for the V_c number of chains must have a proper chain vector distribution, which means that the end-to-end distance must satisfy the Gaussian distribution. (2) Two cross-linking sites are adjacent to each other. The probability of these two conditions is Ω_1 and Ω_2 , respectively. The probability Ω_{el} of spontaneous formation of the deformed network is defined as $\Omega_{el} = \Omega_1 \Omega_2$. Let us first consider Ω_1 . The

probability of finding any given chain i with components x_i , y_i , and z_i within the range Δx , Δy , and Δz can be expressed as:

$$\omega_i = G(x_i, y_i, z_i)\Delta x\Delta y\Delta z \quad (1.11)$$

The probability that each chain has valid coordinates is given by the product of the simple-chain probability:

$$\prod_i \omega_i^{v_i} \quad (1.12)$$

Since Eq.1.12 considers only the possibility of finding chains with end-to-end distance r_i , we have to consider all possible end-to-end distances by multiplying the multisets-permutations of the chains:

$$\Omega_1 = N! \prod \left(\frac{\omega_i^{v_i}}{v_i!} \right) \quad (1.13)$$

With the aid of Stirling's approximation for the factorials $\ln N! = N \ln N - N$, we can write:

$$\ln \Omega_1 = \sum_i v_i \ln(\omega_i N / v_i) \quad (1.14)$$

Substituting Eq.1.9 and Eq.1.10 into Eq.1.14, we obtain:

$$\ln(\omega_i N / v_i) = \beta^2 \left[x_i^2 (1/\alpha_x^2 - 1) + y_i^2 (1/\alpha_y^2 - 1) + z_i^2 (1/\alpha_z^2 - 1) \right] + \ln(\alpha_x \alpha_y \alpha_z) \quad (1.15)$$

Inserting Eq.1.15 into Eq.1.14 together with Eq.1.10, we can replace the summation with an integration and write Eq.1.15:

$$\ln \Omega_1 = -N \left[\frac{(\alpha_x^2 + \alpha_y^2 + \alpha_z^2 - 3)}{2} - \ln(\alpha_x \alpha_y \alpha_z) \right] \quad (1.16)$$

Regarding Ω_2 , we define the volume segment dV , in which two of the N units are able to cross-link. For a given unit, the probability that there is another unit within volume dV is $(N-1)\frac{dV}{V}$, where V is the total volume. After these two sites are cross-linked, the probability that another unit out of the $N-2$ units is cross-linked is $(N-3)\frac{dV}{V}$. Following this reasoning, the probability that all chains are cross-linked

is:

$$\Omega_2 = (N-1)(N-3)\cdots(1)\left(\frac{dV}{V}\right)^{N/2} \approx \left(\frac{N}{2}\right)!\left(\frac{2dV}{V}\right)^{N/2} \quad (1.17)$$

replacing V with $\alpha_x\alpha_y\alpha_zV_0$, where V_0 is the volume in the undeformed state, we have

$$\ln\Omega_2 = -\left(\frac{N}{2}\right)\ln(\alpha_x\alpha_y\alpha_z) + C \quad (1.18)$$

where the constant C only contains N , dV , and V_0 making C independent of the deformation. Following the relation $\Omega_{\text{el}} = \Omega_1\Omega_2$, we can express the configurational entropy of the deformed network as:

$$\begin{aligned} S_{\text{el}} &= -k_B\ln\Omega_{\text{el}} = -k_B\ln\Omega_1 - k_B\ln\Omega_2 \\ &= C - \frac{k_B N}{2} \left[\alpha_x^2 \alpha_y^2 \alpha_z^2 - 3 - \ln(\alpha_x \alpha_y \alpha_z) \right] \end{aligned} \quad (1.19)$$

The entropy S_{el} of the undeformed state can be obtained with Eq.1.19 by setting $\alpha_x = \alpha_y = \alpha_z = 1$. We can express the entropy change due to deformation as:

$$\begin{aligned} \Delta S_{\text{el}} &= S_{\text{el}}(\text{deformed}) - S_{\text{el}}(\text{undeformed}) \\ &= -\frac{k_B N_c}{2} (\alpha_x^2 + \alpha_y^2 + \alpha_z^2 - 3 - \ln(\alpha_x \alpha_y \alpha_z)) \end{aligned} \quad (1.20)$$

Since we have assumed that the swelling is homogenous, we can take $\alpha_x = \alpha_y = \alpha_z = \alpha = \left(\frac{V}{V_0}\right)^{1/3}$, where V and V_0 are the undeformed volume in the deswollen state and the volume in the swollen state, respectively. Since $\Delta U_{\text{el}} = 0$, the difference in the Gibbs free energy due to the deformation becomes:

$$\Delta G_{\text{el}} = -T\Delta S_{\text{el}} = \frac{3k_B T N_c}{2} [\alpha^2 - 1 - \ln\alpha] \quad (1.21)$$

From ΔG_{el} , we can obtain the osmotic pressure due to deformation by taking the derivative with respect to the number of solvent molecules, n_1 ,

$$\Pi_{\text{el}} = -\frac{1}{v_1} \left(\frac{\partial \Delta G_{\text{el}}}{\partial \alpha} \right)_{T,P,n_2} \left(\frac{\partial \alpha}{\partial n_1} \right)_{T,P,n_2} = \frac{k_b T N_c}{V_0} \left[\frac{\phi_2}{2\phi_{2,0}} - \left(\frac{\phi_2}{\phi_{2,0}} \right)^{1/3} \right] \quad (1.22)$$

where ϕ_2 is the microgel volume fraction in the swollen state, and $\phi_{2,0}$, and V_0 are the polymer volume fraction and the particle volume in the deswollen state, respectively,

since the microgels are synthesized under bad-solvent conditions at 70°C.

1.4.3 Ionic effects

Microgels can be divided into neutral microgels and ionic microgels. pNIPAM microgel is believed to be charge-neutral, since no added ionic groups are added during synthesis. However, due to the APS initiator, the pNipam microgels possess charge groups, $\text{O-SO}_2\text{-O}^-$, in the periphery of the particles. Furthermore, to control the size of the microgel, SDS surfactant is used during synthesis and the Na^+ from the SDS remains after cleaning the microgel suspension. The NH_4^+ and Na^+ originate from APS and SDS associated with surface charge groups, forming a counterion cloud. [166, 204]. Moreover, this counterion cloud is believed to be responsible for the spontaneous deswelling behavior observed at high concentrations [150]. The details of this work will be discussed in later sections. The scenario is similar to when charge groups are involved in particle synthesis, such as those of NIPAM copolymerized with acrylic acid. To characterize the entropy related to the ionic effects, we assume that the particle's counterions are not spatially correlated. The entropy associated with them can be approximated as that of an ideal gas. We can now consider that our microgels have a monomer number density $c = N/r_c^3 = (NN_c)/R^3$, where r_c is the average end-to-end distance of the polymer chains, N is the number of monomers between cross-links, N_c is the total number of polymer chains, and $V = R^3$ is the volume of the microgel. In addition, a fraction f of monomers is charged. Therefore, the total number of counterions within the particle is $N^+ = fcV = fNN_c$, where we have assumed that the network is negatively charged. The canonical ensemble partition function Q of counterions can be defined as

$$Q = \frac{1}{N^+!} \left(\frac{V}{\Lambda^3} \right)^{N^+} \quad (1.23)$$

$$\ln Q = N - N \ln N + \ln \left(\frac{V}{\Lambda^3} \right) = N^+ \ln \left[\frac{Ve}{N\Lambda^3} \right]$$

where $\Lambda = \frac{h}{(2\pi m k_B T)^{1/2}}$, e is the irrational number e , m is the mass of the counterion and h is Planck's constant. The Helmholtz free energy F can thus be written as:

$$F(N^+, V, T) = -k_B T \ln Q = -N^+ k_B T \ln \left[\frac{Ve}{N\Lambda^3} \right] \quad (1.24)$$

The energy associated with counterions is then:

$$E = k_B T^2 \left(\frac{\partial \ln Q}{\partial T} \right)_{V, N^+} = N k_B T^2 \frac{d \ln T^{3/2}}{dT} = \frac{3}{2} N^+ k_B T \quad (1.25)$$

Thus, following the definition of the Helmholtz free energy $F = E - T S_{\text{ionic}}$, we can express the entropy S_{ionic} as [71],

$$S_{\text{ionic}} = \frac{E - F}{T} = k_B \ln \Omega = k_B f N N_c \ln \left[\frac{V e^{5/2}}{f N N_c} \left(\frac{2\pi m k_B T}{h^2} \right)^{3/2} \right] \quad (1.26)$$

where m is the counterion mass [113]. The chemical potential of the solvent molecules in the solution with counterions is defined as

$$\mu_1 = -T \left(\frac{\partial S_{\text{ionic}}}{\partial n_1} \right)_{U, V, n} = -\frac{k_B T f N N_c v_s}{V} \quad (1.27)$$

with $V = v_s (n_1 + n_2 + f N N_c)$, we have assumed the volumes of a monomer, a solvent molecule, and a counterion are the same, and n_1 and n_2 are the numbers of monomers and solvent molecules, respectively. Taking the chemical potential of a pure solvent solution as the reference state, $\mu_1^{\text{pure}} = 0$ and without the addition of salt, we can write the osmotic pressure due to ions as:

$$\Pi_{\text{ionic}} = -\frac{\mu_1 - \mu_1^{\text{pure}}}{v_s} = -\frac{\Delta \mu_1}{v_s} = k_B T f c \quad (1.28)$$

1.4.4 Equation of state

Eqs.1.8, 1.22, and 1.28 are the three main contributions to the osmotic pressure of a microgel. Thermodynamic equilibrium is reached when the sum of all three terms equals 0, assuming $\Pi_{\text{out}} = 0$. Thus:

$$\Pi_{\text{in}} = \Pi_{\text{mix}} + \Pi_{\text{el}} + \Pi_{\text{ionic}}$$

$$\Pi_{\text{in}} = \frac{k_b T N_A}{v_s} \left\{ \frac{N_c v_s}{V_0 N_A} \left[\left(f N + \frac{1}{2} \right) \left(\frac{\phi_2}{\phi_{2,0}} \right) - \left(\frac{\phi_2}{\phi_{2,0}} \right)^{1/3} \right] - \phi_2 - \ln(1 - \phi_2) - \chi_1 \phi_2^2 \right\} = 0 \quad (1.29)$$

Eq.1.29 relates the particle size to the thermodynamic parameters; χ_1 reflects

the solvent's quality, $\phi_2/\phi_{2,0}$ relates to the elasticity of the polymer network, and fN indicates the number of counterions. The last term can be neglected if there are no charged groups in the polymer network. The interplay between Π_{mix} , Π_{el} , and Π_{ionic} can lead to a wide range of variations in terms of particle-phase behavior. Importantly, conventional charge-neutral microgels carry charged groups on the periphery of the particles, and depending on the details of the synthesis, the charged groups can have an important effect on the suspension osmotic pressure; they can increase the suspension osmotic pressure Π_{out} outside the particles, which subsequently compresses and deswells the particles at high concentrations. Our measurements were performed at a constant temperature; therefore, the contribution of the polymer-solvent mixing is constant. The balance of the osmotic pressure inside and outside the particle relies on the balance of the pressure due to the elasticity of the chains with the suspension osmotic pressure. This work aims to measure the configuration of the counterion cloud directly and investigate the balance between the suspension osmotic pressure caused by the counterions and the particle softness, defined by the cross-link density.

1.5 Poisson-Boltzmann Calculations

As we have mentioned in previous sections, the charge groups originating from the initiator are located on the surface of the particles. As a result, the counterions associated with these charge groups are also expected to concentrate at the microgel periphery. We use Poisson-Boltzmann calculations to estimate the osmotic pressure induced by these counterions. Microgels are modeled as spheres with radius R with fixed charged groups at the particle surface. It is reasonable to ignore the movement of the surface charge groups because counterions are much more mobile, which allows them to find equilibrium positions much faster than the charge groups. In particular, microgels have an open network, allowing counterions to explore both inside and outside the periphery such that the arrangement minimizes the free energy. With the mean-field approximation, it is assumed that the ion density is low, and there are no correlations between the counterions. With this assumption, the counterion density at distance r with respect to the center of the particle is expressed with the Boltzmann distribution $\rho_c = \rho_0 \exp[-\beta q_e \psi(r)]$, where $\beta = \frac{1}{k_B T}$ and ρ_0 is the counterion density in the region of vanishing $\psi(r)$. The charge density of the fixed charges is represented as $-q_e \rho_f(r) = -Z q_e \delta(r - R)/4\pi R^2$, where q_e is the elementary charge, Z is the number of fixed charges on the particle. The total charge density

of the particle including the density of the counterions and that of the fixed charge groups: $q_e\rho(r) = q_e[\rho_0 e^{-\beta q_e\psi(r)} - \rho_f]$. The electrostatic potential $\psi(r)$ is computed with the Poisson-Boltzmann equation:

$$\Delta\psi(\mathbf{r}) = -\frac{q_e}{\epsilon_r\epsilon_0} \left[\rho_0 e^{-\beta q_e\psi(r)} - \rho_f \right] \quad (1.30)$$

Eq.1.30 can be solved in the spherical Wigner-Seitz cell, assuming every microgel sits in the center of the cell. The cell model is much more reliable for dilute suspension than for concentrated suspension, as the choice of cell dimension becomes difficult in this case [54, 2]. The Wigner-Seitz cell with radius $R_c = R\phi^{-1/3}$, where ϕ is the volume fraction of the microgels. $\Delta\psi$ can be solved by iteratively evaluating the total charge inside a sphere with radius r , $q_e Q(r) = 4\pi \int_0^r q_e r^2 \rho_r dr$, the electric field strength $E(r)$, the electrostatic potential $\psi(r)$, and the total charge density $\rho(r)$:

$$\begin{aligned} Q(r) &= Q(r + dr) - 4\pi r^2 \rho(r + dr) dr \\ E(r) &= \frac{q_e Q(r)}{4\pi \epsilon_r \epsilon_0 r^2} \\ \psi(r) &= E(r) dr + \psi(r + dr) \\ \rho(r) &= \rho_c - \rho_f = \rho_0 e^{-\beta q_e \psi(r)} - \rho_f(r) \end{aligned} \quad (1.31)$$

the calculation starts at the boundary of the Wigner-Seitz cell at $r = R_c$ and proceeds towards $r = 0$. For the calculation of $E(r)$, Gauss's law is used to guarantee the spherical symmetry of the field intensity. The boundary conditions are $\psi(R_c) = 0$ and $\frac{d\psi(R_c)}{dr} = 0$, which implies that $E(R_c) = 0$. The only free parameter needed to start the calculation is ρ_0 . The final value of ρ_0 is obtained at the end of the calculation and compared to the total number of counterions $N_c = 4\pi \int_0^{R_c} \rho_c r^2 dr$ with the number of fixed charge groups Z . Due to charge neutrality, $N_c = Z$ must be satisfied. If the condition is not met, ρ_0 is corrected for a new iteration round. The result of a Poisson-Boltzmann calculation is shown in Fig.1.5. The charged groups are assumed to be distributed as a thin shell at the microgel periphery, and as a result, the counterions are mostly concentrated at the particle surface and distributed throughout the particle. Despite the electrostatic field converges to zero at a large distance r due to the boundary condition, the counterion density ρ_c is non-zero. As a result, it is expected that the microgel counterions are present even far away from the particle boundaries, and this shows that a charged spherical object cannot bind all of its counterions. This serves as the basis for the theory that explains the spontaneous deswelling of microgels at high concentrations [54, 201, 150].

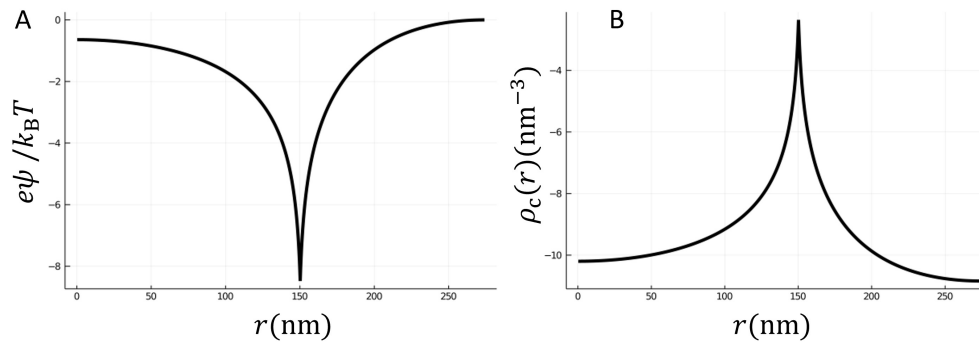


Figure 1.5: Electrostatic potential and counterion density calculated with the cell model. A: Electrostatic potential of a particle with radius 150nm and fixed charge number $Z = 70000$ in the volume fraction $\phi = 0.55$. B: The corresponding counterion charge density as a function of r .

1.6 Summary

In section 1.1, we introduced colloids and explained why colloids are of interest in both scientific research and industrial applications. In this work, we focus on microgels, which are an example of soft colloids. The synthesis details are explained in the section 1.3. What makes microgels interesting is their stimuli-sensitive nature. In Section 1.4, we derived the equation of state that includes the contribution to the osmotic pressure due to polymer-solvent mixing, chain elasticity, and ionic effects, processes that govern the microgel swelling/deswelling behavior. In previous studies, ionic effects were generally ignored for microgels synthesized with nonionic monomers. However, it has been shown that neutral pNIPAM microgels contain surface charge groups originating from the APS initiator and associated counterions can influence the microgel size, especially at high microgel concentrations. This effect generally causes the spontaneous deswelling of microgels observed in concentrated suspensions, which we will discuss in later chapters.

Chapter 2

Neutron scattering

2.1 Introduction

Neutron scattering is a valuable technique that enables scientists to study the structure and properties of materials from the microscopic to the mesoscopic scale. Electrically neutral neutrons interact with nuclei mainly through a short-range, strong nuclear force. Consequently, neutrons exhibit high penetration capabilities, making them particularly suitable for investigating materials that are opaque to other forms of radiation, such as X-rays or electrons. The energy scale associated with neutrons also renders them non-destructive probes, which is particularly advantageous when studying soft materials such as microgels, as they exhibit high sensitivity to thermal fluctuations due to their stimuli-responsive nature. [156, 155, 69, 104].

In this study, we employ neutron scattering to determine particle radii, polydispersities, internal particle structure, and interactions among particles. This chapter will first introduce the elastic scattering of a point scatterer and scattering cross-sections; this is done in Sections 2.2 and 2.4. In Section 2.3, we will discuss the scattering of a collection of scatterers, which is the situation in a scattering experiment. Notably, the elastic scattering intensity can be decomposed into two essential parts: the form factor $P(q)$, and the structure factor $S(q)$. The form factor contains information on the internal composition of the scatterers, as well as their size and shape. In denser suspensions, the structure factor is more prominent and describes the positional correlations among particles. In Section 2.5, we derive the form factor $P(q)$ and structure factor $S(q)$. The details of the techniques used in this work, Small-angle neutron scattering (SANS) and the SANS data reduction, will be described in Sections 2.6 and 2.7.

2.2 Elastic scattering from a single scatterer

For neutron scattering, there are three possible processes: coherent scattering, neutron absorption, and incoherent scattering. In a small-angle neutron scattering experiment, due to the cold neutrons source, the energy of the incident wave is low and elastic scattering is predominant. In addition, neutron absorption can be neglected, as soft matter samples generally have a lower likelihood of neutron capture. For coherent scattering, the resultant momentum change, $\Delta\mathbf{P}$, and energy change, ΔE , are of interest, these can be expressed as,

$$\begin{aligned}\Delta\mathbf{P} &= m\Delta\mathbf{v} = \hbar(\mathbf{k}_i - \mathbf{k}_s) = \hbar\mathbf{q} \\ \Delta E &= \frac{\hbar k_i^2}{2m} - \frac{\hbar k_s^2}{2m}\end{aligned}\tag{2.1}$$

where \mathbf{k} is the wavevector and $k = |\mathbf{k}| = \frac{2\pi}{\lambda}$. $\mathbf{q} = \mathbf{k}_i - \mathbf{k}_s$ is the momentum transfer, and m is the mass of a neutron. $\hbar = \frac{h}{2\pi}$, where h is the Planck's constant. In the case of elastic scattering, $|\mathbf{k}_i| = |\mathbf{k}_s|$ and $\Delta E = 0$, which means that the energy transfer between the neutron radiation and the sample is zero. In an experiment

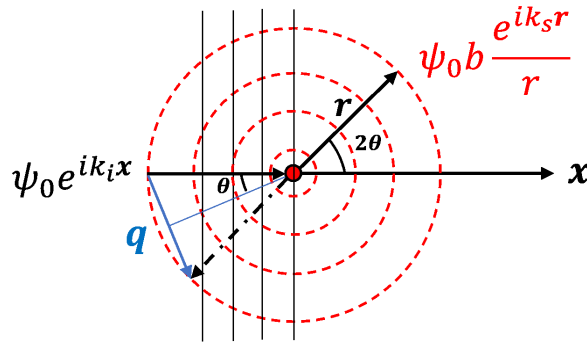


Figure 2.1: A parallel plane wave travels through the sample and gets scattered elastically by a point scatterer at the origin which produces a spherical scattered wave.

with a sample consisting of a single scattering center, an incident plane wave $\psi_0 e^{i\mathbf{k}_i \cdot \mathbf{x}}$ travels towards the sample, Fig.2.1. As the size of the scatterer is much smaller than the wavelength of the incident wave, the resultant scattering produces a spherical scattered wave that travels radially outwards. Note that this scattering is due to the strong nuclear force between the nucleus and the neutron, which will be discussed in Section 2.3. Considering the trigonometry of the problem, the magnitude of the

momentum transfer can be calculated as,

$$q = \frac{4\pi \sin(\theta)}{\lambda} \quad (2.2)$$

where $q = |\mathbf{q}|$ and 2θ is the scattering angle. For the case of elastic scattering, the wave number of the scattered wave is also $|\mathbf{k}_i| = |\mathbf{k}_s| = k$. As the origin of the spherical wave coincides with the scatterer's origin, \mathbf{k}_s is parallel with \mathbf{r} , and the scattered spherical wave function is $\frac{e^{ikr}}{r}$, where $|\mathbf{r}| = r$. More precisely,

$$\psi = \psi_o b \frac{e^{ikr}}{r} \quad (2.3)$$

where we have used that the length scale of nuclei is tiny compared to the wavelength of thermal and cold neutrons, and this nuclei act as point scatterers with an isotropic form factor described by the scattering length b . In addition, $\psi \propto \psi_o$. Since the scattered intensity $I(q) \propto |\psi^2|$, the number of scattered neutrons from a point source follows the inverse square law. The scattering cross-section of one scattering center is defined as $\sigma = 4\pi b^2$, thus the term b^2 gives the probability that a neutron gets scattered by a nucleus. The scattering length b for coherent and incoherent scattering is a tabulated constant that is independent of θ and λ . Its value depends only on the structure of the nucleus and its spin and therefore depends on the considered isotope. This implies that (i) two scattering lengths are expected for nuclei with opposite spins, (ii) b does not vary with atomic number in a simple manner, and (iii) the scattering length is different for different isotopes of the same element. For example, the scattering length of Hydrogen (H) is -3.74×10^{-15} m, while that of Deuterium (D) is 6.67×10^{-15} m [119]. This significant difference allows for contrast matching and deuterium labeling in neutron scattering experiments, which aims to enhance or separate the scattering signal of specific sample structures of interest.

2.3 Scattering from a collection of scatterers

In a neutron scattering experiment, the interaction potential between the neutrons and a particle that contains N scatterers with locations \mathbf{r}_j can be described by Fermi's pseudo-potential,

$$U(\mathbf{r}) = \frac{2\pi\hbar}{m} \sum_{i=1}^N b_i \delta(\mathbf{r} - \mathbf{r}_i) \quad (2.4)$$

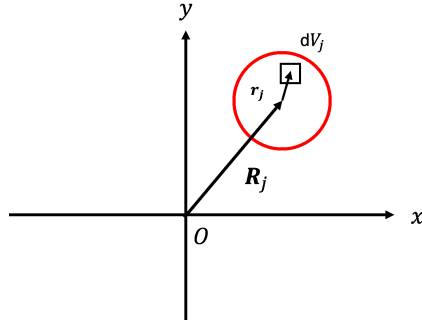


Figure 2.2: The coordinates for a particle relative to the arbitrary origin O . \mathbf{R}_j is the position of particle j . \mathbf{r}_j is the position of a unit scattering volume dV_j .

The Delta function indicates that the nucleus is much smaller compared to the neutron wavelength, and the neutron-nucleus interaction is localized at the nucleus at position \mathbf{r}_i . We can derive the total wavefunction by solving the time-independent Schrödinger equation [145],

$$(\nabla^2 + \mathbf{k}^2)\psi(\mathbf{R}) = \frac{2m}{\hbar^2}U(\mathbf{R})\psi(\mathbf{R}) \quad (2.5)$$

where $\psi(\mathbf{R})$ is the total wavefunction that can be expressed as,

$$\begin{aligned} \psi(\mathbf{R}) &= \psi_o(\mathbf{R}) + \Delta\psi_f \\ \psi(\mathbf{R}) &= \psi_o(\mathbf{R}) + \frac{2m}{\hbar^2} \int U(\mathbf{r})\psi(\mathbf{r}) \frac{e^{ik_s|\mathbf{R}-\mathbf{r}|}}{4\pi|\mathbf{R}-\mathbf{r}|} d\mathbf{r} \end{aligned} \quad (2.6)$$

$\psi_o(\mathbf{R})$ is the incident wave and $\Delta\psi_f$ is the total scattered waves, which can be written as the integration of a single point-scatterer's wave function. R_j is the position of particle j . r_j is the position of a unit scattering volume dV_j , as shown in Fig.2.2. To simplify the problem, the first-order Born approximation is applied, in which we assume that the incident wave is the scattering source for each of the point scatterers. This is a reasonable assumption, as the nucleus-neutron interaction in Eq.2.4 is localized, and we only consider single-scattering events. Therefore, we can approximate the wave function in the integral in Eq.2.6 by writing $\psi(\mathbf{r}) = \psi_o(\mathbf{r}) = e^{i\mathbf{k}_i \cdot \mathbf{r}}$. Hence Eq.2.6 becomes,

$$\psi(\mathbf{R}) = \psi_{(o)}(\mathbf{R}) + \frac{2m}{\hbar^2} \int U(\mathbf{r})\psi_{(o)}(\mathbf{r}) \frac{e^{ik_s|\mathbf{R}-\mathbf{r}|}}{4\pi|\mathbf{R}-\mathbf{r}|} d\mathbf{r} \quad (2.7)$$

The collective contribution of all the scatterers is defined such that each of the point scatterers produces a spherical wave that subsequently interfere with each

other to give rise to the total scattering intensity. Therefore, we can utilize the general principle of wave superposition and write the total contribution from all N scatterers as the summation,

$$\psi(\mathbf{R}) = \psi_{(\circ)}(\mathbf{R}) + e^{ik_i R} \sum_{j=1}^N b_j \frac{e^{i\mathbf{q}\cdot\mathbf{r}_j}}{|\mathbf{R} - \mathbf{r}_j|} \quad (2.8)$$

where b_j is the scattering length of scatterer j . We can then identify the scattered wave equation as,

$$\psi_s(\mathbf{R}) = e^{ik_i R} \sum_{j=1}^N b_j \frac{e^{i\mathbf{q}\cdot\mathbf{r}_j}}{|\mathbf{R} - \mathbf{r}_j|} \quad (2.9)$$

The simple summation assumes that the scattered spherical waves have negligible influence over the incident wave. In addition, multiple scattering events are ignored in this scenario. For a typical neutron scattering experiment, the sample to detector distance $R = |\mathbf{R}|$ is much larger than the typical length scale of the sample, as a result, we can approximate the denominator of Eq.2.9 as,

$$|\mathbf{R} - \mathbf{r}_j| = |\mathbf{R}| = R \quad (2.10)$$

This is known as the far-field or Fraunhofer approximation. To make the connection between the scattering cross section with the structure of the scatterers, one can write the modulus square of Eq.2.9 as,

$$|\psi_s|^2 = \frac{\Phi}{R^2} \left| \sum_{j=1}^N b_j e^{i\mathbf{q}\cdot\mathbf{r}_j} \right|^2 \quad (2.11)$$

where $\Phi = |\psi_{\circ} e^{i\mathbf{k}_i \cdot \mathbf{R}}|^2$ is the incident flux and Eq.2.11 gives the probability density of finding the scattered particle at a specific location. Therefore, the rate of the number of neutrons arriving at a small area ΔA on the detector during an elastic scattering event can be written as

$$R_{\text{el}} = |\psi_s|^2 \Delta A = \Phi \Delta \Omega \left| \sum_{j=1}^N b_j e^{i\mathbf{q}\cdot\mathbf{r}_j} \right|^2 \quad (2.12)$$

where $\Delta \Omega = \frac{\Delta A}{R^2}$ is the solid angle subtended by the detector relative to the sample, as shown in Fig.2.3. As will be discussed further in the Section.2.4, the differential

cross section for an object containing multiple scatterers can be written as,

$$\frac{d\sigma}{d\Omega} = \left| \sum_{j=1}^N b_j e^{i\mathbf{q}\cdot\mathbf{r}_j} \right|^2 \quad (2.13)$$

The scattering length of an element varies for isotopes and depends on the nuclear spin. In our system, it is assumed that there is only one type of atom j with its isotopes and that there is no correlation between the nuclear spin and the position of the isotopes. With this assumption, it is convenient to decompose the scattering length b_j as an average and the deviation around the mean value as $b_j = \langle b_j \rangle + \Delta b_j$, where $(\Delta b_j)^2 = \langle b_j^2 \rangle - \langle b_j \rangle^2$, assuming that the isotopes are randomly distributed. The deviation $(\Delta b_j)^2$ represents the incoherent scattering, which is q -independent. It can be shown that Eq.2.13 can be written as,

$$\begin{aligned} \frac{d\sigma}{d\Omega} &= \left| \sum_{j=1}^N \langle b_j \rangle e^{i\mathbf{q}\cdot\mathbf{r}_j} \right|^2 + N (\langle b_j^2 \rangle - \langle b_j \rangle^2) \\ &= \left(\frac{d\sigma}{d\Omega} \right)_{\text{coh}} + \left(\frac{d\sigma}{d\Omega} \right)_{\text{incoh}} \end{aligned} \quad (2.14)$$

The first term is the q -dependent coherent scattering cross-section due to the interference of the scattered waves of the nuclei. As a result, the coherent scattering intensity contains information on the particle's internal structure. Contrarily, the incoherent part is a flat background and needs to be subtracted when performing data analysis.

Since the small-angle neutron scattering technique does not have atomic resolution, and the typical length scale of our samples is in the range of tens of nano meters, it is convenient to describe the elastic scattering cross-section in terms of scattering length density (SLD), ρ . The scattering length of a single point scatterer j can be recovered when zooming to an infinitesimally small volume dV at position \mathbf{r}_j , $b_j = \rho(\mathbf{r})dV$, Fig.2.2. We can relate the elastic cross-section with the sample structure through the Fourier transform and Eq.2.13 can be rewritten as,

$$\frac{d\sigma}{d\Omega} = \left| \int_V \rho(\mathbf{r}) e^{i\mathbf{q}\cdot\mathbf{r}} d\mathbf{r} \right|^2 \quad (2.15)$$

Conventionally, in a SANS experiment, the sample contains a large number of scattering centers, and we are more interested in the overall averaged scattering behavior of the sample rather than the individual contributions from each scatterer that can-

not be resolved. Additionally, the experiment is usually performed with a fixed sample volume exposed to the beam. The exact number of scatterers in the beam is unknown and might fluctuate. Hence, the macroscopic differential cross-section that gives the scattering per volume is preferred. It relates to the microscopic cross-section as,

$$\frac{d\Sigma}{d\Omega} = \frac{1}{V} \frac{d\sigma}{d\Omega} \quad (2.16)$$

It describes the cross section per unit sample volume and has units of inverse length.

2.4 The differential cross-section

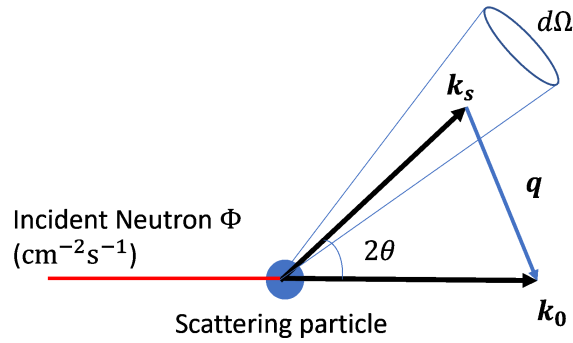


Figure 2.3: Schematic showing a scattering experiment. Incoming wave with flux Φ impinges on a particle containing N scatterers. And the vector diagram for elastic scattering into angle 2θ .

The scattering experiment measures the fraction of the incident wave that emerges in a different direction defined by the momentum transfer vector \mathbf{q} . The incident neutron beam has a flux of Φ and after impinging on a particle that contains N nuclei, the rate of arrival of the scattered wave into a small area ΔA on the detector placed at distance $R = |\mathbf{R}|$ is represented by R_{el} in Eq.2.12. The subscript *el* indicates that only elastic scattering is considered. The ratio between the detected wave per unit solid angle and the incident flux can be described as,

$$ratio = \frac{R_{\text{el}}/\Delta\Omega}{\Phi} \quad (2.17)$$

where $\Delta\Omega = \Delta A/R^2$ is the solid angle subtended by the area ΔA of the detector.

Eq.2.17 is closely related to the microscopic differential cross-section, $\frac{d\sigma}{d\Omega}$ as,

$$\frac{d\sigma}{d\Omega} = \frac{R_{el}}{N \Phi \Delta\Omega} \quad (2.18)$$

It has SI units of m^2sr^{-1} or an area per solid angle. In other words, the ratio $\frac{\Delta\sigma}{d\Omega}(\mathbf{q})$ represents the probability that a neutron is scattered by a nucleus in the direction defined by \mathbf{q} into the solid angle $d\Omega$.

2.5 Form factor and structure factor

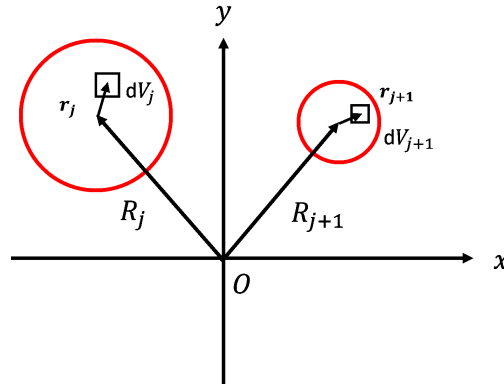


Figure 2.4: The coordinates for two particles. Relative to the arbitrary origin O , \mathbf{R}_j is the position of particle j . $\mathbf{r}_j(t)$ is the position of a unit scattering volume dV_j .

The scattering length density $\rho(\mathbf{r})$ constitutes the mean value of ρ_0 and the excess part, $\Delta\rho(\mathbf{r})$. ρ_0 is the average scattering length density of the whole sample and $\Delta\rho(\mathbf{r})$ describes the fluctuation around the mean. The ρ can therefore be written as,

$$\rho(\mathbf{r}_j) = \rho_0 + \Delta\rho(\mathbf{r}_j) \quad (2.19)$$

The substitution of Eq.2.19 in Eq.2.15 yields,

$$\frac{d\sigma}{d\Omega} = \left\langle \left| \rho_0 (2\pi)^3 \delta(\mathbf{q}) + \int_V \Delta\rho(\mathbf{r}_j) e^{i\mathbf{q}\cdot\mathbf{r}_j} d\mathbf{r}_j \right|^2 \right\rangle$$

The Fourier transform of the constant ρ_0 gives the δ -function, which only contributes to the intensity at $|\mathbf{q}| = 0$. As it coincides with the high-intensity transmitted beam, this sharp-peaked signal is generally ignored in the data analysis and the signal is blocked by the detector's beam stop. Based on Eq.2.15, the single par-

particle scattering amplitude that contains the information of particle shape and size is written as,

$$F_j(\mathbf{q}) = \left\langle \int_{V_p} \Delta\rho(\mathbf{r}_j) e^{i\mathbf{q}\cdot\mathbf{r}_j} d\mathbf{r}_j \right\rangle \quad (2.20)$$

where V_p is the particle volume. In a system that contains multiple particles, Fig. 2.4, the scattering intensity from discrete scatterers can be written as [93],

$$\frac{d\Sigma}{d\Omega} = V^{-1} \left\langle \sum_{j=1}^N \sum_{k=1}^N \langle F_j(q) F_k^*(q) \rangle e^{-i\mathbf{q}\cdot(\mathbf{R}_j - \mathbf{R}_k)} \right\rangle \quad (2.21)$$

The inner bracket indicates that the scattering amplitude is averaged over the particle size distribution and orientations. The outer bracket describes the average over all of the suspension configurations. Assuming that the particle size distribution is uncorrelated with the particle positions and the suspension structure is independent of polydispersity, the bracket can be decomposed as,

$$\langle F_j(q) F_k^*(q) \rangle = (\langle |F(q)|^2 \rangle - |\langle F(q) \rangle|^2) \delta_{jk} + |\langle F(q) \rangle|^2 \quad (2.22)$$

and Eq.2.21 can be written as,

$$\begin{aligned} \frac{d\Sigma}{d\Omega} &= n_p \left(\langle |F(q)|^2 \rangle - \langle |F(q)| \rangle^2 \right) + n_p \langle |F(q)| \rangle^2 \sum_{j \neq k}^N \sum_{k=1}^N e^{-i\mathbf{q}\cdot(\mathbf{R}_j - \mathbf{R}_k)} \\ &= n_p \langle |F(q)|^2 \rangle \left[1 + \frac{\langle |F(q)| \rangle^2}{\langle |F(q)|^2 \rangle} \left(\sum_{j \neq k}^N \sum_{k=1}^N e^{-i\mathbf{q}\cdot(\mathbf{R}_j - \mathbf{R}_k)} - 1 \right) \right] \end{aligned} \quad (2.23)$$

n_p is the number density of the particles. Importantly, Eq.2.23 is based on the assumption that the polydispersity is uncorrelated with the suspension structure, as illustrated in Fig. 2.5. By normalizing $\langle |F(q)|^2 \rangle$ with its value at $q = 0$, $\langle |F(0)|^2 \rangle$, Eq.2.23 can be further written as,

$$\begin{aligned} \frac{d\Sigma}{d\Omega} &= n_p \langle |F(0)|^2 \rangle \frac{\langle |F(q)|^2 \rangle}{\langle |F(0)|^2 \rangle} S'(q) \\ &= n_p \Delta\rho^2 V_p^2 P(q) S'(q) \end{aligned} \quad (2.24)$$

where $\langle |F(0)|^2 \rangle = \Delta\rho^2 V_p^2$ according to Eq.2.20, and $P(q) = \frac{\langle |F(q)|^2 \rangle}{\langle |F(0)|^2 \rangle}$ is the normalized form factor. Note that $P(q) \rightarrow 1$ as $q \rightarrow 0$. $P(q)$ represents the sum of the average scattering intensity of the individual particles. Thus, it characterizes the

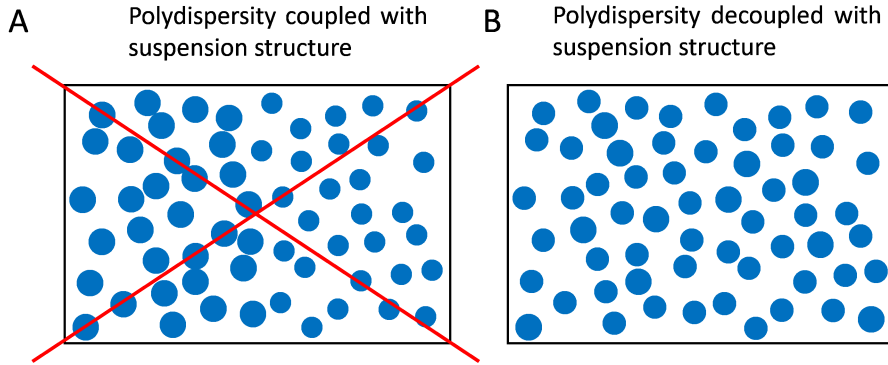


Figure 2.5: A: Microgels with different sizes segregate and the suspension structure is coupled with polydispersity. B: The suspension structure is independent of the polydispersity, where there is no preference for the location of particles with different sizes.

average intraparticle scattering, providing insight into its internal structure, shape and size. Moreover,

$$\begin{aligned} S'(q) &= 1 + \beta(q)(S(q) - 1) \\ \beta(q) &= |\langle F(q) \rangle|^2 / \langle |F(q)|^2 \rangle \end{aligned} \quad (2.25)$$

$S'(q)$ is an apparent structure factor and $S(q)$ is the inter-particle structure factor for monodisperse-spherical objects,

$$S(q) = \sum_{j \neq k}^N \sum_{k=1}^N e^{-i \mathbf{q} \cdot (\mathbf{R}_j - \mathbf{R}_k)} \quad (2.26)$$

$\beta(q)$ is a suppression factor with a value between 0 and 1 that limits the oscillation magnitude of $S(q)$, which is the effect the polydispersity would cause, Fig.2.6. $|\langle F(q) \rangle|^2$ is the numerator of $\beta(q)$ and it is the square of the average of the scattering amplitude $F(q)$ that contains both positive and negative numbers. Therefore $|\langle F(q) \rangle|^2 = 0$ for certain q , which subsequently gives minima to $\beta(q)$. Due to the size distribution, the minima of $|\langle F(q) \rangle|^2$ are close but not equal to the minima of $\langle |F(q)|^2 \rangle$ calculated by averaging over all radii and by weighting with the particle volumes. In addition, $\beta(q)$ is smaller than 1 in the whole q -range. This follows the inequality: $\frac{1}{4}(a+b)^2 \leq \frac{1}{2}(a^2+b^2)$. If the particle size is bidisperse and size-1 and -2 are equally likely, we have the scattering amplitudes $F_1(q)$ and $F_2(q)$, corresponding

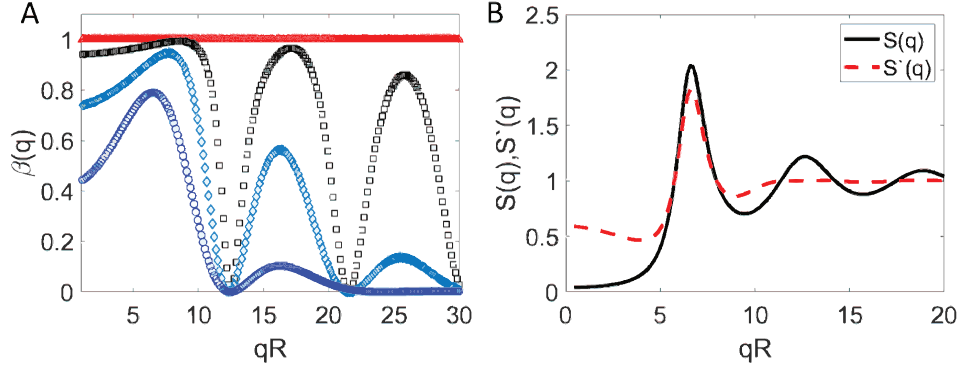


Figure 2.6: A: $\beta(q)$ calculated for the polydispersities 0% (\triangle), 8% (\square), 18% (\diamond) and 30% (\circ). B: Structure factors $S(q)$ (—) and $S'(q)$ (---) calculated for particle radius 140 nm at $\zeta = 0.75$. $S(q)$ is for a monodisperse suspension and the apparent structure factor $S'(q)$ is calculated for a polydispersity of 30%.

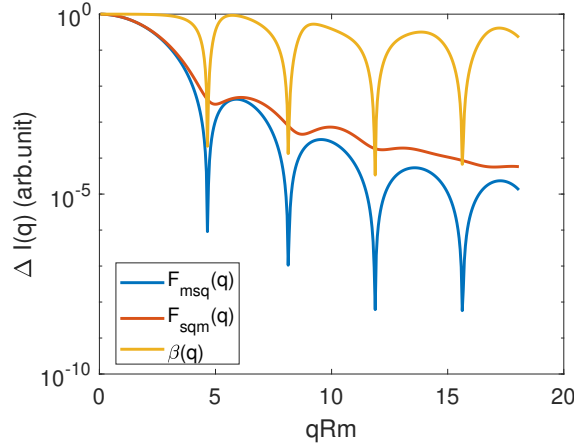


Figure 2.7: $\beta(q)$ (yellow line), $\langle |F(q)| \rangle^2$ also known as Form factor (red line), and $\langle |F(q)|^2 \rangle$ (blue line) calculated based on three particle size is plotted together.

to particles of each size. $\beta(q)$ can be calculated as

$$\beta(q) = \frac{2(F_1(q))^2 + 2F_1(q)F_2(q) + F_2(q)^2}{4(F_1^2(q) + F_2^2(q))} \quad (2.27)$$

If the scattering volume contains only spherical objects of identical size, $F_1(q) = F_2(q)$ and $\beta(q)$ becomes 1, and Equation 5.10 takes the form $\frac{d\Sigma}{d\Omega} = n_p \Delta\rho^2 V_p^2 P(q) S(q)$, which is the general expression for scattering from monodisperse spheres. However, when $F_1(q)$ does not equal $F_2(q)$, the inequality rule states that $\beta(q) \lesssim 1$ for any q . This explains the behavior at low q , where $\beta(q)$ decreases with increasing polydispersity, shown in Fig.2.6A. The maxima of $\beta(q)$ follow the form of both $\langle |F(q)| \rangle^2$ and $\langle |F(q)|^2 \rangle$. It usually appears near the maxima of the numerator $\langle |F(q)| \rangle^2$, where

the value of the numerator and the denominator is very close, as indicated by the nearly overlapped regions between $|\langle F(q) \rangle|^2$ and $|\langle F(q) \rangle^2|$, shown in Fig.2.6.

Note that, at high concentrations or in systems with high polydispersity, the assumptions used to derive the apparent structure factor may not hold, and one should derive the partial structure factor by solving the matrix form of the Ornstein-Zernike equation for the pair potential between particles with different diameters. [7, 45].

In a realistic experiment, the particles are not monodisperse in size. In this work, we assume that the log-normal distribution can describe the size distribution. In the following chapters, we will also introduce the form factor that accounts for polydispersity. Lastly, it is important to consider polydispersity in both the structure factor $S(q)$ and the form factor $P(q)$ to account for the effect of the size distribution, as the monodisperse $S(q)$ tends to overestimate the interaction potential, leading to an overestimation of sample volume fraction.

2.6 Small-angle neutron scattering (SANS)

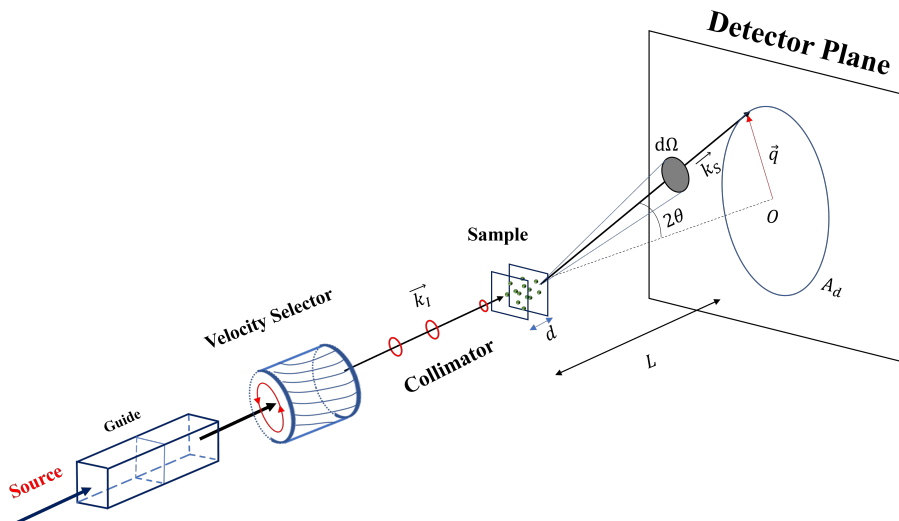


Figure 2.8: Schematic of a typical Small-angle Neutron Scattering (SANS). Neutrons with wanted wavelength λ will pass through the velocity selector, and the sample scatters the neutrons into a range of 2θ angle on the detector plane with area A_d .

In the study of microgels and other soft materials, the relevant length scales of the mesoscopic structure ranges from tens to hundreds of nanometers. According to Bragg's law, which states that $d \approx \frac{2\pi}{q} \Rightarrow \lambda = 2d \sin\theta \approx 2d\theta \Rightarrow 2\theta \approx \frac{\lambda}{d}$, the smaller

the scattering angle, the larger the accessible length scale for a given wavelength. At the Paul Scherrer Institut, the wavelength for the neutron scattering instrument typically ranges from 0.45 nm to 1 nm. To probe a sample containing particles with a length scale between 20 nm and 100 nm, we require an angle 2θ ranging from 0.3° to 3° . These angles are smaller than those used in conventional scattering equipment, and as a result, we refer to this technique as Small-angle Neutron Scattering (SANS).

Figure 2.8 shows the schematic of a typical SANS instrument (SANS-I at Paul Scherrer Institut). The cold neutron source at PSI contains a 20 liter of liquid deuterium at a temperature of 25K, which slows neutrons down and shifts their spectrum to a lower energy level, $< 5\text{meV}$. The cold neutrons are directed by the neutron guide and travel toward the velocity selector, which acts as the monochromator. The velocity selector consists of a rotating cylinder with helical slots. By adjusting the rotation speed, we can select neutrons with a specific desired velocity, allowing only the neutrons with the target velocity v to pass through the rotating helical slots without being absorbed. This enables selecting the desired wavelength $\lambda \pm \Delta\lambda$; the wavelength spread $\frac{\Delta\lambda}{\lambda}$ is normally around 10%. The neutron beam is then collimated after leaving the velocity selector by using a set of pinholes. In this way, the SANS instrument is conceptually similar to a pinhole camera, and the collimation and the sample-detector distance are usually the same. Once the collimation is set, the neutrons reach the sample environment, where scattering occurs. The detector detects the scattered neutrons with a range of scattering angle 2θ , with a small solid angle $\Delta\Omega$. The detector of SANS-I is a 2D position sensitive detector filled with ^3He gas with 128×128 pixels with a pixel area of $7.5 \times 7.5 \text{mm}^2$. Both the detector and the collimator are placed inside vacuum tanks to avoid air scattering. By changing the sample-detector distance L and adjusting the corresponding collimation distance and λ , the q -range can be varied

2.7 Experimental aspects of SANS

In this section, we will investigate the details of how neutron detection connects to the macroscopic differential cross-section of the sample, $\frac{d\Sigma}{d\Omega}$, as well as the basics of data reduction. The incident intensity, which describes the number of neutrons per second, can be defined as

$$I_0(s^{-1}) = \Phi(\lambda) A E(\lambda) \quad (2.28)$$

where $\Phi(\text{cm}^{-2} \text{s}^{-1})$ is the incident flux of the plane wave, $A(\text{cm}^2)$ is the area of the pinhole placed in front of the sample, and $E(\lambda) < 1$ is the detector efficiency. The choice of the pinhole size depends on the geometry of the sample cells, and the goal is to have the incident beam covers as much of the sample cell as possible. When the incident wave travels through the sample, it is attenuated as a result of sample scattering and absorption. The attenuation factor is $\frac{e^{-\mu d}}{\cos 2\theta}$, with μ being the linear attenuation coefficient and d being the sample thickness. The detected intensity at scattering angle 2θ after attenuation can take the form:

$$I(\mathbf{q}) = I_o \Delta\Omega d \frac{e^{-\mu d}}{\cos 2\theta} t n \frac{d\sigma}{d\Omega}(\mathbf{q}) \quad (2.29)$$

where n is the number density and t is the measuring time. $\frac{d\sigma}{d\Omega}$ is the microscopic differential cross-section that represents the probability of the neutron being scattered by a point scatterer. The scattering angle is small for SANS so that $\cos 2\theta \approx 1$ and Eq.2.29 can be written as:

$$\begin{aligned} I(\mathbf{q}) &= I_o \Delta\Omega d e^{-\mu d} t \frac{d\Sigma}{d\Omega}(\mathbf{q}) \\ &= I_o \Delta\Omega d T_s t \frac{d\Sigma}{d\Omega}(\mathbf{q}) \end{aligned} \quad (2.30)$$

where $\frac{d\Sigma}{d\Omega}(\mathbf{q})$ represents the probability of number of neutrons detected at scattering angle 2θ into the solid angle $\Delta\Omega$ per sample volume V and time t . T_s is the transmission of the sample, which describes the attenuation of the incident intensity due to the samples and is defined as the ratio of the outgoing intensity to the incident intensity at the scattering angle $\theta = 0$. Eq.2.30 is a combination of two contributions: $I_x \Delta\Omega$ is determined by the instrument configuration, including wavelength, pinhole size, collimation distance, and detector efficiency. The other contribution $d T_s \frac{d\Sigma}{d\Omega}$ is solely determined by the details of the sample. The detected intensity contains external and internal backgrounds. External background sources include electronic noise and environment scattering. Internal background sources normally originate from the scattering of sample cells and solvent molecules. To correct the measured raw intensity, the following types of measurements are required: transmission measurements with attenuation of the sample assembly (S+SB), sample background(SB), empty beam (EB), and 1mm thick water (H_2O). Transmission measurements are essential for data reduction, as they can be used to separate the sample scattering from the sample backgrounds. The transmission of the measurement is calculated as: $T = \frac{I - I_{\text{Cd}}}{I_{\text{EB}} - I_{\text{Cd}}}$, where I_{Cd} will be introduced in the next paragraph.

In addition, the scattering measurements of samples (I_{S+SB}^m), sample background (I_{SB}^m), cadmium (I_{Cd}), and H_2O are needed. Note that the Cadmium blocks the sample scattering and it becomes possible to quantify the scattering that is not due to the sample. Such measurement is called a dark count measurement; I_{Cd} helps extract the magnitude of the electronic and environmental noise. The scattering intensity corrected for empty sample cells, environmental noise, and electronic noise can be written as,

$$I_s = \frac{I_{S+SB}^m - I_{Cd}}{T_{S+SB}} - \frac{I_{SB}^m - I_{Cd}}{T_{SB}} \quad (2.31)$$

For the measurement of microgels, the solvent is also a sample background in addition to the sample cell. Hence, the solvent scattering I_{Sol+SB}^m should also be corrected following the procedure shown in Eq.2.31. Eventually, the scattering due to the suspended microgels can be obtained by subtracting the corrected solvent scattering from the corrected scattering intensity of the suspension. Lastly, water measurement is reduced following Eq.2.31 and the scattering of the microgels is normalized by the water scattering, $I_{Cal} = (I_s - I_{sol})/I_{H_2O}$. As incoherent scattering dominates for deionized water, the water measurement provides a good flat background that is independent of the scattering angle. This flat background can be used to correct for the detector sensitivity. Before the analysis, the smearing effect due to the limited instrument resolution has to be taken into account for the reduced data. For SANS-I, the fluctuation of the wavelength around the mean $\frac{\Delta\lambda}{\lambda}$ is typically around 10%. This wavelength spread will also induce a similar resolution error in q ,

$$\begin{aligned} dq &= q \frac{d\lambda}{\lambda} + q \frac{d\theta}{\theta} \\ \frac{dq}{q} &= \frac{d\lambda}{\lambda} + \frac{d\theta}{\theta} \end{aligned} \quad (2.32)$$

Eq.2.32 also indicates that the q resolution is worse for lower q , where the pixel size limits the resolution and $\frac{d\theta}{\theta}$ gives an important contribution. Hence, it is important to include a smearing effect. The distribution of q can be described by a Gaussian distribution. Incorporating it into the reduced data, we can describe the smearing effect numerically,

$$I(\langle q \rangle) = \int R(\langle q \rangle, q) \frac{d\sigma(q)}{d\Omega} dq \quad (2.33)$$

where $R(\langle q \rangle, q)$ is the Gaussian associated resolution function [89]:

$$R(\langle q \rangle, q) \approx \frac{1}{(2\pi\sigma_q^2)^{1/2}} \exp\left[-\frac{(q - \langle q \rangle)^2}{2\sigma_q^2}\right] \quad (2.34)$$

where $\langle q \rangle$ is the average value and σ_q is the standard deviation of q .

2.8 Summary

In this chapter, we have introduced the general principles of coherent and incoherent elastic scattering. In sections 2.3 and 2.4, we introduced the differential scattering cross-section, denoted as $\frac{d\sigma}{d\Omega}$, which is proportional to the squared Fourier transform of the scattering length density, $\rho(\mathbf{r})$. This scattering cross-section describes the probability that a neutron is scattered by a nucleus. In section 2.5, we have demonstrated that the measured scattering intensity can be decomposed into the Form factor, denoted as $P(q)$, and the structure factor, denoted as $S(q)$. Importantly, size polydispersity needs to be taken into account not only in $P(q)$ but also in $S(q)$; failing to do so will result in an overestimation of the suspension volume fraction. In section 5.6, we have provided an introduction to the Small-angle Neutron Scattering (SANS) instrument. Additionally, in section 2.7, we have discussed data reduction and how to account for the smearing effects due to the wavelength spread and limited pixel resolution at lower q values.

Chapter 3

Experimental characterization

3.1 Introduction

In this chapter, the primary objective is to provide essential information about the characterization methods used during the preparation of the microgel suspensions. Because of this stimuli-sensitive nature, microgels change in size in response to changes in their environment. This imposes difficulties in characterizing the microgel volume. In section 3.2, we introduce the generalized volume fraction ζ , characterizing the microgel volume fraction, which is equal to the true volume fraction in dilute conditions and independent of the swelling behavior of the microgels. In Section 3.3, we introduce Ubbelohde viscosimetry, which is a reliable way to obtain the collapsed radius of the microgel, R_{coll} , defined as the dry microgel size without solvent. Dynamic light scattering (DLS) is used to obtain the hydrodynamic radius R_{h} of the microgels and the decay time associated to this Brownian motion at 20°C. R_{h} gives a good approximation to the swollen radius of the microgels. The details of DLS are discussed in Section 3.4. Once the collapsed radius R_{coll} and the swollen radius R_{sw} are determined, we can subsequently determine ζ for all samples.

3.2 Generalized Volume Fraction ζ

Due to their softness, microgels deswell, deform, and/or interpenetrate at sufficiently high concentration. In addition, microgels are also stimuli sensitive and can swell or deswell reversibly in response to changes in temperature [57, 83, 132], concentration [202], hydrostatic pressure [101, 99], pH [3, 26]. Moreover, due to the type of synthesis used to make the particles, the microgels studied in this thesis have a core-shell structure, with a polymer-rich core and a polymer-poor fuzzy periphery, and have no

clear boundary like incompressible hard spheres do. As a consequence, it is difficult to characterize the volume fraction ϕ of a microgel suspension. This is an undesirable issue, as ϕ is important to understand the volume phase transition, freezing, melting, the glass transition, and interparticle interactions. A way to address this problem is to define the generalized volume fraction ζ . ζ can be calculated with the microgel swollen radius R_{sw} and collapsed radius R_{coll} , extracted with dynamic light scattering and viscosimetry, respectively. ζ is an effective volume fraction that describes the volume space occupied by microgels, if they retained their size in dilute conditions:

$$\zeta = \frac{\text{number of particles} \times \text{volume of a particle in dilute conditions}}{\text{total suspension volume}} \quad (3.1)$$

The number of particles N can be estimated by the ratio between the total mass of dry microgel powder added m_{pNIPAM} and the mass of the single microgel m_{p} :

$$N = \frac{m_{\text{pNIPAM}}^{\text{tot}}}{m_{\text{p}}} \cong \frac{m_{\text{pNIPAM}}^{\text{tot}}}{\rho_{\text{pNIPAM}} V_{\text{coll}}} = \frac{3m_{\text{pNIPAM}}^{\text{tot}}}{4\pi R_{\text{coll}}^3 \rho_{\text{pNIPAM}}} \quad (3.2)$$

where $\rho_{\text{pNIPAM}} = 1.269 \text{ g/cm}^3$ is the density of pNIPAM [150]. The mass of a microgel m_{p} is calculated with the collapsed radius R_{coll} and ρ_{pNIPAM} . In the collapsed state, the microgel does not contain any solvent molecules. The dilute volume is calculated with the hydrodynamic radius R_{h} extracted with dynamic light scattering (DLS) at 20°C in water below the lowest critical solution temperature (LCST) where the microgels are fully swollen. The total suspension volume V_{tot} is computed under the assumption that the density of the fully swollen microgels is close to that of the solvent, H₂O. As a result, the density of the microgel suspension can be approximated with the density of water $\rho_{\text{H}_2\text{O}}$. If we call m_{tot} the total mass of the suspension, using Eq.3.1 and Eq.3.2, we can calculate the ζ as,

$$\zeta = \frac{m_{\text{pNIPAM}}^{\text{tot}}}{m_{\text{tot}}} \frac{\rho_{\text{H}_2\text{O}}}{\rho_{\text{pNIPAM}}} \frac{R_{\text{h}}^3}{R_{\text{coll}}^3} = c \frac{\rho_{\text{H}_2\text{O}}}{\rho_{\text{pNIPAM}}} \frac{R_{\text{h}}^3}{R_{\text{coll}}^3} \quad (3.3)$$

where c is the mass fraction of the dry pMIPAM microgel powder. We can measure c by weighing the mass of dry pNIPAM powder and the mass of the suspension. The measured R_{h} and R_{coll} all contribute to the error of ζ , which we obtain using propagation calculation [181].

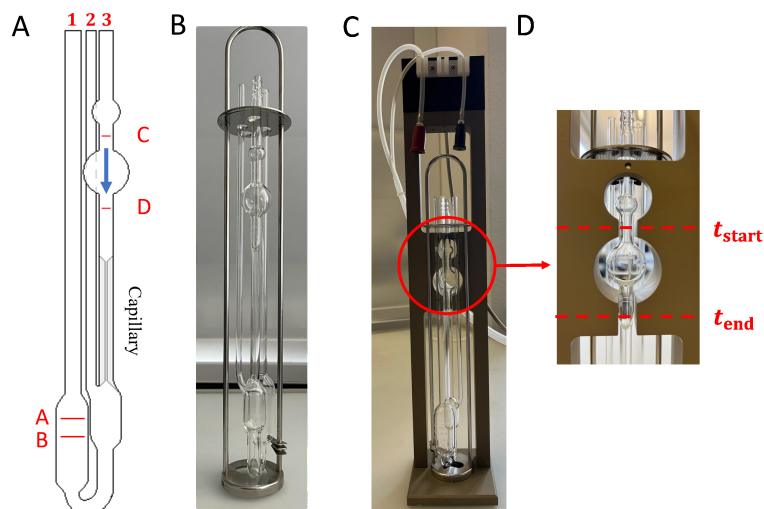


Figure 3.1: A: Sketch of Ubbelohde tube. Sample filling tube, 1. Venting tube, 2. Measuring tube, 3. Lines A and B indicate the maximum and minimum sample volume required for the measurement. Lines C and D indicate the measurement volume interval. B: Ubbelohde tube on the mounting rack. C: The assembly of the measurement setup. The red circle indicates the measurement zone. D: Zoomed view of the measurement zone. The red dots mark the position of the two sensors on the rack. Sensors detect the change in the height of the sample/air interface and record the time that sample takes to drop from t_{start} to t_{end} .

3.3 Viscosimetry

Viscosimetry is a reliable method to determine the collapsed radius of the microgels. Dilute microgel suspensions are prepared with polymer concentrations $10^{-3} < c < 4 \cdot 10^{-3}$ in water and the viscosity of the suspension is investigated using a Ubbelohde viscometer. The Ubbelohde viscometer is based on the capillary method, which measures the kinematic viscosity of the microgel suspension in dilute conditions after monitoring how the sample flows through the capillary within the Ubbelohde tube. The Ubbelohde tube is a U-shaped glassware with three connected tubes, shown in Fig.3.1(A-B). The first tube encompasses a sample reservoir, followed by the second section housing the measuring bulb and a capillary. The third tube is the venting tube that connects to the measuring bulb, which ensures that the pressure in the measuring tube is atmospheric. This design decouples the pressure head from the total sample volume, thereby simplifying the sample preparation process.

The U-tube is mounted on a rack and two sensors are positioned at locations corresponding to lines C and D on the rack, shown in Fig.3.1(A). These sensors detect the sample meniscus when it passes through points C and D, shown by the

blue arrow in Fig.3.1(A). The entire assembly is submerged in a water bath set at a temperature of $T = 20 \pm 0.2^\circ\text{C}$. The pressure valves are connected to Tube-1 and Tube-3, while Tube-2 is open to the air.

Upon exerting pressure, the sample is transferred through the capillary and rises above line C. Subsequently, the pressure is discontinued and the sample gradually flows back to the sample reservoir through the capillary. The measurement procedure records the time it takes for the sample meniscus to drop from point C to point D, with the volume between these two points as the quantified sample volume, as shown in Fig.3.1(A and D). As the flow rate is low and the diameter of the capillary is small, the sample that passes through the capillary exhibits laminar flow. The correlation between the flow rate and the viscosity of a Newtonian fluid under laminar flow is well described by the Hagen-Poiseuille law [175]:

$$\Phi = \frac{dV(t)}{dt} = \frac{\pi R^4 |\Delta P|}{8\eta L} \quad (3.4)$$

with Φ , the flow rate. defined as the change in sample volume per unit of time. The flow rate is directly proportional to the capillary radius R to the power of 4 and the pressure difference ΔP between Tube-1 and Tube 3. Within this context, the term $\frac{\Delta P}{L}$ is the pressure gradient along the capillary. Naturally, the flow rate is inversely proportional to the sample viscosity η and the capillary length L . Furthermore, the flow rate can also be expressed in terms of the capillary dimensions as, $\Phi = \frac{R^2\pi L}{\Delta t}$. This formulation relates the sample viscosity solely with the time taken for the sample to travel from point C to point D:

$$\frac{R^2\pi L}{\Delta t} = \frac{\pi R^4 |\Delta P|}{8\eta L} \Rightarrow \eta = \left(\frac{R^2 |\Delta P|}{8L^2} \right) \Delta t \quad (3.5)$$

To account for differences in density, we define the kinematic viscosity, ν , as $\nu = \eta/\rho$. Using ν , Eq.3.5 becomes:

$$\nu = \left(\frac{R^2 |\Delta P|}{8L^2 \rho} \right) \Delta t = C \Delta t \quad (3.6)$$

where C is the instrument constant provided by the manufacturer, directly relating Δt to ν . For our U-tube, $C = 3.19 \cdot 10^{-9} \text{m}^2 \text{s}^{-2}$. The Δt value and its associated error are determined by averaging the result for six individual measurements, and considering their standard deviation $\sigma_{\Delta t}$, respectively. The measured sample viscosity is

thus defined as:

$$\eta = \nu \rho_{\text{sample}} = C \langle \Delta t \rangle \rho_{\text{sample}} \quad (3.7)$$

As the microgel suspension is very dilute, we can calculate η by approximating $\rho_{\text{sample}} = \rho_{\text{H}_2\text{O}}$. To express the viscosity in terms of R_{coll} , we use the Einstein-Batchelor equation for hard spheres that reasonably describes the viscosity of microgels in the dilute regime [11, 17],

$$\eta = \eta_s \left(1 + 2.5 \phi + 5.9 \phi^2 \right) \quad (3.8)$$

where $\eta_s = \eta_{\text{H}_2\text{O}}$ is the solvent viscosity. Here ϕ is the true volume fraction of the microgel. For a dilute suspension, the microgels are fully swollen at $T = 20^\circ\text{C}$ and $\phi = \zeta$, and then $\eta = \eta_s (1 + 2.5 \zeta + 5.9 \zeta^2)$. Now using Eq.3.3, $\zeta = k c$, where $k = \frac{\rho_{\text{sol}}}{\rho_{\text{NIPAM}}} \frac{R_{\text{sw}}^3}{R_{\text{coll}}^3}$ and then:

$$\eta_r = 1 + 2.5 k c + 5.9 (k c)^2 \quad (3.9)$$

where $\eta_r = \frac{\eta}{\eta_s}$ is the relative viscosity of the suspension. By fitting the $\eta_r(c)$ data

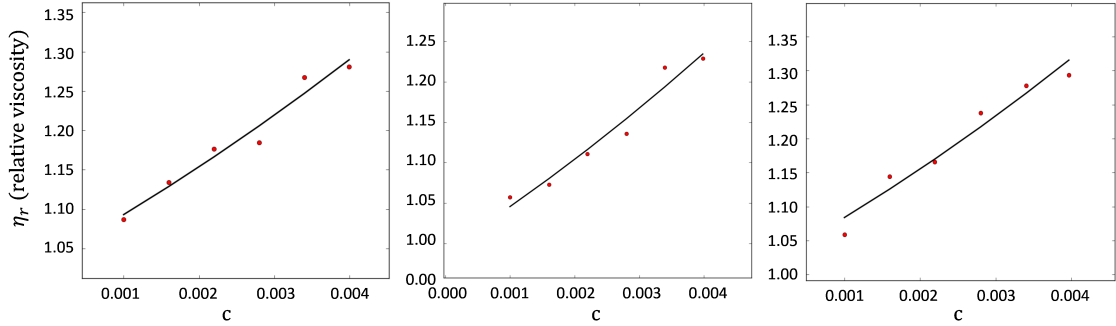


Figure 3.2: The measured relative viscosity, η_r as a function of polymer mass fraction, c . The black curve represents the fit using Eq.3.9

with Eq.3.9 as shown in Fig.3.2, we can extract the conversion constant k and the collapsed radius R_{coll} ,

$$R_{\text{coll}} = \left(\frac{\rho_{\text{sol}}}{\rho_{\text{NIPAM}}} \frac{R_{\text{sw}}^3}{k} \right)^{1/3} \quad (3.10)$$

An equivalent approach is to directly calculate the nominator and denominator of

the equation $k = \frac{\zeta}{c}$ as:

$$k = \frac{\zeta}{c} = \frac{NV_{\text{sw}}}{V_{\text{tot}}} \frac{V_{\text{tot}}\rho_{\text{sol}}}{Nm_{\text{p}}} = \frac{V_{\text{sw}}\rho_{\text{sol}}}{m_{\text{p}}} \quad (3.11)$$

where m_{p} , V_{sw} , and N are the mass of a single microgel, the volume of a swollen microgel with radius R_{sw} , and the number of microgels in the suspension, respectively. Here, we have assumed that the density of the microgel suspension is equal to the solvent density ρ_{s} and the total mass of the sample is calculated as $m_{\text{tot}} = V_{\text{tot}}\rho_{\text{sol}}$. This would only cause a small error since the density of the swollen microgel is close to the density of the solvent; more than 90% of the volume in the microgel is occupied by the solvent. The mass of the single microgel is

$$m_{\text{p}} = \frac{V_{\text{sw}}\rho_{\text{sol}}}{k} \quad (3.12)$$

Here, m_{p} represents the dry mass of the microgel and the dry NIPAM polymer density can be expressed as $\rho_{\text{NIPAM}} = \frac{m_{\text{p}}}{V_{\text{coll}}} = \frac{3m_{\text{p}}}{4\pi R_{\text{coll}}^3}$. Therefore,

$$R_{\text{coll}} = \left(\frac{3m_{\text{p}}}{4\pi\rho_{\text{NIPAM}}} \right)^{1/3} \quad (3.13)$$

3.4 Dynamic light scattering

Dynamic light scattering (DLS) is one of the most common ways to determine the radius of colloidal particles and their size distribution. Wave interference caused by the light scattered by the particles produces a speckle pattern. In dilute suspensions, microgels exhibit Brownian motion, resulting in a non-stationary speckle pattern due to the dynamic nature of particle diffusion. For a DLS measurement, the time correlation function of the scattered intensity stemming from a fixed solid angle of about the size of a single speckle is investigated. This is done at a specific scattering angle 2θ , along with a designated scattering wavevector \vec{q} and wavelength λ . The interaction of scattered waves can lead to both constructive and destructive interference, resulting in fluctuations in the scattered intensity over the course of the measurement. The rate of fluctuation is intricately related to the time scale associated with the diffusion of the particles in suspension. The diffusion time varies depending on the particle size, and larger particles undergo slower diffusion in comparison to smaller particles. As a result, the time dependence of the intensity fluctuation is directly related to the particle radius. To characterize the intensity

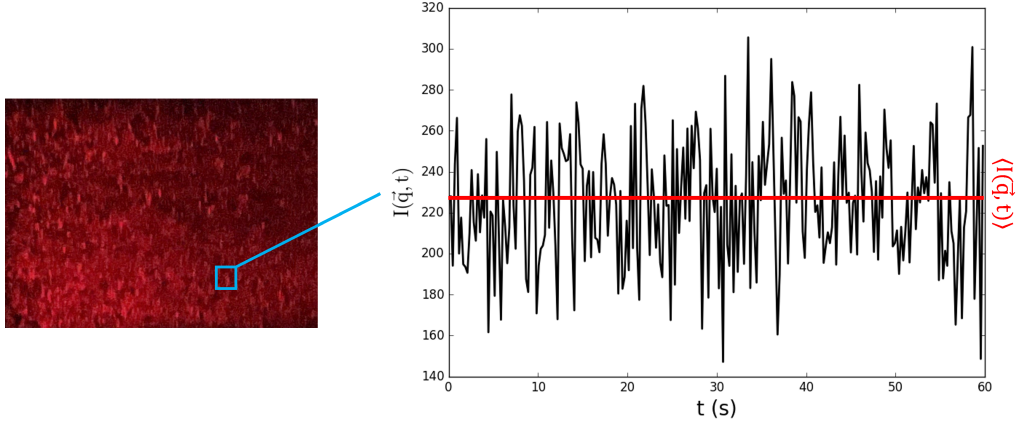


Figure 3.3: Due to the Brownian motion of the microgels, the intensity fluctuation of speckles is measured at a fixed q over time in a DLS experiment. The red line indicates the mean intensity.

fluctuation over time, we construct the intensity auto-correlation function (IACF):

$$G^{(2)}(\vec{q}, \tau) = \langle I(\vec{q}, t)I(\vec{q}, t + \tau) \rangle \quad (3.14)$$

where $\langle \cdot \cdot \cdot \rangle$ is the ensemble average for an ergodic system, which equals the time average over all possible configurations of the suspension. The time average can be interpreted as an average over the measurement time t . The time τ is the correlation time. Eq.3.14 can be expressed in terms of the electric field:

$$G^{(2)}(\vec{q}, \tau) = \frac{\epsilon_f}{4\mu_0} \left\langle E(\vec{q}, t)E^*(\vec{q}, t)E(\vec{q}, t + \tau)E^*(\vec{q}, t + \tau) \right\rangle \quad (3.15)$$

where ϵ_f is the dielectric constant of the solvent and μ_0 is the magnetic permittivity of vacuum. Due to the randomness of Brownian motion, in accordance with the central-limit theorem, the total scattered electric field from all discrete scatterers conforms to a Gaussian variable. Therefore, we can decompose Eq.3.15 using Wick's theorem [192]:

$$G^{(2)}(\vec{q}, \tau) = \frac{\epsilon_f}{4\mu_0} \left[\left\langle E(\vec{q}, t)E^*(\vec{q}, t) \right\rangle \left\langle E(\vec{q}, t + \tau)E^*(\vec{q}, t + \tau) \right\rangle \right. \\ \left. + \left\langle E(\vec{q}, t)E(\vec{q}, t + \tau) \right\rangle \left\langle E^*(\vec{q}, t)E^*(\vec{q}, t + \tau) \right\rangle \right. \\ \left. + \left\langle E(\vec{q}, t)E^*(\vec{q}, t + \tau) \right\rangle \left\langle E^*(\vec{q}, t)E(\vec{q}, t + \tau) \right\rangle \right] \quad (3.16)$$

The first term is simply $\langle I \rangle^2$, where $\langle I \rangle$ is the mean scattered intensity. The second term can be understood as the correlation between two particles at distinct moments, at time t and $t + \tau$. It can be shown that the second term is a Dirac δ -function and converges to 0 for non-zero wavevectors [35]. The third term is related to the electric field autocorrelation function (EACF):

$$\left| G^{(1)}(\vec{q}, \tau) \right|^2 = \frac{\epsilon_f}{4\mu_0} \left\langle E(\vec{q}, t) E^*(\vec{q}, t + \tau) \right\rangle \left\langle E^*(\vec{q}, t) E(\vec{q}, t + \tau) \right\rangle \quad (3.17)$$

Eq.3.16 thus becomes:

$$G^{(2)}(\vec{q}, \tau) = \langle I(\vec{q}) \rangle^2 + \left| G^{(1)}(\vec{q}, \tau) \right|^2 \quad (3.18)$$

In DLS, we usually normalize the IACF and EACF:

$$\begin{aligned} g^{(2)}(\vec{q}, \tau) &= \frac{G^{(2)}(\vec{q}, \tau)}{\langle I(\vec{q}) \rangle^2} \\ |g^{(1)}(\vec{q}, \tau)|^2 &= \frac{|G^{(1)}(\vec{q}, \tau)|^2}{\langle I(\vec{q}) \rangle^2} \end{aligned} \quad (3.19)$$

Eq.3.16 then becomes:

$$g^{(2)}(\vec{q}, \tau) = 1 + |g^{(1)}(\vec{q}, \tau)|^2 \quad (3.20)$$

Eq.3.20 is called Siegert relation and it is valid for an ideal DLS experiment where the instrument is perfectly calibrated and there are no experimental errors. Based on Eq.3.20, $g^{(2)}$ has a value between 2 and 1 and $g^{(1)}$ is between 1 and 0, corresponding to $\tau = 0$ and $\tau \rightarrow \infty$, respectively. However, any imperfection of the instrument will induce noise and errors that can lower $g^{(2)}(\vec{q}, 0)$. To account for the errors, we introduce the so-called intercept β :

$$\begin{aligned} \beta &= g^{(2)}(\vec{q}, 0) - \lim_{\tau \rightarrow \infty} g^{(2)}(\vec{q}, \tau) \\ &= \frac{\langle I(\vec{q}, 0) I(\vec{q}, 0) \rangle - \lim_{\tau \rightarrow \infty} \langle I(\vec{q}, 0) I(\vec{q}, \tau) \rangle}{\lim_{\tau \rightarrow \infty} \langle I(\vec{q}, 0) I(\vec{q}, \tau) \rangle} \\ &= \frac{\langle I(\vec{q})^2 \rangle - \langle I(\vec{q}) \rangle^2}{\langle I(\vec{q}) \rangle^2} \end{aligned} \quad (3.21)$$

This relation is true, since $\langle I(\vec{q}, 0) I(\vec{q}, \tau) \rangle$ loses correlation when $\tau \rightarrow \infty$. The value of β varies from 0 to 1 and reflects the signal-to-noise ratio of a DLS instrument.

It depends on the alignment and geometry of the setup. The value of β is a rough estimate of the inverse of the number of detected speckle patterns. With better laser focus, the speckle pattern is coarser, consequently lowering the number of speckles detected by the detector and enhancing the intensity-intensity correlation. By incorporating β into Eq.3.20, we can write:

$$g^{(2)}(\vec{q}, \tau) = 1 + \beta |g^{(1)}(\vec{q}, \tau)|^2 \quad (3.22)$$

In a DLS experiment, one measures the normalized intensity time correlation function $g^{(2)}(\vec{q}, \tau)$ at a specific \vec{q} as a function of correlation time τ . For monodisperse suspensions, the field correlation function decays as a single exponential: $g^{(1)}(\vec{q}, \tau) = \exp(-\Gamma \tau)$, where $\Gamma = Dq^2$ is the decay rate, and D is the translational diffusion coefficient of a single microgel. From the diffusion coefficient D , we can extract the hydrodynamic radius following the Stokes-Einstein relation [18]:

$$R_h = \frac{k_B T}{6\pi\eta D} \quad (3.23)$$

where k_B is Boltzmann's constant, T is the absolute temperature, and η is the dynamic viscosity of the solvent.

3.4.1 DLS data analysis

We investigate dilute Microgel suspension at $\zeta \leq 0.01$ using the ALV dynamic light scattering instrument. The light source is a vertically polarized He-Ne laser with wavelength $\lambda_o = 632.8\text{nm}$ in vacuum. The sample is kept in a decalin bath at 20°C and the avalanche photodetector is mounted on a goniometer that can cover the scattering angle from 20 to 160 degrees with a minimum step of 1 degree. For our microgel suspension, the polydispersity is around 15%. As a result, there is a distribution of time scales related to particle diffusion, and the field correlation function cannot be described by a single exponential decay. The decay rate has to be expressed by an integral [92]:

$$g^{(1)}(\vec{q}, \tau) = \int_0^\infty G(\Gamma) \exp(-\Gamma \tau) d\Gamma$$

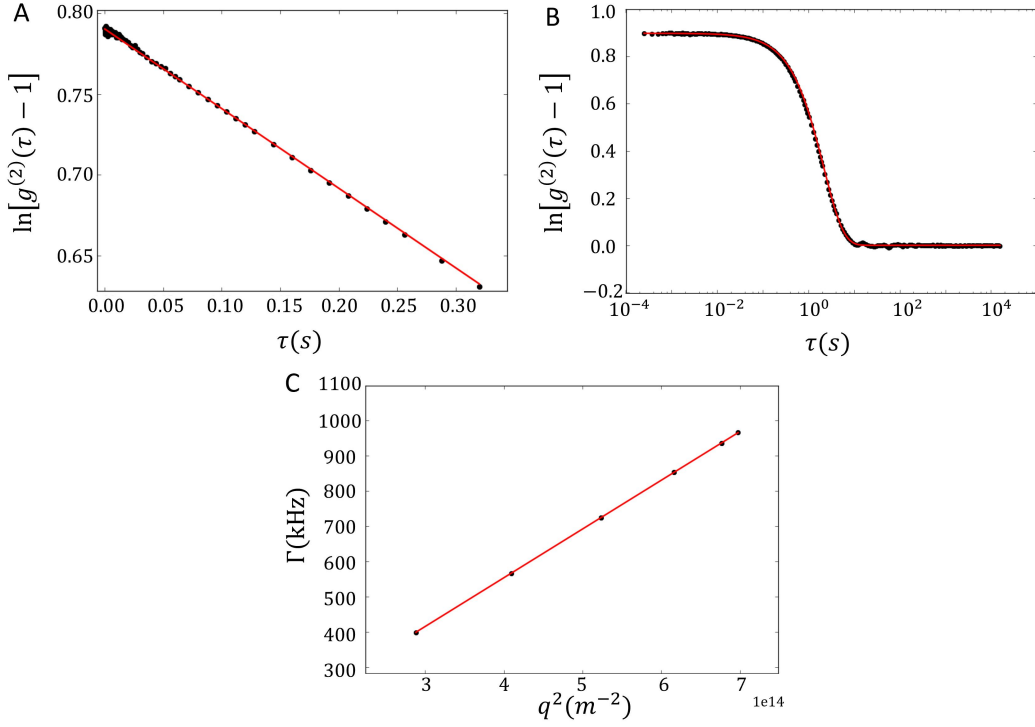


Figure 3.4: The DLS data of sample s5 listed in Table 5.1. (A) The DLS data $\ln[g^{(2)}(\tau) - 1]$ up to 10% of its maximum magnitude is fitted using the cumulant model. (B) DLS data and the plot of $\beta e^{-2\bar{\Gamma}\tau}$ using $\bar{\Gamma}$ and β determined from the fit shown in (A). (C) The plot of $\bar{\Gamma}$ as a function of q^2 and the linear fit with the model Eq.3.23 to obtain the diffusion coefficient and the hydrodynamic radius.

where the $G(\Gamma)$ is the decay rate distribution function that satisfies $\int_0^\infty G(\Gamma)d\Gamma = 1$. We can subsequently express $\exp(-\Gamma\tau)$ as:

$$\begin{aligned} \exp(-\Gamma\tau) &= \exp(-\bar{\Gamma}\tau)\exp[-(\Gamma - \bar{\Gamma})\tau] \\ &\approx \exp(-\bar{\Gamma}\tau) \left[1 - (\Gamma - \bar{\Gamma})\tau + \frac{(\Gamma - \bar{\Gamma})^2}{2}\tau^2 \right] \end{aligned} \quad (3.24)$$

where $\bar{\Gamma} = \int_0^\infty G(\Gamma)\Gamma d\Gamma$ is the mean decay rate, which dominates at short time scales. From Eq.3.4.1 and Eq.3.24, we can write:

$$\begin{aligned} g^{(1)}(\vec{q}, \tau) &\approx \exp(-\bar{\Gamma}\tau) \int_0^\infty G(\Gamma) \left[1 - (\Gamma - \bar{\Gamma})\tau + \frac{(\Gamma - \bar{\Gamma})^2}{2}\tau^2 \right] d\Gamma \\ &= \exp(-\bar{\Gamma}\tau) \left[1 + 0 + \frac{k_2}{2}\tau^2 \right] \end{aligned} \quad (3.25)$$

where $k_2 = \int_0^\infty G(\Gamma)(\Gamma - \bar{\Gamma})^2 d\Gamma$ is the variance of the distribution. The polydispersity can be calculated by the second order cumulant coefficient, $PD = \sqrt{k_2/\bar{\Gamma}^2}$. We rely

only on DLS to extract the hydrodynamic radius. The error of the hydrodynamic radius is obtained by performing a linear regression of $\bar{\Gamma}$ versus q^2 . Furthermore, this procedure allows us to check the linear dependence between $\bar{\Gamma}$ and q^2 , as shown in Fig.3.4. Table.3.1 summarizes the collapsed radius, hydrodynamic radius, conversion constant and radius measured with SANS R_{SANS} for the six microgel samples used in this work. We nevertheless mainly rely on SANS to obtain the particle size and

Sample	R_{sw} (nm)	R_{coll} (nm)	k	R_{SANS}	PD ^{DLS} %	PD ^{SANS} %
s1	77.0 ± 0.6	25.5 ± 0.1	23.62 ± 0.03	71.5 ± 2.3	16.9 ± 3.9	19.4 ± 1.5
s2	96.0 ± 0.8	34.51 ± 0.05	34.51 ± 0.05	93.1 ± 1.5	12.8 ± 2.7	20.9 ± 1.0
s3	87.0 ± 1.0	28.17 ± 0.06	24.78 ± 0.04	84.0 ± 1.0	12.5 ± 1.4	21.0 ± 1.0
s4	78.6 ± 0.6	27.65 ± 0.09	27.65 ± 0.09	71.7 ± 0.2	15.7 ± 5.3	14.9 ± 0.4
s5	125.0 ± 2.7	38.0 ± 0.8	20.56 ± 0.005	124.0 ± 1.7	8.5 ± 1.6	10.0 ± 0.5
s6	140.0 ± 2.3	40.0 ± 0.8	18.74 ± 0.005	134.0 ± 1.6	10.4 ± 1.0	11.0 ± 0.6

Table 3.1: The swollen hydrodynamic radius R_{sw} of all microgel samples is measured via DLS at 20°C. The collapsed radius R_{coll} and the conversion constant k are obtained from viscosimetry. The radius measured with SANS R_{SANS} . PD^{DLS} and PD^{SANS} are the core polydispersity measured by DLS and SANS, respectively.

size distribution. The spread of the end chains hinders diffusion and, therefore contributes to the hydrodynamic radius R_{h} . The radius obtained by SANS R_{SANS} is not sensitive to these chain ends, as the amount of polymer in these ends is negligible. For this reason, $R_{\text{h}} > R_{\text{SANS}}$. Note that the polydispersity measured with SANS is the polydispersity of the microgel core. The polydispersity PD^{DLS} of sample s1-s4 is obtained with the CONTIN method and is taken from previous work [154].

3.5 Summary

In this chapter, we introduced the generalized volume fraction ζ , which is a measure of the microgel concentration regardless of the degree of swelling and equals the microgel volume fraction for dilute suspension. To calculate ζ during sample preparation, knowledge of the collapsed radius, R_{coll} , and the swollen radius, R_{sw} , of the microgel is necessary. The collapsed radius can be determined by measuring the kinematic viscosity of the microgel suspension under dilute conditions using an Ubbelohde tube viscosimeter. The fully swollen radius can be extracted by characterizing the dilute microgel suspension with dynamic light scattering (DLS) and analyzing the DLS data using the cumulant method, we do this for samples s5 and s6, as their polydispersity is low. For samples s1 to s4, microgels have higher poly-

dispersity, and a more accurate approach, such as the CONTIN method [152], must be employed.

Chapter 4

Spontaneous deswelling of microgels

In this chapter, we show the results of the SANS measurements of the microgel suspension prepared in a series of concentrations. The spontaneous deswelling behavior of the microgels at high concentrations is investigated, where the concentration dependence of particle radius and polydispersity is studied in detail to understand the counterion effects on suspension behavior.

Manuscript title: Poly(*N*-isopropylacrylamide) microgel swelling behavior and suspension structure studied with small-angle neutron scattering

Manuscript state: Published manuscript

Reference Zhou, B., U. Gasser, and A. Fernandez-Nieves. "Poly (*N*-isopropylacrylamide) microgel swelling behavior and suspension structure studied with small-angle neutron scattering." *Physical Review E* 108, no. 5 (2023): 054604.

Keywords: microgels, polydispersity, electric double layer, deswelling, SANS

Acknowledgements: We thank the Swiss National Science Foundation (Grant No. 200020_184839), MCIN/AEI/10.13039/501100011033/FEDER, UE (grant No. PID2021-122369NB-I00) and 2021 SGR-00450 for financial support. All SANS data was taken on the instrument SANS-II at SINQ, Paul Scherrer Institut, Switzerland.

Author contributions: B.Z. prepared samples, performed measurements, analyzed the data, and wrote the paper. U.G. designed the research, prepared sample, supported and carried out measurements, analyzed data, and wrote the paper. A.F.-N. designed the research, supported measurements and data analysis, and wrote the paper.

4.1 Abstract

Microgels are of high interest for applications and as model systems due to their volume response to external stimuli. We use small-angle neutron scattering to measure the form and structure factors of poly(*N*-isopropylacrylamide) microgels in dilute and concentrated suspensions and find that microgels keep a constant size up to a concentration, above which they deswell. This happens before random-close packing. We emphasize suspension polydispersity must be considered to obtain accurate form and structure factors. Our results are compatible with microgel deswelling triggered by the osmotic pressure set by counterions associated to charged groups in the microgel periphery, which sharply increases when the counterion clouds surrounding the microgels percolate throughout the suspension volume.

4.2 Introduction

Microgels are cross-linked polymer particles suspended in a solvent that can change between swollen and deswollen states depending on external stimuli such as temperature [132, 170], *pH* [72, 116], and hydrostatic pressure [101, 99, 100]. This responsiveness is due to the softness of the polymer network. Temperature sensitive poly(*N*-isopropylacrylamide) (pNIPAM) microgels are among the most studied microgels due to their close-to-room-temperature lower critical solution temperature (LCST), $T_c \approx 32^\circ\text{C}$ in H_2O . pNIPAM microgels are swollen by the solvent for $T < T_c$, and are deswollen at higher temperatures.

The effect of swelling on suspension behavior is highlighted by the spontaneous deswelling of large pNIPAM microgels surrounded by smaller but otherwise identical microgels above a critical concentration [80]. This selective deswelling reduces the polydispersity of the suspension, allowing for crystallization of suspensions that would otherwise not crystallize. In prior work, we showed that the osmotic pressure, π , due to counterions originating from charged groups located at the periphery of the pNIPAM microgels, Fig. 4.1A, can lead to deswelling in concentrated suspensions,

provided π is comparable or larger than the single-particle bulk modulus [150]. While most counterions are electrostatically bound to the microgel periphery, a fraction of them are bound with a strength comparable to the thermal energy kT , and are thus free to explore the suspension volume. These counterions determine the suspension osmotic pressure, as there are many more counterions than there are microgels. In contrast, at high particle concentrations, the counterion clouds surrounding all microgels begin to overlap, causing the bound counterions to progressively become free [150, 149, 54]; π is then controlled by these ions and becomes significantly larger relative to when there is no overlap between ion clouds, eventually causing microgel deswelling.

This model for deswelling in crowded suspensions suggests that the microgel size should stay constant with increasing particle concentration until the osmotic pressure is comparable to or exceeds the microgel bulk modulus. In contrast, an unexpected deswelling behavior of pNIPAM microgels at exceedingly low concentration was reported in prior work [169, 170, 115].

In this paper, we use small-angle neutron scattering (SANS) to study both the microgel form factor and the suspension structure from dilute to overpacked conditions to follow changes in both the microgel size and internal structure, and the collective liquid-like structure factor of the suspension. Importantly, the polydispersity, which is $\sim 15\%$, is considered in both the form factor and the structure factor and is found to be essential to obtain reasonable results. In all studied suspensions, microgel deswelling starts at a volume fraction, ϕ , below random close packing, i.e. without direct contact between neighboring microgels.

4.3 Microgel suspensions

We study four pNIPAM microgels with a crosslinker concentration of 2 mol% N, N' -methylene-bis-acrylamide (BIS) synthesized using precipitation polymerization at 70°C , which is above the lower critical solution temperature (LCST) of pNIPAM. Ammonium persulfate [APS, $(\text{NH}_4)_2\text{S}_2\text{O}_8$] was used as the initiator of the polymerization reaction. To control the microgel size, we utilized the surfactant sodium dodecyl sulfate [SDS, $\text{CH}_3(\text{CH}_2)_{11}\text{OSO}_3\text{Na}$]. SDS stabilizes the primary particles, which are the seeds of the stable microgels, and grow by incorporating smaller precursor particles. By adding more SDS, smaller primary particles are obtained. Consequently, with a fixed amount of NIPAM monomer and BIS crosslinker, a larger number of smaller microgels is generated. The four pNIPAM microgels used in this

study were synthesized following the same protocol and only the amount of SDS was varied, see Table 5.2, to obtain microgels with different average radii and a polydispersity of $\sim 15\%$, which is relatively monodisperse for pNIPAM microgels [133]. During the synthesis, the BIS crosslinker reacts faster than NIPAM and, therefore, its concentration is higher in the initially formed core of the microgel, decaying in the fuzzy corona, which grows after most of the crosslinker has been used. This implies that larger microgels have a softer corona, as the crosslinker concentration would have decayed more from the core towards the periphery than for smaller microgels.

Due to SDS and APS, Na^+ and NH_4^+ ions are present as mobile counterions, while $-\text{O}-\text{SO}_2-\text{O}^-$ groups originating from APS remain at the end of the pNIPAM chains in the particle periphery. Information about the microgel synthesis can also be found in the Supporting Information of Ref. [150]. After the synthesis, the microgel suspension is cleaned using dialysis to remove any unreacted monomers and SDS. The cleaned, final suspension of pNIPAM microgels thus contains Na^+ and NH_4^+ counterions. Most of these are electrostatically bound to the microgels. Using dynamic light scattering (DLS), we confirm the LSCT of the particles is $T_c \approx 32^\circ\text{C}$ in H_2O . We also find that the swollen radii at $T \approx 18^\circ\text{C}$ is in the range from 77 nm to 96 nm for all four samples. To prepare microgel suspensions for SANS, the microgels are freeze dried and then resuspended in heavy water (D_2O). The change from H_2O to D_2O causes the LCST to increase from $T_c \approx 32^\circ\text{C}$ to $\approx 33^\circ\text{C}$ [95]. This slight change in the swelling behaviour has no consequences for our study at $T \approx 18^\circ\text{C}$, far from the LCST.

Sample	T ($^\circ\text{C}$)	R_{sw} (nm)	R_{coll} (nm)	k	SDS (mM)
s1	17.7	77.0 ± 0.6	25.5 ± 0.1	23.62 ± 0.03	3.00
s2	17.9	96.0 ± 0.8	34.51 ± 0.05	34.51 ± 0.05	2.00
s3	18.0	87.0 ± 1.0	28.17 ± 0.06	24.78 ± 0.04	2.50
s4	17.6	78.6 ± 0.6	27.65 ± 0.09	27.65 ± 0.09	2.95

Table 4.1: Hydrodynamic radius R_{sw} obtained with DLS at temperature T , the collapsed radius R_{coll} , the conversion constant k , and the amount of SDS used in synthesis for the four pNIPAM microgel samples.

Due to the softness and deformability of pNIPAM microgels, suspensions can be overpacked, forcing the particles to deform and deswell to fit in the available volume. This makes knowing the true volume fraction, ϕ , of the suspension difficult.

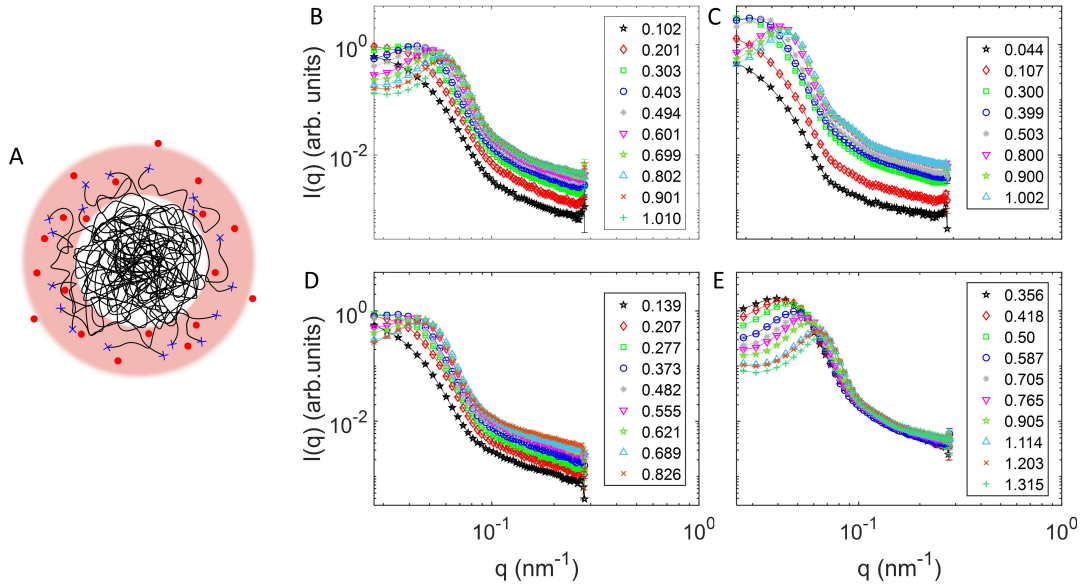


Figure 4.1: (A) Sketch of a microgel with denser core and fuzzy corona. Charges at the ends of pNIPAM chains and counterions are represented by \times and \bullet , respectively. The red, shaded area at the periphery represents the counterion cloud. (B-E) SANS curves for generalized volume fractions ζ given in the legends for sample s1 (B), s2 (C), s3 (D), and s4 (E).

Therefore, we use a generalized volume fraction

$$\zeta = \frac{N_{\text{tot}} V_{\text{sw}}}{V_{\text{tot}}} \approx \frac{m_{\text{p}} \rho_{\text{s}} R_{\text{sw}}^3}{m_{\text{tot}} \rho_{\text{p}} R_{\text{coll}}^3} \quad (4.1)$$

where $V_{\text{sw}} = 4\pi R_{\text{sw}}^3/3$ is the fully swollen particle volume, and V_{tot} , m_{tot} and m_{p} are the total volume and mass of the suspension, and the mass of the dry pNIPAM polymer, respectively. The density of the solvent ρ_{s} is that of D_2O , and $\rho_{\text{p}} = 1.269 \text{ g/cm}^3$ [199] is the density of the pNIPAM polymer. The radii R_{sw} and R_{coll} correspond to the swollen and collapsed states, respectively; we measure R_{sw} using DLS (3D-DLS, LS-Instruments, Fribourg, Switzerland) with a modified CONTIN algorithm [152], and obtain R_{coll} via viscosimetry (Ubbelohde viscosimeter, SI Analytics GmbH, Mainz, Germany), as explained below. Note R_{coll} is different from the deswollen radius reached at $T > T_{\text{c}}$ where the microgels still contain a significant amount of solvent. For dilute suspensions, $\zeta = \phi$. Since microgels can deform, deswell, and interpenetrate, ζ can be larger than 1, while the true volume fraction of spherical particles is limited to $\phi \leq \phi_{\text{rcp}} \approx 0.64$ in disordered suspensions and to $\phi \leq \phi_{\text{cp}} = \pi/(3\sqrt{2})$ in the crystalline state.

The collapsed radius R_{coll} in Eq. 5.5 is obtained from viscosimetry measurements taken at $T = (22.00 \pm 0.01)^\circ\text{C}$ yielding the relative viscosity $\eta_r = \eta/\eta_{\text{H}_2\text{O}}$ of five or six dilute suspensions with polymer mass fraction $c = m_p/m_{\text{tot}}$ in the range $10^{-4} \lesssim c \lesssim 4 \cdot 10^{-4}$. The collapsed radius is extracted from the η_r data using the Einstein-Batchelor relation [11, 17, 158]:

$$\begin{aligned}\eta_r &= 1 + 2.5\zeta + 5.9\zeta^2 \\ &= 1 + 2.5(kc) + 5.9(kc)^2,\end{aligned}\tag{4.2}$$

where we use $\zeta = kc$ and $k = \rho_s R_{\text{sw}}^3 / (\rho_p R_{\text{coll}}^3)$, which depends on both R_{coll} and R_{sw} . The viscosimetry measurements thus allow determining k and obtaining R_{coll} using R_{sw} obtained from DLS:

$$R_{\text{coll}} = \left(\frac{\rho_s R_{\text{sw}}^3}{\rho_p k} \right)^{1/3}.\tag{4.3}$$

The radii R_{sw} , R_{coll} and the sample-dependent conversion constant k are summarized in the Table. 5.2.

4.4 Small-angle neutron scattering (SANS)

SANS measurements were taken on SANS-II at SINQ, Paul Scherrer Institut, with a wavelength of $\lambda = (1.08 \pm 0.04)$ nm and a sample-detector distance of $d_{\text{sd}} = 6$ m at a temperature of $T \approx 18^\circ\text{C}$. The SANS data was corrected for dark counts and solvent (D_2O) background before calibration with a H_2O measurement following standard procedures [86]. The SANS curves obtained with concentration series of the four studied samples are shown in Fig. 4.1B-E. With increasing ζ , we notice the appearance of an interaction peak, which means that inter-particle scattering becomes important. In addition, the peak position shifts to higher q as ζ increases, reflecting the decrease of the inter-particle distance with increasing concentration. The scattering intensity, in arbitrary units, can be expressed as [129, 27]

$$I(q) = n_d V_p^2 \Delta\rho^2 P(q) S(q),\tag{4.4}$$

where $n_d = N/V$ is the particle number density, and $\Delta\rho = \rho_p - \rho_s$ is the scattering contrast given by the difference of the scattering length densities (SLDs) of the pure polymer and the solvent. The factors $P(q)$ and $S(q)$ in Eq. 5.10 represent the particle form factor, with $P(q = 0) = 1$, and the suspension structure factor, respectively.

This factorization is exact for monodisperse spherical particles in suspension but is an approximation when the suspension is polydisperse. In previous work, the polydispersity was considered only in the form factor, but its effect on the structure factor was completely neglected [169], in spite of the significant polydispersity of pNIPAM microgel suspensions, which is $\sim 15\%$. We use the so-called apparent structure factor [93, 27], which is based on the assumption that the suspension structure is decoupled from polydispersity. We then replace the structure factor $S(q)$ of a monodisperse suspension with a corrected structure factor

$$S'(q) = 1 + \beta(q)(S(q) - 1), \quad (4.5)$$

$$\beta(q) = \frac{|\langle F_p(q) \rangle|^2}{\langle |F_p(q)|^2 \rangle}, \quad (4.6)$$

where $\beta(q)$ is the so-called suppression factor, varying between zero and one, and $\langle \dots \rangle$ represents an average with respect to the size distribution. While the numerator of $\beta(q)$ is based on the average scattering amplitude, conceptually standing for the form factor of a monodisperse suspension, the denominator contains a contribution due to the standard deviation $\delta F_p(q)$ of the form factor, since $\delta F_p^2(q) = \langle |F_p(q)|^2 \rangle - |\langle F_p(q) \rangle|^2$. Thus, $\beta(q) = 1$ in the monodisperse case with vanishing $\delta F_p(q)$, and $\beta(q) \rightarrow 0$ for highly polydisperse suspensions, where $\delta F_p(q) \rightarrow \infty$. The q -dependence of β for different polydispersities is shown in Fig. 4.2A. The main effect of $\beta(q)$ is to suppress the characteristic oscillations of the liquid-like structure factor due to polydispersity; see Fig. 4.2B. The monodisperse structure factor $S(q)$ of pNIPAM microgels up to rather high ζ is modeled using the Percus-Yevick result for hard spheres [64].

We use the fuzzy-sphere form factor, which is well accepted for microgels [169, 149]. The single particle scattering amplitude in this model is

$$F_p(q) = \frac{3 [\sin(qR_c) - qR_c \cos(qR_c)]}{(qR_c)^3} \times \exp\left(-\frac{q^2\sigma_s^2}{2}\right), \quad (4.7)$$

where R_c is the core radius of the microgel and σ_s is the half-width of its fuzzy shell. Eq. 5.11 is the Fourier transform of a sphere with radius R_c that is convolved with a Gaussian to obtain a corona with the density decreasing towards the particle periphery over the width $2\sigma_s$ [170]. The radius of the particle is thus calculated as $R_{\text{SANS}} = R_c + 2\sigma_s$. The form factor is defined as $P(q) = \langle |F(q)|^2 \rangle / \langle |F(0)|^2 \rangle$.

We introduce polydispersity in $P(q)$ using a log-normal distribution of the core

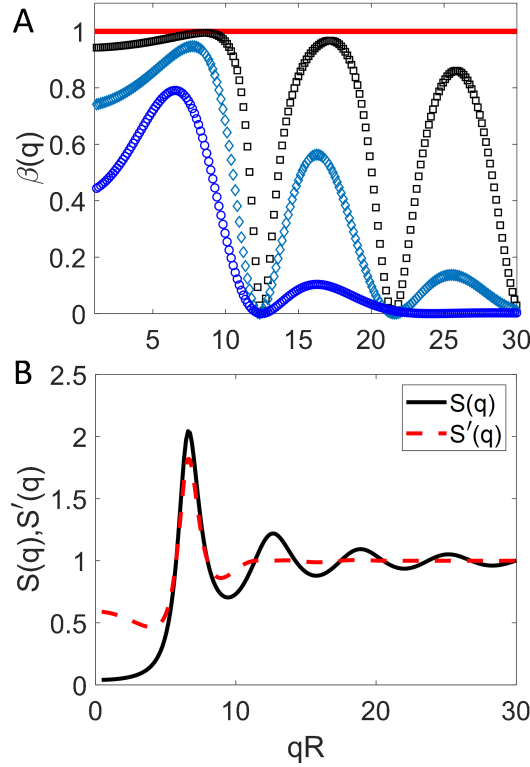


Figure 4.2: (A) $\beta(q)$ calculated for polydispersities 0% (—), 8% (□), 18% (◇) and 30% (◊). (B) Structure factors $S(q)$ (—) and $S'(q)$ (---) calculated for particle radius 140 nm at $\zeta = 0.75$. $S(q)$ is for a monodisperse suspension and the apparent structure factor $S'(q)$ is calculated for a polydispersity of 30%.

radius with a standard deviation of σ :

$$D(R) = \frac{1}{R} \frac{1}{\sqrt{2\pi}\sigma} \exp\left(-\frac{(\ln R - \mu)^2}{2\sigma^2}\right), \quad (4.8)$$

where the average core radius is given by $\langle R \rangle = e^{\mu + \frac{\sigma^2}{2}}$, and the polydispersity is $\langle (R - \langle R \rangle)^2 \rangle / \langle R \rangle^2 = e^{\sigma^2} - 1$. The form factor is then convoluted with $D(R)$ (Eq. 5.12),

$$P_{\text{poly}}(q) = \frac{1}{\langle V^2 \rangle} \int_0^\infty D(R_c) V^2(R_c) P(q) dR_c, \quad (4.9)$$

where $V(R_c) = 4\pi R_c^3/3$ is the volume of the core and $\langle V^2 \rangle = \int_0^\infty D(R_c) V^2(R_c) dR_c$ is the average-squared-core volume. As shown in a simulation study [49], the apparent structure factor is valid for moderate polydispersities and concentrations and breaks down for significant polydispersities and high concentration, where the matrix form of the Ornstein-Zernicke equation for the pair potential needs to be solved to obtain

a valid structure factor [7, 58]. For the suspensions studied here, the polydispersity is $\sim 15\%$ and the highest volume fraction is limited to $\phi < 0.5$ due to microgel deswelling. No crystalline phase is observed either. Therefore, we use the apparent structure factor as a good approximation to model the effect of polydispersity on $S(q)$. Including polydispersity, the scattering signal becomes

$$I_{\text{poly}}(q) = n_{\text{d}} \langle V^2 \rangle \Delta \rho^2 P_{\text{poly}}(q) S'(q).$$

Finally, we consider the instrument resolution by convoluting $I_{\text{poly}}(q)$ with a Gaussian [130],

$$\begin{aligned} I(q) = & \frac{1}{\sqrt{2\pi}\sigma_{\text{r}}(q)} \\ & \times \int_0^{\infty} \exp\left(-\frac{(q-q')^2}{2\sigma_{\text{r}}^2(q)}\right) I_{\text{poly}}(q') dq' \\ & + I_{\text{chain}}(q) + B, \end{aligned} \quad (4.10)$$

where we have also included the scattering due to inhomogeneities within the polymer mesh of the microgel using a Lorentzian term, $I_{\text{chain}}(q) = I_{\text{chain}}(0)/[1 + (\xi q)^2]$, with ξ the correlation length given by the polymer-network-mesh size, and $I_{\text{chain}}(0)$ the intensity of this contribution at $q = 0$ [42, 94]. Additionally, the constant B represents the background due to incoherent scattering. All in all, Eq. 5.14 is the model that we use to describe our SANS data.

4.5 Results and discussion

Using the model given by Eq. 5.14 we extract the parameters R_{c} , σ_{s} , σ , $I_{\text{chain}}(0)$, and ξ defining the microgel form factor and the parameters n_{d} and $R_{\text{SANS}} = R_{\text{c}} + 2\sigma_{\text{s}}$ relevant for the suspension structure given by $S'(q)$, see Table 5.3. We start with the suspension with the lowest concentration at $\zeta \lesssim 0.1$, where the structure factor is essentially equal to 1, and obtain the parameters for the form factor. The result is then used to start the analysis of the suspension with the next higher ζ , where we now include the structure factor. This scheme is repeated up to the highest concentration we probe in our experiments. In Fig. 4.3, we show the fit result at $\zeta \approx 0.75$ for each sample. Note that the structure factor depends on the microgel diameter and that n_{d} is calculated with the radius R_{SANS} obtained with the fuzzy-sphere model. Both the peak due to the structure factor and the intensity decay at higher q are very well captured by the model.

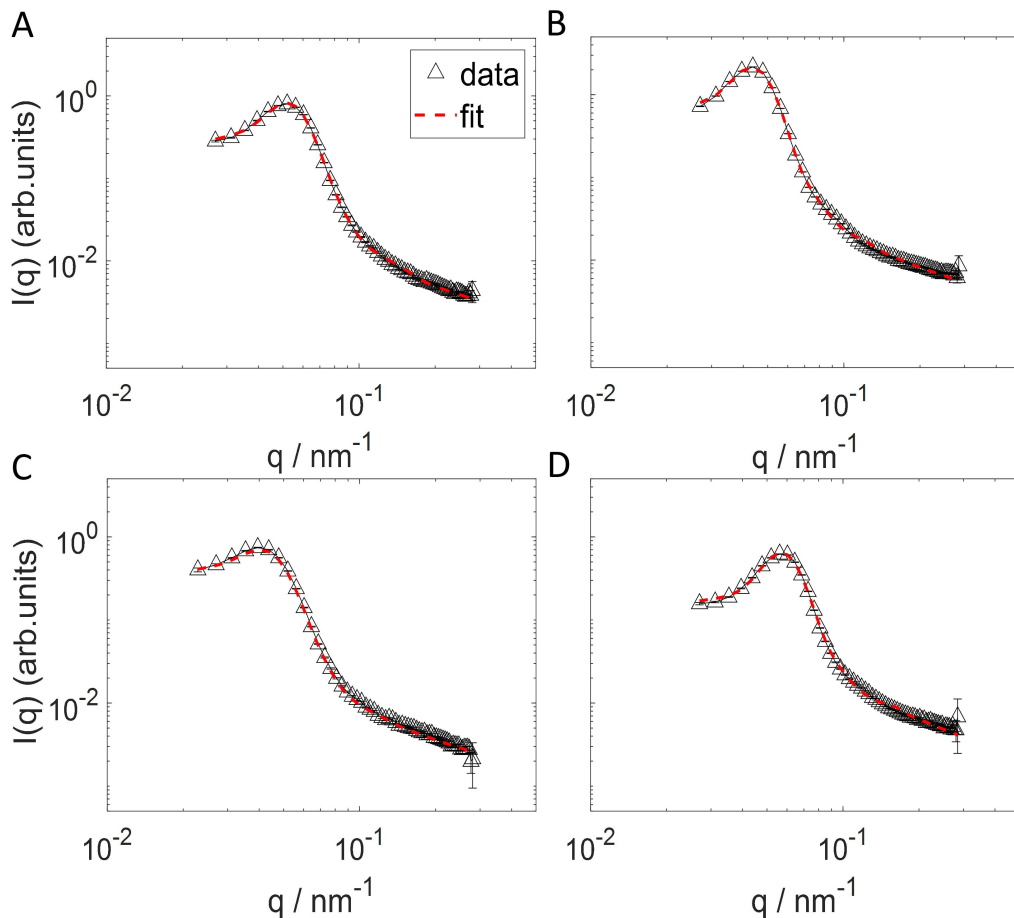


Figure 4.3: SANS data (Δ) for samples s1 at $\zeta = 0.601$ (A), s2 at $\zeta = 0.80$ (B), s3 at $\zeta = 0.706$ (C), and s4 at $\zeta = 0.705$ (D) and fits to the data ($---$) obtained using the model given in Eq. 5.14. For other SANS measurements, the model fits are as good as in the examples shown here or better.

In addition to the Percus-Yevick structure factor, we have also applied the mean-spherical approximation (MSA) closure to use a structure factor that accounts for charges on the particles. The quality of the fits, however, did not at all improve. Furthermore, the effective charge of the microgels, used as a fitting parameter, was found to take on very low values, confirming the validity of the Percus-Yevick structure factor when applied to our system. This may be understood by considering that the open structure of the microgels appears to allow for an effective screening of the charged groups in the microgel periphery [54], together with the fact that microgel deswelling suppresses the influence of charges on the suspension structure due to the associated decrease in the suspension volume fraction ϕ .

The results obtained with the model given by Eq. 5.14 are summarized in Fig. 4.4. For samples s1, s2, and s3, the microgel volume is constant at the lowest

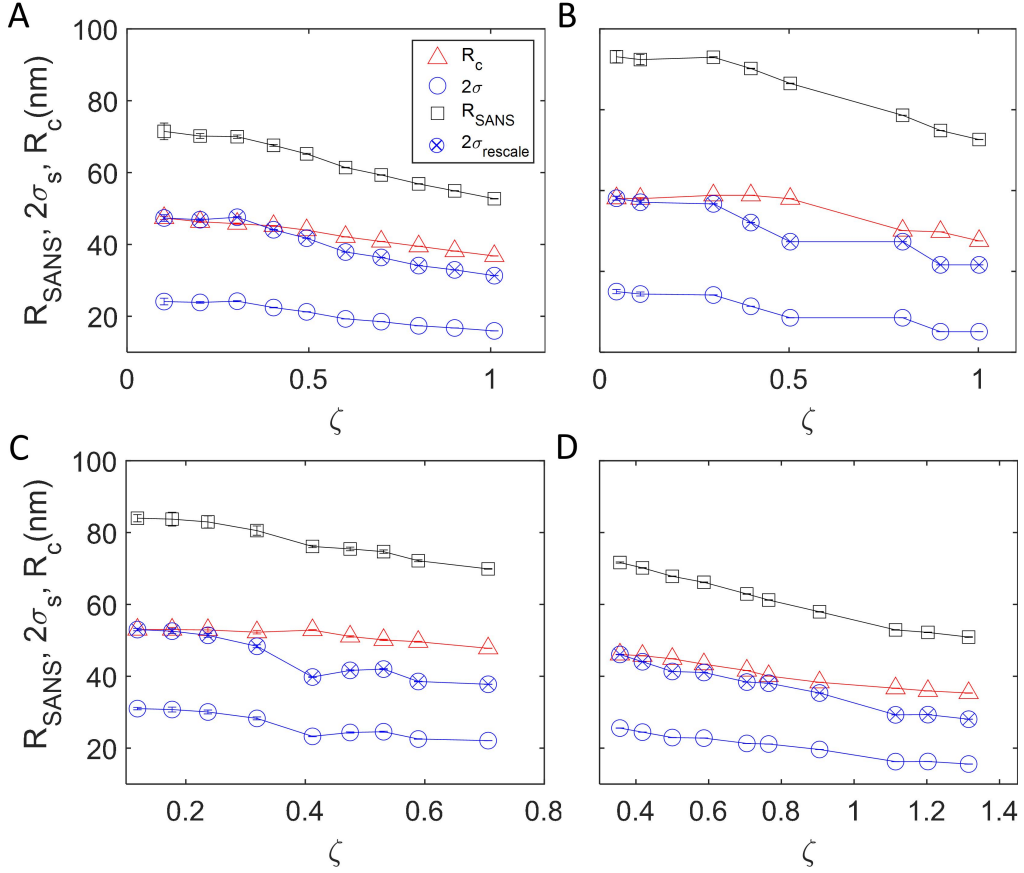


Figure 4.4: R_{SANS} (\square), R_c (\triangle), and $2\sigma_s$ (\circ) of sample s1 (A), s2 (B), s3 (C) and s4 (D) versus generalized volume fraction ζ . $2\sigma_s$ rescaled for comparison with R_c is shown by \otimes . Lines are guides to the eye.

measured concentrations, as shown by the low- ζ plateaus of R_{SANS} and R_c . An osmotic pressure difference between the interior of the microgel and its surrounding comparable to or exceeding the microgel bulk modulus has to be reached for the microgels to deswell. As we will show below, deswelling occurs at volume fractions below $\phi_{\text{rcp}} \approx 0.64$. This observation supports the deswelling due to an osmotic pressure increase possibly triggered by the percolation of counterion clouds surrounding the microgels [150, 201], which naturally explains deswelling without direct contact. The fuzzy corona with width $2\sigma_s$ starts to deswell first, reflecting that it is softer than the denser and more crosslinked core of the microgel. At a slightly higher ζ , R_c also deswells, but the core is compressed to a lesser extent than the fuzzy corona, as shown by the rescaled $2\sigma_s$ data (\otimes symbols) in Fig. 4.4.

While R_{SANS} and R_c are constant at $\zeta \lesssim 0.3$ for samples s1, s2, and s3, the shell and the core of the microgels in sample s4 decrease in the whole ζ range studied, which starts at $\zeta \approx 0.36$, significantly higher than the lowest ζ studied for samples

s1, s2, and s3; see Fig. 4.4D.

To obtain an estimate of the true volume fraction ϕ , we replace the fully swollen microgel radius R_{sw} used in Eq. 5.5 with the radius measured at ζ : $\phi = \zeta \left(\frac{R_{\text{SANS}}(\zeta)}{R_{\text{sw}}} \right)^3$. The result is shown in Fig. 4.5A-D. We find $\phi < \phi_{\text{rcp}}$ in all suspensions studied. For $\zeta \lesssim 0.3$, $\phi \approx \zeta$ reflects that no deswelling takes place at these low and moderate concentrations. At higher ζ , $\phi < \zeta$, and eventually ϕ plateaus. This shows that the microgels must deswell with increasing ζ . To characterize the deswelling, we determine the nearest-neighbor distance from the observed peak positions q^* in $S(q)$: $d_{\text{nn}} = 2\pi/q^*$. With increasing ζ , d_{nn} decreases, as the microgels move closer to each other to fit into the available space. We fit the high- ζ data with the model $d_{\text{nn}} = c\zeta^{-k}$, where c and k are fit parameters. As shown by the red curves in Fig. 4.5E-H, good agreement with the measured data is obtained for $k = 1/3$, which is expected for isotropic deswelling. Therefore, we find that microgels are isotropically deswell without being in direct contact. Note that this scenario is supported by fits to the measured SANS data using the model for spherical microgels given by Eq. 5.10. The fuzzy sphere model is found to apply up to the highest concentration studied, $\zeta \approx 1.3$, without signs of particle deformation or interpenetration; however, these could occur at even higher concentrations ζ .

These results support our model for deswelling triggered by the percolation of counterion clouds in the space between microgels, which effectively frees previously bound counterions, allowing them to exert an osmotic pressure, π . The pressure in the interior of the microgels does not appreciably change, as the percolation of the clouds only alters the pressure outside the microgels. Therefore, a pressure difference between the inside and the outside, $\Delta\pi$, builds up, and microgel deswelling occurs when $\Delta\pi$ becomes comparable to or exceeds the microgel bulk modulus [150, 54]. This scenario is expected to apply when the counterion clouds fill the space between the microgels.

To test whether our data support this scenario, we think of an effective particle consisting of a microgel and the surrounding cloud of counterions that are bound to the particle in dilute conditions [150, 201]. In analogy to ζ , the effective volume fraction of these effective particles is $\zeta_{\text{eff}} = \zeta \left(\frac{R_{\text{sw}} + \Delta r}{R_{\text{sw}}} \right)^3$, where Δr is the thickness of the counterion cloud located in the outside region of the microgel, see Fig. 4.1A. In prior work, we obtained an estimate of $\Delta r = 35$ nm from measurements of the freezing point of polydisperse microgel suspensions [150, 149]. Here, we estimate Δr using the condition that $\zeta_{\text{eff}}(\zeta) = 1$ (Fig. 4.5I-L) when $R_{\text{SANS}}(\zeta)$ starts to decrease from the fully swollen size and, therefore, ϕ starts to deviate from ζ (Fig. 4.5A-D).

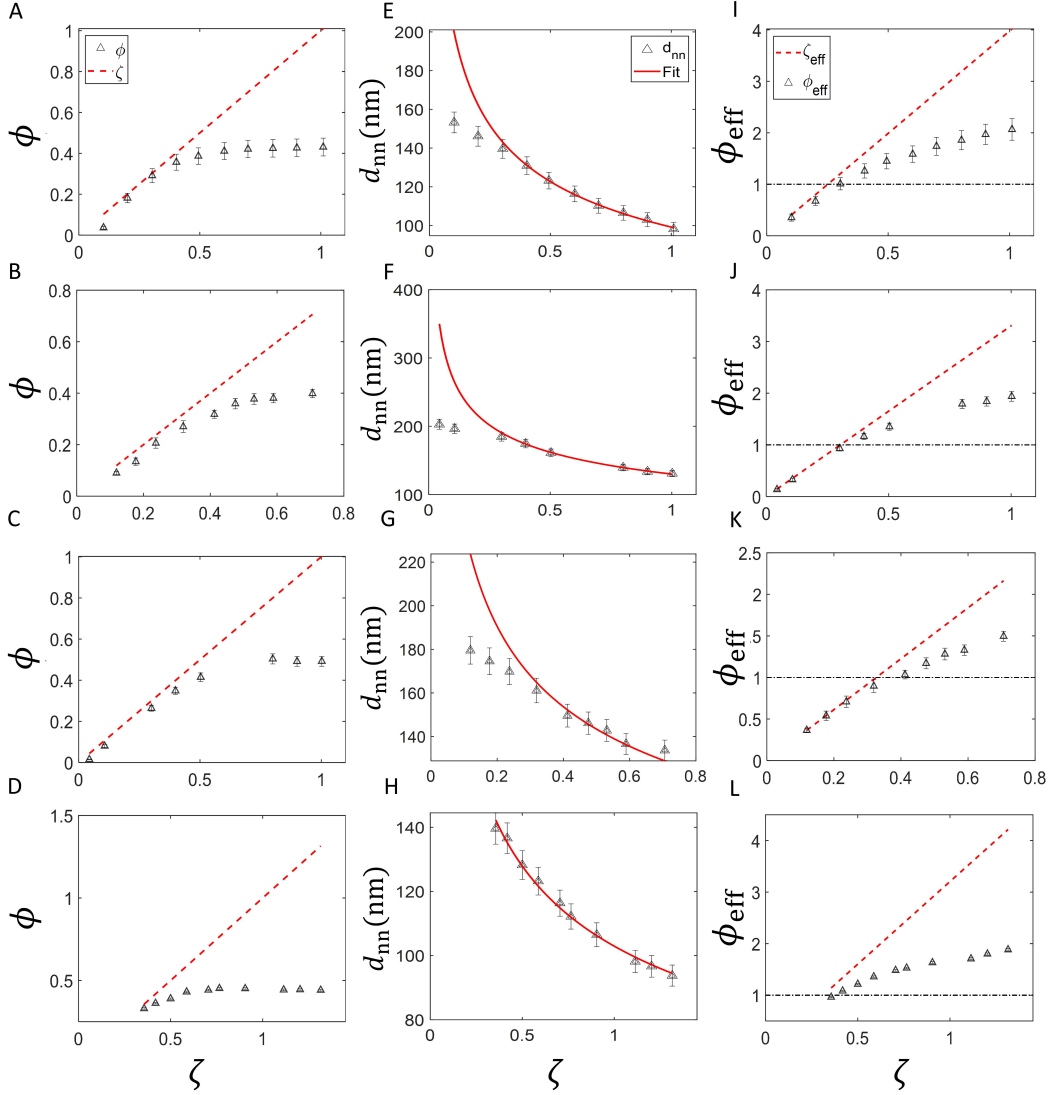


Figure 4.5: (A-D): True volume fraction (Δ) of sample s1 (A), s2 (B), s3 (C) and s4 (D) versus generalized volume fraction ζ . The dashed lines represent $\phi = \zeta$. (E-H): Nearest-neighbor distances (Δ) in suspensions of sample s1 (E), s2 (F), s3 (G) and s4 (H). The red curves show fits to the high- q data with $d_{nn} = c\zeta^{-k}$. The fits are $99\zeta^{-0.32}$ (s1), $131\zeta^{-0.32}$ (s2), $122\zeta^{-0.31}$ (s3), and $103\zeta^{-0.33}$ (s4). (I-L): Calculated effective volume fraction $\phi_{eff}(\zeta)$ (Δ) for s1 (I), s2 (J), s3 (K) and s4 (L). The dashed line represents $\zeta_{eff}(\zeta)$. The dash-dotted line highlights a volume fraction of one.

We obtain $\Delta r = (44 \pm 5)$ nm (s1), (47 ± 5) nm (s2), (38 ± 6) nm (s3), and (37 ± 3) nm (s4), which are all in good agreement with the previously determined value. This condition is also reflected by comparing ζ_{eff} with the true volume fraction of the effective particles, defined by $\phi_{eff} = \zeta \left(\frac{R_{SANS}(\zeta) + \Delta r}{R_{sw}} \right)^3$, shown by the triangles (Δ) in Fig. 4.5I-L. We find that ϕ_{eff} stays close to ζ_{eff} at the lowest concentrations, where the microgels retain their fully swollen state. As soon as deswelling begins, the curve

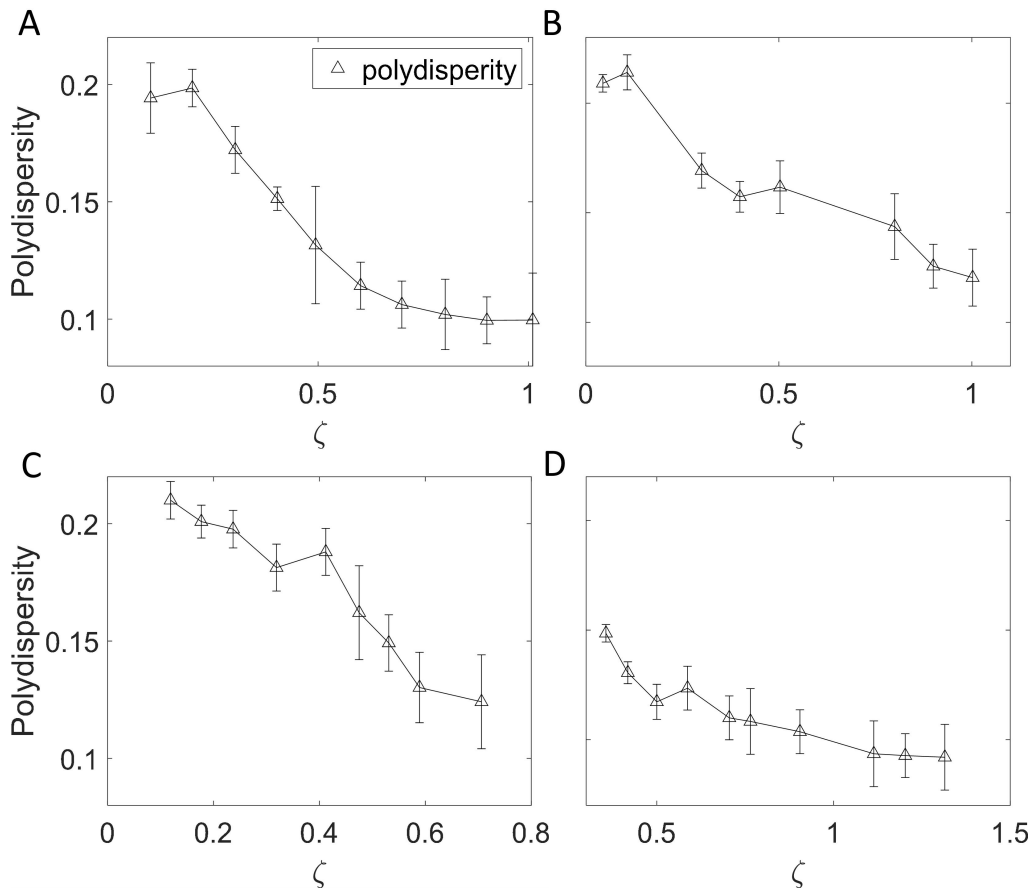


Figure 4.6: Polydispersity (Δ) of samples s1 (A), s2 (B), s3 (C), and s4 (D) as a function of generalized volume fraction ζ . Lines are guides to the eye.

given by ϕ_{eff} flattens in analogy to $\phi(\zeta)$; see Fig. 4.5I-L. For samples s1, s2, and s3, $\zeta_{\text{eff}} = 1$ is reached at $\zeta \approx 0.25$, 0.30, and 0.31, respectively.

With these observations, we can explain the apparently different behaviour of sample s4. The lowest $\zeta \approx 0.36$ studied for this sample corresponds to $\zeta_{\text{eff}} \approx 1$, indicating the condition for percolation of the counterion clouds and for deswelling to occur has already been met. The microgels thus deswell in the whole studied ζ range and, as for the other samples, isotropic deswelling is observed, see Fig. 4.5H. All these results support our model for microgel deswelling as a consequence of the percolation of counterion clouds.

As the largest microgels synthesized using precipitation polymerization are expected to be the softest, it is expected that the largest microgels deswell first and that suspension polydispersity decreases as $\zeta_{\text{eff}} > 1$. The polydispersities obtained from our SANS data indeed confirm this scenario, as shown in Fig. 4.6. In the fully swollen state, polydispersities are in the range from 0.15 to 0.22, and they are seen

to decrease to values close to 0.1 at the highest studied ζ for all samples.

4.6 Conclusions

The presented SANS data for pNIPAM microgels with 2 mol% BIS crosslinker confirm our previous results for spontaneous microgel deswelling at high ζ triggered by the osmotic pressure increase due to the percolation of the counterion clouds surrounding the microgels. We find that microgels stay fully swollen up to $\zeta \approx 0.3$, and that it is at approximately this ζ that the percolation of counterion clouds first occurs. The observed critical concentration for deswelling agrees with the width of the counterion clouds determined in previous work [150, 149, 54]. Furthermore, the observed suspension polydispersity σ also supports the model for spontaneous deswelling. It decreases when deswelling occurs, as expected for suspensions with all microgels synthesized according to the same protocol [149]. We find the inclusion of polydispersity is essential to obtain consistent results for the microgel size and the suspension structure, particularly at low ζ , where deswelling should not have occurred. The apparent structure factor (Eq. 4.5) appears to be sufficient for polydispersities $\lesssim 0.2$. The suspension structure can be modeled with the Percus-Yevick structure factor for hard spheres although the microgels carry charged groups and counterions at their periphery. The spontaneous deswelling at high concentrations and the resulting reduction in the volume fraction ϕ is likely an important factor to explain the apparently charge-neutral structure, as deswelling allows for more screening volume between the microgels, reducing the effect of charges. Additionally, microgels are open particles, and the charges on the polymer network are partly screened within the particle. These considerations, as well as polymer-solvent mixing, and polymer network elasticity, must all be at the heart of improved models aimed at predicting the phase behavior [194, 53, 185, 149, 21] and the interaction [68] of these soft colloids at low and high concentrations.

Sample	ζ ± 0.05	R_c (nm)	σ_s (nm)	R_{SANS} (nm)	ϕ	PD	ξ (nm)
s1	0.102	47.37 ± 0.47	12.05 ± 0.92	71.47 ± 2.3	0.04 ± 0.01	0.194 ± 0.015	9.50 ± 3.93
s1	0.201	46.31 ± 0.23	11.93 ± 0.23	70.18 ± 0.69	0.18 ± 0.003	0.199 ± 0.008	9.07 ± 0.92
s1	0.303	45.78 ± 0.17	12.10 ± 0.15	69.99 ± 0.46	0.29 ± 0.003	0.172 ± 0.010	13.24 ± 0.99
s1	0.403	45.15 ± 0.12	11.22 ± 0.08	67.58 ± 0.28	0.36 ± 0.001	0.151 ± 0.005	15.63 ± 0.84
s1	0.494	43.98 ± 0.06	10.62 ± 0.04	65.22 ± 0.14	0.39 ± 0.001	0.132 ± 0.025	15.03 ± 1.23
s1	0.601	42.11 ± 0.03	9.64 ± 0.02	61.39 ± 0.08	0.41 ± 0.001	0.114 ± 0.010	12.72 ± 0.48
s1	0.699	40.82 ± 0.03	9.26 ± 0.02	59.33 ± 0.07	0.42 ± 0.001	0.106 ± 0.010	12.68 ± 0.24
s1	0.802	39.49 ± 0.03	8.68 ± 0.02	56.86 ± 0.06	0.43 ± 0.001	0.102 ± 0.015	11.28 ± 0.79
s1	0.901	38.16 ± 0.03	8.28 ± 0.02	54.91 ± 0.06	0.43 ± 0.001	0.099 ± 0.010	8.49 ± 2.23
s1	1.01	36.79 ± 0.03	7.97 ± 0.02	52.73 ± 0.07	0.43 ± 0.001	0.098 ± 0.020	14.79 ± 0.42
s2	0.044	58.1 ± 0.46	17.5 ± 0.51	93.1 ± 1.49	0.02 ± 0.003	0.209 ± 0.004	10.68 ± 2.08
s2	0.107	58.0 ± 0.27	17.2 ± 0.49	92.4 ± 1.26	0.08 ± 0.003	0.214 ± 0.008	17.95 ± 6.36
s2	0.30	58.82 ± 0.04	17.08 ± 0.04	92.98 ± 0.13	0.26 ± 0.003	0.169 ± 0.008	15.09 ± 1.35
s2	0.399	58.82 ± 0.03	15.69 ± 0.02	90.20 ± 0.07	0.35 ± 0.001	0.157 ± 0.007	14.99 ± 0.29
s2	0.503	57.98 ± 0.03	14.26 ± 0.02	86.50 ± 0.08	0.41 ± 0.001	0.162 ± 0.012	11.45 ± 0.18
s2	0.80	50.10 ± 0.01	14.22 ± 0.02	78.62 ± 0.02	0.50 ± 0.001	0.144 ± 0.015	14.98 ± 1.55
s2	0.90	49.78 ± 0.01	12.53 ± 0.01	74.85 ± 0.02	0.49 ± 0.001	0.126 ± 0.010	14.88 ± 1.67
s2	1.002	47.55 ± 0.01	12.53 ± 0.01	72.62 ± 0.02	0.49 ± 0.001	0.121 ± 0.013	15.05 ± 1.46
s3	0.119	53.00 ± 0.36	15.51 ± 0.33	84.00 ± 1.01	0.09 ± 0.01	0.210 ± 0.008	7.47 ± 0.52
s3	0.177	53.01 ± 0.58	15.37 ± 0.67	83.74 ± 1.92	0.13 ± 0.001	0.201 ± 0.007	9.97 ± 1.47
s3	0.237	52.90 ± 0.59	15.03 ± 0.54	82.96 ± 1.67	0.21 ± 0.008	0.198 ± 0.008	9.99 ± 1.09
s3	0.319	52.27 ± 0.48	14.14 ± 0.41	80.55 ± 1.28	0.27 ± 0.001	0.181 ± 0.010	9.01 ± 0.75
s3	0.412	52.86 ± 0.13	11.64 ± 0.10	76.13 ± 0.33	0.31 ± 0.001	0.188 ± 0.010	5.93 ± 0.19
s3	0.475	51.09 ± 0.19	12.18 ± 0.16	75.45 ± 0.51	0.36 ± 0.002	0.162 ± 0.020	7.81 ± 0.39
s3	0.531	50.12 ± 0.18	12.28 ± 0.15	74.69 ± 0.47	0.37 ± 0.001	0.149 ± 0.012	9.86 ± 0.44
s3	0.589	49.62 ± 0.11	11.27 ± 0.08	72.16 ± 0.26	0.38 ± 0.001	0.130 ± 0.015	9.98 ± 1.27
s3	0.706	47.79 ± 0.04	11.05 ± 0.03	69.89 ± 0.09	0.40 ± 0.001	0.124 ± 0.020	10.02 ± 0.84
s4	0.356	46.08 ± 0.07	12.79 ± 0.05	71.66 ± 0.17	0.33 ± 0.60	0.149 ± 0.004	10.07 ± 1.55
s4	0.418	45.72 ± 0.04	12.23 ± 0.03	70.17 ± 0.10	0.36 ± 0.37	0.131 ± 0.005	10.01 ± 1.22
s4	0.50	44.87 ± 0.03	11.48 ± 0.02	67.82 ± 0.07	0.39 ± 0.25	0.117 ± 0.008	9.99 ± 1.10
s4	0.587	43.37 ± 0.04	11.39 ± 0.03	66.16 ± 0.09	0.43 ± 0.55	0.124 ± 0.010	10.05 ± 0.88
s4	0.705	41.60 ± 0.03	10.66 ± 0.02	62.91 ± 0.08	0.44 ± 0.39	0.109 ± 0.010	12.65 ± 0.58
s4	0.765	40.08 ± 0.03	10.57 ± 0.02	61.23 ± 0.08	0.45 ± 0.29	0.108 ± 0.015	10.95 ± 1.02
s4	0.905	38.33 ± 0.03	9.81 ± 0.02	57.95 ± 0.07	0.45 ± 0.25	0.104 ± 0.010	10.02 ± 0.44
s4	1.114	36.66 ± 0.04	8.13 ± 0.02	52.92 ± 0.08	0.44 ± 0.18	0.094 ± 0.015	9.98 ± 1.89
s4	1.203	35.93 ± 0.03	8.14 ± 0.02	52.21 ± 0.08	0.44 ± 0.17	0.093 ± 0.010	10.66 ± 0.93
s4	1.315	35.34 ± 0.05	7.79 ± 0.03	50.92 ± 0.10	0.44 ± 0.19	0.092 ± 0.015	10.08 ± 0.73

Table 4.2: Generalized volume fraction, ζ , core radius, R_c , half width of the fuzzy shell, σ_s , SANS radius, R_{SANS} , volume fraction, ϕ , polydispersity, PD, and the mesh size, ξ , for all studied suspensions of samples s1, s2, s3, and s4. R_c , σ_s , PD, and ξ are fit parameters, see Eqs.(4.7) - (4.10).

Chapter 5

Measuring the counterion cloud of soft microgels using SANS with contrast variation

In this chapter, we show the results of the first direct measurement of the counterion clouds at the microgel periphery via Small-angle neutron scattering (SANS). This study shows solid proof of the theory of explaining the spontaneous deswelling behavior of the microgels at high concentrations.

Manuscript title: Measuring the counterion cloud of soft microgels using SANS with contrast variation

Manuscript state: Published manuscript

Reference Zhou, Boyang, Urs Gasser, and Alberto Fernandez-Nieves. "Measuring the counterion cloud of soft microgels using SANS with contrast variation." *Nature Communications* 14, no. 1 (2023): 3827.

Keywords: microgels, electric double layer, deswelling, SANS, contrast variation, ion exchange

Acknowledgements: We acknowledge financial support from the Swiss National Science Foundation (200020_184839, U. G.) and MCIN/AEI/10.13039/501100011033/FEDER, UE (Grant No. PID2021-122369NB-100, A. F.-N.). SANS data was taken on the instruments SANS-I and SANS-II at SINQ, Paul Scherrer Institut.

Author contributions: B.Z. prepared samples, performed measurements, analyzed the data, and wrote the paper. U.G. designed the research, supported and carried out measurements and sample preparation, analyzed data, and wrote the paper. A.F.-N. designed the research, supported measurements and data analysis, and wrote the paper.

5.1 Abstract

The behavior of microgels and other soft, compressible colloids depends on particle concentration in ways that are absent in their hard-particulate counterparts. For instance, poly-*N*-isopropylacrylamide (pNIPAM) microgels can spontaneously deswell and reduce suspension polydispersity when concentrated enough. Despite the pNIPAM network in these microgels is neutral, the key to understanding this distinct behavior relies on the existence of peripheric charged groups, responsible for providing colloidal stability when deswollen, and the associated counterion cloud. When in close proximity, clouds of different particles overlap, effectively freeing the associated counterions, which are then able to exert an osmotic pressure that can potentially cause the microgels to decrease their size. However, up to now, no direct measurement of such an ionic cloud exists, perhaps even also for hard colloids, where it is referred to as an electric double layer. Here, we use small-angle neutron scattering with contrast variation with different ions to isolate the change in the form factor directly related to the counterion cloud, and obtain its radius and width. Our results highlight that the modeling of microgel suspensions must unavoidably and explicitly consider the presence of this cloud, which exists for nearly all microgels synthesized today.

5.2 Introduction

Soft and deformable colloids exhibit a phase behavior that is more complex than that of hard and incompressible colloids. Furthermore, there is no generally accepted model for their interactions and overall behavior covering both dilute and concentrated conditions. Microgels, cross-linked polymer particles immersed in a solvent, are an important class of soft colloids that is of interest both for applications and for fundamental studies aimed, for example, at understanding the role of colloidal softness. It is in fact this softness that renders microgels responsive to

changes in variables like temperature [132, 170], pH [72, 116], and hydrostatic pressure [101, 99, 100]. Their shape, size, internal architecture, and, as a consequence, their particle-particle interaction all depend on the conditions of their surroundings.

The importance of particle softness was highlighted by the spontaneous deswelling of large particles in bidisperse suspensions of poly-*N*-isopropylacrylamide (pNIPAM) microgels suspended in water. With increasing concentration, the large and less numerous microgels were found to spontaneously deswell to about the size of the smaller and more numerous microgels [80]. This reduced the bidispersity of the suspension, a behavior not known for other colloids or particulate materials, allowing crystallization in the absence of point defects. For pNIPAM microgels, deswelling can start at concentrations below random close packing, i.e. without direct contact between particles [52, 150, 149]. We previously identified the fixed charges at the periphery of the particles and their associated counterions to be the key to understand this spontaneous deswelling [150, 54, 153]. Charged $-\text{O}-\text{SO}_2-\text{O}^-$ groups originating from the initiator of the polymerization reaction remain at the ends of pNIPAM chains and locate at the microgel outskirts [203]; their counterions thus form a cloud surrounding the microgel. Most of these counterions are electrostatically bound to the particle, but there is always a number of them that, for entropic reasons, overcome this electrostatic attraction and wander around contributing to the suspension osmotic pressure. Deswelling occurs when the distribution of counterions inside and outside the microgel causes an osmotic-pressure difference $\Delta\pi$ comparable to the microgel bulk modulus. This can happen when the counterion clouds percolate through the accessible volume, causing a steep increase in $\Delta\pi$, as counterions that were previously bound to a particle become effectively free. We have shown that this mechanism can explain both the observed spontaneous deswelling [150] and also the concentration-dependent freezing transition in polydisperse microgel suspensions with either a bimodal or a Gaussian size distribution [149].

The distribution of fixed charges and the associated counterion cloud in an otherwise totally charge-neutral pNIPAM network is, therefore, of utmost importance to model and understand the deswelling behavior and the interaction between pNIPAM microgels. As the amount of fixed charge is related to particle synthesis, one can envision synthesizing microgels with tailored interactions and thus phase behavior. Up to now, however, no direct measurement of this cloud exists. Since the counterion density in this cloud is expected to provide a small contribution to the microgel form factor, directly proving its existence is challenging. In this paper, we use small-angle neutron scattering (SANS) to reveal the signal due to the coun-

terion cloud by taking the difference between two samples that contain the same microgels at the essentially same number densities but in the presence of different counterions, sodium (Na^+) or ammonium (NH_4^+). Suspensions containing either ion can be obtained using dialysis [203]. The contrast difference for neutron radiation between these two ions is the key that allows obtaining the signal due to the counterion cloud. Note that this cloud exists as an electric double layer in charged hard colloids. However, in this case, the particle rigidity prevents the suspension polydispersity from changing. For microgels, this change can happen due to their softness, highlighting the role that these ions can have in the suspension behavior. To our knowledge, however, no direct measurement of the counterion cloud exists for soft colloids. Our work with SANS thus opens the door for exploring the details of ion clouds in any charged colloidal species.

5.3 Method

Sample preparation and characterization. The poly-*N*-isopropylacrylamide (pNIPAM) microgels of three different sizes are used as obtained from the group of Prof. L. A. Lyon (Chapman University, USA). The hydrodynamic radii in the fully swollen state at $T = 20^\circ\text{C}$, determined using DLS, are $R_{\text{sw}} = (87 \pm 1.7) \text{ nm}$ (s1), $R_{\text{sw}} = (125 \pm 2.7) \text{ nm}$ (s2), and $R_{\text{sw}} = (140 \pm 2.3) \text{ nm}$ (s3) [203]. The collapsed radii, R_{coll} , of the microgels are determined using viscometry with dilute microgel suspensions with the aid of the Einstein-Batchelor equation for the relative viscosity [11, 203]. These characterization measurements allow obtaining the selling ratio

$$k = \frac{\rho_{\text{solvent}}}{\rho_{\text{pNIPAM}}} \frac{R_{\text{sw}}^3}{R_{\text{coll}}^3} \quad (5.1)$$

used to obtain the effective volume fraction

$$\zeta = k \frac{m_{\text{pNIPAM}}}{m_{\text{tot}}}. \quad (5.2)$$

Dialysis. To extract key parameters of the counterion cloud, suspensions that differ in the counterion type but are otherwise identical are prepared for SANS measurements. The two counterions, NH_4^+ and Na^+ , present after the synthesis, are used for this purpose. Using dialysis, we exchange the counterions to obtain one suspension with NH_4^+ and another with Na^+ counterions [203]. We first dialyze the microgel suspension, contained inside a dialysis bag, against a NaCl or NH_4Cl

solution at a concentration of $\sim (167 \pm 5)$ mM for five days, exchanging the salt solution once a day. The resultant suspension then contains either Na^+ or NH_4^+ , plus Cl^- ions. We then remove the excess salt dialyzing against ultrapure H_2O , again for 5 days and exchanging the H_2O bath daily. The resultant suspensions with either NH_4^+ or Na^+ counterions are freeze-dried and resuspended in D_2O at a fixed ζ . These suspensions only differ in the type of counterion and show the same suspension behavior, as the counterion concentration is too low to cause significant differences due to Hofmeister effects [203].

Small-angle neutron scattering (SANS). SANS was performed with dilute, $0.1 \lesssim \zeta \lesssim 0.2$, and more concentrated suspensions, $0.45 \lesssim \zeta \lesssim 0.58$, on the instruments SANS-I [91] and SANS-II [173] of the SINQ neutron source at Paul Scherrer Institut, Switzerland [14]. The microgel suspensions were measured in quartz-glass cuvettes at fixed temperatures of $T = (20 \pm 0.5)^\circ\text{C}$ and $(45 \pm 0.5)^\circ\text{C}$. The instruments were configured to cover the q range from about 0.025 nm^{-1} to 0.35 nm^{-1} , corresponding to length scales between 30 nm and 600 nm in real space. Both instruments have position-sensitive area detectors covering about one order of magnitude of the momentum transfer $q = \frac{4\pi}{\lambda} \sin(\theta/2)$ depending on the wavelength, λ , and the scattering angle θ . The 2D raw data was corrected for dark counts due to electronic noise and stray neutrons and for the sample background originating from the quartz-glass sample container and solvent scattering. The corrected image was calibrated for detector efficiency with a H_2O measurement and was azimuthally averaged to obtain the SANS scattering signal $I(q)$ [86].

5.4 Results

We study three temperature-sensitive pNIPAM microgels with a lower critical solution temperature (LCST) $T_c \approx 32^\circ\text{C}$ in water. Their swollen radii determined by SANS are $(85 \pm 1.1) \text{ nm}$ (s1), $(124.3 \pm 1.2) \text{ nm}$ (s2), and $(135.6 \pm 2.6) \text{ nm}$ (s3). They all contain 2.0 mol% of crosslinker N, N' -methylene-bis-acrylamide (BIS) and are synthesized with ammonium persulfate (APS) as initiator. Besides the temperature, the suspension behavior is controlled by the particle volume fraction ϕ . Since microgels can deswell, deform, and interpenetrate, ϕ is hard to know at high concentrations. Therefore, we use a generalized volume fraction ζ , defined in terms of the dilute microgel size [203]. Consequently for dilute suspensions $\phi = \zeta$, while at higher concentrations, $\zeta > \phi$, reflecting deswelling, shape change, or interpenetration. To learn about the counterion cloud of the pNIPAM microgels, we prepare

pairs of samples containing the same microgels at essentially the same ζ , but with Na^+ or NH_4^+ as counterions. We achieve this by dialyzing against a NaCl or NH_4Cl solution at a high concentration, (167 ± 5) mM in our case; this guarantees the positive ion is the wanted one. The process, however, results in excess salt, which we remove by dialyzing again but against pure H_2O [203]. The suspensions are then freeze-dried and re-suspended in D_2O for SANS measurements. We prepare pairs of samples at $0.1 \lesssim \zeta \lesssim 0.2$ to investigate microgels in relatively dilute states and at $0.48 \lesssim \zeta \lesssim 0.55$, where the percolation of counterion clouds is expected [150, 54].

SANS measurements taken in the swollen [$T = (20 \pm 0.5)^\circ\text{C}$] and deswollen [$(45 \pm 0.5)^\circ\text{C}$] states for a representative sample pair are shown in Fig. 5.1. Recall that the scattering is dominated by the particles and that the counterions only provide a second order contribution to the scattered intensity $I(q)$. Similarly, any small changes in the microgel structure, as induced by the ions, would also result in second-order effects. However, studies of the Hofmeister series have shown that

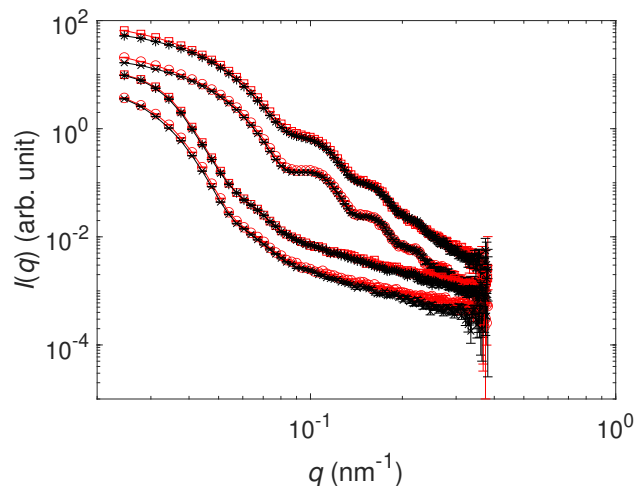


Figure 5.1: SANS data of sample s3 with Na^+ (red circles and squares) and NH_4^+ counterions (black crosses and asterisks) taken at $(45 \pm 0.5)^\circ\text{C}$ (two upper curves) and at $(20 \pm 0.5)^\circ\text{C}$ (two lower curves). For each counterion, two samples with concentrations $\zeta \approx 0.18$ (circles, crosses) and $\zeta \approx 0.54$ (squares, asterisks) were measured. The error bars represent the uncertainty due to the counting statistics of the SANS instrument.

the swelling behavior of pNIPAM is only affected and becomes dependent on the ion type at salt concentrations $\gtrsim 300$ mM. In the suspensions studied here, the ion concentration is at least ten times lower. Therefore, the pNIPAM structure is not expected to change with the exchange of counterions [105, 84]. We then analyze our SANS measurements considering that the ions do not significantly change the

scattering of the microgel particles and that they only weakly contribute to the form factor. Our data analysis is based on a model that either directly includes the signal due to the ion cloud, or indirectly accounts for the effect of the ions through a change in the structure of the polymer network. In the following, we present our analysis considering that the signal directly results from the ion cloud, and later discuss the alternative possibility that the detected signal is caused by the ions but that it manifests as a small change in the form factor of the polymer network.

We use accepted models for pNIPAM microgels, the fuzzy-sphere form factor [169] and the Percus-Yevick structure factor, including polydispersity [134, 93, 39]. For each data pair, we extract the radius of the particle core R_c , the associated polydispersity σ , and the width of the fuzzy microgel corona σ_s ; see Supplementary Table 2 [203]. To correct for small differences in particle number density n_d between samples with Na^+ and NH_4^+ ions, which is essential to extract the weak scattering signal due to the counterion cloud, we consider that, except for a small signal due to the counterion cloud, $I(q)/n_d$ should not depend on the ion type. Thus, we introduce the corrected scattering signal as $I_{\text{corr}}^{\text{Na}^+}(q) = I^{\text{Na}^+}(q) n_d^{\text{NH}_4^+} / n_d^{\text{Na}^+}$. This corrected Na^+ curve is hard to distinguish from the uncorrected curves, confirming that n_d is indeed very close in every sample pair; see Supplementary Fig. 3.

To explicitly consider the signal due to the counterion cloud, we divide the scattering amplitude of a microgel into the contributions due to the polymer network and the signal caused by the ion cloud: $F^X(q) = F_p(q) + F_{\text{ic}}^X(q)$, where the superscript X refers to the ion type, either Na^+ or NH_4^+ . Note that the term due to the polymer does not depend on the ion type, as argued in section 5 of the Supplementary Information [203], and that the scattered intensity $I^X(q) \propto |F^X(q)|^2$. We then take the difference of the scattered intensities in the presence of Na^+ and NH_4^+ ions, and obtain $\Delta I_{\text{corr}}(q) = I_{\text{corr}}^{\text{Na}^+}(q) - I^{\text{NH}_4^+}(q) \approx 2F_p(q) \left[F_{\text{ic}}^{\text{NH}_4^+}(q) - F_{\text{ic}}^{\text{Na}^+}(q) \right]$, where we have neglected higher order terms $\propto |F_{\text{ic}}^X(q)|^2$. We then consider the pre-factor due to the scattering contrast, $\Delta\rho^X$, and the volume of ions, V^X , and write $F_{\text{ic}}^X(q) = \Delta\rho^X V^X f_{\text{ic}}(q)$, where $f_{\text{ic}}(q)$ no longer depends on the ion type. This reveals that $\Delta I_{\text{corr}}(q)$ is directly proportional to the scattering amplitude of the cloud:

$$\Delta I_{\text{corr}}(q) \approx 2F_p(q) \left(\Delta\rho^{\text{NH}_4^+} V^{\text{NH}_4^+} - \Delta\rho^{\text{Na}^+} V^{\text{Na}^+} \right) f_{\text{ic}}(q) \quad (5.3)$$

We thus exploit the large contrast difference between the ions, $\Delta\rho^{\text{Na}^+} - \Delta\rho^{\text{NH}_4^+} \approx 9.8 \times 10^{-4} \text{ nm}^{-2}$, as well as the large scattering amplitude of the polymer network, to amplify the signal, which is shown in Fig. 5.2A.

We model the counterion cloud as a spherical surface that is smeared out due

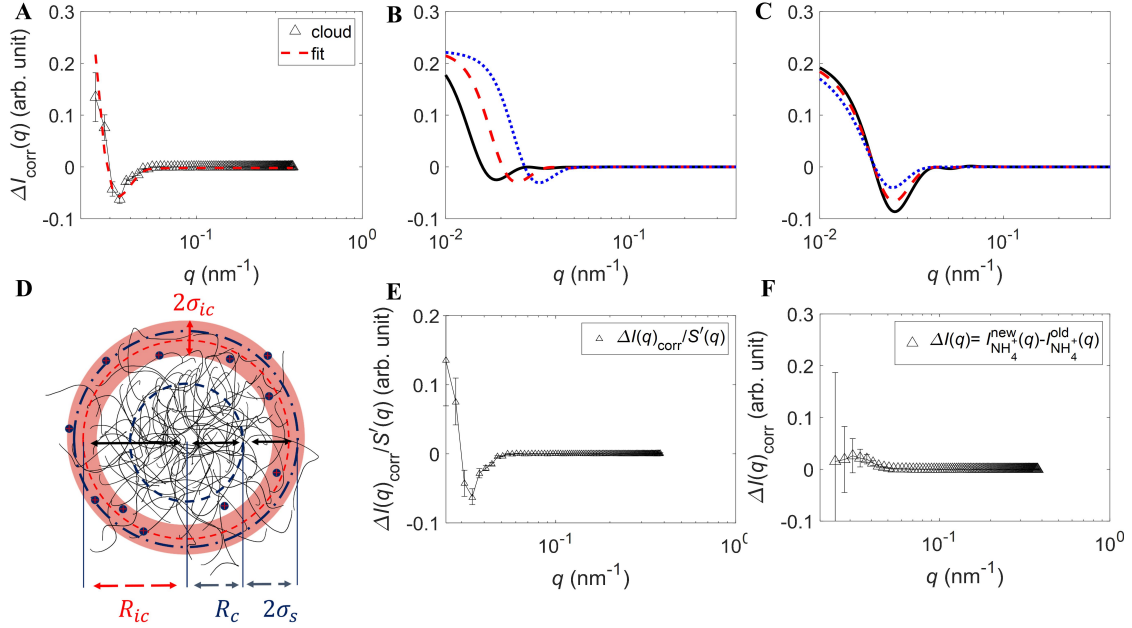


Figure 5.2: SANS signal due to the counterion cloud. (A) Subtraction $I^{\text{NH}_4^+}(q) - I^{\text{Na}^+}(q)$ of sample s3 at $\zeta \approx 0.2$ and $T \approx 20^\circ\text{C}$, the cloud fit is shown by the red, dashed curve. (B,C) Counterion cloud model including $S'(q)$, polydispersity, and instrument resolution for (B) $R_{\text{ic}} = R_{\text{SANS}} = 90$ nm (blue, dotted curve), 130 nm (red, dashed curve), 180 nm (black curve) with fixed parameters $\sigma_{\text{ic}} = 30$ nm, $\sigma_s = 15$ nm, $\phi = 0.2$, and $\sigma = 0.05$. (C) Counterion cloud model for $\sigma_{\text{ic}} = 50$ nm (blue, dotted curve), 30 nm (red, dashed curve), 10 nm (black curve) with fixed parameters $R_{\text{ic}} = R_{\text{SANS}} = 130$ nm, $R_c = 100$ nm, $\sigma_s = 15$ nm, $\phi = 0.2$, and $\sigma = 0.05$. (D) Sketch of a pNIPAM microgel with $R_{\text{SANS}} = R_c + 2\sigma_s$ and the counterion cloud with width $2\sigma_{\text{ic}}$ and radius R_{ic} located at the particle periphery. (E) Data shown in panel A divided by $S'(q)$. (F) Direct subtraction $I_{\text{old}}^{\text{NH}_4^+}(q) - I_{\text{new}}^{\text{NH}_4^+}(q)$ at $\zeta \approx 0.2$, $T \approx 20^\circ\text{C}$, and with corrected number density. The error bars in panels A, E, and F represent the uncertainty due to the counting statistics of the SANS instrument.

to the mobility of the ions and the arrangement of the fixed charges in the pNIPAM network. In reciprocal space we have

$$F_{\text{ic}}^X(q) = \Delta\rho^X V^X \frac{\sin(qR_{\text{ic}})}{qR_{\text{ic}}} \exp\left(-\frac{[q\sigma_{\text{ic}}]^2}{2}\right) \quad (5.4)$$

where R_{ic} is the distance from the microgel center to the spherical counterion cloud, and σ_{ic} quantifies the width of the cloud. Additionally, we include the structure factor of the suspension $S(q)$, the polydispersity, and the resolution of the SANS instrument [203]. This model reproduces the measured signal for all investigated samples, as shown by the dashed curve in Fig. 5.2A and in Supplementary Fig. 2

[203], which is a fit to the data with R_{ic} and σ_{ic} as fitting parameters. Note that the detected cloud signal has the expected intensity. We take the ratio of the measured intensities at $q = 0$, obtained from an extrapolation of our fits, and obtain $\Delta I_{\text{corr}}(0)/I_{\text{corr}}(0) = 0.06 \pm 0.01$, which we compare with the corresponding ratio of the calculated prefactors $s_{\text{ic}} = 2V_{\text{p}}\Delta\rho_{\text{p}} \left(\Delta\rho^{\text{NH}_4^+} V^{\text{NH}_4^+} - \Delta\rho^{\text{Na}^+} V^{\text{Na}^+} \right)$ with $\Delta\rho_{\text{p}} = \rho_{\text{p}} - \rho_{\text{D}_2\text{O}}$ the contrast of the polymer network and $s_{\text{p}} = (V_{\text{p}}\Delta\rho_{\text{p}})^2$; we find $s_{\text{ic}}/s_{\text{p}} = 0.05 \pm 0.02$, where the error reflects the significant uncertainty in the number of counterions per microgel entering in $V^{\text{NH}_4^+}$ and V^{Na^+} [203].

The agreement is very good, indicating that the observed signal is directly caused by the counterion cloud.

The fingerprint of the counterion cloud in $\Delta I_{\text{corr}}(q)$ is the presence of a negative minimum and an associated steep upturn at lower q . The q -position of the minimum is most sensitive to the cloud radius, and its depth is directly related to the width of the cloud, as illustrated in Figs. 5.2B and C.

The radii and widths of the whole microgel, obtained from the fits to the data shown in Fig. 5.1, as well as those for the counterion cloud are shown in Figs. 5.3 and Supplementary Fig. 5 and are listed in Supplementary Table 2. For all investigated

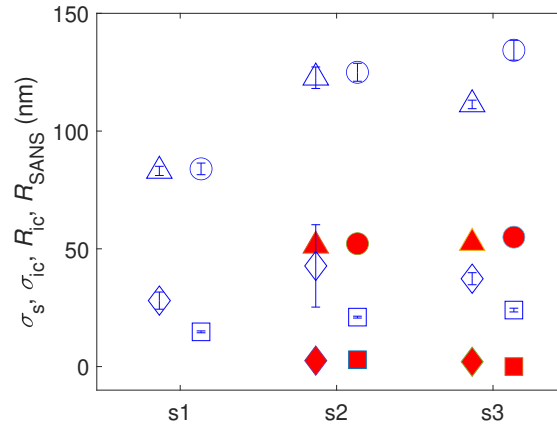


Figure 5.3: Radii and shell widths of microgels and counterion clouds. The radii R_{SANS} (circles) and R_{ic} (triangles) as well as the half widths of the fuzzy corona σ_s (squares) and the counterion cloud σ_{ic} (diamonds) for samples s1, s2, and s3 at $0.1 \lesssim \zeta \lesssim 0.2$ measured at $T \approx 20^\circ\text{C}$ (blue open symbols) and $T \approx 45^\circ\text{C}$ (red full symbols). All values shown are also listed in Supplementary Tables 2 and 3. The error bars result from the least-squares fit to the SANS data; see text for discussion.

samples at $T \approx 20^\circ\text{C}$, we find R_{ic} to be smaller but close to R_{SANS} , indicating the counterion cloud is located inside the fuzzy shell of the microgel; see schematic

in Fig. 5.2D. This confirms that the $-\text{O}-\text{SO}_2-\text{O}^-$ groups are indeed located in the particle periphery, as expected from the synthesis and in agreement with our model for particle deswelling at high concentrations [150, 54]. In addition, the extent of the counterion cloud σ_{ic} is on the order of the thickness of the fuzzy corona $2\sigma_s$. This is in good agreement with a prior estimate of the counterion cloud width, (35 ± 4) nm, obtained from the onset of microgel deswelling in bidisperse pNIPAM suspensions [149]. In that study, the freezing point, ζ_f , was found to increase with the bidispersity of the suspension. As the bidispersity of the fully swollen microgels was too large for crystallization to occur, the formation of crystals relied on the deswelling of the largest and softest microgels and the corresponding reduction in bidispersity. Therefore, ζ_f could be used as a measure of the onset of deswelling due to the percolation of the counterion clouds and allowed estimating the extent of the counterion clouds. Note σ_{ic} is clearly larger than the Debye screening length, which is $\kappa^{-1} \approx 14$ nm, due to the counterions in a microgel suspension at $\zeta = 0.5$. This suggests that, in the swollen state, the $-\text{O}-\text{SO}_2-\text{O}^-$ groups are distributed in the outskirts of the microgel's fuzzy corona and that this distribution increases the width of the counterion cloud.

While the microgels are fully swollen at $T = 20^\circ\text{C}$ and $\zeta = 0.2$, their diameter is reduced by $\approx 4\%$ at $\zeta = 0.5$. If we consider an effective microgel including the counterion cloud, and calculate the volume fraction of these effective particles, we obtain $\zeta_{\text{eff}} = \zeta \left(\frac{R_{\text{sw}} + \sigma_{\text{ic}}}{R_{\text{sw}}} \right)^3 \approx 1.15$ for $\zeta = 0.5$, where R_{sw} is the fully swollen microgel radius obtained with SANS. The suspension is, therefore, overpacked with these effective microgels and the counterion clouds must have percolated through the sample. The associated ions would then contribute to the suspension osmotic pressure, causing the observed deswelling of the particles. We note that the counterion-cloud model is expected to remain valid at $\zeta \approx 0.5$, since the increase in osmotic pressure is caused by a relatively small fraction of the ions in the counterion clouds. The associated deswelling of the microgels with increasing ζ then keeps the surface-to-surface distance between nearest neighbors, d_{nn} , larger than κ^{-1} ; for $\zeta \approx 0.5$, we find $d_{\text{nn}} \approx 38$ nm, which is clearly larger than the Debye screening length $\kappa^{-1} \approx 14$ nm for sample s1 at $\zeta \approx 0.5$. Thus most of the counterions remain in the spherical shell surrounding the microgels even at $\zeta \approx 0.5$.

We always find that the counterion cloud shrinks with the pNIPAM network. For measurements at $T \approx 45^\circ\text{C}$, where the microgels are in the deswollen state, the core-shell structure disappears and the pNIPAM network essentially becomes a spherical particle with approximately constant polymer density. As illustrated by the filled

symbols in Fig. 5.3, the counterion cloud is narrower and centered essentially at the particle surface, as expected if the fuzzy corona shrinks with the microgel, which should occur at temperatures above T_c . In this deswollen state, the same behavior is observed for both $\zeta \approx 0.2$ and 0.5 , since, at this high T , the microgel bulk modulus is significantly higher than at 20°C and $\zeta_{\text{eff}} < 1$ due to the reduced particle volume in the deswollen state; hence no counterion-induced deswelling is expected in this case. The width of the cloud decreases by a factor of 10 to 20 due to deswelling. Note that despite the error in $\Delta I_{\text{corr}}(q)$, associated with incoherent scattering and instrument-specific backgrounds, the depth of the minimum is larger than the error for samples s1 and s3 at $T \approx 20^\circ\text{C}$, see Supplementary Fig. 2 [203], and that σ_{ic} is observed to be strongly correlated to $2\sigma_s$.

To confirm our results, we perform additional tests for our analysis. First, we confirm that the observed minimum is not caused by the structure factor of the suspension. We divide both $I^{\text{NH}_4^+}(q)$ and $I^{\text{Na}^+}(q)$ by their structure factors and determine $\Delta I_{\text{corr}}(q)$ after this operation. The minimum and a low- q upturn in $\Delta I_{\text{corr}}(q)$ are still present, as shown in Fig 5.2E. Furthermore, we obtain the same cloud parameters within the accuracy of the analysis. Second, we prepare a new sample with NH_4^+ counterions at $\zeta \approx 0.5$ and measure it at $T \approx 20^\circ\text{C}$ to compare the result with the previously prepared NH_4^+ sample. Since the two samples both contain NH_4^+ counterions, data subtraction should not allow extracting the signal due to the counterion cloud, as there is no contrast difference between the ions. We follow the procedure described above to extract the counterion cloud and, after the correction due to the possible slight difference in the particle number density of the samples, find that the difference $\Delta I(q)$, shown in Fig. 5.2F, has neither a negative minimum nor an increased intensity upturn at low q within the error of the measurements. No difference between the two samples is detected, corroborating the validity of our approach to extract the counterion cloud parameters. When we use the newly prepared sample with NH_4^+ counterions together with the sample containing Na^+ counterions, we can again detect the expected signal due to the counterion cloud and obtain the same cloud parameters as before within the accuracy of the analysis (see Supplementary Fig. 4) [203].

We now address whether the fingerprint signal of the counterion cloud presented above could be reproduced without taking the counterions into account but by assuming instead a small structural difference in the pNIPAM network depending on the type of counterion. We had previously mentioned that this might perhaps be expected if the counterion concentration in the ion cloud was higher than what it

actually is for our microgels. We nevertheless consider this possibility. If the signal shown in Fig. 5.2A is due to a change in the polymer network, the spherical shell model given by Equation (5.4) can still be applied for its analysis. The radii and widths listed above for the counterion cloud, however, now characterize the volume of the polymer network that is affected by exchanging the counterion. With this interpretation, the observed signal is still a consequence of the counterion cloud, but it is an indirect and not a direct measurement of the cloud. We now assume that the fuzzy-sphere model for the microgel form factor is accurate enough to model a change in the polymer network caused by the counterions and use it to try to explain the signal shown in Fig. 5.2A. As the change in the form factor happens close to the particle radius, the width of the fuzzy corona must be affected. We thus keep the core radius, R_c , fixed and consider the effects of small changes in σ_s . This approach can result in a negative minimum with the observed depth, but the width of the minimum is broader than in the measured signal. Hence the fuzzy sphere model cannot capture the low- q upturn that is otherwise naturally explained with the counterion-cloud model presented above, see Supplementary Fig. 6 [203]. A change in the polymer form factor must, therefore, be modeled with a contribution that goes beyond the fuzzy-sphere model and is analogous to the cloud model given by Equation (5.4).

5.5 Discussion

Our results emphasize the power of SANS with contrast variation to extract weak signals of interest. We are not aware of another method that has allowed extracting the spatial structure of an ion cloud with a density as low as that in the studied microgels. To put our analysis in perspective, we compare with previous cloud measurements for micellar systems [174]. In micelles, the charged head groups of the lipids or surfactants are arranged in a thin spherical shell that is not wider than 1 nm and contribute a charge density of $\sim 0.7e \text{ nm}^{-3}$ [174]. In contrast, the charged groups in a fully swollen pNIPAM microgel are distributed in the fuzzy periphery in a spherical shell with a thickness close to σ_s , which results in a charge density of $\sim 0.015e \text{ nm}^{-3}$, which is significantly lower than for a micellar system. As the counterions arrange around the fixed charges on the particles, the counterions are spread out and have very low charge density. This low ion density explains the inability of anomalous small-angle x-ray scattering (ASAXS), a method that can extract the signal due to specific elements in the sample, to detect the counterion cloud. Other

methods were also, in principle, applicable to our purposes. Ellipsometric light scattering (ELS), which can resolve structures close to the surface of colloidal particles [40], is an example. However, since this technique requires transparent samples, it could not be used with our concentrated, turbid suspensions. A second example is transmission-electron microscopy (TEM) with energy-dispersive x-ray spectroscopy (EDX), which allows for extracting the chemical composition of a sample. However, the ion density in our microgel suspension is too low for this technique to work. Additionally, the need to work with frozen samples makes it difficult to distinguish samples in swollen and deswollen states.

In the literature, the structure of counterion clouds has been reported for micellar systems by means of SANS [174, 186, 61], the combination of SANS and SAXS [9], and by means of ELS [40]. For the study of the coil-to-globule transition of DNA and sulfonated polystyrene, SANS was used to determine the ion distribution around the rod-shaped molecules [85]. The ion density in the counterion clouds in all these systems is at least a factor of 4 larger compared to the significantly spread-out counterion cloud of the pNIPAM microgels studied here.

Importantly, our measurements of the counterion cloud confirm previous results suggesting that the counterion cloud of pNIPAM microgels is the key to their spontaneous deswelling at high microgel concentrations [150, 54] and the phase behavior in polydisperse suspensions [149]. This is in good agreement with several observations that microgels deswell at concentrations below random close packing and, therefore, before direct contact between neighboring particles [158, 31, 169, 171]. This observation is not captured by the Hertzian interaction [128, 185, 13], the soft-sphere potential [75, 1, 41, 68], or a brush-like interaction between the fuzzy coronae [205, 206, 147] that have been used to model the behavior of soft colloids. The spontaneous deswelling can explain why the rich phase diagrams predicted with simulations of soft particles [59, 128] have not been observed in the experiment, where microgels have been found to form close-packed [66, 51] or body-centered cubic crystals [116, 53], as expected for hard spheres and weakly charged colloids [78].

We also note that the presence of fixed charges and their counterions in pNIPAM microgels was found to be relevant for their swelling behavior in several studies [142, 73, 125]. In particular, simulation and dynamic light scattering (DLS) results with pNIPAM microgels are consistent with the charge arrangement we observe in our study [34]. DLS measurements across the volume-phase-transition temperature revealed that the deswelling of the charged shell is slower than that of the microgel

core. With the aid of detailed computer simulations, these experimental results were taken as indirect evidence for the presence of fixed charges in the outer fuzzy corona of the microgels.

The screened electrostatic potential due to the charges carried by the microgel and the counterion cloud can be expected to result in an electrostatic microgel-microgel interaction in addition to the interaction of soft, crosslinked pNIPAM spheres in direct contact. In contrast to hard, incompressible colloids with a Yukawa interaction [78], the softness of microgels must play an important role and be at the heart of the shift to higher ζ of the freezing and melting points. Also, the Percus-Yevick structure factor, $S_{PY}(q)$, [134] has been found to give a good description of the structure of microgel suspensions, albeit with an adapted hard-sphere radius that decreases with concentration [169, 149], suggesting that charges can be accounted for in this way. In contrast, $S_{PY}(q)$ cannot describe the suspension structure of other charged colloids [106] or micelles [200], as the electrostatic interaction has a more direct effect on the suspension structure. The open structure and the softness of microgels allow explaining this difference. When the osmotic pressure due to the counterions increases and becomes comparable to the bulk modulus of the microgels, spontaneous deswelling occurs [150, 54]. With increasing concentration, the surface-to-surface distance of nearest neighbors, therefore, does not decrease as fast as for incompressible particles. This leaves more screening volume and reduces the effect of electrostatic interaction on the suspension structure. Further, due to the distribution of the fixed charges in the fuzzy corona, about half of the counterions are located inside the microgel, where they screen these fixed charges, lowering the effective charge of the microgel and weakening the electrostatic interaction between particles [117]. It is, therefore, the structure of the counterion cloud that sets the osmotic pressure, triggers the deswelling of the microgels above a critical concentration, and causes the freezing and the melting point of the suspension to shift to higher ζ . Microgel deswelling is certainly the most important effect of the counterion cloud with consequences for the phase behavior. In addition, the cloud structure determines the screened electrostatic interaction between microgels that is expected to support the colloidal stabilization of the microgels and to have an effect on the phase behavior at high volume fractions.

Although the charge density in the periphery of pNIPAM microgels is low, these charges and the corresponding counterions play a decisive role in setting the particle size, consequently affecting interparticle interactions and the suspension phase behavior. Probing its existence and quantifying its properties is thus important,

albeit challenging. We have shown that SANS can exploit the contrast difference between different elements or isotopes to resolve the weak signal due to the counterion cloud. We have provided the first measurement of this cloud and showed that it indeed locates in the fuzzy periphery of the microgels. Since contributions to osmotic equilibrium due to polymer-solvent mixing and network elasticity are largely independent of suspension concentration [142], ionic effects turn out to be key to understand the suspension behavior; while at low particle densities, free ions can wander inside and outside the microgels without causing a pressure difference between the inside and outside, at high particle densities, the percolation of counterion clouds can cause the outside osmotic pressure to increase and to induce deswelling. As a result, any model or simulation aiming to capture the phase behavior and mechanics of nearly all microgel suspensions, which are based on either network-charged or peripherally-charged microgels, should explicitly consider the effect of ions. Our work confirms the existence of this cloud of counterions in pNIPAM microgels, which are generally deemed as neutral and have been approached by neglecting their peripheric charge. Future theoretical and simulation work should thus consider this fact.

Data Availability: The SANS scattering curves generated in this study are available in the Zenodo database under accession code 10.5281/zenodo.7137207 [<https://doi.org/10.5281/zenodo.7137207>]. The data analysis and results based on these scattering curves are presented in the main text and in the Supplementary Information [203].

Code Availability: The data analysis procedures underlying this article are described in the main text and the Supplementary Information [203].

5.6 Appendices

Supplementary Information: Measuring the counterion cloud of soft microgels using SANS with contrast variation

Microgel suspensions

We study three temperature-sensitive pNIPAM microgels with different swollen radii containing 2.7 wt% of crosslinker *N*'-methylene-bis-acrylamide (BIS). Ammonium persulfate [APS, $(\text{NH}_4)_2\text{S}_2\text{O}_8$] is used as the initiator of the polymerization reaction. Charged $-\text{O}-\text{SO}_2-\text{O}^-$ groups remain in the pNIPAM network and are assumed to be located in the periphery of the microgel, while NH_4^+ are present as

counterions. The SO_4^- groups originating from the APS attack a carbon-carbon double bond to form a radical $\text{O}_3\text{S}-\text{O}-\text{C}-\text{C}(\cdot)$, where the (\cdot) symbol indicates the radical is centered on the distal carbon. The end-group structure formed by the sulfate, therefore, looks like a sulfonic acid with an $\text{O}-\text{C}$ bond attaching it to the growing polymer. Therefore, the charged group is $-\text{SO}_2-\text{O}^-$ and not SO_4^- [28]. The surfactant sodium dodecyl sulfate [SDS, $\text{CH}_3(\text{CH}_2)_{11}\text{OSO}_3\text{Na}$] is used to control the microgel size and to obtain monodisperse particles; Na^+ ions are therefore also present as counterions. After the synthesis, the microgel suspension is cleaned to remove any unreacted monomers and the SDS. The cleaned, final suspension of pNIPAM microgels thus contains Na^+ and NH_4^+ counterions. Most of these are electrostatically bound to the microgels.

We count counterions with electrostatic potential energy $|e\psi| > 1.5k_{\text{B}}T$ as bound to the microgel. These ions are mobile within the ion cloud but cannot escape to explore the whole suspension volume. Our Poisson-Boltzmann calculations using the cell model [54] allow us to estimate the fraction of bound counterions to be about 98% at $\phi = 0.1$ and 89% at $\phi = 0.5$. The bound counterions cannot leave the counterion cloud at the periphery of the microgel, while the remaining counterions are essentially free, bound with a strength $\lesssim k_{\text{B}}T$, and can thus explore all of the suspension volume; these ions, therefore, contribute to the osmotic pressure.

Besides temperature, the suspension behavior is controlled by the volume fraction ϕ , which can vary in a microgel suspension in non-trivial ways, as microgels may deswell and interpenetrate when sufficiently concentrated. Therefore, we use a generalized volume fraction

$$\zeta = \frac{N_{\text{tot}}V}{V_{\text{tot}}} \approx \frac{m_{\text{pNIPAM}}}{m_{\text{tot}}} \frac{\rho_{\text{solvent}}}{\rho_{\text{pNIPAM}}} \frac{R_{\text{sw}}^3}{R_{\text{coll}}^3} \quad (5.5)$$

where V is the microgel volume in the fully swollen state, and N_{tot} , V_{tot} , m_{pNIPAM} , and m_{tot} are the number of particles, the suspension volume, the mass of pNIPAM polymer, and the mass of the suspension, respectively. The density of the polymer is $\rho_{\text{pNIPAM}} = 1.269 \text{ g/cm}^3$ [199] and that of the suspension is assumed to be the same as the density of the H_2O or D_2O solvent given the polymer concentration is low. The radii R_{sw} and R_{coll} correspond to the swollen and collapsed states, respectively. The latter is the radius of the dry microgel without any solvent.

The swollen radius is obtained using dynamic light scattering (DLS). For DLS, samples are prepared in Milli-Q H_2O with $\zeta < 0.01$. This is dilute enough for microgel-microgel interactions to be negligible. Hence, the single-particle diffusion

coefficient, D , can readily be obtained from the time-correlation function of the scattered intensity. We then use the Stokes-Einstein equation, $D = \frac{k_B T}{6\pi\eta_s R_h}$, with k_B the Boltzmann constant, T the absolute temperature and η_s the solvent viscosity, to obtain the hydrodynamic radius, R_h , which corresponds to R_{sw} [142].

The collapsed radius R_{coll} in Eq. 5.5 is obtained via viscosimetry. We measure the suspension viscosity, η , as a function of the polymer mass fraction in the suspension, $c = m_{pNIPAM}/m_{tot}$, and use the Einstein-Batchelor relation [11] for the relative viscosity,

$$\begin{aligned}\eta_r &= 1 + 2.5\zeta + 5.9\zeta^2 \\ &= 1 + 2.5(kc) + 5.9(kc)^2,\end{aligned}\tag{5.6}$$

to obtain the proportionality constant

$$k = \frac{\rho_{solvent} R_{sw}^3}{\rho_{pNIPAM} R_{coll}^3}\tag{5.7}$$

between ζ and the mass ratio $c = m_{pNIPAM}/m_{tot}$. From k , we obtain R_{coll} , using R_{sw} obtained with DLS:

$$R_{coll} = \left(\frac{\rho_{solvent}}{\rho_{pNIPAM}} \frac{R_{sw}^3}{k} \right)^{1/3}.\tag{5.8}$$

The radii R_{sw} and R_{coll} , as well as the conversion constant k , are reported in Supplementary Tab. 5.1.

To learn about the counterion cloud of the pNIPAM microgels, we prepare two samples for each microgel, one with sodium, Na^+ , and the other one with ammonium, NH_4^+ , counterions. To exchange the counterions, we prepare dilute microgel suspensions in Milli-Q H_2O , introduce them in dialysis bags, and place them in solutions of $NaCl$ or NH_4Cl at a concentration of (167 ± 5) mM to allow for counterion exchange. The salt solutions are exchanged daily for 5 days to obtain a full exchange of ions. The samples are then dialyzed against ultrapure Milli-Q H_2O for another 5 days to remove the salt from the microgel suspensions. After the dialysis, we freeze dry the suspensions to obtain the dry microgel powder, which we finally re-suspend in D_2O . After freeze drying, about one H_2O molecule per NIPAM monomer is expected to remain in the pNIPAM powder [96]. The resultant contamination after resuspension in D_2O is thus expected to be < 1 wt%. This implies a $< 1\%$ reduction in the scattering length density of the solvent, which does not affect our analysis and conclusions.

SANS data analysis

Sample	R_{sw} (nm)	R_{coll} (nm)	k (at 20°C)
s1	87 ± 1.7	25 ± 0.6	24.78 ± 0.004
s2	125 ± 2.7	38 ± 0.8	20.56 ± 0.005
s3	140 ± 2.3	40 ± 0.8	18.74 ± 0.005

Table 5.1: The swollen hydrodynamic radius R_{sw} measured with DLS at 20 °C and the collapsed radius R_{coll} calculated with Eq. 5.8 from the conversion constant k obtained with viscosimetry at 20 °C for the three used microgel samples.

SANS data of all our samples was taken at $T \approx 20^\circ\text{C} < T_{\text{LCST}}$ and $T \approx 45^\circ\text{C} > T_{\text{LCST}}$ to investigate microgels with their Na^+ or NH_4^+ ion clouds in both the fully swollen and the deswollen states. Data was taken to obtain $\sim 2 \cdot 10^6$ counts on the detector to have good statistics in the q range of interest. All scattering curves are fitted with a model including the fuzzy-sphere form factor [169], the Percus-Yevick structure factor, $S(q)$, with polydispersity, and the q resolution of the SANS instrument. The Percus-Yevick structure factor has been found to be adequate for microgel suspensions [39]. The polydispersity of pNIPAM suspensions is typically close to 10% [149]. Hence we use the so-called apparent structure factor [93]

$$S'(q) = 1 + \beta(q)[S(q) - 1], \quad (5.9)$$

where $\beta(q) = |\langle F_{\text{p}}(q) \rangle|^2 / \langle |F_{\text{p}}(q)|^2 \rangle$ is a factor varying between zero and one that suppresses the oscillations of the monodisperse structure factor $S(q)$ and, therefore, approximates the effect of polydispersity. The assumption behind this approach is that the microgel size is not correlated with the structure of the suspension. This is a good approximation for modest polydispersities $\sim 10\%$ and for moderate concentrations, $\zeta \lesssim 0.5$. If the polydispersity is significant and the suspension is concentrated, one should obtain the pair structure factors by solving the matrix form of the Ornstein-Zernike equation for the pair potential [7]. Using the apparent structure factor $S'(q)$, the scattering intensity becomes

$$I(q) = n_{\text{d}} \langle V_{\text{c}}^2 \Delta \rho_{\text{c}}^2 \rangle P(q) S'(q). \quad (5.10)$$

For the form factor $P(q) = \langle |F_{\text{p}}(q)|^2 \rangle / \langle |F_{\text{p}}(0)|^2 \rangle$, we use the fuzzy sphere model

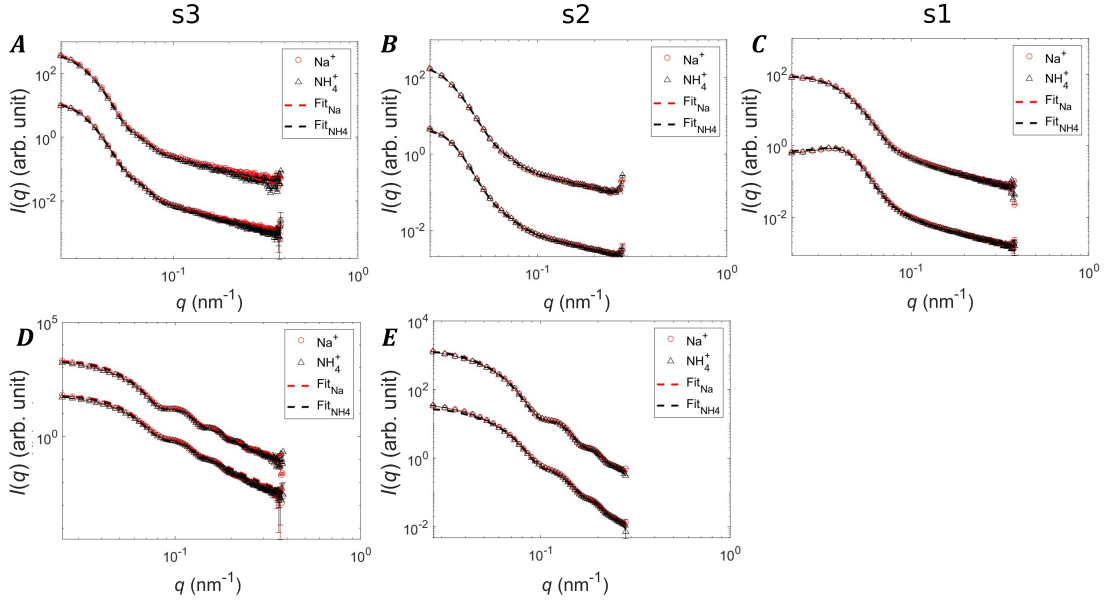


Figure 5.4: Simultaneous fits (—) to SANS measurements with Na^+ (\circ) and NH_4^+ (\triangle) counterions for all samples: top curves are for $0.1 \lesssim \zeta \lesssim 0.2$ and bottom curves are for $0.48 \lesssim \zeta \lesssim 0.55$. A: sample s3 at 20 °C. B: sample s2 at 20 °C. C: sample s1 at 20 °C. D: sample s3 at 45 °C. E: sample s2 at 45 °C. Data from samples with $0.1 \lesssim \zeta \lesssim 0.2$ (upper curves) has been multiplied by 10^3 for the sake of clarity. The error bars represent the uncertainty due to the counting statistics of the SANS instrument.

[170]

$$F_p(q) = V_c \Delta \rho_c \frac{3 [\sin(qR_c) - qR_c \cos(qR_c)]}{(qR_c)^3} \exp\left(-\frac{q^2 \sigma_s^2}{2}\right), \quad (5.11)$$

which is well-accepted for microgels. In this expression, $V_c = 4\pi R_c^3/3$ is the volume of the core, and $\Delta \rho_c$ is the scattering-length-density contrast between the microgel core and the pure solvent. The prefactor $V_c \Delta \rho_c$ can also be expressed using the contrast of pure pNIPAM and the solvent, $\Delta \rho_p = \rho_p - \rho_s$, if the pNIPAM volume, V_p , is used as the volume of the scatterer: $V_c \Delta \rho_c = V_p \Delta \rho_p$. In real space, Eq. 5.11 corresponds to a spherical core of radius R_c and a constant scattering-length density that is convolved with a Gaussian with standard deviation σ_s to obtain the fuzzy corona. The width of the corona is $2\sigma_s$ and the radius of the particle seen by SANS is $R_{\text{SANS}} = R_c + 2\sigma_s$. The size polydispersity is modeled with a log-normal distribution for the core radius, which is used for microgels and polydispersities that are too high to be modeled with a Gaussian distribution [195]:

$$D(x) = \frac{1}{x} \frac{1}{\sqrt{2\pi}\sigma} \exp\left[-\frac{(\log x - \mu)^2}{2\sigma^2}\right], \quad (5.12)$$

where σ is the parameter setting the polydispersity $\langle (x - \langle x \rangle)^2 \rangle = \langle x \rangle^2 (e^{\sigma^2} - 1)$ and the mean is $\langle x \rangle = e^{\mu + \frac{\sigma^2}{2}}$. Inhomogeneities within the microgel contribute to the form factor and are taken into account with a Lorentzian term $I_{\text{chain}}(q) = I_{\text{chain}}(0)/[1 + (\xi q)^2]$, where ξ is the correlation length of the polymer network and $I_{\text{chain}}(0)$ is the zero- q intensity due to these inhomogeneities [42, 94]. This signal dominates the form factor for $q \gtrsim \pi/\sigma_s$. With this, the average form factor is

$$P(q) = \frac{1}{\langle V_c^2 \Delta \rho_c^2 \rangle} \int_0^\infty D(R_c) |F_p(q; R_c)|^2 dR_c + I_{\text{chain}}(q) \quad (5.13)$$

with the normalization factor $\langle |F_p(0)|^2 \rangle = \langle V_c^2 \Delta \rho_c^2 \rangle = \int_0^\infty V_c^2(R_c) \Delta \rho_c^2 D(R_c) dR_c$. Lastly, the smearing effect due to instrument resolution is considered by convolving $I(q)$ with a Gaussian [130]:

$$I_s(q) = \frac{1}{\sqrt{2\pi}\sigma_r(q)} \int_0^\infty \exp\left[-\frac{(q - q')^2}{2\sigma_r^2(q)}\right] I(q') dq' + B, \quad (5.14)$$

where the constant B accounts for the background due to incoherent scattering. We use this model to fit the scattering signal of our microgel suspensions to extract the particle size, the particle number density, and the polydispersity, which are listed in Supplementary Tab. 5.2. We find that the microgel size and internal structure do not depend on the counterion species. The number density appears as a parameter for the structure factor $S'(q)$; it is through this dependence that we can extract n_d from the SANS curve. Recall n_d also appears as a prefactor in $I(q)$, because the scattered intensity depends on the number of microgels present in the suspension, see Eq. 5.10.

Counterion cloud model

As the scattering signal originating from the ion cloud is small compared to the total measured signal, we amplify the signal strength by subtracting $I^{\text{Na}^+}(q)$ from $I^{\text{NH}_4^+}(q)$ after correcting for small differences in $n_d \cdot S'(q)$:

$$\begin{aligned} \Delta I(q) &= I^{\text{NH}_4^+}(q) - I_{\text{corr}}^{\text{Na}^+}(q) \\ &= n_d \Delta \rho_c^2 V_c^2 \left(P^{\text{NH}_4^+}(q) - P^{\text{Na}^+}(q) \right) S'(q), \end{aligned} \quad (5.15)$$

where the prefactor includes the number density n_d , the particle scattering contrast $\Delta \rho_c$, and the core volume V_c . Furthermore, we consider the contribution of the counterion cloud to the form factor, $F_{\text{ic}}(q)$, in addition to the polymer contribution,

$F_p(q)$, that is modeled with Eq. 5.11:

$$[F_p(q) + F_{ic}^X(q)]^2 = F_p^2(q) + 2F_p(q)F_{ic}^X(q) + F_{ic}^{X^2}(q). \quad (5.16)$$

With this, we rewrite the difference between the signals of the samples with NH_4^+ and Na^+ counterions:

$$\Delta I_m(q) \approx 2 n_d F_p(q) \left[F_{ic}^{\text{NH}_4^+}(q) - F_{ic}^{\text{Na}^+}(q) \right] S'(q), \quad (5.17)$$

where we have assumed that the terms $\propto F_{ic}^2(q)$ are negligible due to the low counterion density. The subscript ‘m’ indicates that the scattering intensity is given for the monodisperse case with fixed microgel size; polydispersity will be included below in Eq. 5.22. $\Delta I_m(q)$ is directly proportional to the difference between the scattering amplitudes $F_{ic}^X(q)$ of the clouds, which we split into an ion-specific prefactor and an ion-independent structural part:

$$F_{ic}^X(q) = \Delta\rho^X V_{ic}^X f_{ic}(q), \quad (5.18)$$

where $\Delta\rho^X$ is the scattering-length density contrast of the ion with respect to the solvent and V_{ic} is the volume taken by the ions, which is given by the product of the number of ions and the volume of a single ion. We estimate that there are approximately $7 \cdot 10^4$ counterions per microgel [150, 54]. For the ion volumes, we use the ion radii for Na^+ , 0.116 nm, and for NH_4^+ , 0.146 nm, as reported in the literature.

As the $-\text{O}-\text{SO}_2-\text{O}^-$ groups at the ends of the pNIPAM chains are expected to be located in the periphery of the microgel, we model the counterion cloud as a smeared-out spherical surface. We use a convolution with a Gaussian with standard deviation σ_{ic} to obtain the smearing:

$$f_{ic}(q) = \frac{\sin(qR_{ic})}{qR_{ic}} \exp\left(-\frac{q^2\sigma_{ic}^2}{2}\right), \quad (5.19)$$

where the cloud radius is given by the core radius of the microgel, R_c , and an offset Δr , such that $R_{ic} = R_c + \Delta r$. This links the cloud radius to the structure of the pNIPAM network of the microgel and implies that the polydispersity of the pNIPAM core is also applied to the counterion cloud. By inserting Eq. 5.18 into Eq. 5.17, we have

$$\Delta I_m(q) \approx 2 n_d \left(\Delta\rho^{\text{NH}_4^+} V_{ic}^{\text{NH}_4^+} - \Delta\rho^{\text{Na}^+} V_{ic}^{\text{Na}^+} \right) F_p(q) f_{ic}(q) S'(q). \quad (5.20)$$

Sample	ζ $\pm 0.04 \pm 0.5$	T (°C)	Individual fit				Simultaneous fit				Figs.
			R_c (nm)	σ_s (nm)	R_{SANS} (nm)	ξ (nm)	σ (%)	R_{SANS} (nm)	n_d^X (nm ⁻³) $\times 10^{-8}$	n	
s1 Na ⁺	0.10	20	55.6 ± 0.5	14.9 ± 0.3	85.4 ± 1.1	12 ± 1	15 ± 1.0	83.9 ± 1.5	3.43 ± 0.18	0.95 ± 0.07	S1(C)
s1 NH ₄ ⁺	0.09	20	56.0 ± 0.4	14.3 ± 0.5	84.6 ± 1.4	12 ± 1	15 ± 1.0	"	3.27 ± 0.18	"	S2(C)
s1 Na ⁺	0.47	20	50.9 ± 0.5	13.5 ± 0.4	77.9 ± 1.3	12.4 ± 1	115 ± 1.0	78.8 ± 0.8	17.22 ± 0.58	0.96 ± 0.04	S1(C)
s1 NH ₄ ⁺	0.46	20	51.0 ± 0.5	14.2 ± 0.3	79.4 ± 1.1	12.9 ± 1	115 ± 0.9	"	16.49 ± 0.58	"	S2(H)
s2 Na ⁺	0.11	20	82.0 ± 0.7	21.1 ± 0.2	124.2 ± 1.1	14.5 ± 1	110 ± 0.5	124.4 ± 1.7	1.33 ± 0.06	1.01 ± 0.06	S1(B)
s2 NH ₄ ⁺	0.11	20	82.1 ± 0.5	21.2 ± 0.4	124.5 ± 1.3	14 ± 1	11 ± 0.5	"	1.34 ± 0.06	"	S2(B)
s2 Na ⁺	0.48	20	80.6 ± 0.5	19.3 ± 0.4	119.2 ± 1.3	9.2 ± 1	13 ± 0.7	118.7 ± 1.2	5.91 ± 0.19	0.99 ± 0.05	S1(B)
s2 NH ₄ ⁺	0.47	20	81.3 ± 1.1	18.7 ± 0.4	118.7 ± 1.9	8.6 ± 1	12 ± 0.5	"	5.82 ± 0.19	"	S2(G)
s2 Na ⁺	0.11	45	46.7 ± 0.3	2.4 ± 0.7	51.4 ± 1.3	N/A	11 ± 0.9	49.5 ± 1.3	1.38 ± 0.05	0.95 ± 0.08	S1(E)
s2 NH ₄ ⁺	0.11	45	46.7 ± 0.3	2.2 ± 0.7	51.2 ± 1.3	N/A	11 ± 1.0	"	1.30 ± 0.07	"	S2(E)
s2 Na ⁺	0.48	45	46.7 ± 0.5	2.8 ± 0.7	52.3 ± 1.9	N/A	13 ± 0.5	49.4 ± 1.2	5.94 ± 0.29	0.94 ± 0.06	S1(E)
s2 NH ₄ ⁺	0.46	45	46.7 ± 0.3	2.7 ± 0.8	52.2 ± 1.9	N/A	13 ± 0.5	"	5.54 ± 0.21	"	S2(J)
s3 Na ⁺	0.18	20	87.5 ± 1.0	24.1 ± 0.8	135.6 ± 2.6	14 ± 1	11 ± 0.6	134.3 ± 1.6	1.57 ± 0.06	0.93 ± 0.05	1, 2, S1(A), S2(A), S3, S4
s3 NH ₄ ⁺	0.17	20	87.9 ± 1.0	23.9 ± 0.8	135.7 ± 2.6	14 ± 1	11 ± 0.6	"	1.45 ± 0.06	"	S1(A)
s3 Na ⁺	0.56	20	88.2 ± 0.8	21.8 ± 0.3	131.8 ± 1.4	8.6 ± 1	10 ± 0.4	128.8 ± 1.8	4.89 ± 0.21	0.94 ± 0.06	S2(F)
s3 NH ₄ ⁺	0.53	20	88.6 ± 0.8	21.3 ± 0.4	131.2 ± 1.6	9.0 ± 1	9 ± 0.6	"	4.61 ± 0.20	"	1
s3 Na ⁺	0.18	45	54.4 ± 1.3	0 ± 0.01	54.4 ± 1.3	N/A	12 ± 0.9	54.61 ± 0.8	1.62 ± 0.08	0.92 ± 0.06	S1(D)
s3 NH ₄ ⁺	0.17	45	54.5 ± 1.2	0 ± 0.01	54.5 ± 1.2	N/A	12 ± 1.0	"	1.49 ± 0.06	"	1, S2(D)
s3 Na ⁺	0.57	45	55.4 ± 0.9	0 ± 0.01	55.4 ± 0.9	N/A	12 ± 0.8	55.24 ± 0.7	4.96 ± 0.19	0.91 ± 0.05	S1(D), S2(I)
s3 NH ₄ ⁺	0.52	45	55.6 ± 1.1	0 ± 0.01	55.6 ± 1.1	N/A	12 ± 0.8	"	4.53 ± 0.18	"	

Table 5.2: Results from individual SANS fits (Eq. 5.14) for all samples and from simultaneous fits for sample pairs. The sample name with ion species, the generalized volume fraction (ζ) obtained from the fit, and the temperature of the SANS measurement are given to identify sample and measurement. For individual fits, the core radius (R_c), corona width (σ_s), SANS radius (R_{SANS}), and polydispersity (σ) are listed. For simultaneous fits, the SANS radius (R_{SANS}), the microgel number density (n_d^X), and the number-density ratio ($n = n_d^{\text{NH}_4^+} / n_d^{\text{Na}^+}$) are given. In the last column, the figures displaying the respective measurement and fit are indicated.

In this difference, the counterion cloud signal, $f_{\text{ic}}(q)$, is amplified by the stronger signal from the polymer, $F_{\text{p}}(q)$. The magnitude is determined by the scattering-length-density contrast between NH_4^+ and Na^+ . As $\rho^{\text{NH}_4^+} \approx -4.3 \cdot 10^{-6} \text{\AA}^{-2}$ and $\rho^{\text{Na}^+} \approx 5.6 \cdot 10^{-6} \text{\AA}^{-2}$, the contrast is significant and strengthens the signal originating from the cloud.

Our analysis of the scattering curves indicates that samples are indeed prepared at very similar concentrations and can be expected to have the same structure factor. The exchange of counterions using dialysis does not appear to affect the contribution of the pNIPAM polymer to the form factor, as shown by the structural parameters listed in Supplementary Tab. 5.2.

Combining Eqs. 5.11 and 5.19 with Eq. 5.20, we obtain the model for the scattering-intensity difference:

$$\begin{aligned} \Delta I_{\text{m}}(q) &\approx 2 n_{\text{d}} \Delta \rho_{\text{c}} V_{\text{c}} \left(\Delta \rho^{\text{NH}_4^+} V_{\text{ic}}^{\text{NH}_4^+} - \Delta \rho^{\text{Na}^+} V_{\text{ic}}^{\text{Na}^+} \right) \\ &\times \frac{3 [\sin(qR_{\text{c}}) - qR_{\text{c}} \cos(qR_{\text{c}})] \sin(qR_{\text{ic}})}{(qR_{\text{c}})^3 qR_{\text{ic}}} \\ &\times \exp \left[-\frac{q^2 (\sigma_{\text{ic}}^2 + \sigma_{\text{s}}^2)}{2} \right] S'(q), \end{aligned} \quad (5.21)$$

which is then convolved with the log-normal distribution to account for the polydispersity of R_{c} , as also done in Eq. 5.13:

$$\Delta I(q) = \int_0^{\infty} D(R_{\text{c}}) \Delta I_{\text{m}}(q) dR_{\text{c}}. \quad (5.22)$$

Note that the microgel polydispersity is also used for the counterion cloud, as R_{ic} is defined to depend on the core radius R_{c} . We also emphasize that since $S'(q)$ already accounts for polydispersity, it is taken out of the R_{c} average above to avoid over-considering polydispersity effects in the suspension structure factor. Finally, we consider the instrument resolution by integrating $\Delta I(q)$ with a Gaussian distribution, analogous to Eq. 5.14:

$$\Delta I_{\text{s}}(q) = \frac{1}{\sqrt{2\pi}\sigma_{\text{r}}(q)} \int_0^{\infty} \exp \left(-\frac{[q - q']^2}{2\sigma_{\text{r}}^2(q)} \right) \Delta I(q') dq'. \quad (5.23)$$

Using this model, we extract the key parameters R_{ic} and σ_{ic} of the counterion cloud. The number density, n_{d} , the core radius, R_{c} , the width of the corona, σ_{s} , and the polydispersity, σ , also enter. The dependence of the model given by Eq. 5.23 on the parameters is illustrated in Fig. 2C, D of the main text.

Counterion cloud fits

The general steps of data preparation before fitting with the cloud model (Eqs. 5.21,

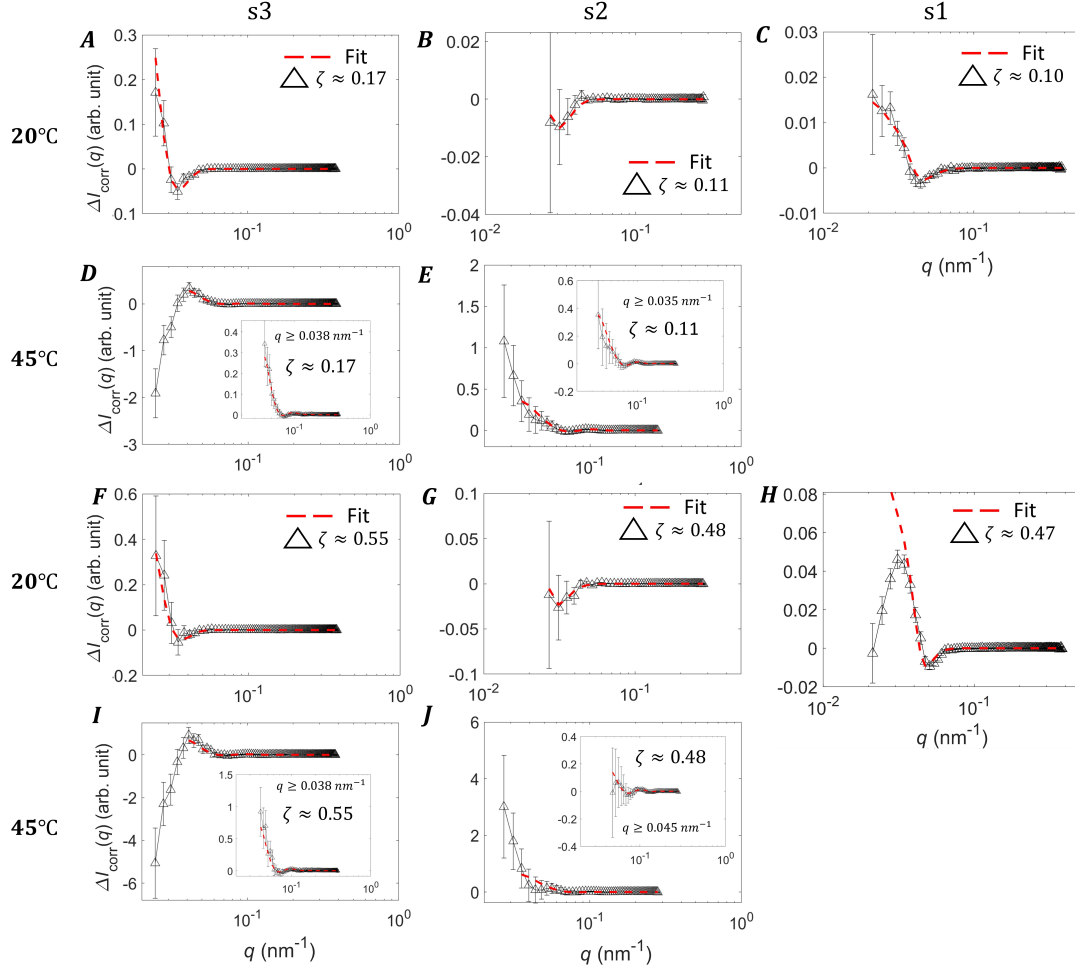


Figure 5.5: $\Delta I(q)$ and counterion cloud fits for the samples s3 (1st column, panels A, D, F, I), s2 (2nd column, panels B, E, G, J), and s1 (3rd column, panels C, H). The temperature of the SANS measurements is given on the left for each row. Samples with $0.1 \lesssim \zeta \lesssim 0.2$ are shown in the two upper rows (panels A-E), and the two lower rows (panels F-J) are for $0.48 \lesssim \zeta \lesssim 0.55$. The inserts in panels D, E, I, and J are magnifications to show the counterion cloud signal more clearly. The error bars represent the uncertainty due to the counting statistics of the SANS instrument.

5.22 and 5.23) are mentioned in the main text. To correct for differences in concentration, we assume that the counterion species, Na^+ or NH_4^+ , do not change the microgel architecture given by R_c and σ_s , the polydispersity (σ), and the correlation length (ξ); only the number density is expected to slightly differ for samples containing Na^+ and NH_4^+ counterions. We perform a simultaneous fit with the model given by Eq. 5.14 using as common free parameters R_c , σ_s , σ and ξ , and then the two

number densities, $n_d^{\text{Na}^+}$ and $n_d^{\text{NH}_4^+}$. The assumption is that the small concentration difference does not cause a change in the form factor or the structure factor; this is supported by our results obtained with individual fits, see Supplementary Tab. 5.2. The simultaneous fits shown in Supplementary Fig. 5.4 confirm that these fits and the extracted number densities are in good agreement with the raw data. The number density n_d^X ($X = \text{Na}^+$ or NH_4^+) for each set of data is summarized in Supplementary Tab. 5.2. We then calculate the number density ratio, $n = n_d^{\text{NH}_4^+} / n_d^{\text{Na}^+}$

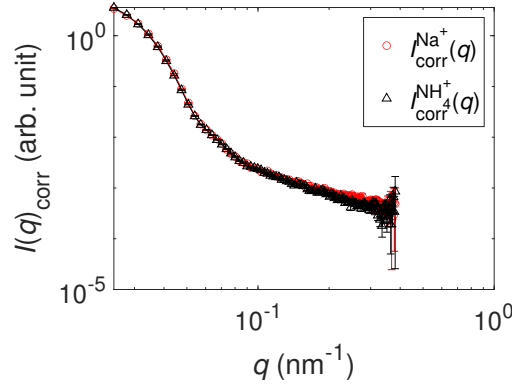


Figure 5.6: Number-density corrected $I_{\text{corr}}^{\text{Na}^+}(q) = n I^{\text{Na}^+}(q)$ with $n = 0.925$ and the uncorrected $I^{\text{NH}_4^+}(q)$ for sample s3 at $\zeta \approx 0.2$. The error bars represent the uncertainty due to the counting statistics of the SANS instrument.

and correct $I^{\text{Na}^+}(q)$ as $I_{\text{corr}}^{\text{Na}^+}(q) = n I^{\text{Na}^+}(q)$. For each Na^+ , NH_4^+ pair, the correction factor n is expected to be the same for the measurements taken below and above T_{LCST} , as the number density n_d does not depend on temperature. This is the case within the error limits, see Supplementary Tab. 5.2.

In Supplementary Fig. 5.6, we show the corrected $I_{\text{corr}}^{\text{Na}^+}(q)$ together with $I^{\text{NH}_4^+}(q)$. As the correction is small, we can barely notice any difference with respect to the uncorrected data shown in Fig. 1 (main text). But the number-density correction is important to reveal the signal due to the counterions.

After the correction, we fit all the number-density-corrected $\Delta I(q)$ data with the model introduced in Eqs. 5.21, 5.22, and 5.23. The results for all samples are summarized in Supplementary Tab. 5.3, Fig. 3 (main text), and Supplementary Fig. 5.8. The radius of the cloud, R_{ic} , is always smaller but close to R_{SANS} , which implies that the fixed charges are located in the outskirts of the microgel. The width of the cloud, σ_{ic} , is found to be comparable to the width of the fuzzy shell, $2\sigma_s$, and is in good agreement with our previous estimate, (35 ± 4) nm [150, 149]. When we average σ_{ic} for all samples measured at $T \approx 20^\circ\text{C}$ listed in Supplementary Tab. 5.3, we get $\langle \sigma_{\text{ic}} \rangle = (38 \pm 8)$ nm.

Sample	$T(^{\circ}C)$ ± 0.1	ζ ± 0.04	R_{ic} (nm)	σ_{ic} (nm)	R_{SANS} (nm)
s1	20	0.10	83 ± 3	28 ± 4	83.9 ± 1.1
s1	20	0.47	72.4 ± 0.5	38 ± 4	78.8 ± 1.4
s2	20	0.11	123 ± 5	43 ± 17	124.5 ± 1.4
s2	20	0.48	117 ± 4	43 ± 21	118.7 ± 1.2
s2	45	0.11	51 ± 1	3 ± 3	49.5 ± 1.6
s2	45	0.48	50 ± 3	3 ± 2	49.4 ± 1.2
s3	20	0.17	111 ± 2	37 ± 2	134.3 ± 1.6
s3	20	0.55	110 ± 3	38 ± 5	128.8 ± 1.8
s3	45	0.17	52.5 ± 0.4	2 ± 1	54.6 ± 0.5
s3	45	0.55	51.8 ± 0.3	2.2 ± 0.3	55.2 ± 1.3
s3 with $\Delta I(q)/S'(q)$	20	0.17	112 ± 1	37 ± 3	134.3 ± 1.6
s3 New NH_4^+	20	0.17	112 ± 2	39 ± 2	135.0 ± 1.3

Table 5.3: Results for the counterion cloud radius (R_{ic}) and width (σ_{ic}) obtained at $T \approx 20^{\circ}C$ and $45^{\circ}C$ using the model given in Eqs. 5.21, 5.22, and 5.23.

We compare the intensity of the observed signal due to the ions with the expected intensity given by the prefactors of the form factor of the polymer network and the counterion cloud, which are a product of the volume and the contrast of the scatterer, see Eq. 5.21. For the polymer network, we use that $\Delta\rho_c V_c = \Delta\rho_p V_p$ and take the scattering-length densities of pure NIPAM, $\rho_p = (0.939 \pm 0.001) \cdot 10^{-4} \text{ nm}^{-2}$, and the D_2O solvent, $\rho_{D_2O} = (6.335 \pm 0.001) \cdot 10^{-4} \text{ nm}^{-2}$ to obtain the contrast $\Delta\rho_p = \rho_p - \rho_{D_2O} = (-5.497 \pm 0.002) \cdot 10^{-4} \text{ nm}^{-2}$. With this contrast, the volume of the scatterer is that of the pure polymer, which is given by the collapsed radius of the microgel, $V_p = (4\pi/3)R_{coll}^3$ with R_{coll} given in Supplementary Tab. 5.1. For the counterion cloud, we use the tabulated scattering lengths of H, N, and Na and the ion radii given above to obtain the contrasts $\Delta\rho^{NH_4} = \rho^{NH_4} - \rho_{D_2O} = (-10.6 \pm 0.1) \cdot 10^{-4} \text{ nm}^{-2}$ and $\Delta\rho^{Na} = \rho^{Na} - \rho_{D_2O} = (-0.78 \pm 0.01) \cdot 10^{-4} \text{ nm}^{-2}$. The number of counterions per microgel, $N_i = (7 \pm 1) \cdot 10^4$, estimated from particle synthesis [150], is used to obtain the total volume taken by the ions in the cloud, $V_{ic} = (4\pi/3)R_X^3 N_i$ with the ion radius R_X and X representing either Na^+ or NH_4^+ . The prefactor of the form factor of a microgel including the counterion cloud, therefore, is $s = (V_p \Delta\rho_p + V_{ic} \Delta\rho^X)^2 \approx (V_p \Delta\rho_p)^2$ and that of the ion-cloud signal is $s_{ic} = 2V_p \Delta\rho_p (V_{ic}^{NH_4} \Delta\rho^{NH_4} - V_{ic}^{Na} \Delta\rho^{Na})$. We obtain the ratio $s_{ic}/s = 0.05 \pm 0.02$, where the uncertainty in the number of counterions per microgel gives the largest contribution to the error. The measured ratio, obtained from extrapolating the fits of the data to zero q , is $\Delta I_{corr}(0)/I_{corr}(0) = 0.06 \pm 0.01$, as mentioned in the main text. The agreement with the calculated ratio

is very good and supports our interpretation that the signal due to the ions is a direct measurement of the counterion cloud.

At the lowest measured q , $I^{\text{NH}_4^+}(q)$ is expected to have a slightly higher intensity than $I^{\text{Na}^+}(q)$, as NH_4^+ has a larger contrast than Na^+ in the D_2O solvent. This is the case in all our measurements with the exception of sample s3 at $T \approx 45^\circ\text{C}$ in the deswollen state for $q < 0.038 \text{ nm}^{-1}$. In this q -range, the scattering signal is due to objects as large or larger than the whole microgel. Therefore, a small number of aggregates can explain the issue. At $T \geq T_{\text{LCST}}$, the steric stabilization of microgels is weakened and some aggregation is possible [169]. As the s3 samples at $\zeta \approx 0.2$ are prepared by diluting the $\zeta = 0.55$ suspensions, it is reasonable that we observe a higher intensity of I^{Na^+} at low q 's for both concentrations. In both cases, $\Delta I_{\text{corr}}(q)$ is negative for $q < 0.038 \text{ nm}^{-1}$, but the minimum due to the counterion cloud appears at a higher q and is still visible. We only use the data points at $q \geq 0.038 \text{ nm}^{-1}$ to extract the parameters of the counterion cloud. As shown in Supplementary Fig. 5.5D and I, the minimum is not as obvious as for $T \approx 20^\circ\text{C}$. However, as shown in the insets, the depth is of the same order as for the samples at $T = 20^\circ\text{C}$, despite being less visible over the whole q range due to the negative signal at the lowest q 's; the cloud model captures the data nicely as shown in the insets of Supplementary Fig. 5.5D and I. For sample s2, the errors in σ_{ic} at $T = 20^\circ\text{C}$ given in

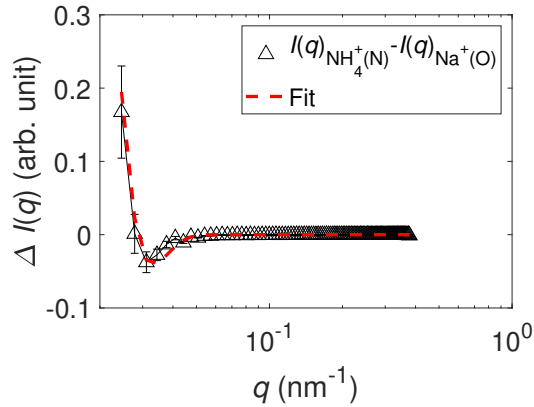


Figure 5.7: Cloud signal and fit for s3 at $\zeta \approx 0.2$ with newly prepared NH_4^+ sample and old Na^+ sample. $\Delta I_{\text{corr}}(q) = I_{\text{new}}^{\text{NH}_4^+}(q) - I_{\text{old}}^{\text{Na}^+}(q)$ with correction factor $n = 1.035$. The error bars represent the uncertainty due to the counting statistics of the SANS instrument.

Supplementary Tab. 5.3 are larger than for samples s1 and s3. This is caused by the low resolution of the raw data and the limited q range. The magnitude of the error bars is comparable to the depth of the minimum and we are at the detection limit

of the instrument SANS-II at SINQ that was used for these measurements; samples s1 and s3 were measured on SANS-I at SINQ. However, the minimum position is better defined and, as a result, reliable results are obtained for the cloud radius, R_{ic} . At $T = 45^\circ\text{C}$, we find the cloud to be centered close to the particle periphery for both $\zeta \approx 0.1$ and $\zeta \approx 0.5$. Due to the large errors in $\Delta I(q)$, Supplementary Fig. 5.5E and J, we fit the data with the limited q range $q \geq 0.035 \text{ nm}^{-1}$ around the minimum for the sample at $\zeta \approx 0.1$ and $q \geq 0.045 \text{ nm}^{-1}$ for the sample at $\zeta \approx 0.5$; the two lowest- q data points were excluded due to the large errors and because of large uncertainty in q . As the minimum is located at $q \approx 0.07 \text{ nm}^{-1}$, the quality of the two lowest- q points does not affect the cloud signal. The results obtained with sample s2 are similar to those from sample s3, which is reassuring since the particle sizes are comparable and we expect analogous results. For sample s1 at $\zeta \approx 0.1$ and

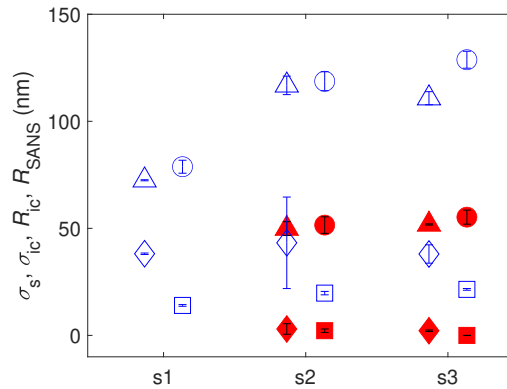


Figure 5.8: The radii R_{SANS} (\circ) and R_{ic} (\triangle) as well as the half widths of the fuzzy corona, σ_s , (\square) and of the counterion cloud, σ_{ic} , (\diamond) for samples s1, s2, and s3 at $\zeta \approx 0.48$ measured at $T \approx 20^\circ\text{C}$ (open symbols) and $T \approx 45^\circ\text{C}$ (full symbols). All values shown are also listed in Supplementary Tabs. 5.2 and 5.3. The error bars result from the least-squares fit to the SANS data.

0.5, the cloud model fits the $\Delta I(q)$ data shown in Supplementary Fig. 5.5C and H. The counterion cloud is found to be located close to R_{SANS} or slightly inside the fuzzy shell of the microgel. As for samples s3 and s2, σ_{ic} is about equal or slightly smaller than $2\sigma_s$, that is, the width of the cloud is comparable to the thickness of the fuzzy corona. For sample s1 at $\zeta \approx 0.5$ and $q < 0.03 \text{ nm}^{-1}$, Supplementary Fig. 5.5H, the fit lies above the measured data. The peak in the measured data at $q \approx 0.03 \text{ nm}^{-1}$ is probably due to a small difference in the structure factors of $I^{\text{NH}_4^+}(q)$ and $I^{\text{Na}^+}(q)$. $S'(q=0)$ is directly related to the compressibility and, therefore, the microgel density n_d of the suspension. As we find a small difference in n_d that we correct for in $I_{\text{corr}}^{\text{Na}^+}(q)$, this can explain a discrepancy at the lowest

q 's. As the fit works well around the minimum at $q \approx 0.05 \text{ nm}^{-1}$, we obtain reliable parameters for the ion cloud. Further, we notice that R_{SANS} is smaller at $\zeta \approx 0.5$ compared to $\zeta \approx 0.1$, which implies that the true volume fraction at $\zeta \approx 0.5$ is $\phi \approx 0.4$, clearly below random close packing. This minor deswelling at $\zeta \approx 0.5$ is expected, as the counterion clouds are known to percolate at $\zeta \gtrsim 0.45$.

In addition, we have checked that the counterion cloud signal that we extract from the direct subtraction of $I^{\text{NH}_4^+}(q)$ and $I^{\text{Na}^+}(q)$ is a direct consequence of the ions in the sample and is repeatable. We have prepared a new s3 sample with NH_4^+ counterions from dry powder at $\zeta \approx 0.2$ and have measured it with SANS at $T = 20^\circ\text{C}$ to compare it with the previously prepared NH_4^+ sample shown in Supplementary Fig. 5.4A. We then follow the same protocol to analyze the data and find that the subtraction of the new and the old samples with NH_4^+ counterions does not have a minimum, see Fig. 2F in the main text. This is expected, as there is no contrast to detect the counterion cloud with NH_4^+ in both samples. As shown in Supplementary Fig. 5.7, we also find that the subtraction of the new NH_4^+ sample and the old Na^+ sample again shows the expected signal due to the counterion cloud, and we obtain the same radius and width within the accuracy of the analysis, see Supplementary Tab. 5.3.

Effect of a possible structural change as modeled via changes in σ_s

To see the effect of changing the width of the fuzzy shell given by σ_s , as perhaps induced by the ions, we fix the core radius, R_c , and calculate $\Delta I(q) = I_{\text{large}}(q) - I_{\text{small}}(q)$, see Supplementary Fig. 5.9, where we subtract the $I(q)$ of the particle with smaller σ_s from the $I(q)$ with larger σ_s . As shown in Eqs. 5.11 and 5.21, a larger σ_s causes a faster decay of the microgel form factor with increasing q . Therefore, a negative minimum in the range $0.02 \text{ nm}^{-1} < q < 0.05 \text{ nm}^{-1}$ in $\Delta I(q)$ is obtained with the subtraction given above. The positive maximum close to $q = 0.01 \text{ nm}^{-1}$ is due to the structure factor that also depends on σ_s through the microgel radius $R_{\text{SANS}} = R_c + 2\sigma_s$. We find that a change in σ_s in the range from 0.1 nm to 0.7 nm can give a minimum with the observed depth. While we can adjust the small difference in σ_s to reproduce the high- q side of the minimum in the experimental data, the low- q side of the observed minimum is not well reproduced, as the change in σ_s does not give the upturn observed in samples s1 and s3. As this upturn is quite pronounced, our ion-cloud model clearly provides a better fit to the data (see Fig. 2A in the main text and Supplementary Fig. 5.5A-C,F-H). Therefore, we find that the counterion-cloud model can reproduce all the observed data, while this is not pos-

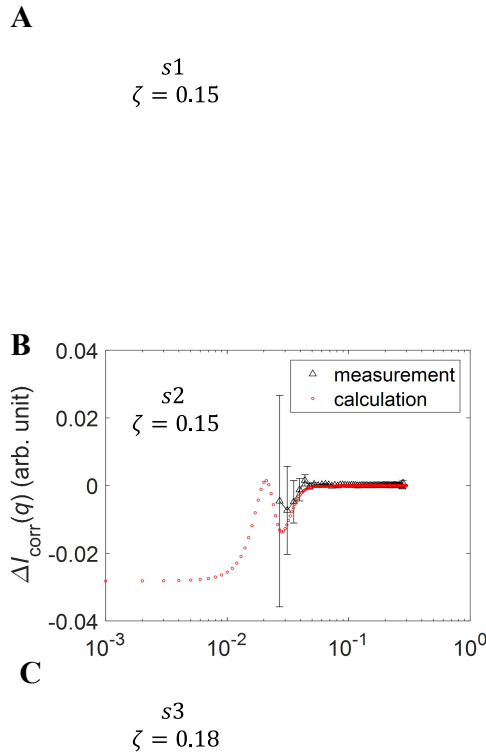


Figure 5.9: Comparison of (Δ) the measured $\Delta I(q)$ signal and (\circ) the calculated signal due to a small change of σ_s . The change of σ_s is adjusted to capture the higher- q part of the measured signal: (A) sample s1, $R_c = 56$ nm and $\sigma_s = 15$ nm for the larger particle and $\sigma_s = 14.9$ nm for the smaller particle (B) sample s2, $R_c = 82$ nm and $\sigma_s = 21$ nm for the larger particle and $\sigma_s = 20.9$ nm for the smaller particle and (C) sample s3, $R_c = 87$ nm and $\sigma_s = 24$ nm for the larger particle and $\sigma_s = 23.2$ nm for the smaller particle. The error bars represent the uncertainty due to the counting statistics of the SANS instrument.

sible with a change in the fuzzy shell thickness. This supports our interpretation of the observed $\Delta I(q)$ data with the counterion-cloud model.

The structural insensitivity to a change of counterions is further supported by studies on the influence that ions in the Hofmeister series have on the swelling behavior of pNIPAM [105]. A significant effect on the swelling behavior of pNIPAM, as well as a significant difference between ion types, was only found at high ion concentrations, $\gtrsim 300$ mM. The counterion concentration in the samples we study is

well below this concentration. We estimate the maximum counterion concentration in our samples by assuming that $N = 5 \cdot 10^4$ counterions are distributed in the fuzzy shell of the microgel and obtain $N/[N_A 4\pi(R_c + \sigma_s)^2(2\sigma_s)] \approx 16$ mM. Here, we use the middle radius $R_c + \sigma_s$ and the thickness $2\sigma_s$ of the fuzzy corona; N_A is Avogadro's number. Consistent with this, additional work on the Hofmeister series also finds that a salt concentration of ~ 10 mM has negligible effects on the lower critical solution temperature (LCST) of pNIPAM [84]. The low concentration of ions in our ion clouds and the fact that our SANS measurements do not show a structural difference between samples with NH_4^+ and Na^+ ions provide further support for the presented analysis of the counterion clouds of the microgels.

5.7 Particle softness dependence of counterion clouds

As we have demonstrated in Chapter 4 and in the previous sections of Chapter 5, the spontaneous deswelling of the microgels is controlled by the balance of suspension osmotic pressure inside Π_{in} and outside the particle Π_{out} . In particular, as we introduced in Section 1.4.2, Π_{in} can be largely varied by the elasticity of the microgels controlled by the degree of crosslinking. The relationship between the configuration of the counterion clouds and the particle softness remains unclear. In this section, we investigate the softness dependence of the characteristics of counterion clouds with microgels synthesized with three different crosslinker concentrations, provided by the collaborator at RWTH Aachen university. Microgel with an Ultra-low crosslinker (ULC) concentration is synthesized via atom abstraction reactions without crosslinks, 5.4. Microgels synthesized with the 2.5mol% BIS crosslinker have intermediate softness. The stiffest microgels are synthesized with 5.0mol% BIS. The details of these three samples are summarized in Table.5.4. Following the dialysis

Sample	cross-link density (mol.%)	hydrodynamic radius R_h (nm)	conversion constant κ
sULC	0.0	151.0 ± 2.8	44.8
s2.5	2.5	138.0 ± 3.0	14.2
s5.0	5.0	154.0 ± 3.0	11.0

Table 5.4: The details of microgels with different softness. The collapsed radius is not provided, however, the conversion constants reflect the compressibility of the microgels, hence the softness of the particles.

procedure introduced in Section.5.3, all three types of microgels are prepared with

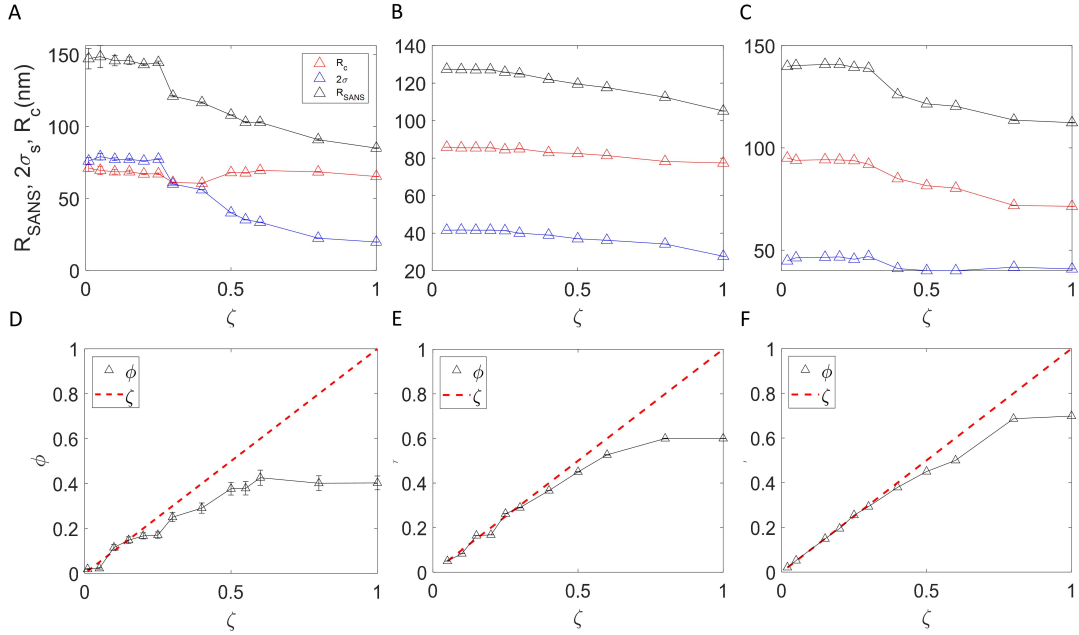


Figure 5.10: R_{SANS} (\square), R_c (\triangle), and $2\sigma_s$ (\circ) of samples sULC (A), s2.5 (B), s5.0 (C). The true volume fraction ϕ of samples sULC (D), s2.5 (E), s5.0 (F) versus generalized volume fraction ζ . The dashed lines represent $\phi = \zeta$

either Na^+ or NH_4^+ . The dry microgel powder obtained by freeze-drying is subsequently resuspended in a concentration series in the range of $\zeta \sim 0.01$ to $\zeta \sim 1.0$. The particle radii and the characteristics of the counterion clouds are obtained with the same procedure for all three samples. The scattering curves are fitted to the fuzzy-sphere form factor together with the Percus-Yevick structure factor $S_{\text{PY}}(q)$ for neutral hard-spheres, as introduced in Eq.5.20. Despite the fact that microgels carry counterions, $S_{\text{PY}}(q)$ is able to describe the data nicely. The possible reason is that the charges are screened, and the averaged effect of the charges is not significant, such that the interaction among the microgels is not dominated by electric charges. In addition, as microgels are isotropically compressed at high ζ and a direct interaction between neighboring microgels is absent, the suspension still satisfies the non-interpenetration assumption of the hard-sphere interaction.

The fitting results of R_{SANS} , R_c , $2\sigma_s$, and the true volume fraction ϕ of the microgels are summarized in Fig.5.10. ULC microgels remain at their swollen size at low concentrations and start to deswell at $\zeta \approx 0.25$. Note that the true volume fraction ϕ is below the random close packing density $\phi_{\text{rcp}} \approx 0.64$ at $\zeta = 1.0$. A similar radii plateau is observed for samples s2.5 and s5.0, however, R_{SANS} starts to decrease at a slightly higher $\zeta \approx 0.3$ for sample s2.5 and even higher $\zeta \approx 0.4$ for sample s5.0.

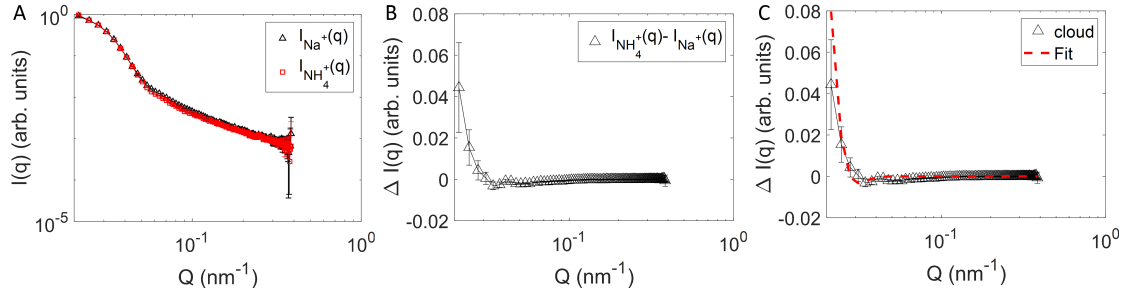


Figure 5.11: Cloud measurements for sample sULC. A: The scattering intensity of ULC microgels with Na^+ and NH_4^+ ions at $\zeta = 0.2$ are plotted together. B: Direct subtraction of the two intensity curves reveals the strongly reduced cloud signal. C: The cloud signal and its fit with the spherical shell model.

This reflects the difference in particle softness because a higher osmotic pressure is required to isotropically compress microgels with a higher crosslink density. For sample s2.5, the true volume fraction ϕ is less than ϕ_{rcp} , but much closer to ϕ_{rcp} than for ULC microgels at $\zeta = 1.0$. For the toughest microgel, ϕ of the sample s5.0 becomes higher than ϕ_{rcp} at high ζ . This indicates that microgels interact directly and that particle deformation or interpenetration can occur.

To obtain the counterion cloud signal of the ULC microgels, the scattering intensity of the Na^+ sample is directly subtracted from that of the NH_4^+ sample. As shown in Fig.5.11A, the two scattering curves are very similar, indicating that the sample concentrations are virtually identical. After the direct subtraction, we notice that the incline at the low q -range still presents, however, the 'dip' is strongly reduced, as shown in Fig.5.11B. Indicated by the model plot shown in Fig.5.2, the 'dip' tends to be less prominent with the cloud width being significant compared to the particle radius. ULC microgels are synthesized without cross-linkers; hence, it is reasonable to assume that the fuzzy core-shell structure is not as pronounced as that of microgels synthesized with crosslinks, and the internal structure is more uniform across the particle. The simple spherical shell model can still capture most of the data points, as shown in Fig.5.11C. The cloud width obtained is $\sigma_{\text{ic}} = 78 \pm 25$ nm, which is significantly larger than that of the microgel synthesized with 2.0mol% BIS. $R_{\text{ic}} = 125 \pm 10$ nm and $R_{\text{ic}} < R_{\text{SANS}} = 144 \pm 2$ nm, which shows that the cloud is within the particle and close to the microgel surface, consistent with the previous results. Additionally, indicated by the fitting result shown in Fig.5.10A, the width of the fuzzy shell is nearly the same value as the radius of the core for low ζ , which corroborates the assumption. As a result of the wider fuzzy corona, the charge groups at the chain ends are expected to be distributed over a wider range

inside the microgel. As a result, counterion clouds that are electrostatically bound to these charge groups are probably widely distributed, resulting in a cloud signal with a strongly reduced minimum 'dip'. Note that, our simple spherical shell model

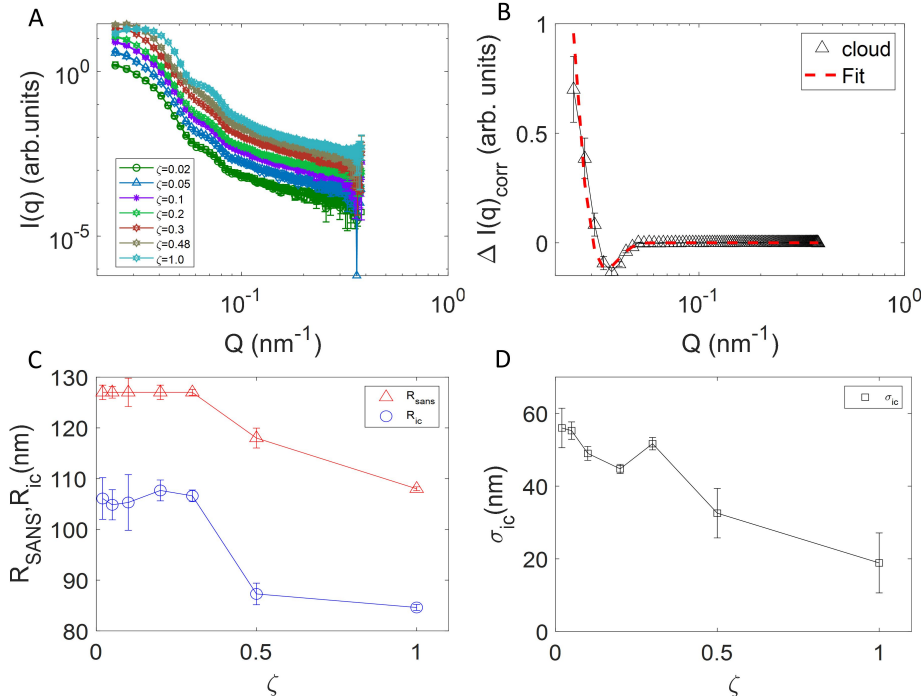


Figure 5.12: Cloud measurements for sample s2.5. A: Scattering curves of the Na^+ and NH_4^+ samples plotted together for all ζ . B: The cloud signal and its fit at $\zeta = 0.2$. The cloud signals and the fits at other ζ have similar quality. C: Comparison of R_{SANS} and R_{ic} with increasing ζ . D: ζ dependence of the counterion cloud width σ_{ic} .

assumes that charged groups are distributed on the thin shell with radius R_{ic} , that is convolved with a Gaussian function to account for the distribution of counterions. The distribution of the charged groups can also be taken into account for further modification of the model, so that the signals resulting from a wide distribution of the charged groups can be more accurately described.

With microgels synthesized with 2.5 mol.% crosslinks, the result is comparable to that of the microgel with 2.0 mol.% cross-linkers discussed in Chapter 4 and in the previous sections of this chapter. The fuzzy shell is much narrower than that of the ULC microgels. As shown in Fig.5.12A-B, the scattering curves for Na^+ and NH_4^+ samples overlap each other in the ζ range, and the cloud signal can be nicely described by the spherical shell model. For all ζ studied, a counterion cloud signal with a minimum and low- q upturn can be obtained by directly subtracting the

scattering intensity of the Na^+ sample from that of the NH_4^+ sample. By fitting the cloud signal to the spherical shell model in Eq.5.20, the cloud radii R_{ic} and the cloud width σ_{ic} are obtained. The results indicate that the radius of the cloud is smaller, but close to R_{SANS} and R_{ic} decreases with R_{SANS} with increasing concentration. The width of the cloud σ_{ic} is close to 50 nm for $\zeta < 0.3$ and decreases together with increasing ζ . The decrease in σ_{ic} can be explained by the decrease in the width of the fuzzy corona; the charge groups have a narrower spatial distribution at high ζ , resulting in a narrower counterion cloud.

For the toughest particle with 5.0 mol.% crosslinks, an interesting behavior is observed, in which the cloud signal can be obtained at low ζ but not at high ζ . At $\zeta = 0.2$ the cloud signal can be obtained by direct subtraction $I^{\text{NH}_4^+}(q) - I_{\text{corr}}^{\text{Na}^+}(q)$ and the spherical shell model in Eq.5.20 can nicely describe the data, as shown in Fig.5.13A. For s5.0 at $\zeta = 0.2$, $R_{\text{ic}} = 118.6 \pm 3.0$ nm and $\sigma_{\text{ic}} = 51.68 \pm 2.50$ nm, similar to the results obtained for s2.5. However, at $\zeta = 0.6$ and $\zeta = 1.0$, the scattering curves I^{Na^+} and $I^{\text{NH}_4^+}$ overlap nicely, but the expected cloud signal is not obtained, as shown in Fig.5.13C-D. The magnitude of the 'dip' is significantly larger than the prediction of the model, and the increase of the intensity in the low q -range is also absent. In addition, $\Delta I(q)$ at $\zeta = 0.6$ and $\zeta = 1.0$ shows similar shapes but opposite magnitudes. This indicates that the obtained $\Delta I(q)$ is not likely due to counterion clouds but due to a shared property that is independent of the ion type. Note that, as shown in Fig.5.13B, the polydispersity (PD) of the core increases significantly at $\zeta \approx 0.4$, contradicting the expectation of isotropically deswollen microgels; spontaneous deswelling behavior that occurred at high concentration should decrease the polydispersity. According to previous work, the Fuzzy-Sphere form factor describes spherical objects, and polydispersity tends to increase when applying this model to a deformed sphere [77, 155]. ϕ is observed to increase and exceed ϕ_{rcp} and therefore microgels with 5.0 mol.% BIS are expected to be in direct contact and deformed at high ζ . Because of the direct interaction among microgels, it is possible that the fuzzy-shell width and core polydispersity of the two samples could be different, reflecting the deformation of the shell and core. In Fig.5.13E, we show that the $\Delta I(q)$ signal for $\zeta = 0.6$ can be reproduced by subtracting two scattering intensities of the samples with different core polydispersity and fuzzy-shell width. $\Delta I(q)$ signal is calculated by subtracting the intensity of a smaller particle from that of the larger particle $I_{\text{large}} - I_{\text{small}}$. For the calculation of $I_{\text{large}}(q)$, $R_{\text{c}} = 77$ nm, $\sigma_{\text{s}} = 14$ nm, and PD= 0.29 are used. $R_{\text{c}} = 77$ nm, $\sigma_{\text{s}} = 13.6$ nm, and PD= 0.292 are used to calculate $I_{\text{small}}(q)$. The PD of the smaller particle is larger than that of the larger particle

to account for the deformation. $\Delta I(q)$ signal of $\zeta = 1.0$ can be reproduced with $I_{\text{small}} - I_{\text{large}}$, since the signal is not due to the ion types and the order of subtraction does not matter in this case. Since the observed magnitude of $\Delta I(q)$ due to deformation is approximately ten times larger than that due to the counterion clouds, the cloud signal is easily buried, and we do not observe it at a high ζ of s5.0.

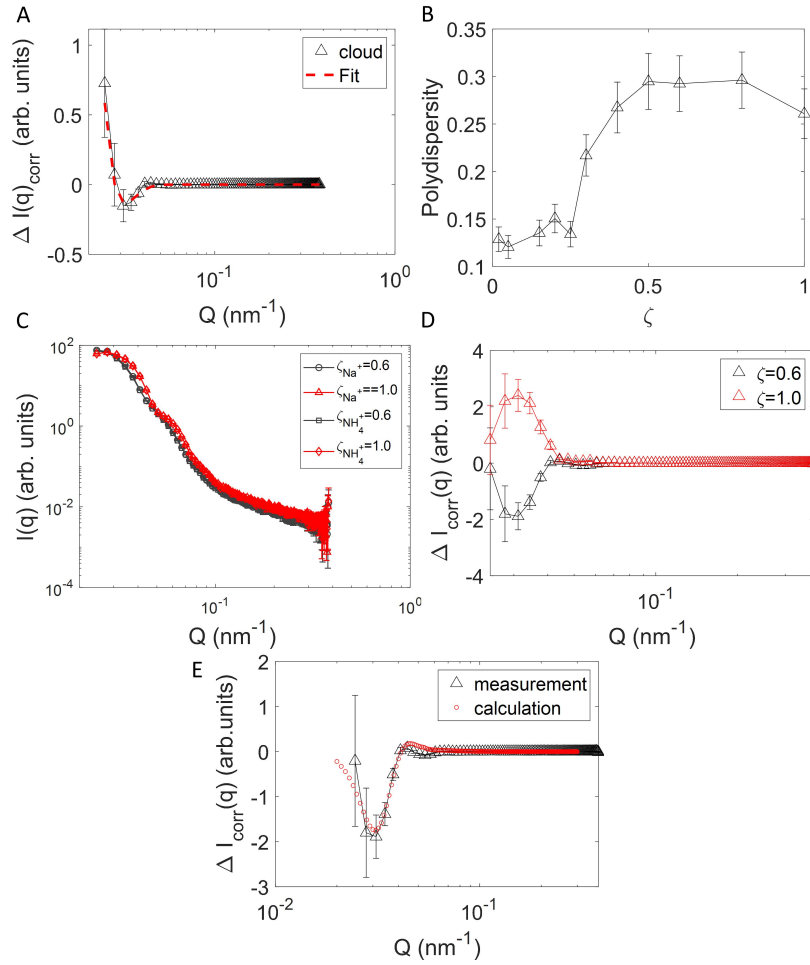


Figure 5.13: Cloud measurement of sample s5.0. A: Subtraction of $I^{\text{NH}_4^+}(q) - I_{\text{corr}}^{\text{Na}^+}(q)$ of s5.0 at $\zeta = 0.2$ (black triangle) and fit to the data (red dotted line). B: The polydispersity of the core as a function of the generalized volume fraction ζ . C: SANS data of s5.0 with Na^+ at $\zeta = 0.6$ (black Δ) and $\zeta = 1.0$ (red \circ), and NH_4^+ at $\zeta = 0.6$ (black \square) and $\zeta = 1.0$ (red \diamond). D: Subtraction of $I^{\text{NH}_4^+}(q) - I_{\text{corr}}^{\text{Na}^+}(q)$ of s5.0 at $\zeta = 0.6$ and $\zeta = 1.0$. E: comparison of the measured $\Delta I(q)$ signal and the calculated signal due to a small change of fuzzy shell width σ_s and the core polydispersity PD: $R_c = 77$ nm, $\sigma_s = 14$ nm and PD = 0.29 for the larger particle and $\sigma_s = 13.65$ nm and PD = 0.2913 for the smaller particle.

5.7.1 Summary

In this section, we have investigated the concentration and particle softness dependence of the microgel counterion clouds. For the ULC microgels, the cloud signal indicates a wide counterion cloud, which is reflected by a strongly reduced minimum detected in the SANS signal. The wide cloud is likely due to the internal structure of the ULC microgel synthesized without cross-linkers. Cloud signals are visible for microgels synthesized with 2.5 mol.% crosslinkers throughout the ζ range. The cloud is located a bit inside the particle with a width around 50 nm. Furthermore, the radius of the cloud and the width of the cloud decrease with increasing concentration, reflecting the spontaneous deswelling of the microgels at high concentrations. Lastly, the cloud signal is visible for the microgel containing 5.0 mol.% crosslinkers at low ζ . At higher concentrations, however, spontaneous deswelling is less pronounced due to increased stiffness and the microgels get into direct contact, which leads to deformation. The $\Delta I(q)$ signal due to particle deformation is significantly larger than that due to counterion clouds, and, as a result, cloud signals are not observable for sample s5.0 at high concentrations.

Chapter 6

Lattice vibrations in microgel crystals studies using confocal microscopy

6.1 Introduction

We have seen that the microgel carries charged groups on the periphery of the particle. As a result, there is a cloud of counterions around every particles. At sufficiently high ζ , the clouds of all microgels percolate, and the associated counterions break free and explore the suspension volume. This increases the osmotic pressure of the suspension, causing particle deswelling. To understand the influence of the delocalized counterions at high ζ , we study the normal modes of the microgel crystals directly via confocal microscopy, which to our knowledge, have not been investigated in detail so far. Following the ideas of Reinke and Wallace [140, 190], the force constants that define normal modes can be extracted from the analysis and the centrality of the interaction force can be investigated based on the force constants of nearest and second-nearest neighbors. Interestingly, the microgel crystals with wandering counterions are analogous to crystal structures of charged hard spheres with ions wandering between them, as well as to metals with the gas of free electrons between the ions. However, the key difference is that microgels can deswell in a crowded environment with osmotic pressure larger than the microgel bulk modulus. The presence of these counterions in microgel crystals cause the interaction forces between microgels to have a non-central character, as explained in this chapter. The results of this study are compared to the studies of charged hard-sphere crystals [140] and metals [111, 160]. Note that unlike charged hard/soft-

sphere crystals, it is oversimplifying to narrow the interaction among metal ions to electrostatic interactions, since an electrostatic approximation is not sufficient to describe metals; there are quantum mechanical aspects that need to be considered. In the previous chapters, it is assumed that it is sufficient to use a pair potential to analyze the structure and dynamics of dilute suspensions, as the suspension structure is close to that of hard sphere suspensions [63]. However, as will be shown in this study, in concentrated suspensions or in the colloidal crystalline phase, the screening length is longer than the inter-particle spacing, and many-body forces become important. As the interaction forces between microgels is non-central, it is therefore not enough to simply use a radially symmetric effective pair potential, such as the Derjaguin-Landau-Verwey-Overbeek (DLVO) potential [76, 146].

In sections 6.2 and 6.3, we introduce confocal microscopy and experimental details. In Section 6.4, the details of data acquisition are introduced. In Section 6.5, we discuss particle finding and tracking methods. In Section 6.6, the theory of harmonic crystals, which is the cornerstone of our analysis is introduced. In Section 6.7, we discuss the dynamic matrix, the eigenvalues of the modes, and the extraction of force constants. In Section 6.8, the theory of lattice elasticity is introduced, which is closely related to the dynamic matrix in the long wavelength limit, where the elasticity coefficient and bulk modulus of the microgel crystal can be extracted. Finally, we show the results of the measured eigenvalues and the dispersion relations for different modes, as well as the force constants extracted from the dispersion relations. In Section 6.9, we discuss the results and conclusions.

6.2 Confocal microscopy

In this work, microgels containing a fluorescent center are investigated with a confocal microscope. Images of a crystal of microgels are taken with a Nikon Spinning Disk SoRa. SoRa stands for Super-resolution via Optical Re-Assignment. The purpose of a confocal microscope is to reduce the collection of out-of-focus light. The confocal principle describes two processes during acquisition: focused illumination and a pinhole in the image plane with the focal plane and the image plane being conjugate focal planes, as illustrated in Fig. 6.1. The collimated laser light is focused on a spot in the sample to be imaged. The illumination point in the focus plane is subject to the point-spread function and has a radius that can be calculated as $R_{\text{illu}} = \frac{0.61\lambda}{NA}$, where λ is the wavelength and NA is the numerical aperture of the objective lens. Any part of the sample, whether in or out of the focal plane, that is

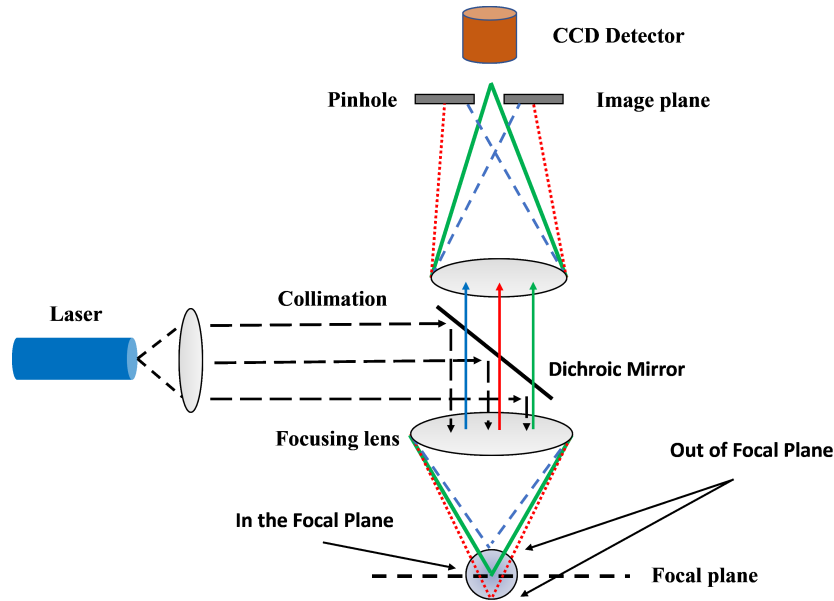


Figure 6.1: The schematic represents the confocal mechanism applied by the point-by-point scanning microscope. The collimated beam is focused by the focusing lens. The emitted lights from inside and outside of the focal plane are focused before reaching the pinhole. The pinhole blocks most of the out-of-focus emitted lights and only lets the images from the focal plane pass to the CCD detector.

excited by the laser can emit photons that are collected by the objective lens. The emitted fluorescence passes through the focusing process and reaches the pinhole in the image plane. Light originating from the part of the sample outside the focal plane will be out of focus when it reaches the pinhole, and will ideally be blocked. Importantly, only the focal plane is imaged, whereas light from many planes is collected without confocal setup; as a result, the confocal mode significantly improves the resolution along the optical axis and greatly enhances the signal-to-noise ratio, producing images with good contrast. By changing the position of the focal plane, we can image thin slices of the sample; this is only possible with a confocal setup. Naturally, the size of the pinhole affects the image quality. When the size of the pinhole matches the size of the object focused on the image plane, the maximum amount of out-of-plane fluorescence is blocked by the pinhole, whereas a larger pinhole size allows more out-of-focus light to pass through. As a result, the size of the pinhole is an essential parameter for the confocal microscope. Note that the image produced by a point source illumination is also a point source. The size of the image can be calculated with the diameter of the point spread function (PSF): $2 \left(\frac{0.61\lambda}{NA} \right) \times M$, where M is the magnification. This gives an optimal physical size of the pinhole that maximizes the reduction of out-of-focus fluorescence. The confocal

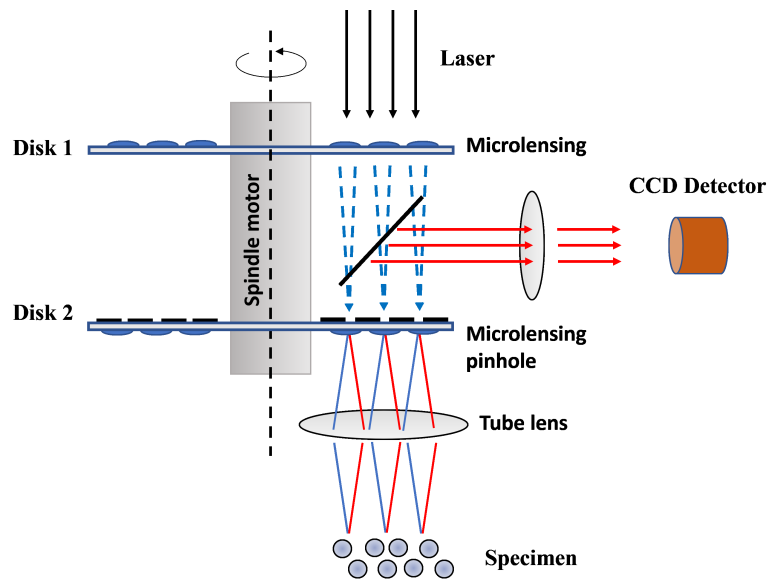


Figure 6.2: A simplified schematic diagram of a Spinning disk confocal microscope. Disk1 contains microlens that focus the excitation beam. The focused excitation beam passes through the pinholes on Disk2 and is refocused by the tube lens. The emitted light is reflected by the Dichroic mirror and reaches the CCD camera.

setup shown in Fig.6.1 describes a point-by-point scanning and relies on constant laser light exposure, which produces clear images. The disadvantage of the confocal is that a single point in the sample is imaged. Therefore, one needs to scan to obtain a 2d or 3d image, which makes image collection much slower. The microscope we use is equipped with two spinning disks, as illustrated in Fig.6.2. The microlens on the top disk focuses the light that subsequently passes through the pinhole on the bottom disk. This process dramatically improves illumination and scanning speed, as many pinholes are used. The dual-disk setup with microlensing pinholes allows multiple excitation sources to reach different locations of the specimen at the same time, greatly reducing the acquisition time while producing high-resolution images [10]. Fluorescence microscopy is often used on cofocal microscopes, in which the fluorescence allows to obtain light from fluorescent objects that are of interest, and it also allows to separate the light used for illumination and for imaging, so that even clear images can be obtained.

6.3 Fluorescent microgel

The microgels used in this experiment are provided by a collaborator at University of Bordeaux. Details regarding the microgel synthesis is reported elsewhere [187].

The microgels contain a hard PTFMA core with a radius of 200 nm. The pNIPAM is copolymerized with acrylic acid (AAC) and the growth of the pNIPAM-co-AAC shells on the surface of the PTFMA core is achieved via radical polymerization. The isoelectric point of the microgels is estimated to be $pH \approx 4.4$. The hydrodynamic radius at $pH \approx 2, 4.2,$ and 6.7 is $R_h = (93 \pm 4) \times 10 \text{ nm}$, $(1.20 \pm 0.07) \mu\text{m}$, and $(1.40 \pm 0.06) \mu\text{m}$. Measurements are performed at $pH \approx 3.5$ and $pH \approx 7.0$. For measurements at $pH \approx 3.5$, the AAC is not charged and the microgel is effectively charge-neutral, except for the charged groups resulting from the initiators, explained in Section 1.3. At $pH \approx 7.0$ the microgels are mildly charged throughout and are more swollen compared to $pH \approx 3.5$. Samples are investigated at two concentrations $\zeta \approx 1.62$ and 1.40 , and at $T = 22^\circ\text{C}$.

6.4 Data Acquisition

A capillary with a suitable wall thickness is used as the sample container, and the flat wall of the capillary facilitates crystal growth. For sample preparation, microgel suspension is extracted from a bulk sample and introduced into the glass capillary through capillary action. Subsequently, the glass capillary is sealed on a glass slide with UV-curable glue. Measurements are taken at room temperature, $T = 20^\circ\text{C}$. The glass slide is attached to the microscope 60 minutes before measurement, allowing sample to equilibrate. The illumination wavelength is $\lambda = 600 \text{ nm}$. Measurement takes sixty-one steps in the z direction with a step of $0.2 \mu\text{m}$. The size of the pixels is $0.065 \mu\text{m}$ in the x - y plane and $0.2 \mu\text{m}$ in the z -direction, indicating that the resolution is nearly three times lower in the z -direction than in the x - and y -direction. A 3d image stack is taken within 7 s, and the stack is repeated 72 times to follow the motion of the microgels. As the image contains 1024 pixels in the x - and y - direction and 61 pixels in the z -direction, the total measured sample volume is around $5 \times 10^4 \mu\text{m}^3$. Example raw images are shown in Fig.6.3. As the particles have a fluorescent center, it is clear that they are well separated, and there is no visible aggregation of the cores. Note that the z -direction along the optical axis corresponds to the $[111]$ direction of the face-centered cubic crystal lattice and that the hexagonal plane is visible throughout the sample, implying that the crystal structure is dominated by the random hexagonal close packing (rhcp) with layers of fcc or hcp stacking.

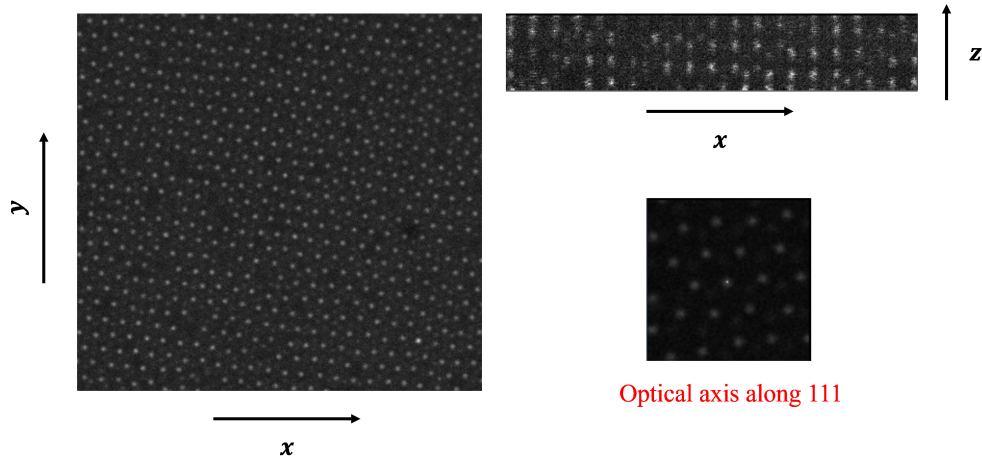


Figure 6.3: Left: A fraction of the raw image is shown in the x - y plane. Top right: A fraction of the raw image is shown in the x - z plane. Bottom right: A zoomed-in view of the image in the x - y plane along the optical axis, which corresponds to the $[111]$ direction. The hexagonal plan is visible.

6.5 Particle finding method

We utilize the centroid calculation method of Crocker and Grier (CG) to detect the particle position in our confocal images [30]. These images contain noise originating from instrument and environment, and additionally have blurred features due to the convolution of the particle images with the point spread function of the microscope. As a result, the raw images have to be processed to accurately find particle positions. First, to achieve better separation of bright features, the raw image is smoothed with a Gaussian kernel to remove any noise resulting from fluctuations in the number of photons counted per pixel, fluctuations of the laser intensity, and electronic noise from the environment. The smoothed image I_s is obtained by convolving the raw images with the Gaussian kernel: $I_s = I_r \otimes G$, where

$$G(i, j, k) = \frac{1}{N} \exp\left(\frac{-(i^2 + j^2 + k^2)}{2\sigma^2}\right) \quad (6.1)$$

$$N = \sum_{i,j,k} \exp\left(\frac{-(i^2 + j^2 + k^2)}{2\sigma^2}\right)$$

with i , j and, k the pixel coordinates in the x , y , and z direction. The standard deviation σ is usually close to the size of one pixel. When convolving with this Gaussian kernel, all noise with a correlation length smaller than and equal to σ is removed from the raw image. An example of a smoothed image is shown in Fig.6.4. To obtain well-separated bright features, the background of the image $I_{bg} = I_r \otimes k_b$

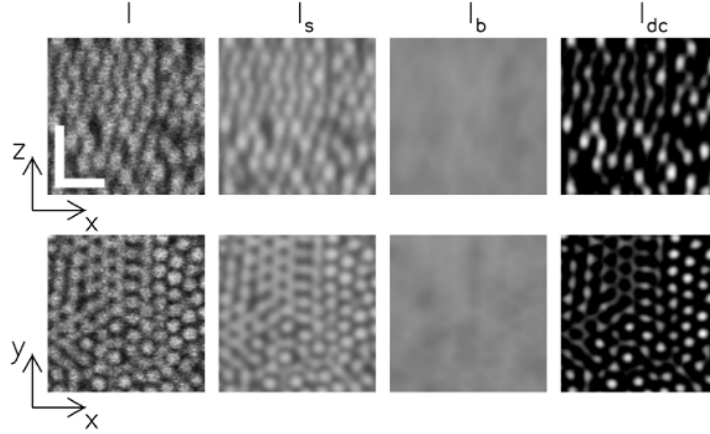


Figure 6.4: The image is taken from [55]. Left to right: raw, smoothed, background, and clipped sectional views in a measured 3D confocal microscopy image. The z direction (upper row) is along the axial direction of the microscope. Scale bars of $5 \mu\text{m}$ are shown in the upper left panel. The scale is the same for x - and y -direction. The expected resolution is (220 ± 10) nm in x - and y -direction and (400 ± 10) nm in z direction

is estimated by convolving the raw image I_r with the spherical boxcar kernel,

$$k_b(i, j, k) = \begin{cases} \frac{1}{N_b} & \text{for } \sqrt{i^2 + j^2 + k^2} < R_0 \\ 0 & \text{otherwise} \end{cases} \quad (6.2)$$

$$N_b = \sum_{\substack{i, j, k \\ \sqrt{i^2 + j^2 + k^2} < R_0}} 1$$

where R_0 is the radius of the largest particle of interest. Eq.6.2 normalizes the intensity with the number of pixels within the region having the largest feature size. After subtracting the background from the smoothed image, we obtain the image $I_d = I_s - I_{bg}$. We further clip the minimum of I_d to zero, to have $I_{dc} \geq 0$ everywhere; in this way, the features are well separated:

$$I_{dc}(\mathbf{r}) = \begin{cases} I_d(\mathbf{r}) & I_d(\mathbf{r}) > 0 \\ 0 & I_d(\mathbf{r}) \leq 0 \end{cases} \quad (6.3)$$

The pixels in image I_{dc} are then sorted by their intensity. The rough position of the particle \mathbf{R} is determined by finding the pixels in decreasing order of brightness. Pixels within the minimum particle separation distance are excluded from the search for further particle centers. The minimum separation distance is generally set to an odd integer a bit smaller than the presumed object size. Subsequently, we calculate the centroid for each detected particle to obtain accurate positions. As the CG

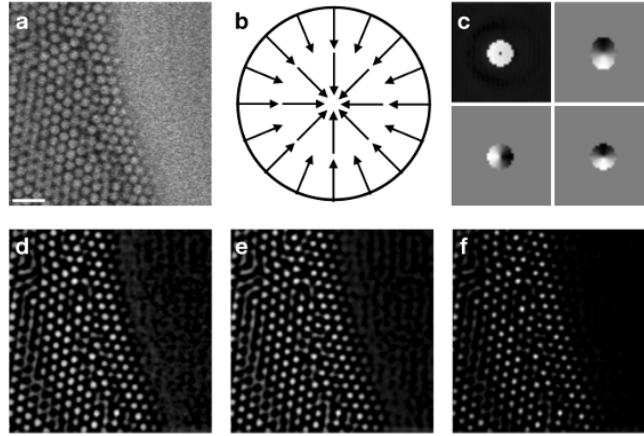


Figure 6.5: The image is taken from [55]. (a) Section of a measured 3D confocal microscopy image with colloidal particles next to an impenetrable region. The scale bar corresponds to $10\mu\text{m}$. (b) 2D sketch of the convolution kernel \mathbf{k}_c containing unit vectors pointing toward the center of the kernel inside a spherical region and zero vectors outside the spherical region. (c) Sections through the kernel \mathbf{k}_c : (x,y) plane (upper left) and (x,z) plane (upper right) of $k_{c,z}$, (x,y) plane of $k_{c,x}$ (lower left) and (x, y) plane of $k_{c,y}$ (lower right). (d) Image I_{dc} is obtained with the CG method. (e) Image I_{gc} , see Eq.6.6. (f) Combined image $I_2 = I_{dc} \cdot I_{gc}$.

method finds all bright features, this implies that bright unwanted features can also be detected by this method. As microgels are spherical objects, only the bright-spherical features are of interest. To select the spherical objects, we first calculate the gradient image of the smoothed image:

$$\nabla I_s = (\partial x, \partial y, \partial z)^T I_s \quad (6.4)$$

For bright, spherical objects, the gradient is expected to be directed towards the particle center, as shown in Fig.6.5b. A spherical kernel k_c is used to detect gradients that are directed toward the center of the particle. Explicitly,

$$k_c = \begin{cases} -\mathbf{r} & \text{for } |\mathbf{r}| < R_f \\ 0 & \text{for } |\mathbf{r}| > R_f \end{cases} \quad (6.5)$$

where $\tilde{\mathbf{r}} = \frac{\mathbf{r}}{|\mathbf{r}|}$ is the unit vector pointing towards the origin and R_f is the expected radius. The image of spherical objects detected using the gradient image is defined as:

$$I_g = \sum_i \partial_i I_s \otimes k_{ci} \quad (6.6)$$

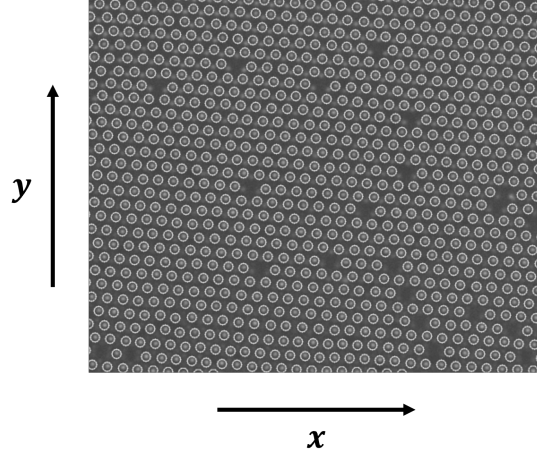


Figure 6.6: Confocal image of a microgel crystal with microgels detected using the method of CG with spherical kernel highlighted by circles. To check whether all the particle positions are found, we plotted the detected positions with a circle on the corresponding particles in the $x - y$ plane. All particles are identified in the section shown. The voids shown in the images are possibly due to particles without a fluorescent center.

which is further clipped to zero, so that $I_{gc} \geq 0$. The image that contains bright and spherical objects is obtained as $I_2 = I_{dc} \cdot I_{gc}$. Lastly, the 'center of mass' in terms of intensity is calculated for the particles detected from image I_2 to obtain higher positional accuracy.

The total brightness B and the intensity-weighted radius of gyration are defined as

$$\begin{aligned}
 B &= \sum_{|(i,j,k) - \mathbf{R}| < R_f} I_{i,j,k} \\
 R_g &= \left[\frac{1}{B} \sum_{|(i,j,k) - \mathbf{R}| < R_f} I_{i,j,k} [(i,j,k) - \mathbf{R}]^2 \right]^{1/2}
 \end{aligned} \tag{6.7}$$

where (i,j,k) gives the pixel position. In this way, we only detect bright and spherical features from the microscopy images. The detected particle position is plotted over the original images to show the quality of the detected position, as illustrated in Fig.6.6.

6.5.1 Particle tracking

The tracking and reconstruction of the particle trajectories is done via the open access IDL code by Crocker, Weeks, and Gasser [82, 30, 55]. To link the particle

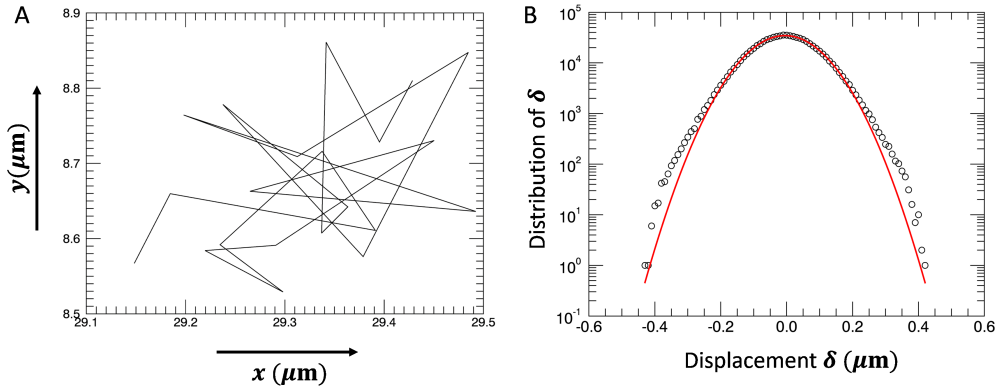


Figure 6.7: A: The trajectory of a single particle in a crystal over the whole measurement time in the $x - y$ plane is shown. B: The histogram of displacement is shown in the x direction (black circle) fitted to a Gaussian distribution (red line). The Gaussian-like behavior with a single peak indicates the pixel biasing is negligible and the quality of the tracks is good.

from two frames at time 0 and τ , we can consider the probability that a particle diffuses a distance δ in time τ due to Brownian motion:

$$P(\delta|\tau) = \frac{1}{\sqrt{4\pi D\tau}} \exp\left(-\frac{\delta^2}{4D\tau}\right) \quad (6.8)$$

where D is the particle self-diffusion coefficient. For a system containing N non-interacting monodisperse particles, the probability distribution is the product of the single-particle probabilities:

$$P(\{\delta_i\}|\tau) = \left(\frac{1}{\sqrt{4\pi D\tau}}\right)^N \exp\left(-\sum_{i=1}^N \frac{\delta_i^2}{4D\tau}\right) \quad (6.9)$$

The particles in consecutive images are identified such that the displacements δ_i are short and $P(\{\delta_i\}|\tau)$ is maximized. For implementation, the algorithm takes three limiting parameters: the maximum travel distance of a given particle, the minimum track Tr_{mini} required for one particle, and the maximum missing steps Tr_{max} allowed before the particle is treated as missing. In our analysis, the maximum allowed travel distance is $\delta \approx 0.45\mu\text{m}$, which is equivalent to one-third of the particle radius, and $\text{Tr}_{\text{mini}} = 15$ and $\text{Tr}_{\text{max}} = 5$ are used to determine the trajectory of the particle. An example of the particle tracking result is shown in Fig.6.7. From the single particle track shown in Fig.6.7(A), we can tell that there is no preferred direction with respect to particle movement, indicating that the particle is not jammed. In addition, particle drift is removed if present. The drift is defined as a particle

deviation in the synchronized direction for all particles in a region. Furthermore, by plotting the histogram of the displacement distance δ , we notice that it goes to zero before reaching the maximum allowed travel distance $d = 0.45 \mu\text{m}$, which means that all possible displacement distances of the particles have been considered and the probability of finding more tracks with $d > 0.45$ is zero. The histogram also appears Gaussian-like and only one single peak is observed, which means that there is no pixel bias on the particle deviation distance δ , as shown in Fig.6.7B.

6.5.2 Local Bond-order parameters

In disordered systems such as glasses, the bond order parameters are used to measure the local order. In addition, they can also be used to detect small crystal nuclei and grains during crystallization. The bond order parameter is based on spherical harmonics. The term "bond" does not refer to a chemical bond but represents the spatial configuration of one particle with respect to its nearest neighbors. As the microgel suspension shows clear crystalline regions, the bond order parameter is useful to identify the local crystal structures. To analyze the microgel crystals, the sixth-order spherical harmonics \mathbf{Y}_6^m are used for the calculation. As there are twelve nearest neighbors for the FCC structure, the sixth-order spherical harmonic has 13 complex components, the lobes, all corresponding to $l = 6$. Other parameters, e.g. $l = 4$, can also be used to further characterize the local structure. The bond-order parameter $q_{lm}(i)$ of particle i is defined as:

$$q_{lm}(i) = \frac{1}{N(i)} \sum_{j=1}^{N(i)} \mathbf{Y}_l^m(\mathbf{r}_{ij}) \quad (6.10)$$

where N_i is the number of nearest neighbors. To find the nearest neighbor, a cutoff radius R_{12} is used. The subscript "12" indicates that 12 nearest neighbors are expected for fcc crystals. All particles within this radius with respect to the particle i are considered to be nearest neighbors. The cutoff radius R_{12} can be obtained with the radial distribution function $g(r)$:

$$4\pi n \int_0^{R_{12}} g(r) dr = 12 \quad (6.11)$$

where n is the number density. To identify a crystal-like surrounding, we compare

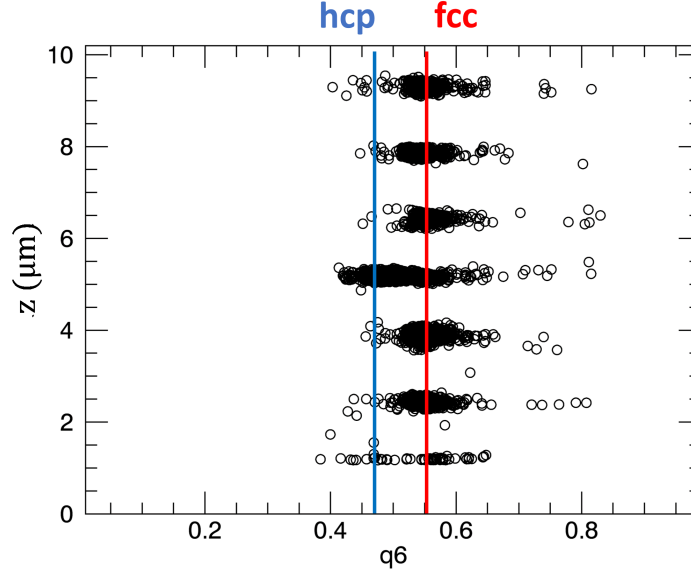


Figure 6.8: The mean z position in μm of each layer of the crystalline plane is plotted against the mean q_6 values of all particles. As the q_6 mostly lies in the range $0.50 - 0.60$ (red line), it is clear that the crystal structure is mainly fcc structures. Additionally, the q_6 values for hcp structure are indicated by the blue line.

the q_{lm} of nearest neighbors using the inner product:

$$s_6(i, j) = \sum_{m=-l}^l \hat{q}_{6m}(i) \hat{q}_{6m}^*(j) \quad (6.12)$$

where $\hat{q}_{lm} = q_{lm} / \sqrt{\sum_m q_{lm} q_{lm}^*}$ is the normalized bond order parameter. The 'bond', which describes the spatial arrangement between neighbors, is said to be a crystal-like bond if $s_6(i, j) > 0.5$. A particle that has eight or more crystal-like bonds is considered a crystal-like particle. For the determination of the local crystal structure, we do not care about a particular orientation of the crystal. Therefore, the rotational invariant of q_{lm} is defined:

$$q_l(i) = \left[\frac{4\pi}{2l+1} \sum_{m=-l}^l |q_{lm}(i)|^2 \right]^{1/2} \quad (6.13)$$

In our measurement, q_6 is calculated for all detected particles to identify the crystal structure. In Fig.6.8, the local bond order parameter of all particles is represented in the x -axis, with layers along the z direction represented in the y -axis. From previous simulation work, q_6 for an FCC structure is expected to be between 0.5

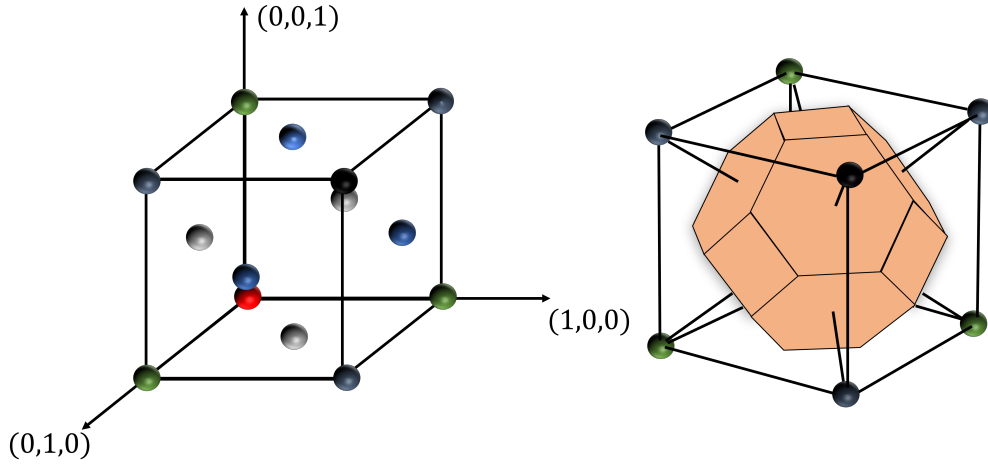


Figure 6.9: (Left) The schematic of a fcc crystal in the conventional coordinate system. Gray, green, and blue represent the 1st, 2nd, and 3rd neighbors with respect to the red ball at the origin. (Right) Schematic of the reciprocal lattice of the fcc crystal, which is a bcc lattice. The first Brillouin zone is shown by the orange polyhedron.

and 0.6 [56, 168]. In general, the crystal planes are mixed with fcc and hcp layers; however, it is clear that most of the crystal planes are fcc in this example, as shown in Fig.6.8 and Fig.6.9 (left). The layer at $z = 5.0 \mu\text{m}$ has an hcp structure with $0.42 \geq q_6 \leq 0.48$, as shown in Fig.6.8 (blue line) [56]. The hcp structure has minimal influence, as the analysis is done only in regions with fcc stacking, such as $5.5 \mu\text{m} < z < 10.0 \mu\text{m}$. As we will demonstrate later, the analysis is done in the reciprocal space of the fcc crystal, which is a bcc lattice, as shown in Fig.6.9 (right).

6.6 The Harmonic Approximation

For a crystal in equilibrium, the particles are jiggling in their equilibrium locations. Analyzing the energy associated with the deviation of the particles from their mean positions reveals significant physical properties of the crystal, such as its elastic modulus. The classic approach uses the harmonic approximation, which relies on two main assumptions: first, the equilibrium position of each particle is a crystal site indexed as $\mathbf{R}_\alpha = \sum_{i=1}^3 \alpha_i \mathbf{a}_i$, where $\boldsymbol{\alpha} = (\alpha_1, \alpha_2, \alpha_3)$ is a vector with three components, and \mathbf{a}_i are the basis vectors. The fcc structure can be described in terms of perpendicular basis vectors, such that $\mathbf{a}_i \cdot \mathbf{a}_j = \frac{a^2}{4} \delta_{ij}$, with a the lattice constant of the underlying simple cubic lattice. Second, the excursions of each particle from its equilibrium position are small compared to the nearest neighbor distance. The displacement field from the mean position \mathbf{R}_α is denoted as \mathbf{u}_α , so

that the particle position is $\mathbf{r}_\alpha = \mathbf{R}_\alpha + \mathbf{u}_\alpha$. Assuming pairwise interactions, the total potential energy of the crystal is the sum of the contributions of all distinct pairs:

$$U(\{\mathbf{R}_\alpha\}) = \frac{1}{2} \sum_{\alpha, \beta; \alpha \neq \beta} \phi(\mathbf{r}_\alpha - \mathbf{r}_\beta) \quad (6.14)$$

with $\phi(\mathbf{r}_\alpha - \mathbf{r}_\beta)$ being a pair potential between particles α and β . Inserting $\mathbf{r}_\alpha = \mathbf{R}_\alpha + \mathbf{u}_\alpha$ into Eq.6.14:

$$U(\{\mathbf{R}_\alpha + \mathbf{u}_\alpha\}) = \frac{1}{2} \sum_{\alpha, \beta; \alpha \neq \beta} \phi\left(\mathbf{R}_\alpha - \mathbf{R}_\beta + \mathbf{u}(\mathbf{R}_\alpha) - \mathbf{u}(\mathbf{R}_\beta)\right) \quad (6.15)$$

Assuming the deviation $u(\mathbf{R})$ is not substantial, Eq.6.15 can be expanded using the three-dimensional form of Taylor's theorem:

$$\begin{aligned} U(\{\mathbf{R}_\alpha + \mathbf{u}_\alpha\}) &= \frac{1}{2} N \sum_{\alpha, \beta} \phi(\mathbf{R}_\alpha - \mathbf{R}_\beta) + \frac{1}{2} \sum_{\alpha, \beta} (\mathbf{u}(\mathbf{R}_\alpha) - \mathbf{u}(\mathbf{R}_\beta)) \cdot \nabla \phi(\mathbf{R}_\alpha - \mathbf{R}_\beta) \\ &\quad + \frac{1}{4} \sum_{\alpha, \beta} \left[(\mathbf{u}(\mathbf{R}_\alpha) - \mathbf{u}(\mathbf{R}_\beta)) \cdot \nabla \right]^2 \phi(\mathbf{R}_\alpha - \mathbf{R}_\beta) + O(u^3) \end{aligned} \quad (6.16)$$

where $\sum_{\beta} \nabla \phi(\mathbf{R}_\alpha - \mathbf{R}_\beta)$ describes the minus of the force exerted on particle α by all other particles. As there is no net force exerted on the particles when they are in their equilibrium positions, the second term of Eq.6.16 is zero. As a result, we can rewrite Eq.6.16 in more general forms as [6]:

$$U(\{\mathbf{R}_\alpha + \mathbf{u}_\alpha\}) = U(\{\mathbf{R}_\alpha\}) + \frac{1}{2} \sum_{\alpha, i, \beta, j} A_{ij}^{\alpha\beta} u_i(\mathbf{R}_\alpha) u_j(\mathbf{R}_\beta) \quad (6.17)$$

i, j are the components index, and α, β represent particle at different position. In this expression, $U(\{\mathbf{R}_\alpha\}) = \frac{N}{2} \sum_{\alpha} \phi(\mathbf{R}_\alpha - \mathbf{R}_\beta) = U_{\text{eq}}$. The second term is the harmonic potential energy, U_{harm} . $A_{ij}^{\alpha\beta}$ is derivatives of the potential energy at equilibrium:

$$A_{ij}^{\alpha\beta} = \left. \frac{\partial^2 \phi}{\partial R_i^\alpha \partial R_j^\beta} \right|_{\{\mathbf{R}^\alpha\}} \quad (6.18)$$

and $A_{ij}^{\alpha\beta}$ are the force constants associated to the harmonic interaction between particles.

6.6.1 Force constants

$A_{ij}^{\alpha\beta}$ describes the force acting on the particle at position \mathbf{R}_α in the direction \mathbf{a}_i due to the displacement u_j in the direction \mathbf{a}_j of the particle at position \mathbf{R}_β . There are three symmetries related to $A_{ij}^{\alpha\beta}$. First symmetry: $A_{ij}^{\alpha\beta} = A_{ji}^{\beta\alpha}$, meaning that the order of differentiation does not matter. The potential energy depends only on the relative distance between the particles at \mathbf{R}_α and \mathbf{R}_β . If we set the position \mathbf{R}_α as the origin of the coordinate system, we can write:

$$A_{ij}^{\alpha\beta} = \frac{\partial^2 \phi}{\partial R_i^\alpha \partial R_j^\beta} = \frac{\partial^2 \phi}{\partial R_i^0 \partial R_j^\beta} = A_{ij}^\beta \quad (6.19)$$

As a result, the first symmetry is also expressed as: $A_{ij}^\beta = A_{ji}^\beta$. If the crystal has inversion symmetry, the energy associated with the configuration $R + u(R)$ is the same as the energy of the configuration $R - u(-R)$. As a result, there is a second symmetry that can be stated as: $A_{ij}^\beta = A_{ij}^{-\beta}$. The third symmetry results from $U(\{\mathbf{R}_\alpha + \mathbf{d}\}) = U(\{\mathbf{R}_\alpha\})$, expressing that if every particle on the lattice shifts by the same vector \mathbf{d} , the crystal is displaced without any distortion and therefore, $\sum_\beta A_{ij}^\beta = 0$. We now determine the force constants of the first nearest neighbor of the particle at the origin based on the symmetry of the [110] direction. The lattice has two-fold symmetry about the [110] direction. By rotating the lattice along the [110] direction by 180° , the coordinates transform into $x \rightarrow y$, $y \rightarrow x$, and $z \rightarrow -z$, but the lattice remains unchanged. As the matrix A_{ij}^β is symmetric, all terms in the matrix with one single index z become zero. Therefore, the force constant describing the coupling of the particle at the origin and the particle at the location [110] is determined:

$$A^{(1)} : A^{(110)} = \begin{pmatrix} A_{xx}^{(1)} & A_{xy}^{(1)} & 0 \\ A_{xy}^{(1)} & A_{xx}^{(1)} & 0 \\ 0 & 0 & A_{zz}^{(1)} \end{pmatrix} \quad (6.20)$$

where the notation $A^{(1)}$ indicates the first nearest neighbor, and only three parameters are needed to describe the coupling between them. Additionally, the matrix has an inversion symmetry, $A_{ij}^{(110)} = A_{ij}^{(-1-10)}$. By matrix transformation, we can calculate the force constant matrix of the other ten first nearest neighbors.

Following the same procedure, the force constants of the second neighbors can be determined by rotating the lattice around the [100] axis by 90° , which leaves only

the diagonal terms and z and y are equivalent due to the symmetry:

$$A^{(2)} : A^{(200)} = \begin{pmatrix} A_{xx}^{(2)} & 0 & 0 \\ 0 & A_{yy}^{(2)} & 0 \\ 0 & 0 & A_{yy}^{(2)} \end{pmatrix} \quad (6.21)$$

There are only two parameters needed to describe the force between the second neighbors. For further representation, it is easier to use dimensionless parameters. A_{ij}^α has the dimension of $\frac{\text{Energy}}{\text{Length}^2}$. Therefore, by multiplying with $a^2/k_B T$, we have the dimensionless parameter: $\tilde{A}_{ij}^\alpha = a^2/k_B T A_{ij}^\alpha$.

6.6.2 Lattice vibrations

Considering that particles are connected with a massless spring, the equation of motion is nothing but Newton's second law:

$$M\ddot{u}_i(\mathbf{R}_\alpha) = -\frac{\partial U_{\text{harm}}}{\partial u_i(\mathbf{R}_\alpha)} = -\sum_{\beta,j} A_{ij}^\beta u_j(\mathbf{R}_\beta) \quad (6.22)$$

where M is the mass of particle. For clarity, Eq.6.22 can be written in matrix notation as:

$$M\ddot{\mathbf{u}}(\mathbf{R}_\alpha) = -\sum_{\beta} A^{\alpha\beta} \mathbf{u}(\mathbf{R}_\beta) \quad (6.23)$$

The solution of Eq.6.22 are plane waves: $\mathbf{u}(\mathbf{R}_\alpha, t) = \mathbf{e} \exp[i(\mathbf{q} \cdot \mathbf{R}_\alpha - \omega t)]$, with \mathbf{q} the wave vector in the reciprocal space. \mathbf{e} is the polarization vector of the normal mode and ω is the frequency associated with the mode. By inserting $\mathbf{u}_\alpha(t)$ into Eq.6.22, it is obvious that we find the frequency ω whenever \mathbf{e} is an eigenvector of the eigenvalue problem:

$$\begin{aligned} M\omega(\mathbf{q})^2 \mathbf{e} &= D(\mathbf{q})\mathbf{e} \\ \lambda(\mathbf{q})\mathbf{e} &= D(\mathbf{q})\mathbf{e} \end{aligned} \quad (6.24)$$

where the frequency $\omega(\mathbf{q}) = \sqrt{\lambda(\mathbf{q})/M}$, with $\lambda(\mathbf{q})$ the eigenvalue, and $D_{ij}(\mathbf{q})$ is the dynamic matrix that is defined as:

$$D_{ij}(\mathbf{q}) = \sum_{\alpha} A_{ij}^\alpha \exp(i\mathbf{q} \cdot \mathbf{R}_\alpha) \quad (6.25)$$

There are three solutions to Eq.6.24 associated with each N particles, hence there are $3N$ normal modes. To incorporate the second and the third symmetry of A_{ij}^β introduced before, the dynamic matrix can be written as [7]:

$$\begin{aligned}
D_{ij}(\mathbf{q}) &= \frac{1}{2} \sum_{\alpha} A_{ij}^{\alpha} [\exp(i\mathbf{q} \cdot \mathbf{R}_{\alpha}) + \exp(-i\mathbf{q} \cdot \mathbf{R}_{\alpha}) - 2] \\
&= \sum_{\alpha} A_{ij}^{\alpha} [\cos(\mathbf{q} \cdot \mathbf{R}_{\alpha}) - 1] \\
&= \sum_{\alpha} A_{ij}^{\alpha} \left[\cos^2\left(\frac{\mathbf{q} \cdot \mathbf{R}_{\alpha}}{2}\right) - \sin^2\left(\frac{\mathbf{q} \cdot \mathbf{R}_{\alpha}}{2}\right) - 1 \right] \\
&= -2 \sum_{\alpha} A_{ij}^{\alpha} \sin^2\left(\frac{\mathbf{q} \cdot \mathbf{R}_{\alpha}}{2}\right)
\end{aligned} \tag{6.26}$$

If \mathbf{q} lies in the direction of the 2-, 3-, and 4-fold rotation axis, there is one eigenvector lying on the rotation axis and two eigenvectors perpendicular to it. Eigenvalues for each of these three eigenvectors can be calculated using Eq.6.24, resulting in the dispersion relations of the eigenmodes. The displacement along \mathbf{q} describes the longitudinal mode. The oscillations perpendicular to \mathbf{q} are two transverse modes. At higher symmetry, the two transverse modes have the same eigenvalue and can be degenerate. To derive the eigenvectors and eigenvalues of the dynamic matrix in the [110] direction, we can first rewrite Eq.6.26 as the sum of two neighboring shells $k = 1$ or 2 containing all first neighbors and second neighbors, respectively. Note that the first and second neighbors are used to describe the dispersion relations, because the forces exerted by the third and higher neighbors are weak and not important to our accuracy. By decomposing D_{ij} in the sum of force constants of particles in the two shells, we can write:

$$D_{ij}(\mathbf{q}) = -2 \sum_k \sum_{\alpha_k} A_{ij}^{\alpha_k} \sin^2\left(\frac{\mathbf{q} \cdot \mathbf{R}_{\alpha_k}}{2}\right) \tag{6.27}$$

where α_k indicates the force constant of the particles in shell k . Taking into account the projection of the position vector \mathbf{R}_{α_k} onto the propagation vector \mathbf{q} , we can

write $\tilde{D}_{ij}(q)$ up to the second shell of neighbors as,

$$\begin{aligned} \tilde{D}(q) = & -4\sin^2\left(\frac{a}{2\sqrt{2}}q\right) \begin{pmatrix} \tilde{A}_{xx}^{(1)} + \tilde{A}_{xx}^{(2)} + \tilde{A}_{yy}^{(2)} & \tilde{A}_{xy}^{(1)} & 0 \\ \tilde{A}_{xy}^{(1)} & \tilde{A}_{xx}^{(1)} + \tilde{A}_{xx}^{(2)} + \tilde{A}_{yy}^{(2)} & 0 \\ 0 & 0 & \tilde{A}_{zz}^{(1)} + 2\tilde{A}_{yy}^{(2)} \end{pmatrix} \\ & - 8\sin^2\left(\frac{a}{4\sqrt{2}}q\right) \begin{pmatrix} \tilde{A}_{xx}^{(1)} + \tilde{A}_{zz}^{(1)} & 0 & 0 \\ 0 & \tilde{A}_{xx}^{(1)} + \tilde{A}_{zz}^{(1)} & 0 \\ 0 & 0 & 2\tilde{A}_{xx}^{(1)} \end{pmatrix} \end{aligned} \quad (6.28)$$

After diagonalizing the matrix, we find three eigenvectors $\mathbf{e}_l = \frac{1}{\sqrt{2}}(1, 1, 0)$, $\mathbf{e}_{t_1} = \frac{1}{\sqrt{2}}(-1, 1, 0)$, and $\mathbf{e}_{t_2} = (0, 0, 1)$ and their eigenvalues:

$$\begin{aligned} \tilde{\lambda}_l &= -4\sin^2\left(\frac{a}{2\sqrt{2}}q\right) \left[\tilde{A}_{xx}^{(1)} + \tilde{A}_{xy}^{(1)} + \tilde{A}_{xx}^{(2)} + \tilde{A}_{yy}^{(2)} \right] - 8\sin^2\left(\frac{a}{4\sqrt{2}}q\right) \left[\tilde{A}_{xx}^{(1)} + \tilde{A}_{zz}^{(1)} \right] \\ \tilde{\lambda}_{t_1} &= -4\sin^2\left(\frac{a}{2\sqrt{2}}q\right) \left[\tilde{A}_{xx}^{(1)} - \tilde{A}_{xy}^{(1)} + \tilde{A}_{xx}^{(2)} + \tilde{A}_{yy}^{(2)} \right] - 8\sin^2\left(\frac{a}{4\sqrt{2}}q\right) \left[\tilde{A}_{xx}^{(1)} + \tilde{A}_{zz}^{(1)} \right] \\ \tilde{\lambda}_{t_2} &= -4\sin^2\left(\frac{a}{2\sqrt{2}}q\right) \left[\tilde{A}_{zz}^{(1)} + 2\tilde{A}_{yy}^{(2)} \right] - 8\sin^2\left(\frac{a}{4\sqrt{2}}q\right) \left[2\tilde{A}_{xx}^{(1)} \right] \end{aligned} \quad (6.29)$$

6.7 Measuring the dynamic matrix

So far, the displacement \mathbf{u}_α of the particle with respect to the mean position \mathbf{R}_α is expressed as a function of \mathbf{R} . By the Fourier transform of the displacement field, we obtain the following.

$$\mathbf{u}(\mathbf{q}) = \frac{1}{\sqrt{N}} \sum_{\alpha} \mathbf{u}_\alpha \exp(-i\mathbf{q} \cdot \mathbf{R}_\alpha) \quad (6.30)$$

\mathbf{u}_α can be decomposed into the different displacement modes. Due to hydrodynamic interactions, only modes with large wavelengths are vibrational modes that propagate. As the motions of these modes are much slower than those of the solvent molecules, the hydrodynamic friction is small, and the modes are not damped. Based on Eq.6.17, the harmonic potential energy U_{harm} due to particle displacement is $U(\{\mathbf{R}_\alpha + \mathbf{u}_\alpha\}) - U_{\text{eq}}$. In reciprocal space, U_{harm} is defined as:

$$U_{\text{harm}} = \frac{1}{2} \sum_{\mathbf{q} \in \text{1st.BZ}} \sum_{i,j} u_i(\mathbf{q}) D_{ij}(\mathbf{q}) u_j^*(\mathbf{q}) \quad (6.31)$$

This describes the potential energy in terms of normal modes (plane waves) instead of the displacement $\mathbf{u}_\alpha(\{\mathbf{R}_\alpha\})$. Due to the periodicity of the crystal, \mathbf{q} -vectors are chosen within the 1st Brillouin-Zone to yield distinct solutions. Considering that the deviation u_α is small compared to the distance between the particles and that the system is in the classical regime, the equipartition theorem holds. The energy of each mode is $k_B T/2$, and then:

$$D_{ij}(\mathbf{q})\langle u_i(\mathbf{q})u_j^*(\mathbf{q}) \rangle = k_B T \quad (6.32)$$

where the bracket represents the ensemble average over all particle configurations. As shown in Eq.6.32, calculating $\langle u_i(\mathbf{q})u_j^*(\mathbf{q}) \rangle$ enables determining the dynamic matrix $D_{ij}(\mathbf{q})$. As $D_{ij}(\mathbf{q})$ is real and symmetric, it can be diagonalized and the eigenvectors \mathbf{e}_p are mutually orthogonal. Therefore, the eigenvalues of the dynamic matrix associated to each of the $p \in \{l, t_1, t_2\}$ eigenvectors are:

$$\lambda_p(\mathbf{q}) = \frac{k_B T}{\langle |u_p(\mathbf{q})|^2 \rangle} \quad (6.33)$$

where the deviation field of the mode with eigenvector \mathbf{e}_p is written as:

$$u_p(\mathbf{q}) = \frac{1}{\sqrt{N}} \sum_{\alpha} [\mathbf{u}_\alpha \cdot \mathbf{e}_p] \exp(-i\mathbf{q} \cdot \mathbf{R}_\alpha) \quad (6.34)$$

Eq.6.33 and Eq. 6.34 illustrate how to relate the measurable particle deviations from their mean value to the eigenvalues of the dynamic matrix via the equipartition theorem. As shown in Eq.6.24, the frequency of each mode is $\omega_p = \sqrt{\lambda_p(\mathbf{q})/M}$. Since $\lambda_p(\mathbf{q})$ is a function of force constants A_{ij}^α , as shown in Eq.6.29, we can then extract the force constants from the dispersion relation.

6.7.1 Displacement modes with polarization perpendicular to the scan direction

The scanning along the optical axis \mathbf{z} of the microscope has the lowest pixel resolution; as a result, generally, only displacement modes perpendicular to \mathbf{z} are considered. Due to the periodicity of the lattice, the reference lattice sites $\{\mathbf{R}_\alpha\}$ can be obtained by averaging the positions of the particles obtained from the measurement and the dynamic matrix can be determined using only displacements $u_p(\{\mathbf{R}\})$ in the x and y directions. For simplicity, the miller index of the simple cubic lattice is used for future descriptions. On a flat surface, a hexagonal plane begins to grow on the

surface of the capillary wall perpendicular to the scanning direction and is followed by further hexagonal planes with fcc or hcp stacking. As the scanning direction \mathbf{z} is parallel to the [111] direction, the hexagonal plane (111) can be imaged directly with high resolution. Although we can only use particle deviations in the hexagonal plane perpendicular to the optical axis, the choice of \mathbf{q} -vector is arbitrary, and includes the \mathbf{z} direction.

For the [110] direction, the longitudinal mode is along the direction with the eigenvector $\mathbf{e}_l = \frac{1}{\sqrt{2}}(1, 1, 0)$. The two transverse modes are perpendicular to the longitudinal mode: $\mathbf{e}_{t_1} = \frac{1}{\sqrt{2}}(-1, 1, 0)$ and $\mathbf{e}_{t_2} = (0, 0, 1)$. The eigenvalue of the longitudinal mode $\lambda_l^{110}(\mathbf{q})$, is obtained using Eq.6.29. Only one transverse mode t_1 is on the [111] plane and can be measured directly. However, the projection of transverse modes t_1 and t_2 propagating along $\mathbf{e}_s = \frac{1}{\sqrt{6}}(-1, 1, 2)$ can be directly measured. This unit vector \mathbf{e}_s can be represented in terms of \mathbf{e}_{t_1} and \mathbf{e}_{t_2} :

$$\mathbf{e}_s = \frac{1}{\sqrt{3}}\mathbf{e}_{t_1} + \frac{2}{\sqrt{6}}\mathbf{e}_{t_2} \quad (6.35)$$

The Fourier component $|u_p(\mathbf{q})|^2$ is then:

$$\begin{aligned} |u_s(\mathbf{q})|^2 &= \left| \frac{1}{\sqrt{3}}e_{t_1}u_{t_1}(\mathbf{q}) + \frac{2}{\sqrt{6}}e_{t_2}u_{t_2}(\mathbf{q}) \right|^2 \\ &= \frac{1}{3}|u_{t_1}|^2 + \frac{2}{3}|u_{t_2}|^2 \end{aligned} \quad (6.36)$$

By the equipartition theorem, we can calculate the eigenvalue of the $u_s(\mathbf{q})$ following Eq.6.33:

$$\tilde{\lambda}_s(\mathbf{q}) = \frac{k_B T}{\langle |u_s(\mathbf{q})|^2 \rangle} = \frac{3\tilde{\lambda}_{t_1}(\mathbf{q})\tilde{\lambda}_{t_2}(\mathbf{q})}{2\tilde{\lambda}_{t_1}(\mathbf{q}) + \tilde{\lambda}_{t_2}(\mathbf{q})} \quad (6.37)$$

where the expressions of $\tilde{\lambda}_{t_1}(\mathbf{q})$ and $\tilde{\lambda}_{t_2}(\mathbf{q})$ were introduced in Eq.6.29.

For \mathbf{q} in the [001] direction, an axis with four-fold rotational order, the longitudinal mode is in the direction $\mathbf{e}_l = (0, 0, 1)$ and the two transverse modes are in the $\mathbf{e}_{t_1} = (1, 0, 0)$ and $\mathbf{e}_{t_2} = (0, 1, 0)$ directions. Due to the 4-fold symmetry in this direction, the two transverse modes are degenerate, and the dispersion relation of modes with polarization perpendicular to \mathbf{e}_l is written as:

$$\tilde{\lambda}_t^{100}(q) = -4\sin^2\left(\frac{aq}{2}\right)\tilde{A}_{yy}^{(2)} - 8\sin^2\left(\frac{aq}{4}\right)\left[\tilde{A}_{xx}^{(1)} + \tilde{A}_{zz}^{(1)}\right] \quad (6.38)$$

Since the longitudinal mode is not in the $[111]$ plane, its direct measurement is not feasible. However, due to crystal symmetry, the mixed mode containing projections of the longitudinal and the two transverse modes can be measured in the direction $\mathbf{e}_m = \frac{1}{\sqrt{6}}(1, 1, 2)$, which can be written as:

$$\mathbf{e}_m = \frac{1}{\sqrt{6}}(2\mathbf{e}_l + \mathbf{e}_{t_1} + \mathbf{e}_{t_2}) \quad (6.39)$$

Following Eq.6.37, we can calculate the dispersion relation:

$$\tilde{\lambda}_m^{100}(q) = 3 \frac{\tilde{\lambda}_l^{100} \tilde{\lambda}_t^{100}}{2\tilde{\lambda}_t^{100} + \tilde{\lambda}_l^{100}} \quad (6.40)$$

where

$$\tilde{\lambda}_l^{100}(q) = -16\tilde{A}_{xx}^{(1)} \sin^2\left(\frac{qa}{4}\right) - 4\tilde{A}_{xx}^{(2)} \sin^2\left(\frac{qa}{2}\right) \quad (6.41)$$

is the eigenvalue of the longitudinal mode. For modes along direction $[-1 - 11]$, the eigenvector of the longitudinal mode is $\mathbf{e}_l = \frac{1}{\sqrt{3}}(-1, -1, 1)$ and the two transverse modes are in the directions: $\mathbf{e}_{t_1} = \frac{1}{\sqrt{2}}(-1, 1, 0)$ and $\mathbf{e}_{t_2} = \frac{1}{\sqrt{6}}(1, 1, 2)$. As the $[111]$ axis is a three-fold rotation axis, the two transverse modes are degenerate and perpendicular to $[111]$, and can be measured directly. They are given by eigenvalue:

$$\tilde{\lambda}_t^{111}(q) = -4 \left[2\tilde{A}_{xx}^{(1)} + \tilde{A}_{zz}^{(1)} - \tilde{A}_{xy}^{(1)} + \tilde{A}_{xx}^{(2)} + 2\tilde{A}_{yy}^{(2)} \right] \sin^2\left(\frac{aq}{2\sqrt{3}}\right) \quad (6.42)$$

Since the longitudinal mode \mathbf{e}_l is parallel to $[-1 - 11]$, an indirect measurement is necessary: a mix of longitudinal and a transverse mode in the direction $\mathbf{e}_m = \frac{1}{\sqrt{6}}(-1, -1, 2)$, which is perpendicular to $[111]$, can be measured directly. \mathbf{e}_m is a mixture of longitudinal and transverse modes

$$\mathbf{e}_m = \frac{2\sqrt{2}}{3}e_l + \frac{1}{3}e_{t_2} \quad (6.43)$$

and has associated eigenvalue

$$\tilde{\lambda}_s^{111}(q) = \frac{9\tilde{\lambda}_l^{111}(q)\tilde{\lambda}_t^{111}(q)}{8\tilde{\lambda}_t^{111}(q) + \tilde{\lambda}_l^{111}(q)} \quad (6.44)$$

where

$$\tilde{\lambda}_l^{111}(q) = -4 \left[2\tilde{A}_{xx}^{(1)} + \tilde{A}_{zz}^{(1)} + 2\tilde{A}_{xy}^{(1)} + \tilde{A}_{xx}^{(2)} + 2\tilde{A}_{yy}^{(2)} \right] \sin^2 \left(\frac{aq}{2\sqrt{3}} \right) \quad (6.45)$$

Importantly, if the interparticle force is central in nature, the force constants must satisfy:

$$\Gamma = \frac{\tilde{A}_{xy}^{(1)}}{(\tilde{A}_{xx}^{(1)} - \tilde{A}_{zz}^{(1)})} = 1 \quad (6.46)$$

where Γ is a ratio we can calculate from fitting the dispersion relation obtained experimentally. This is a direct method to test for non-central interactions, which is something that is not easily assessed with other methods [22, 23, 144]. The value of Γ will be the main result of this study.

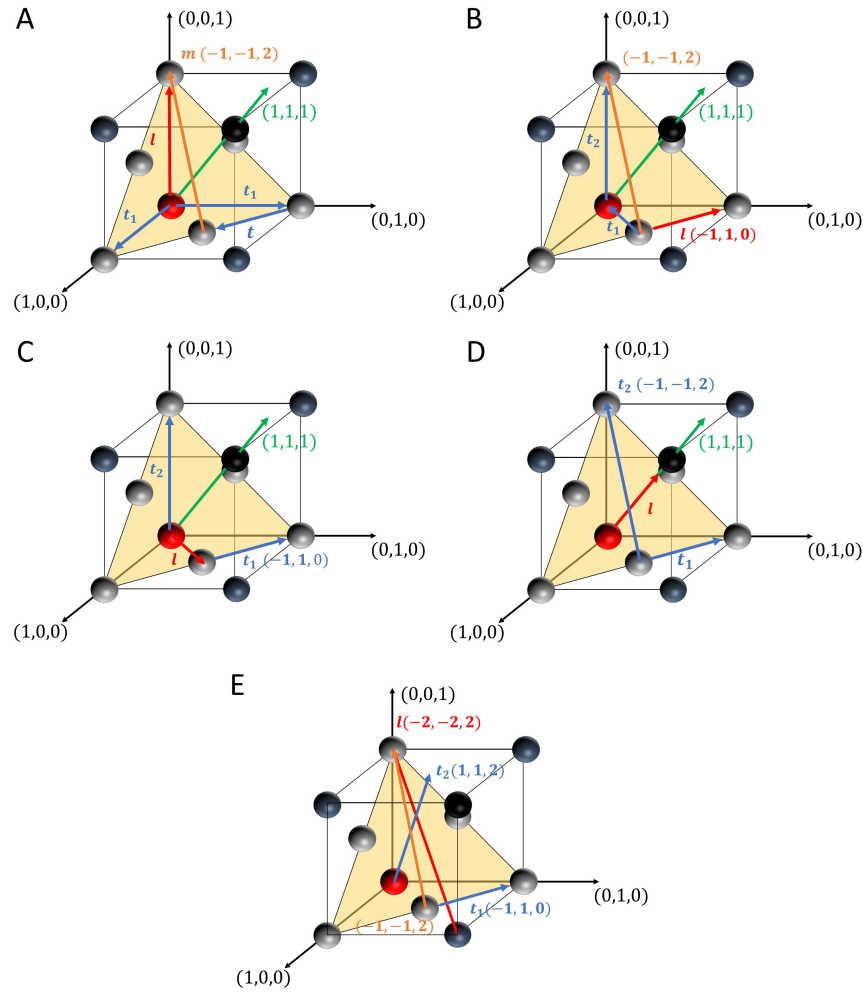


Figure 6.10: Polarization vectors of selected wave vector q . The scanning direction is $[111]$ and the plane (111) (yellow) can be measured directly. The modes are drawn in such a way that they are all in the (111) plane. A: $q = (0, 0, 1)$: longitudinal mode (red) and two transverse modes (t_1 and t_2) (blue). The mixed mode m along $(-1, -1, 2)$ can be measured. The degenerate mode t along $(1, -1, 0)$ can be measured in any direction perpendicular to the q -direction. B: $q = (-1, 1, 0)$: the longitudinal mode l can be measured directly. The projection of modes t_1 and t_2 along $(-1, -1, 2)$ can be measured directly. C: $q = (1, 1, 0)$: The translation mode t_1 can be measured directly. D: $q = (1, 1, 1)$: the two transverse modes are degenerate and can be measured directly. E: $q = (-1, 1, 1)$: the mixed mode m along $(-1, 1, 2)$ or equivalent directions can be measured.

6.7.2 Measurement of the eigenvalues of the dynamic matrix

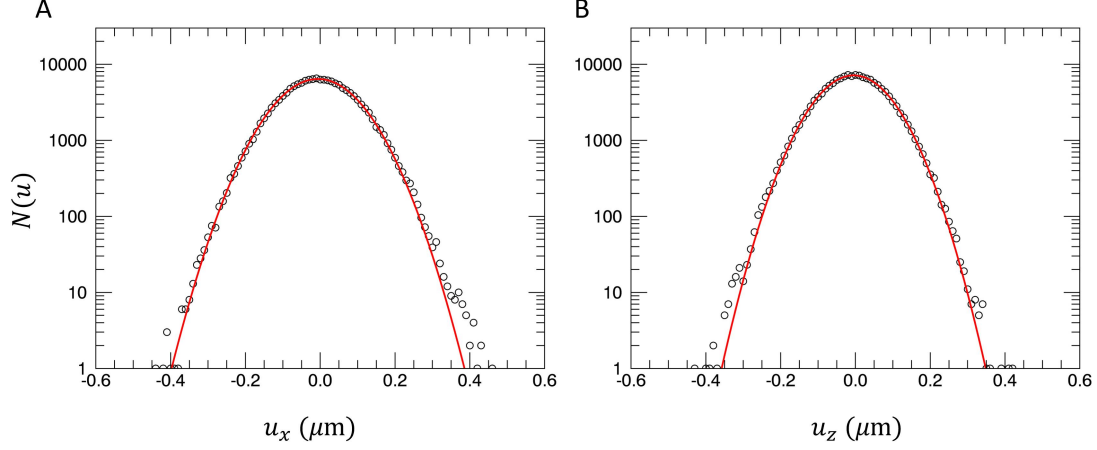


Figure 6.11: Particle deviation u in the x and z direction.(black circle) Fitted curve with Gaussian distribution. (Red line) The deviations satisfy the Gaussian distribution, meaning the harmonic approximation is applicable.

To determine the $\tilde{\lambda}_t^{110}$, $\tilde{\lambda}_s^{110}$, $\tilde{\lambda}_{t1}^{110}$, $\tilde{\lambda}_t^{100}$, $\tilde{\lambda}_m^{100}$, $\tilde{\lambda}_m^{111}$, and, $\tilde{\lambda}_t^{111}$ introduced in Sec. 6.7.1, a sequence of snapshot of fcc crystal is taken. The drift-corrected images are obtained by subtracting the average displacement between frames, considering that the average displacement is zero for a crystal in equilibrium. The extraction of the modes comes in three steps: First, from drift-corrected configurations, we can extract the displacement field of particle α , $\{\mathbf{u}^\alpha(t)\}$ by subtracting the center of gravity of the trajectory of the particle, given by \mathbf{R}_α , from the current location of the particle at time t , $\mathbf{r}_\alpha(t)$:

$$\mathbf{u}_\alpha(t) = \mathbf{r}_\alpha(t) - \mathbf{R}_\alpha \quad (6.47)$$

Second, according to Eq.6.34, the displacement field is calculated with \mathbf{q} and $\hat{\mathbf{p}}$ in conventional coordinate systems:

$$u_p(\mathbf{q}, t) = \frac{1}{\sqrt{N}} \sum_{\alpha} [\mathbf{u}_\alpha \cdot \hat{\mathbf{p}}] \exp\left(-iq[\hat{\mathbf{q}} \cdot \mathbf{R}_\alpha]\right) \quad (6.48)$$

where N is the number of lattice sites in the selected crystalline region. The wavelength of mode propagation is related to the size of the crystal L , and the smallest q for which the modes can be measured is given by the size L of the observed crystal: $q_{\min} = 2\pi/L$. The size of the crystal L is determined by calculating how many

lattice planes M are perpendicular to the wavevector \mathbf{q} . Suppose that the lattice spacing is d , then $L = Md$. Due to the periodicity of the crystal, the choice of wave vector q should be the integer multiple of q_{\min} . Lastly, the eigenvalues of the modes can be obtained following Eq.6.33.

6.8 Lattice Elasticity

In this section, we discuss the elasticity of the crystals and deformations with scales much larger than the lattice constant. The position of small volume elements in the initial configuration in the nondeformed state is denoted as \mathbf{R} . After deformation, the position in the final configuration is denoted as \mathbf{r} . The deformation can be measured with both transformation coefficients α_{ij} and the displacement gradients u_{ij} as,

$$\begin{aligned}\alpha_{ij} &= \frac{\partial r_i}{\partial R_j} \\ u_{ij} &= \frac{\partial u_i}{\partial R_j}\end{aligned}\tag{6.49}$$

where $u_i = r_i - R_i$. By substituting u_i into Eq.6.49, the two deformation parameters can be related as:

$$\alpha_{ij} = \delta_{ij} + u_{ij}\tag{6.50}$$

The deformation field is represented by the Lagrangian strain tensor η_{ij} :

$$\eta_{ij} = \frac{1}{2}(\alpha_{ki}\alpha_{kj} - \delta_{ij}) = \frac{1}{2}(u_{ij} + u_{ji} + u_{ki}u_{kj})\tag{6.51}$$

where η_{ij} follow the Einstein summation convention. Note that η_{ij} is symmetric, if Δr and ΔR are the distances between a pair of nearby particles in the final and initial configurations, respectively, the strain in the initial configuration is homogeneous and η_{ij} is constant for all pairs of particles with separation ΔR , we can then write:

$$|\Delta r|^2 = |\Delta R|^2 + 2\eta_{ij}\Delta R_i\Delta R_j\tag{6.52}$$

Additionally, if η_{ij} only varies over distances much larger than the range of the interactions within the material, we can represent the Helmholtz free energy F

through $\{\mathbf{R}\}$, η_{ij} , and T :

$$F = F(\{\mathbf{r}\}, T) = F(\{\mathbf{R}\}, \eta_{ij}, T) \quad (6.53)$$

For small distortions, we can expand F around the undeformed state. We then have:

$$\rho_1 F(\{\mathbf{R}\}, \eta_{ij}, T) = \rho_1 F(\{\mathbf{R}\}, 0, T) + C_{ij} \eta_{ij} + \frac{1}{2} C_{ijkl} \eta_{ij} \eta_{kl} \quad (6.54)$$

where $\rho_1 = \rho(\mathbf{R})$ is the material density in the undistorted state. The coefficients C_{ij} and C_{ijkl} are partial derivatives of the free energy of the material in configuration $\{\mathbf{R}\}$:

$$\begin{aligned} C_{ij} &= \rho \left(\frac{\partial F}{\partial \eta_{ij}} \right) = T_{ij}(\mathbf{R}) \\ C_{ijkl} &= \rho \left(\frac{\partial^2 F}{\partial \eta_{ij} \partial \eta_{kl}} \right) \end{aligned} \quad (6.55)$$

where $T_{ij}(\mathbf{R})$ is the stress tensor in configuration $\{\mathbf{R}\}$. The C_{ijkl} are second-order isothermal elastic constants; They have complete Voigt symmetry, implying index pairs ij and kl can be interchanged. As a result, $C_{ijkl} = C_{ijlk} = C_{jikl} = \dots$, and it is convenient to use the Greek letter α to represent the pair of ij :

$$\begin{aligned} ij &= 11 \quad 22 \quad 33 \quad 32 \text{ or } 23 \quad 31 \text{ or } 13 \quad 21 \text{ or } 12 \\ \alpha &= 1 \quad 2 \quad 3 \quad 4 \quad 5 \quad 6 \end{aligned} \quad (6.56)$$

In the following sections, we express the elastic constants with the Voigt notation: $C_{\alpha\beta} = C_{\beta\alpha}$. Realize that the $C_{\alpha\beta}$ are the components of a rank-four tensor, with $3^4 = 81$ components in 3D, but that of using Voigt notation reduces to the 6×6 matrix with 21 independent components, each of them related to definitions of Young's modulus and Poisson's ratio. Depending on the symmetry of the material, the number of independent elements in $C_{\alpha\beta}$ can be further reduced.

6.8.1 Wave propagation

We use the Einstein summation convention. Newton's second law applied to material particles in a continuous medium and in the absence of body forces can be expressed

as:

$$\rho \ddot{r}_i = \frac{\partial T_{ij}}{\partial r_j} \quad (6.57)$$

Eq.6.57 is based on distorted state \mathbf{r} and ρ . We can express the stress tensor components T_{ij} in terms of initial configuration variables \mathbf{R} and ρ_1 , as [190]:

$$\begin{aligned} \rho \ddot{r}_i &= [C_{jl}\delta_{ik} + C_{ijkl}] \frac{\partial^2 r_k}{\partial R_j \partial R_l} \\ &= A_{ijkl} \frac{\partial^2 r_k}{\partial R_j \partial R_l} \end{aligned} \quad (6.58)$$

where A_{ijkl} are the wave propagation coefficients. They relate to the elastic constants:

$$A_{ijkl} = T_{jl}\delta_{ik} + C_{ijkl} \quad (6.59)$$

As shown in Eq.6.22, the solution of the equation of motion is a plane wave:

$$\mathbf{r} - \mathbf{R} = \mathbf{e} \exp[i(\mathbf{q} \cdot \mathbf{R} - \omega t)] \quad (6.60)$$

By inserting Eq.6.60 into Eq.6.58, we can write:

$$\begin{aligned} \rho_1 (\omega/q)^2 e_i &= A_{ijkl} \hat{q}_j \hat{q}_l e_k \\ &= L_{ik} e_k \end{aligned} \quad (6.61)$$

where $\hat{\mathbf{q}} = \mathbf{q}/|\mathbf{q}|$. L are the components of a 3×3 matrix that is independent of the magnitude $|\mathbf{q}|$ but that depends on the direction of \mathbf{q} . Based on the symmetry properties of A_{ijkl} , see Eq.6.59, L_{ik} are components of a symmetric matrix, which has three eigenvectors and its eigenvalues are real and positive. For \mathbf{q} along the direction of high crystalline symmetry such as 2-, 3-, and 4 - fold rotational symmetry, there are eigenvectors associated with the pure longitudinal mode l and two pure transverse modes t_1 and t_2 . This is the case when there is one atom per unit cell; more modes are present for multi-particle cells. We can in general express dispersion relations as:

$$\omega(q) = v_p q, \quad \text{where } p = \{(l, t_1, t_2)\} \quad (6.62)$$

where v_p is the speed for mode with polarization p . Note that there is no dispersion of the modes, as v_p is constant. Note also that this linear relation is only valid in the long-wavelength limit, where the displacements can be seen as sound waves of an elastic continuum. Conversely, in the short wavelength limit, the microscopic definition of elastic constants are connected to the force constants, as discussed in previous sections in connection to the harmonic approximation and lattice vibrations.

6.8.2 Strain and stress relation

The strain and stress relation in the linear regime is generally written as:

$$T_{ij} = B_{ijkl}\eta_{kl} \quad (6.63)$$

For small deformations, η_{kl} and the rotation gradients ω_{kl} are:

$$\begin{aligned} \eta_{kl} &= \frac{1}{2}(u_{kl} + u_{lk}) = \frac{1}{2}(\alpha_{kl} + \alpha_{lk} - 2\delta_{kl}) \\ \omega_{kl} &= \frac{1}{2}(u_{kl} - u_{lk}) = \frac{1}{2}(\alpha_{kl} - \alpha_{lk}) \end{aligned} \quad (6.64)$$

They correspond to the symmetric and antisymmetric parts of $\nabla \mathbf{u}$. Solving for α_{kl} , we have:

$$\begin{aligned} \alpha_{kl} &= \frac{1}{2}(\eta_{kl} + \eta_{lk} + \omega_{kl} - \omega_{lk} + 2\delta_{kl}) \\ \frac{\partial \alpha_{kl}}{\partial \eta_{nm}} &= \frac{1}{2}(\delta_{km}\delta_{ln} + \delta_{lm}\delta_{kn}) \\ \frac{\partial \alpha_{kl}}{\partial \omega_{nm}} &= \frac{1}{2}(\delta_{km}\delta_{ln} - \delta_{lm}\delta_{kn}) \end{aligned} \quad (6.65)$$

Following the derivation in [190], we then have:

$$B_{ijkl} = \frac{\partial T_{ij}}{\partial \eta_{kl}} = \frac{1}{2}(T_{ik}\delta_{jl} + T_{il}\delta_{jk} + T_{jk}\delta_{il} + T_{jl}\delta_{ik} - 2T_{ij}\delta_{kl}) + C_{ijkl} \quad (6.66)$$

6.8.3 Isotropic initial pressure

With an initial isotropic pressure, the stress can be written as:

$$T_{ij}(\mathbf{R}) = -P\delta_{ij} \quad (6.67)$$

Eq.6.59 and Eq.6.66 can be expressed as:

$$\begin{aligned} A_{ijkl} &= -P\delta_{jl}\delta_{ik} + C_{ijkl} \\ B_{ijkl} &= -P(\delta_{jl}\delta_{ik} + \delta_{il}\delta_{jk} - \delta_{ij}\delta_{kl}) + C_{ijkl} \end{aligned} \quad (6.68)$$

where A_{ijkl} does not have the complete Voigt symmetry, unless $P = 0$. According to Eq.6.61, the propagation matrix $L_{ik} = A_{ijkl}\hat{q}_j\hat{q}_l$, where we sum on j and l , contains the combination $(A_{ijkl} + A_{ilkj})$, which is the same as the corresponding combination in B_{ijkl} . Thus,

$$A_{ijkl} + A_{ilkj} = B_{ijkl} + B_{ilkj} \quad (6.69)$$

In our experiment, the crystal is an fcc. Due to the cubic symmetry, there are only three independent components in the elasticity tensor C_{ijkl} [7]:

$$\begin{aligned} C_{11} &= C_{1111} = C_{2222} = C_{3333} \\ C_{12} &= C_{1122} = C_{1133} = C_{2233} \\ C_{44} &= C_{1212} = C_{1313} = C_{2323} \end{aligned} \quad (6.70)$$

Following Eq.6.69, we can express B_{ijkl} in terms of C_{ijkl} using the Voigt notation as:

$$\begin{aligned} B_{11} &= C_{11} - P \\ B_{12} &= C_{12} + P \\ B_{44} &= C_{44} - P \end{aligned} \quad (6.71)$$

The bulk modulus K of the crystal can be determined by compressing or dilating the materials such that the deformation is $\eta_{kl}^K = 1/3 \sum_i \eta_{ii}\delta_{kl}$ and the volume change is $\frac{\Delta V}{V} = \sum_i \eta_{ii}$. With Hook's law, Eq.6.63, and having an initial isotropic pressure applied to the material, we obtain:

$$\begin{aligned} -\Delta P\delta_{ij} &= B_{ijkl}\eta_{kl}^K \\ &= (B_{11} + 2B_{12})\eta_{kl}^K \end{aligned} \quad (6.72)$$

Taking the trace, we obtain $-3P = (B_{11} + 2B_{12})\frac{\Delta V}{V}$, from which, we obtain the compressibility κ and bulk modulus K at constant T:

$$\begin{aligned}\kappa_T &= \frac{1}{V} \left(\frac{\partial V}{\partial P} \right)_T = \frac{3}{B_{11} + 2B_{12}} \\ K &= \frac{1}{\kappa_T} = \frac{B_{11} + 2B_{12}}{3} = \frac{C_{11} + 2C_{12} + P}{3}\end{aligned}\quad (6.73)$$

6.8.4 Elastic constants

As we have discussed in Section 6.8.1, in the long wavelength limit, Eq.6.24 should transform into the eigenvalue equation for the sound wave:

$$\frac{1}{V_0} \lim_{q \rightarrow 0} \frac{k_B T}{a^2} \frac{\tilde{D}_{ij}}{q^2} = L_{ij} \quad (6.74)$$

where $V_0 = mN/\rho$ is the volume of the crystal. L_{ik} in the [110] direction with $\tilde{q} = \frac{1}{\sqrt{2}}[110]$ is

$$\begin{aligned}L &= \frac{1}{2} \begin{pmatrix} A_{1111} + A_{1212} & A_{2211} + A_{2112} & 0 \\ A_{2211} + A_{2112} & A_{1111} + A_{1212} & 0 \\ 0 & 0 & A_{3131} + A_{3232} \end{pmatrix} \\ &= \frac{1}{2} \begin{pmatrix} B_{11} + B_{44} & B_{12} + B_{44} & 0 \\ B_{12} + B_{44} & B_{11} + B_{44} & 0 \\ 0 & 0 & 2B_{44} \end{pmatrix}\end{aligned}\quad (6.75)$$

With the definition of L_{ij} and the dynamic matrix D_{ij} in the direction $\frac{1}{\sqrt{2}}[110]$ in Eq.6.75 and Eq.6.29, we can write the coefficients as:

$$\begin{aligned}\frac{v_0}{k_B T} B_{11} &= b_{11} = -[\tilde{A}_{xx}^{(1)} + \tilde{A}_{xx}^{(2)}] \\ \frac{v_0}{k_B T} B_{12} &= b_{12} = -\frac{1}{2}[2\tilde{A}_{xy}^{(1)} + \tilde{A}_{xx}^{(1)} + \tilde{A}_{zz}^{(1)} - 2\tilde{A}_{yy}^{(2)}] \\ \frac{v_0}{k_B T} B_{44} &= b_{44} = -\frac{1}{2}[\tilde{A}_{xx}^{(1)} + \tilde{A}_{zz}^{(1)} + 2\tilde{A}_{yy}^{(2)}]\end{aligned}\quad (6.76)$$

With the known force constants, we can then calculate the elastic constants. If the force is central, the force constants and the elastic constants follow the Cauchy

relation: $C_{12} = C_{44}$ [109], which implies that:

$$\begin{aligned} B_{12} &= B_{44} + 2P \\ b_{12} &= b_{44} + 2P \end{aligned} \tag{6.77}$$

6.9 Results and discussion

In this chapter, the normal modes of the microgel crystals are investigated, where the force constants and bulk modulus of the microgel crystals are obtained by fitting the dispersion relations to the dynamic matrix. In total, we investigate three samples: s1, s2, and s3; sample details are summarized in Table 6.1. Sample s1 is prepared at $\text{pH} = 6.9 \pm 0.2$ and $\zeta = 1.6 \pm 0.2$. Sample s2 is prepared by diluting sample s1 by 10% at $\text{pH} = 7.0 \pm 0.2$ and $\zeta = 1.4 \pm 0.2$. Lastly, sample s3 is prepared at $\text{pH} = 3.5 \pm 0.05$ and $\zeta = 1.6 \pm 0.2$. The microgel size should be determined directly from the microscopy data, as the size depends on the concentration and temperature of the sample. However, since the microgel contains only a fluorescent core and the particle boundary is difficult to locate, the true volume fraction ϕ for all samples is hard to determine. However, based on particle tracking and deviation from the mean, samples are below the random close packing density, ϕ_{rcp} , and the microgels are not jammed. The isoelectric point is around $\text{pH} \sim 4.4$, samples s1 and s2 are charged and swollen. Sample s3 at $\text{pH} \sim 3.5$ consists of microgels that are less charged and are smaller. Indicated by the lattice constant of the crystal, the interparticle spacing is around $2 \mu\text{m}$ for all the samples, suggesting that the true volume fractions are relatively close to each other. When inspecting the particle trajectories, there is no sign showing directional preference, and the particles are free to deviate from their lattice position in all directions within their lattice site, as shown in Fig.6.7. This indicates that there is no direct interaction between the microgels and their polymer networks do not get in contact, suggesting that the microgels have spontaneously deswellen due to the osmotic pressure exerted by the outside ions. Following Eq.6.47, we obtain the particle displacements, as illustrated in Fig.6.11. The deviation in the x -, y -, and z - directions can all be described by Gaussian distributions, which means that the harmonic approximation is applicable for the potential energy, and that equipartition can be used to approximate the energy associated with the degrees of freedom of the crystal lattice (the normal modes). In Section 6.7.1, we demonstrate that the polarization \mathbf{p} and the wave vector \mathbf{q} of the normal modes can be chosen such that all modes can be measured without using the deviation \mathbf{u}_z in z direction, along the optical axis of the microscope.

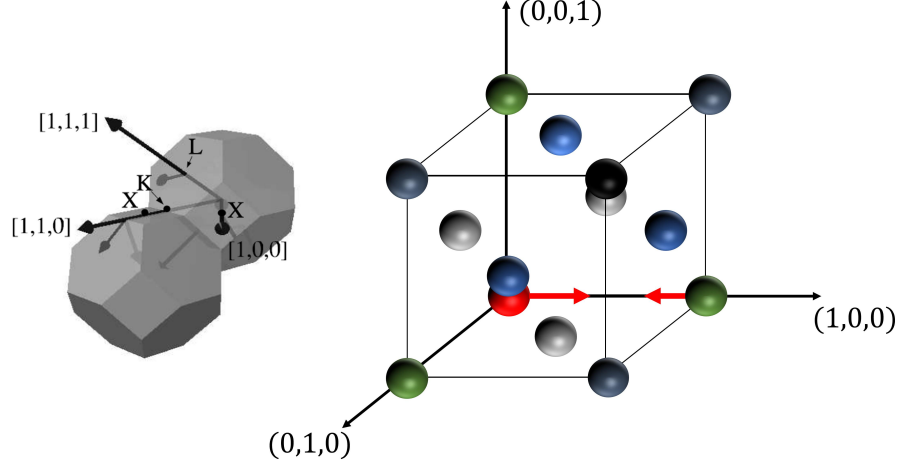


Figure 6.12: (Left) The schematic of Brillouin zones of a fcc crystal taken from [139]. Γ is the center of the zone. K , X , and L denote the edge of the zone in the direction of high symmetry. (Right) The schematic of a fcc crystal in the conventional coordinate system. Gray, green, and blue represent the 1st, 2nd, and 3rd neighbors with respect to the red ball at the origin. The arrows indicate the displacement between the red ball with its 2nd neighbor in the x -direction.

Following Eq.6.33, we can use the displacement field $\mathbf{u}_\alpha(t)$ to calculate the dispersion relation for the longitudinal modes $\tilde{\lambda}_l^{110}$, the transverse modes $\tilde{\lambda}_{t_1}^{110}$, $\tilde{\lambda}_s^{110}$, $\tilde{\lambda}_t^{100}$, $\tilde{\lambda}_t^{111}$, and the mixed modes $\tilde{\lambda}_m^{100}$ and $\tilde{\lambda}_m^{111}$. The superscript 110, 100, and 111 give the propagation direction (q direction). Dispersion relations of all three samples are summarized in Fig.6.13, Fig.6.14, and Fig.6.15. The dispersion relations of three equivalent directions are plotted together (black lines) for [110], [100], and [111] directions, and the average is calculated, as shown by the red line in panel A-D of Fig.6.13, Fig.6.14, and Fig.6.15. Note that q of the direction [110] follows the direction in the Brillouin zone: Γ , K , X , K , Γ . q of the direction [100] follows the direction: Γ , X , Γ and q of the direction [111] follows the direction: Γ , L , Γ . These directions are shown in Fig.6.12 (Left)

In total, there are five fitting parameters for all cases, [110], [100], and [111]. Three of them are the force constants of the 1st neighbors: $\tilde{A}_{xx}^{(1)}$, $\tilde{A}_{xy}^{(1)}$, and $\tilde{A}_{zz}^{(1)}$. The other two are the force constants of the 2nd neighbors: $\tilde{A}_{xx}^{(2)}$ and $\tilde{A}_{yy}^{(2)}$. We can fit the dispersion relations of different modes to the eigenvalues $\lambda(\mathbf{q})$, functions of force constants, introduced in Sec.6.7.1 to obtain the force constants results.

With this, we fit the averaged dispersion relation, the red curves in panels A-D, as illustrated in Fig.6.13E, where the dispersion relations within the 1st Brillouin zone are plotted sequentially following the order [110], [100], and [111]. The fitting results are summarized in Table 6.1, the errors were calculated based on several measurements of the same volume fraction ζ . Based on Eq.6.46, we obtain $\Gamma < 1.0$ for all measurements, where Γ is a ratio between force constants, which is known for central interactions. This indicates that the interaction force is noncentral and incompatible with the behavior expected for a radially symmetric pairwise central interaction. Furthermore, $\tilde{A}_{xx}^{(2)} \approx -1/2\tilde{A}_{xx}^{(1)}$ for sample s1 and sample s2, which means that the movement of the particle at $(0,0,0)$ in the direction of $(1,0,0)$ attracts the second nearest neighbor at $(a,0,0)$, where a is the lattice constant, as shown in Fig.6.12 (right). $\tilde{A}_{xx}^{(2)} \approx -1/3\tilde{A}_{xx}^{(1)}$ for sample s3, indicating that the first neighbor exerts less force in a suspension where the microgels are more deswollen at lower pH. Note that the shape of the dispersion relations remains the same for samples s1, s2, and s3. However, the magnitude of the modes for sample s1 is larger than that of s2 and s3, due to the fact that the suspension is more dilute for s2, and the microgels are more deswollen in sample s3, all leading to the fact that the microgel-microgel interaction is not as strong as that of sample s1.

In addition, the same normal mode analysis is performed with an fcc crystal obtained from a Monte Carlo simulation, consisting of 8788 neutral hard spheres with volume fraction $\phi = 0.55$. Interestingly, the magnitude of the t mode in the [111] direction is half that of the t mode in the [100] direction, and the magnitude of the s mode in the [110] direction and the m modes in [100] is smaller than that of the l mode in the [110] direction, as shown in Fig.6.16E. Although the magnitude of the force constants of the simulated fcc crystal is on the same order as that of s3, the ratio of the magnitudes of $\tilde{A}_{xy}^{(1)}$ and $\tilde{A}_{zz}^{(1)}$ differs compared to those of s3. We obtain $\Gamma = 1.05 \pm 0.04$, indicating that the interaction force is central. Moreover, $\tilde{A}_{xx}^{(1)}$ and $\tilde{A}_{xx}^{(2)}$ have the same sign, which means that the deviation of the first neighbor along the x axis weakly repels the second neighbor, as expected for central forces.

Sample	pH	ζ	$\tilde{A}_{xx}^{(1)}$	$\tilde{A}_{xy}^{(1)}$	$\tilde{A}_{zz}^{(1)}$	$\tilde{A}_{xx}^{(2)}$	$\tilde{A}_{yy}^{(2)}$	Γ
s1	7.0	1.6	-1439 ± 100	-646 ± 48	419 ± 55	811 ± 50	-560 ± 30	0.35 ± 0.03
s2	7.0	1.4	-790 ± 40	-308 ± 28	226 ± 20	389 ± 30	-198 ± 15	0.30 ± 0.03
s3	3.5	1.6	-117 ± 10	-58 ± 6	43 ± 3	37 ± 3	-58 ± 5	0.36 ± 0.04
simulate fcc	--	0.55	-100 ± 3	-100 ± 3	5.7 ± 0.5	-3.0 ± 0.2	-0.30 ± 0.01	1.05 ± 0.04

Table 6.1: Dimensionless force constants of the first and second nearest neighbors. Γ indicates that the many-body interaction is present. The results for the simulated hard-sphere fcc crystal as compatible with central forces.

The dimensionless wave propagation coefficients b can be calculated following Eq.6.76. The results are summarized in Table.6.2. According to the Cauchy relation in Eq.6.77, the central force predicts $b_{12} = b_{44} + 2P$. For all three samples, $b_{12} < b_{44}$ and the Cauchy relation, $b_{12} = b_{44} + 2P$, can be satisfied only with unrealistic negative pressures, again indicating the noncentral nature of the interaction between the microgels. For central forces, $b_{12} > b_{44}$. The simulated fcc hard-sphere crystal fulfills this; see Table 6.1. From Eq.6.73, we calculate the bulk modulus, $\tilde{K} = \frac{b_{11}+2b_{12}}{3}$. Our results show that \tilde{K} of samples s2 and s3 is smaller than that of sample s1, due to the fact that the microgel-microgel interaction is weaker for samples s2 and s3 compared to sample s1, as indicated by the force constants, which causes the crystals to be softer. Note that \tilde{K} is dimensionless and, using the particle volume v_0 and the thermal energy $k_B T$, the actual bulk modulus K of the crystal can be obtained. We find: (3.0 ± 0.3) Pa for s1, and the crystal becomes softer for s2 and s3, see Table 6.2. The large softness of the microgel crystal can lead to melting even with vibration of the sample cell and/or with elevated temperatures.

Sample	pH	ζ	b_{11}	b_{12}	b_{44}	\tilde{K}	$K(\text{Pa})$
s1	7.0	1.6	628 ± 100	596 ± 80	1070 ± 60	606 ± 60	3.0 ± 0.4
s2	7.0	1.4	401 ± 50	392 ± 40	480 ± 30	395 ± 30	1.6 ± 0.3
s3	3.5	1.6	81 ± 10	53 ± 9	95 ± 7	62 ± 7	0.26 ± 0.03
simulate fcc	--	0.55	103 ± 3	151 ± 3	47 ± 2	135 ± 2	0.55 ± 0.01

Table 6.2: Dimensionless b parameters calculated with force constants of the first and second nearest neighbors. (\tilde{K}) K is the (dimensionless) bulk modulus.

Our results clearly demonstrate that the interaction force between the microgels in the crystal is dominated by noncentral many-body interactions. The distribution of counterions can hardly be described by a linear superposition of distributions around the microgels. As a result, the interaction force and elasticity of the microgel crystal are similar to those observed for charged hard colloidal crystals. The most common pairwise interaction potential for charged colloids, such as the hard-sphere Yukawa potential [78], can be useful for describing charged colloids in a dilute suspension. However, it is not sufficient to describe the dense microgel suspension or the microgel crystal with surface counterion clouds. The Poisson-Boltzmann equation can be used to calculate the distribution of counterions inside a crystal [54], so that the charge effect that leads to non-central forces can be better understood. The key difference from charged colloids is that microgels can respond to outside charges and deswell. Additionally, the true volume fraction of the sample can possibly be obtained from bright-field microscopy, and the bulk modulus of the simulated fcc

crystal can be compared to that of the microgel crystals to better understand the effects of the charges on the crystal elasticity.

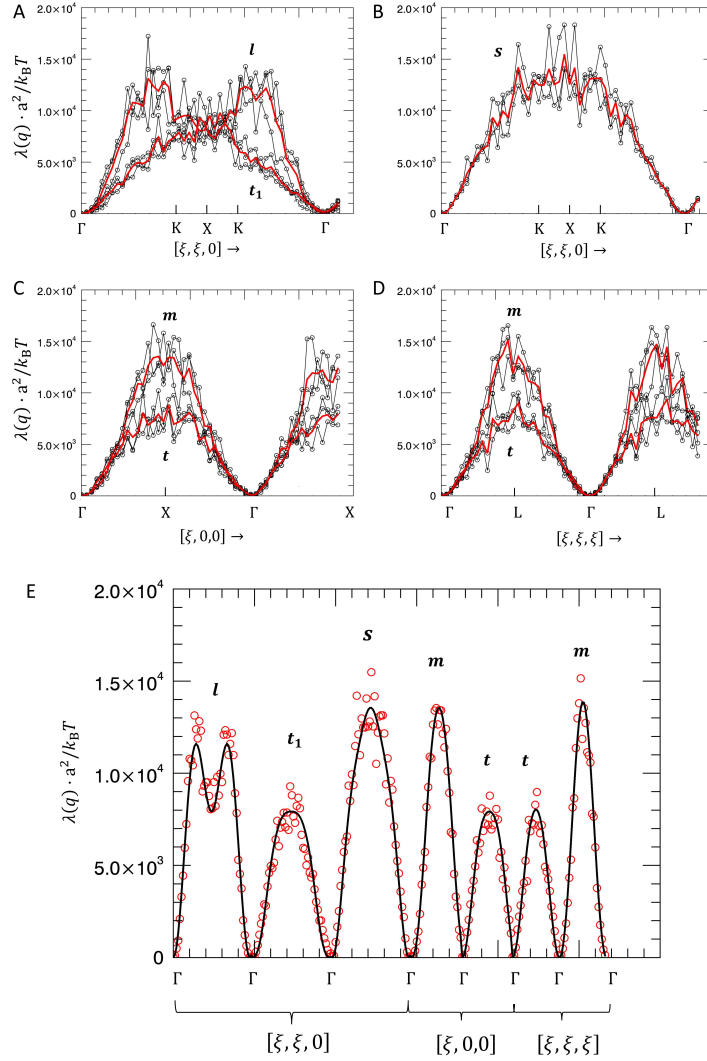


Figure 6.13: Dispersion relations of the crystal at $\text{pH} \sim 7$ at $\zeta \sim 1.6$. $\xi = q \cdot a$. A-B: dispersion relations for the longitudinal l and transverse mode t_1 and the mode $s = t_1 + t_2$ in the $[110]$ direction. (Black lines). The dispersion relations in three equivalent directions are averaged. (red line) C-D: dispersion relation of modes $m = l + t_1 + t_2$ and t , which represents the degenerate transverse mode in the $[100]$ and $[111]$ directions. E: All dispersion relations are fitted by the dynamic matrix to extract the force constants.

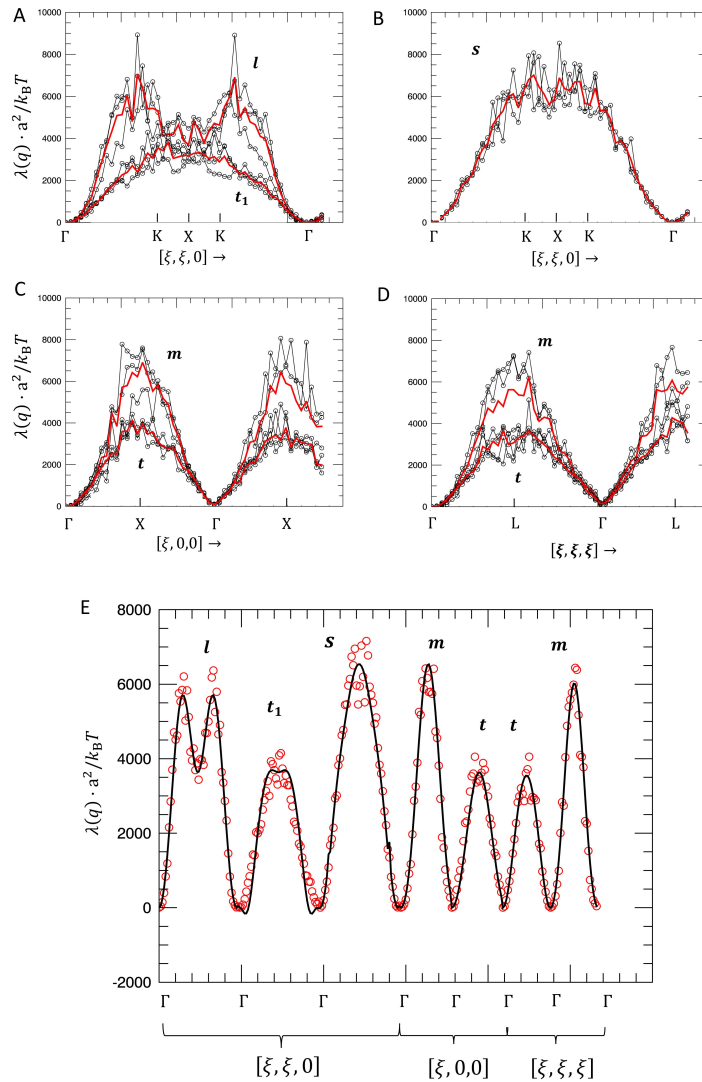


Figure 6.14: Dispersion relations of the crystal at $\text{pH} \sim 7$ at $\zeta \sim 1.4$. A-B: dispersion relations for the longitudinal l and transverse mode t_1 and the mode $s = t_1 + t_2$ in the $[110]$ direction. (Black lines). The dispersion relations in three equivalent directions are averaged. (red line) C-D: dispersion relation of modes $m = l + t_1 + t_2$ and t , which represents the degenerate transverse mode in the $[100]$ and $[111]$ directions. E: All dispersion relations are fitted by the dynamic matrix to extract the force constants.

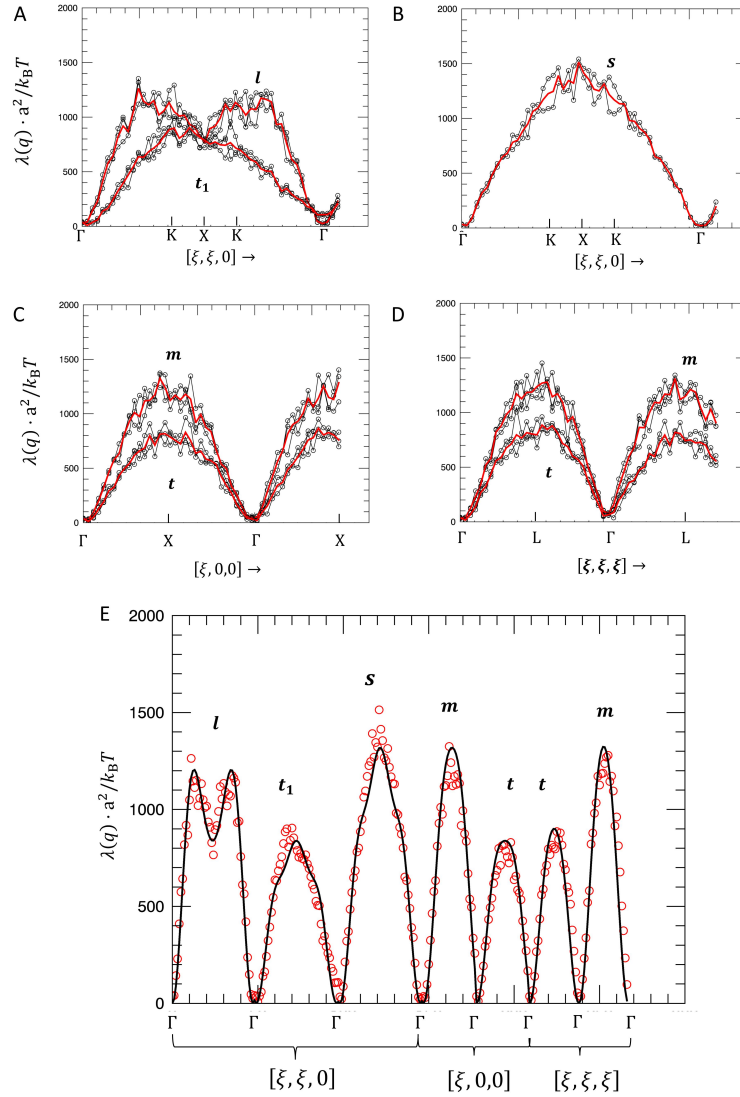


Figure 6.15: Dispersion relations of the crystal at $\text{pH} \sim 3.6$ at $\zeta \sim 1.6$. A-B: dispersion relations for the longitudinal l and transverse mode t_1 and the mode $s = t_1 + t_2$ in the $[110]$ direction. (Black lines). The dispersion relations in three equivalent directions are averaged. (red line) C-D: dispersion relation of modes $m = l + t_1 + t_2$ and t , which represents the degenerate transverse mode in the $[100]$ and $[111]$ directions. E: All dispersion relations are fitted by the dynamic matrix to extract the force constants.

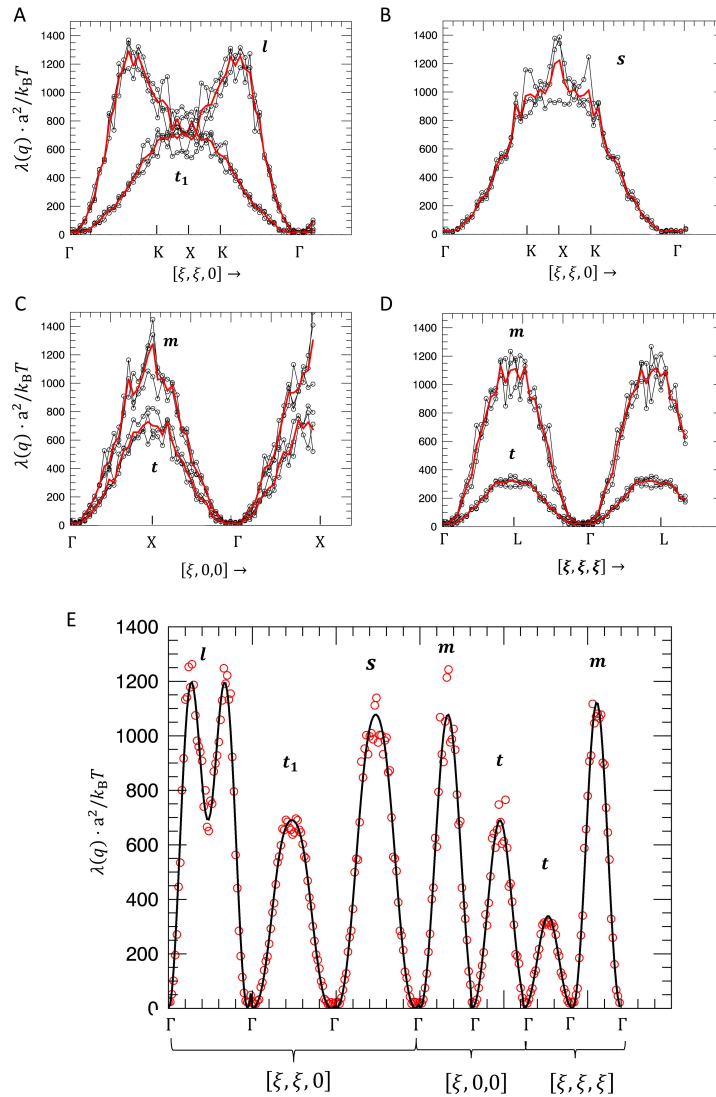


Figure 6.16: Dispersion relations of the simulated fcc crystal at $\phi = 0.55$. A-B: dispersion relations for the longitudinal l and transverse mode t_1 and the mode $s = t_1 + t_2$ in the $[110]$ direction. (Black lines). The dispersion relations in three equivalent directions are averaged. (red line) C-D: dispersion relation of modes $m = l + t_1 + t_2$ and t , which represents the degenerate transverse mode in the $[100]$ and $[111]$ directions. E: All dispersion relations are fitted by the dynamic matrix to extract the force constants.

Chapter 7

Rapid-heating-induced phase-coexistence of pNIPAM hydrogel

7.1 Introduction

Polymer hydrogels are made of cross-linked polymer networks immersed in a solvent. Similarly to the microgel, the hydrogel can undergo a volume phase transition in response to changes in external stimuli, such as temperature, solvent compositions, and osmotic pressure, where the hydrogel can swell and deswell reversibly. However, this occurs much more slowly than that of the microgel as a result of the longer equilibrium time. Simulation work has demonstrated that upon rapid deswelling, the microgel forms chain bundles in the periphery and network coarsening occurs [124]. This causes microgels to have an inhomogeneous structure during the volume phase transition, and similar behavior has also been observed for isochore phase separation in macrogels, where a macro-network consisting of polymer-rich and solvent-rich regions forms [164]. Furthermore, the volume phase transition can be continuous or discontinuous and the gels can exhibit metastable states. Upon rapid heating, the gel does not have enough time to equalibrate its volume, and the phase transition is nearly isochoric, which leads to very interesting phenomena. In previous work, cylindrical gels have been shown to exhibit interesting surface patterns, such as ballooning, wrinkling, and bambooning, upon rapid heating [19, 180]. According to the Flory-Rehner model, the gel network equilibrates when the chemical potential of solvent molecules in and out of the chain networks matches, and the total free energy consisting of a polymer-solvent mixing contribution and an elasticity term

is minimized [47]. However, this theory does not fully describe the case where the polymer gel undergoes a thermodynamically unstable phase-coexistence; for thermo-responsive gels below a threshold temperature, T_{LCST} , the system is in an equilibrium swollen state. On the contrary, if the temperature increases above T_{LCST} rapidly, the gel can reach phase co-existence and can be characterized by a free energy with two minima, corresponding to solvent-poor and solvent-rich regions. The solvent-poor regime is characterized by a dense polymer skin on the gel surface and theoretical work has shown that the skin grows inward from the boundary, and continuous growth of the skin implies a reduction in the density of polymers in the inner region, featuring the solvent-rich regime [36]. Furthermore, despite the fact that the transition between swollen and deswollen gels is similar to the gas-liquid transition, the shear rigidity limits the available configurations of the polymer network after rapid temperature changes, and consequently, shear rigidity alters the phase-co-existence equilibria. Macroscopic separation between a polymer-rich skin and a solvent-rich core creates an anisotropic stress distribution that may cause gel deformation, such as bulking or transverse deflection, phenomena observed for toroidal gels [25, 36]. As a result, the phase coexistence equilibrium of the gel is also believed to be shape dependent. So far, the understanding of the skin is limited and there are no direct measurements of the thickness of the polymer-rich skin after rapid heating. However, this information is essential to calculate the free energy associated with the volume constrained state, as well as to determine the flow rate of the solvent from the swollen inner region, making the dynamical study of this process possible. As the Flory-Rehner model only provides a reliable description of the equilibrium state, another model is necessary to describe the dynamics associated with the formation of the two-phase regime. In addition, with the characterization of the skin and solvent-rich interior, the coupling between the spatial distribution of the solvent and the gel elasticity could be understood. This information is related to the volume phase transition of polymer gels under rapid heating, which can be used to design gels that achieve a shape actuation not available for thermodynamically stable gels [36, 25]. The idea of utilizing the thermodynamic instability in material design has been called extreme thermodynamics, in analogy to the so-called extreme mechanics in materials, where mechanical instability is explored to achieve shape actuation. The simplest of which is perhaps Euler buckling.

In this work, we will show a comprehensive study of the polymer gel upon rapid heating. In Section 7.3, uniaxial normal force is applied to the gel in the swollen, deswollen, and swollen-with-skin states. Subsequently, we aim to extract

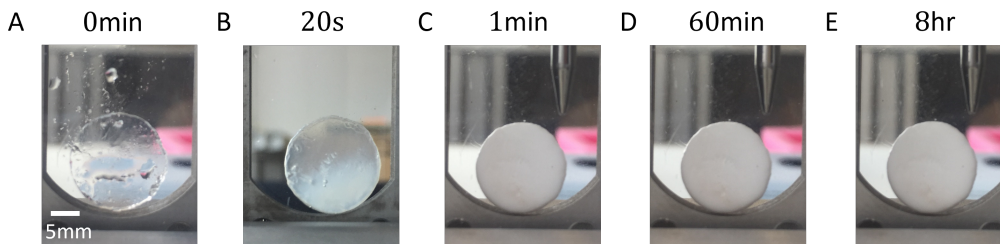


Figure 7.1: Sharp increase of the solvent temperature. A: Gel in disk shape in the container without any solvent, with the entire sample environment heated to 45°C . B: 20s after pouring water at $T = 45^\circ\text{C}$ into the container. C: 1 min after temperature quench. C: 60 min after temperature quench. D: eight hours after the temperature quench.

the skin thickness by treating the gel with skin as a three-layered composite material. Furthermore, in Section 7.4, we investigate the internal structure of the gel via small-angle neutron scattering (SANS). Finally, in Section 7.5, neutron imaging is used to study the macroscopic properties of the gels and visualize the change in solvent composition under rapid heating.

7.2 Skin formation under rapid heating

The pNIPAM macrogel used in this study was synthesized with the precipitation polymerization protocol, in which a water-based Pregel solution containing 156mM NIPAM monomers and 1wt.% of BIS crosslinking agent and APS initiator is prepared in a petri dish. The reaction was performed under bad solvent condition at $T = 70^\circ\text{C}$. The macrogel product reaches its fully swollen state by soaking it in a clean water bath at 20°C for three days. The disk-shaped gel used in this work was cut directly from the bulk macrogel sheet. As shown in Fig.7.1, by the rapid increase in temperature above the volume phase transition temperature of pNIPAM $T_{\text{LCST}} = 32^\circ\text{C}$, the hydrogel does not reach the deswollen state but remains essentially in its swollen size. Rapid heating is carried out by pouring water at $T = 45^\circ\text{C}$ directly into the gel container. In this test, the diameter of the cross section is only reduced by 2%, as some solvent molecules may have left the gel before the skin forms, leading to a small decrease in gel volume, as shown in Fig.7.1B. Note, however, that the skin has certainly formed, as the gel appears completely white and is not transparent as $T < T_{\text{LCST}}$.

If the heating is progressive, the hydrogel can reach the deswollen state and the skin does not appear. As shown in Fig.7.2, the temperature of the solvent bath

increases with a step of 1°C to 2°C . The cross-sectional area of the gel was checked for two consecutive hours, and the temperature was only increased after stable size was observed, which means that the equilibrium state is reached. With progressive heating, the diameter of the cross section decreases by 50% compared to that of the swollen gel. As the cross-sectional area of the gel remains unchanged with further temperature increment, it can be concluded that it has reached the deswollen state. The size change normalized by the swollen diameter for the rapid- and moderate-heating experiments is shown in Fig.7.3

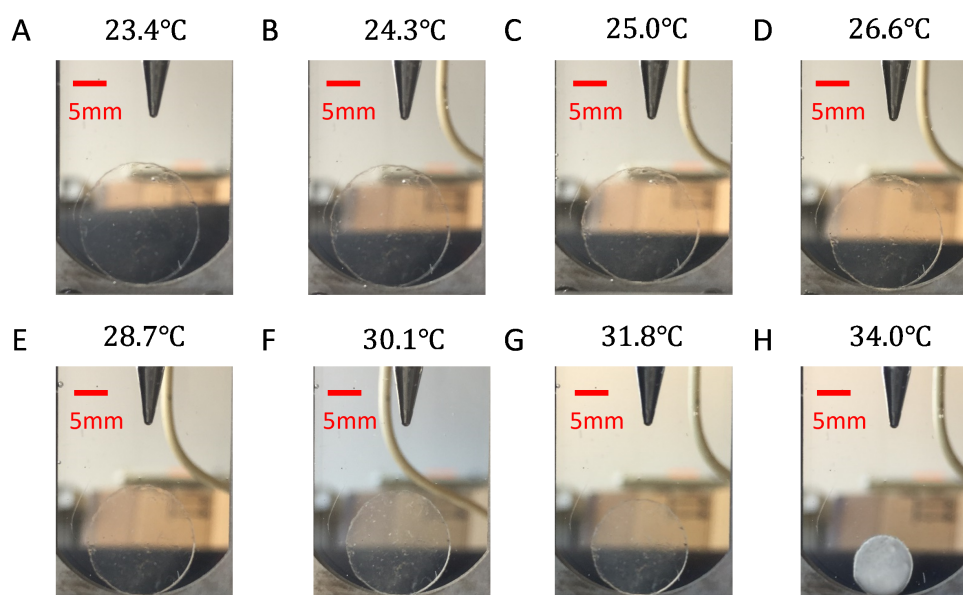


Figure 7.2: The water bath is progressively heated up above the T_{LCST} . A: the starting temperature is at $T = 23.4^{\circ}\text{C}$. B: 1°C increases in temperature, and it takes two hours for the gel to equilibrate with the solvent. C: the gel takes five hours to equilibrate at $T = 25.0^{\circ}\text{C}$. D: It takes eight hours for the gel to equilibrate at $T = 26.6^{\circ}\text{C}$. E: the gel takes eight hours to equilibrate at $T = 28.7^{\circ}\text{C}$. F: the gel is left in the bath for eight hours to equilibrate at $T = 30.1^{\circ}\text{C}$. G: The gel is left in the bath for seventeen hours to equilibrate at $T = 31.8^{\circ}\text{C}$. H: the gel is left in the bath for 17 hours to equilibrate at $T = 34.0^{\circ}\text{C}$.

7.3 Macrogel under an uni-axial compression

As introduced in the previous section, a polymer-dense skin and a solvent-rich interior coexist, if it is heated rapidly above T_{LCST} . It is reasonable to assume that the bulk modulus of the polymer skin is comparable to that of the gel in the deswollen state and that the bulk modulus of the solvent-rich interior is comparable to that

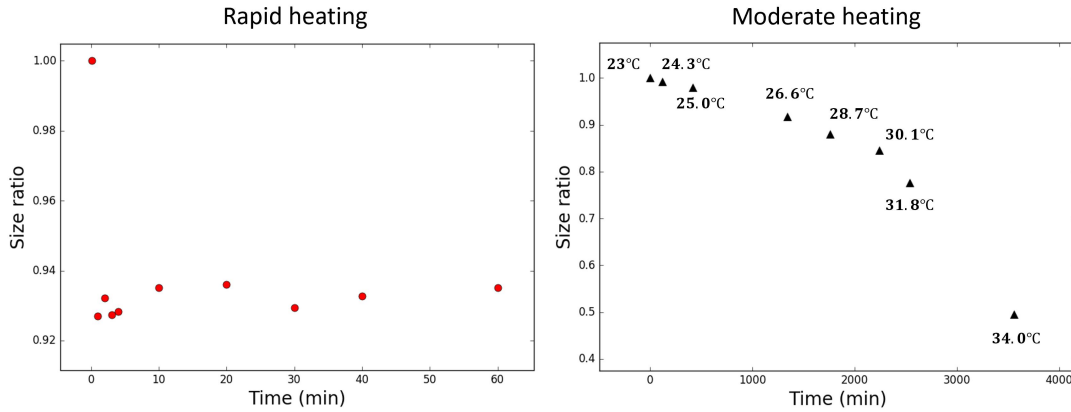


Figure 7.3: The diameter change normalized by the diameter of the swollen gel. A: the size changes with rapid temperature change. B: the size changes with moderate heating.

of the gel in the swollen state. By normally pressing a disk-shaped gel on the circular cross section in the swollen, deswollen, and swollen-with-skin states, we should be able to extract the bulk modulus of the swollen, deswollen, and swollen-with-skin gel. We ultimately aim to extract the thickness of the skin by treating the swollen-with-skin gel as a layer composite material with deswollen gel in the first and third layers and swollen gel in the second intermediate layer. The rheometer used in this work is an Anton-Paar 302e with a flat parallel plate. The minimum measurable normal force is 5 mN with a normal force resolution of 0.5 mN and a response time of less than 20 ms. As shown in Fig.7.5A, a fully swollen gel is placed in the center of the pressing stage, and the gel surface is wet with water to prevent evaporation. As shown in Fig.7.4, the gel is pressed and released for three consecutive runs with an increasing compression ratio. From Fig.7.4, with an initial compression of 0.3 mm, which represents a compression ratio of 16.6% of the gel thickness $h = (1.80 \pm 0.05)$ mm, there is no noticeable deviation between the pressing and releasing curves. With an increasing compression ratio, deviations are observed between both curves. The possible explanation is that pressing, forces the gel to deform and laterally expand. As the recovery of the original shape is slower than the elevating speed of the flat plate, the gel exhibits a smaller restoring force compared to the normal force during pressing. In addition, the three pressing curves overlap each other, indicating that compression does not influence the mechanical properties of the gel in a significant way.

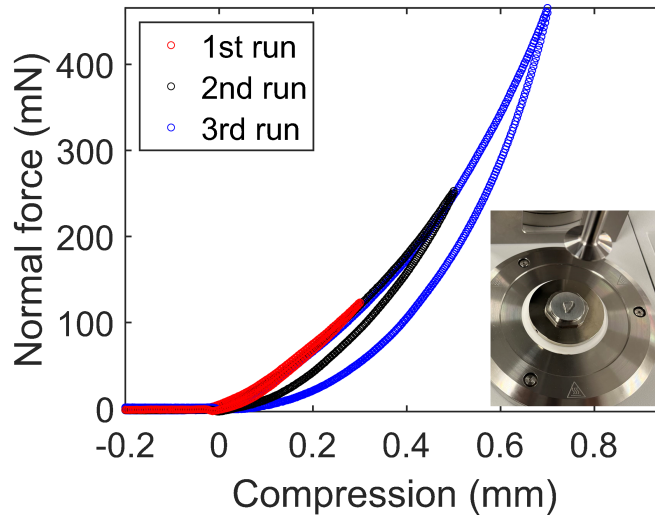


Figure 7.4: Three consecutive press(top) - release(bottom) curves of the same gel with increasing compression ratio. The insert shows that a testing gel is placed on the pressing stage and a flat plate is used to press. The set-up is representative of the pressing experiments

7.3.1 Fully swollen gel

The macrogel was cut in a disk shape and completely immersed in water for three days at $T = 20^\circ\text{C}$ to ensure the gel was fully swollen. The gel is placed in the sample stage and pressing is performed at a speed of 0.0015mm/s . As the water is just above the gel surface, the surface tension pulls the flat plate downwards and causes the discontinuity observed in the pressing line, as shown in Fig.7.5C. This would induce a small error in the slope extracted from the linear fit; however, it will not significantly influence the result ¹. The maximum compression is around a quarter of the gel thickness. The regime with compression of 0.08 mm is used to extract Young's modulus, which represents only 4% of the compression in terms of the gel thickness. The slope extracted from the fit is $(336 \pm 10)\text{ N/m}$. The Young's modulus of the gel results directly from Hooke's law:

$$E = \frac{\text{force}}{\text{compression} * \text{area}} * \text{thickness} \quad (7.1)$$

We obtain $E = (10.9 \pm 0.6)\text{ kPa}$. This value agrees with the result of a previous study [176].

¹The error is less than 4%

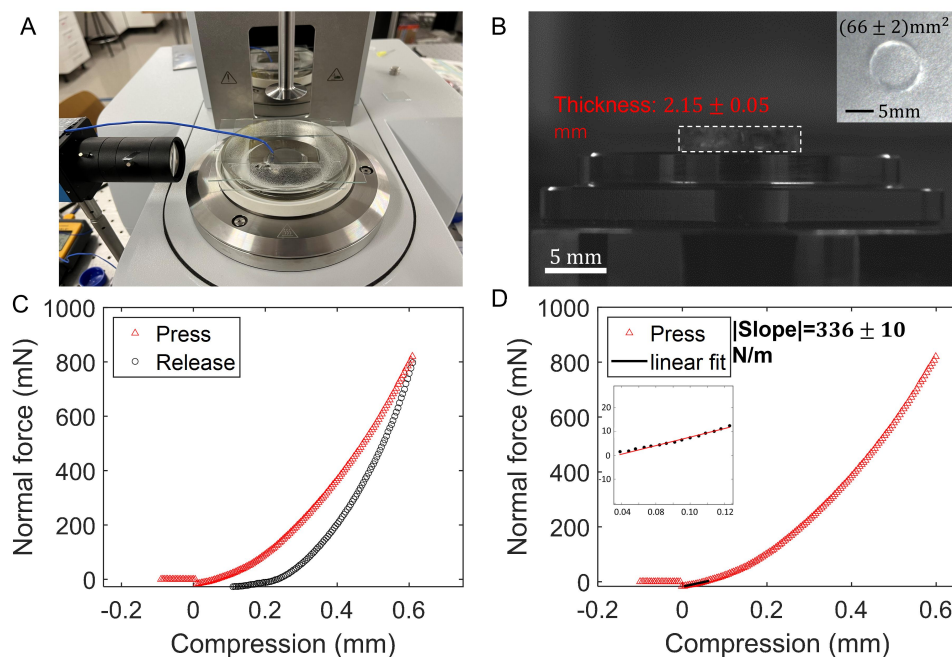


Figure 7.5: A: A water pool is built around the sample stage of the rheometer. A thermocouple is used to monitor the temperature (blue wire). A camera is set up to obtain a side view of the sample. B: Macrogel with a thickness of (2.15 ± 0.05) mm in the sample stage (marked by the white-dash contour). The insert shows the circular gel subject to pressing. The area of the cross section is $(66 \pm 2) \text{ mm}^2$. C: The pressing and release curves are plotted against the gap distance. D: part of the pressing curve is fitted linearly to obtain the slope.

7.3.2 Fully deswollen gel

Due to the slow diffusion of water from the polymer chain network, it can take tens of hours or even days until the gel reaches the deswollen state. In addition, sudden temperature changes can lead to skin formation, and with the gel remaining in the two-phase state for very long times. In this experiment, the fully swollen gel is placed in a water bath heated from 23°C to 38°C in steps of 1°C over five days. As soon as the gel has reached a stationary state and its size remains constant, the size is measured, and the temperature is increased. In addition, at temperatures close to the volume phase transition temperature $T_{\text{LCST}} = 32^\circ\text{C}$, each temperature step can take up to 13 hours to ensure that the gel reaches the equilibrium state. Above 34°C , the gel no longer changes its size and shape. Therefore, we conclude that the gel has reached the deswollen state at the highest temperature of the water bath. Subsequently, the gel is transported to the preheated water bath of the rheometer at 40°C . As shown in Fig.7.6, the deswollen gel has a cross-sectional area of $(12.56 \pm$

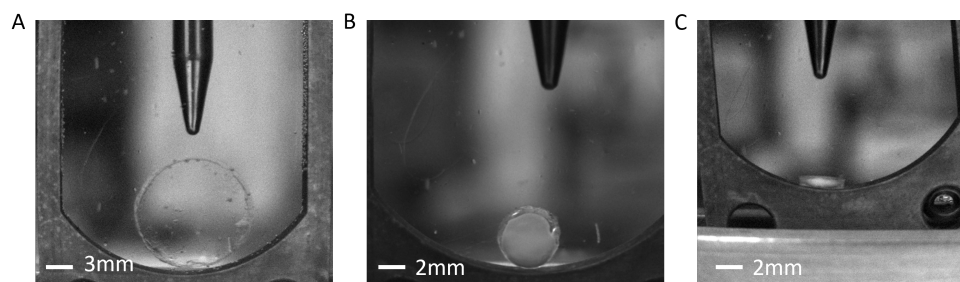


Figure 7.6: A: The cross section of the swollen gel. B: cross section of the deswollen gel. C: The side view showing the thickness of the deswollen gel.

2.51) mm² and a thickness of (0.8 ± 0.1) mm. The volume of the deswollen gel is (10.05 ± 2.37) mm³, which is more than ten times smaller than the volume of the swollen gel. In Fig.7.7 A, the press-release curve is plotted against the gap distance.

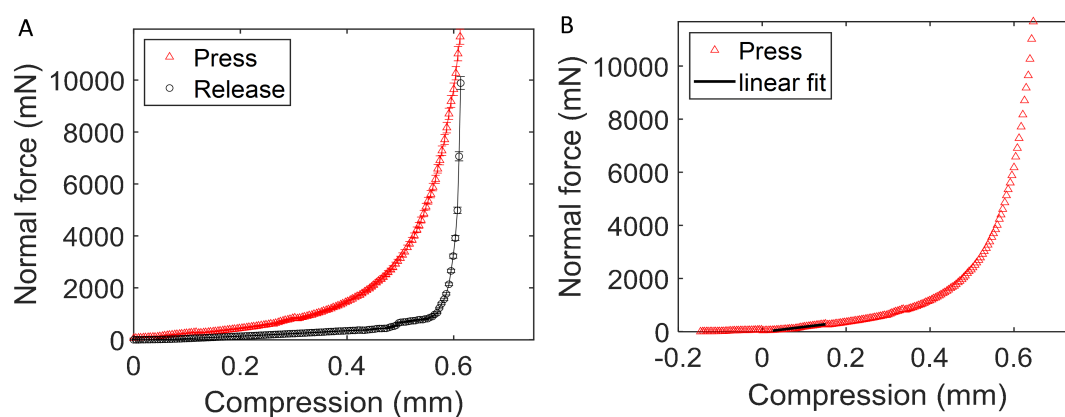


Figure 7.7: A: The press-release curve of the deswollen gel. B: The pressing curve and fitting of the linear regime (black line).

The maximum compression is around three-quarters of the gel thickness. Similarly to the press-release curve of the swollen gel, the gel is laterally expanded due to compression, and the flat plate loses contact at compression of ~ 0.5 mm with the normal force approaching 0 mN. Data between the compression 0.02 mm to 0.1 mm are fitted with a linear model; this corresponds to a $\approx 10\%$ uniaxial compression. The slope obtained from the linear fit is $(24 \pm 6) \times 100$ N/m, and with a cross section area of 12.56 mm² and a thickness of 0.8 mm, the Young's modulus of the deswollen gel is (153 ± 13) kPa. This is ≈ 15 times larger than the value obtained for the swollen gel.

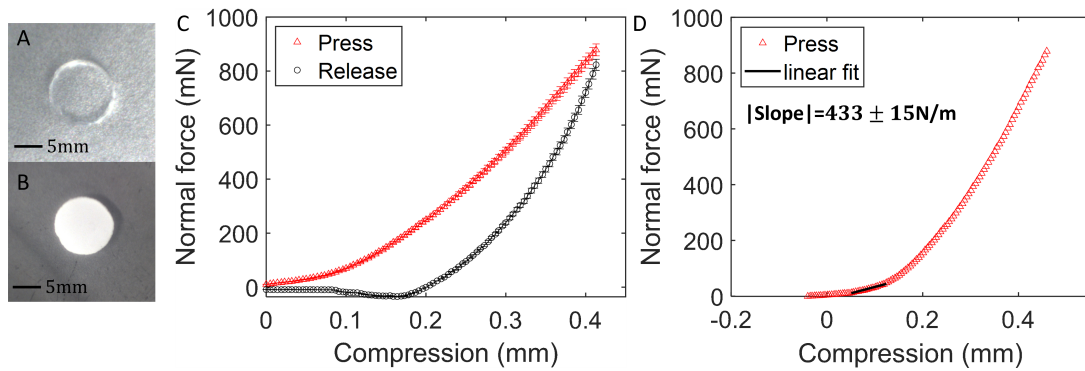


Figure 7.8: A-B: Cross section of the swollen gel and of the gel that is swollen with skin. C: Press-release curve of the gel that is swollen with skin at 40 °C. D: Linear fit of the part of the pressing curve.

7.3.3 Swollen gel with skin

To prepare a gel that is swollen with skin, a sudden temperature quench is applied; a swollen gel at 20 °C is dropped in a water bath at 45 °C. The cross section of the gel is $(61 \pm 3) \text{ mm}^2$, which decreases around 10% compared to the fully swollen gel, and the size remains the same onward, as illustrated in Fig.7.8 A-B. The thickness of the gel is about $(2.10 \pm 0.05) \text{ mm}$, which remains the same as that of the swollen gel. The slope obtained from the linear fit is $(43 \pm 1.5) \times 10 \text{ N/m}$, and Young's modulus

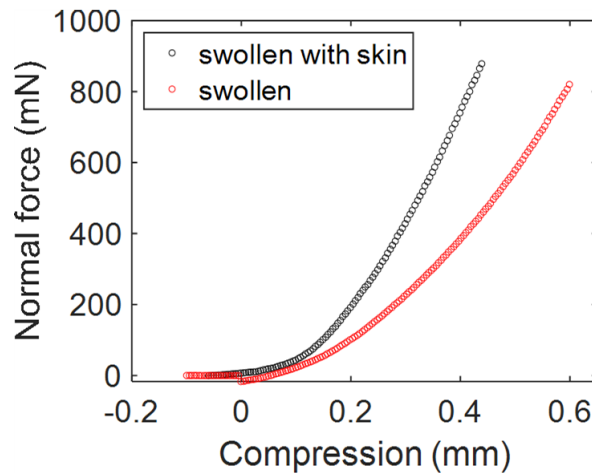


Figure 7.9: The comparison of the press curves between the swollen gel at 20 °C and the gel that is swollen with the skin at 40 °C.

of the heterogeneous gel is $(15 \pm 1) \text{ kPa}$, which is about 40% larger compared to that of the swollen gel. However, the most significant difference is observed at higher compression, as shown in Fig.7.9. Despite the small difference between the size of the gels in the two states, the curves appear significantly different. The same normal

force is obtained with only half of the compression distance applied to the swollen gel.

7.3.4 Estimation of the skin thickness

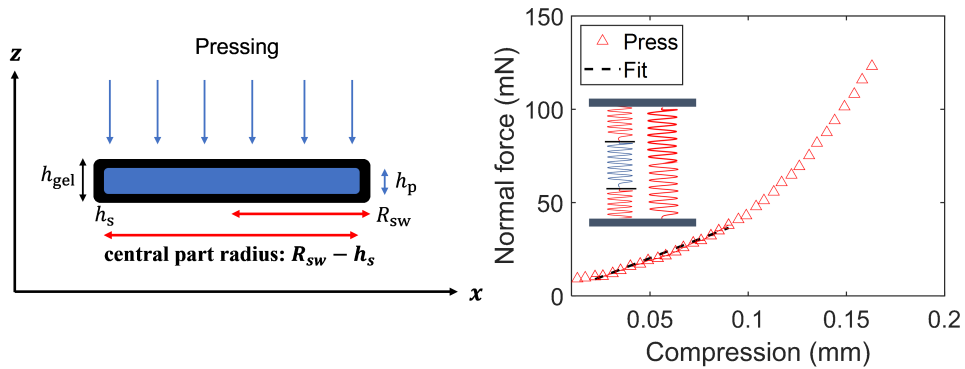


Figure 7.10: Left: the schematic representation of the gel in the x - z plane. The cross section area of the gel subjected to pressing has a radius of R_{sw} . The gel has a solvent-rich interior with thickness h_p , and the thickness of the gel sample is h_{gel} . The skin thickness is h_s . The central part has the radius of $R_{sw} - h_s$, excluding the skin on the side. Right: fitting of the linear regime to the model based on the Modified rule of mixture (MRM). The insert shows the spring representation of the swollen gel with skin. The red and blue springs represent the skin and swollen interior, respectively.

As shown in Fig.7.10, the gel has a swollen interior with skin on the outside and is pressed along the z direction on the circular face. In the central region, there are skins on the upper and lower layers with a swollen interior in between. This is represented by three springs connected in series, shown in Fig.7.10. On the side, there is also skin, which is represented by one spring connected in parallel to the three springs in series. Note that it is assumed that the skin thickness is identical for the top/bottom and the side. The schematic shows the simplified geometry of the gel, and, by treating the gel as a layered composite material, the effective Young's modulus can be estimated from the volume fraction and Young's modulus of the layers according to the Modified Rule of Mixture (MRM) [183, 98], that provides reliable estimates of the elastic modulus of dual-phase materials [193, 87, 44]. According to the MRM, the uniaxial strain ϵ and stress σ are expressed in terms of the average strain ϵ_j and the average stress σ_j of each phase, and their volume

fraction ϕ_j , ($j \in (s, p)$), with $\phi_s + \phi_p = 1$, such that

$$\begin{aligned}\sigma &= \phi_s \sigma_s + \phi_p \sigma_p \\ \epsilon &= \phi_s \epsilon_s + \phi_p \epsilon_p\end{aligned}\tag{7.2}$$

where the subscripts s and p represent the skin and the gel interior on the central part of the gel containing the swollen polymer chain network. The quantity

$$q = \left| \frac{\sigma_s - \sigma_p}{\epsilon_s - \epsilon_p} \right|\tag{7.3}$$

is an empirical parameter that accounts for factors like microstructure arrangement, internal constraints, and material composition of the phases [62]. The Young's modulus of the composite materials is then approximated as:

$$E = \frac{\phi_s (E_p + q) E_s}{\phi_s (E_p + q) + \phi_p (E_s + q)} + \frac{\phi_p (E_s + q) E_p}{\phi_s (E_p + q) + \phi_p (E_s + q)}\tag{7.4}$$

where E_s and E_p are the Young's moduli of the two phases. In the experiment, the gel was uniformly pressed by flat parallel plates, which is analogous to compressing the springs connected in series; hence, for the central part, it is reasonable to assume that different layers experience the same stress. Therefore, $\sigma_s = \sigma_p$ and $q = 0$. Eq.7.4 then becomes:

$$E_c = \frac{\phi_s E_p E_s + \phi_p E_p E_s}{\phi_s E_p + \phi_p E_s} = \frac{E_p E_s}{\phi_s E_p + \phi_p E_s}\tag{7.5}$$

where E_c is the effective Young's modulus of the central part with three layers. Eq.7.5 is the Reuss estimate (RE) model [70], which assumes that each layer is subjected to uniform stress and different strains [123]. However, for the skin on the side, the strain is the same as that of the central part, and the Voigt estimate (VE), $E_{VE} = E_1 \phi_1 + E_2 \phi_2$, can be applied, where 1 and 2 indicate different phases, in analogy to springs in parallel [121]. For our gel sample, it is reasonable to assume that the polymer-dense skin and solvent-rich interior form distinct layers inside the gel with skin also appearing on the side. In addition, we expect no shear deformation during pressing. Therefore, the system is much simpler than other composite materials with a more complicated phase distribution. With this in mind, it is reasonable to assume that the RE and VE approximations can serve as a useful tool for understanding the layer structure of the swollen gel with the skin surface [107, 123].

As a result, the effective Young's modulus of the whole gel can be estimated as

$$E_{\text{eff}} = \phi_c E_c + \phi_{\text{ss}} E_s \quad (7.6)$$

where ϕ_{ss} is the volume fraction of the skin on the side of the gel with width h_s , and ϕ_c is the volume fraction of the central part, composed of skin and swollen interior. The linear regime of the compression curve of the swollen gel with the skin is fitted to the model given in Eq.7.6. The Young's modulus of the swollen interior is equal to that of the swollen gel, $E_p = E_{\text{sw}} = (10.9 \pm 0.6)$ kPa. Similarly, the Young's modulus of the skin should be very similar to that of the deswollen gel, where $E_s = E_{\text{dsw}} = (153 \pm 13)$ kPa. The volume fraction of the solvent-rich interior respecting to the central part can be written as $\phi_p = h_p / (h_p + 2h_s)$, where the thickness of the gel is given by $h_p + 2h_s = (2.10 \pm 0.05)$ mm. The volume fraction of the skin in the central part is $\phi_s = 1 - \phi_p$. With this, the slope of the linear fit of the data in Fig.7.10 becomes a function of the layer thickness. Then from the stress-strain relation $\sigma = E \epsilon$, and the fit of the data, we obtain an average skin thickness of $h_s = (49 \pm 5)$ μm . The error in h_s is estimated from the errors of the Young's modulus for each layer and the gel dimensions. This result is a rough estimate of skin thickness based on the assumptions that the layers are distinctive and there is no shear deformation in the linear regime.

7.4 SANS: Investigation of the polymer skin

As we have demonstrated, the astonishing behavior of our hydrogels when subject to a rapid increase in temperature above T_{LCST} prompts investigating the details of the internal structure of the hydrogel. In this section, we investigate the microscopic structure of the hydrogel with increasing temperature via SANS, which has been demonstrated to be very useful in studying the structural changes originating from the volume phase transition of the gels [163].

The hydrogel was let to dry out by exposure to air, and subsequently, the dry gel was soaked in a deuterated water bath for three days to reach the fully swollen state. In this way, we can minimize incoherent scattering and maximize the contrast between the polymer gel and the solvent. The scattering intensity of the swollen gel is measured at $T = (18.0 \pm 0.2)$ °C. Subsequently, the gel was measured at increasing temperatures: 25 °C, 32 °C, 34 °C, 36 °C, and 43 °C. At each temperature, the gel was left for two hours to reach the equilibrium state, and we also measured a swollen gel with skin. Before loading the gel into the sample cell, the gel was dropped into

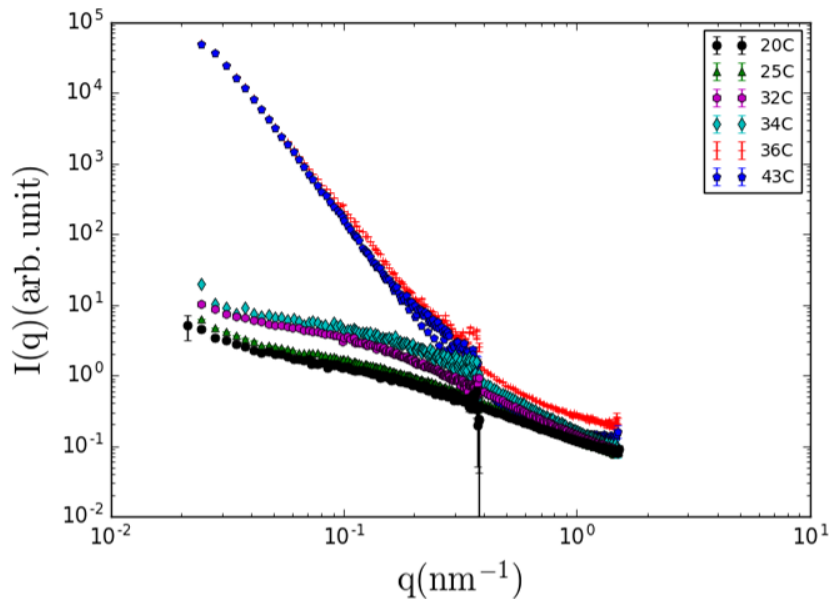


Figure 7.11: SANS curves of the hydrogel at increasing temperature plotted. The SANS curve is constructed by the data taken at two connecting q -range at sample-to-detector distances of 18 m and 5 m.

a hot D_2O bath at $T = 45^\circ C$ to let the skin form. The gel was subsequently loaded into the preheated sample cell and the sample environment. The SANS curves of the hydrogel obtained at different temperatures are shown in Fig.7.11. The scattering intensity increases in magnitude as the temperature increases. The curves show a dramatic change at temperatures above $32^\circ C$, indicating the volume phase transition of the hydrogel. The measurement at $36^\circ C$ and $43^\circ C$ appear very similar, indicating that the gel has reached equilibrium and that the internal structure of the hydrogel no longer evolves with temperature. The comparison between the scattering curves of the gel in the swollen state and the swollen gel with skin is shown in Fig.7.12A. There is a dramatic difference between the two curves. In contrast, the scattering curve of the deswollen state is very similar to that of the swollen gel with skin, as shown in Fig.7.12B. Therefore, the data suggest that the structure of the gel with skin varies significantly compared to that of the swollen gel. The polymer skin has a much higher scattering amplitude than that of the swollen gel because the polymer volume fraction increases as a result of the collapsed chains making the skin, which is why the scattering is similar to that of the gel in the deswollen state [136]. This essentially suggests that the internal structure of the skin is close to that of the deswollen state.

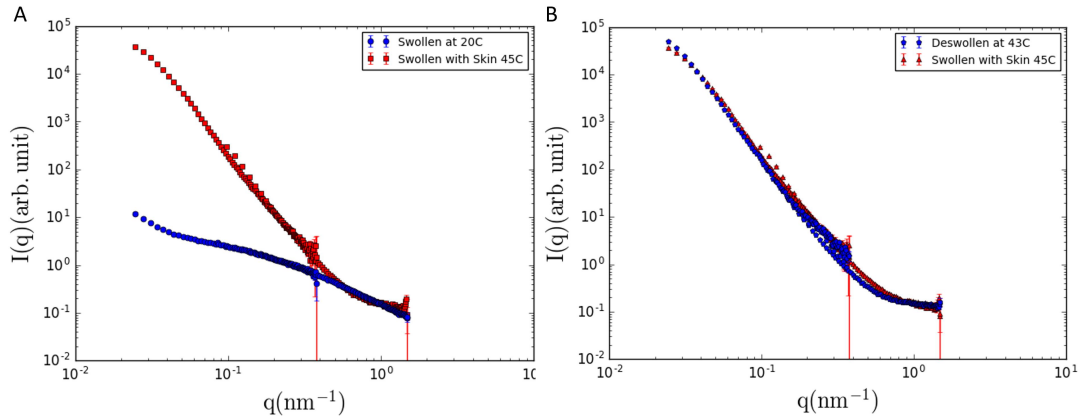


Figure 7.12: SANS curves comparison. A: The scattering intensity of the gel that is swollen with skin is plotted together with that of the swollen state. B: The scattering intensity of the deswollen gel is plotted with that of the swollen-with-skin gel.

7.4.1 Scattering model of polymer gels

The scattering intensity of polymer gels can often be decomposed into two terms, which describe the scattering owing to thermal fluctuation of the polymer chains and the spatial fluctuation owing to inhomogeneities originating from the distribution of crosslinks [164]. The scattering due to fluctuations of static solid-like density is described by the exponential function with an exponent 2, assuming the non-interacting domains with higher and lower crosslink density are randomly distributed [161]. In this case, the Gauss function reduces to the Guinier function:

$$I(q) = I_G(0) \exp \left[- (q \Xi)^2 \right] = I_G(0) \exp \left[- \frac{R_g q^2}{3} \right] \quad (7.7)$$

where the size of the domain Ξ is related to the radius of gyration $R_g = \sqrt{3}\Xi$, representing the size of the domain consisting of the built-in inhomogeneity due to cross-linkers. $I_G(0) = I_G(q = 0)$ is related to the bulk modulus of the system [161]. For the swollen gel, the polymer concentration is generally within the semidilute regime, and in the high q -range, the scattering due to inhomogeneities can be ignored, and the scattering function is given by:

$$I_L(q) = \frac{I_L(0)}{\left\{ 1 + \left[(D + 1)/3 \right] \xi^2 q^2 \right\}^{D/2}} \quad (7.8)$$

where $I_L(0)$ relates to the osmotic modulus of the system. Eq.7.8 is the generalized Ornstein-Zernike equation for polymer solutions. It describes the polymer gel network consisting of uncorrelated polymer mesh domains of size ξ , in which the polymer chains are correlated with each other and have fractal dimension D [162]. ξ is in the range of 10 nm for swollen gels, and is much smaller than Ξ . For large q , Eq.7.8 predicts an asymptotic behavior of $I(q) \sim q^{-D}$. In the case of ideal polymer chains, the dimension $D = 2$ and $I(q) \sim q^{-2}$ is recovered. The same result is obtained for polymers in a Θ solvent. The simple addition of the above two contributions often constructs the scattering from the gel samples:

$$I(q) = I_G(0) \exp\left[-\frac{R_g^2 q^2}{3}\right] + \frac{I_L(0)}{\left\{1 + [(D+1)/3] \xi^2 q^2\right\}^{D/2}} \quad (7.9)$$

By fitting the data with this model, we can extract the radius of gyration R_g of the domain consisting of inhomogeneities originating from cross-linking, and the correlation length ξ of the polymer chain blobs. In the q -range where $q > \xi^{-1}$, the structure factor shows asymptotic behavior $\sim q^{-D_m}$, where the mass fractal dimension D_m is related to the inverse of the Flory exponent. For the swollen chain in a good solvent, $D_m = 5/3$. $D_m = 2$ describes a Gaussian chain, and $D_m = 3$ describes collapsed chains.

7.4.2 Characterization of the hydrogel internal structure

In Fig.7.13, SANS data of the swollen gel and the gel with skin are summarized together with fits using the model introduced in Eq.7.9. For the swollen gel at 20 °C, we obtained $R_g = (57 \pm 3)$ nm, $\xi = (7.8 \pm 0.5)$ nm, and $D_m = 1.59 \pm 0.04$. Note that the correlation length is very similar to that of 2 mol.% BIS microgels, which have a similar cross-linker concentration [201, 149]. This is reasonable considering that the internal structures of the gel and the microgel are similar. At 20 °C, D_m is close to 5/3, which is the asymptotic behavior expected for polymer chains in good solvents. For the swollen gel with skin at 45 °C, we obtained $R_g = (62 \pm 4)$ nm, $\xi = (90 \pm 7)$ nm, and the dimension $D = 3.94 \pm 0.25$. However, having a dimension of $D = 4$ for this system is not realistic, and $\xi > R_g$ is observed, which is not expected by the model. Consequently, it may be necessary to explore a different model to accurately describe the internal structure of the gel at high temperatures. The exponent of -4 suggests scattering from a smooth surface; however, it is not clear what this surface is. Although the deswollen gel still contains a significant

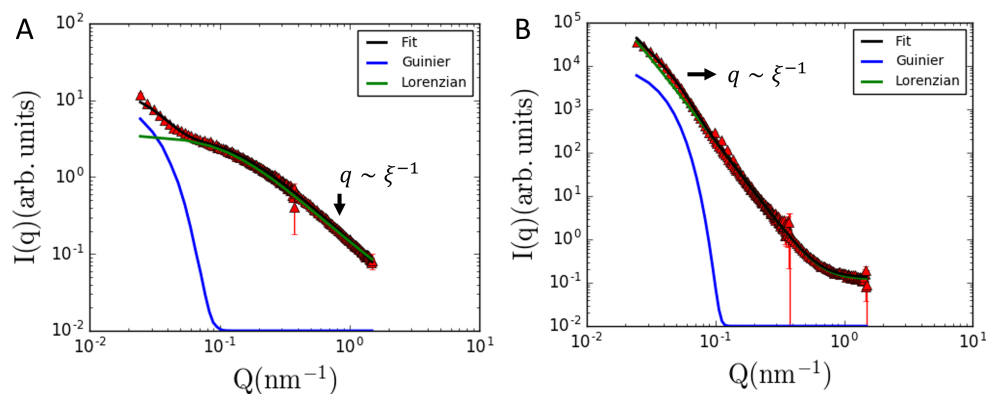


Figure 7.13: SANS data and fits for hydrogel. A: Swollen gel at 20 °C and fits of the data. B: Gel with skin at 45 °C and fits of the data. The Guinier function (blue line) and the Lorenzian function (green line) of Eq.7.9 are plotted separately to show the contribution of each function. $q \sim \xi^{-1}$ is marked by the black arrow.

amount of water, it is possible that the skin surface appears quite smooth on the length scale corresponding to the low-range of the SANS measurement. The radius of gyration R_g does not change significantly at two temperatures; however, we observe a sharp increase in the correlation length. The correlation length ξ corresponds to the distance in the real space in which the order is lost. The sharp increase in ξ indicates the formation of features that reflect correlation over a larger distance than those in the swollen gel.

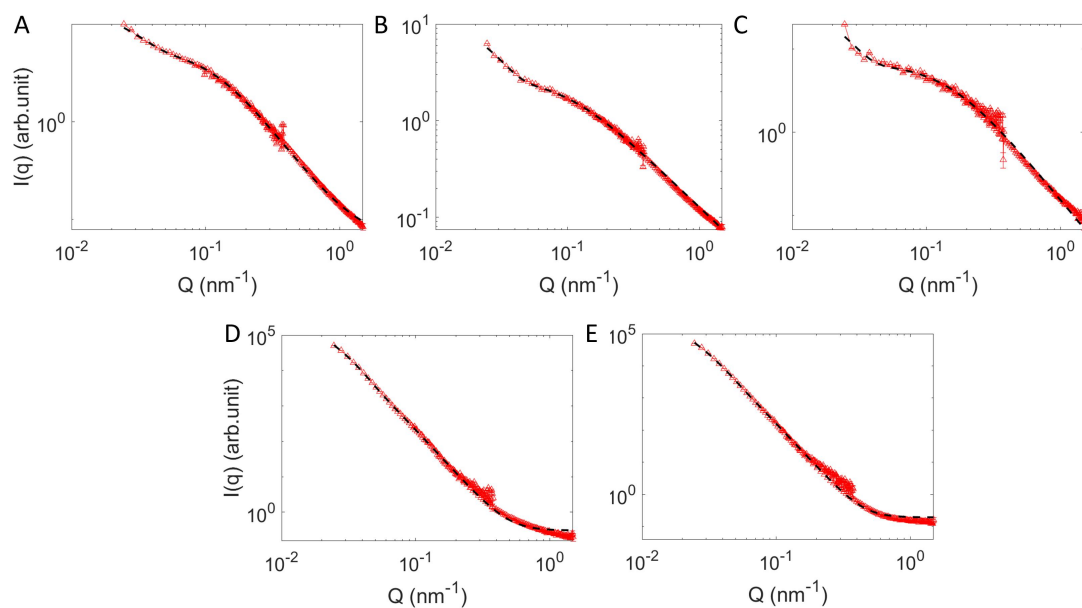


Figure 7.14: SANS data and fits for hydrogel at increasing temperatures. A: gel at 25 °C. B: gel at 32 °C. C: gel at 34 °C. D: gel at 36 °C. E: gel at 43 °C.

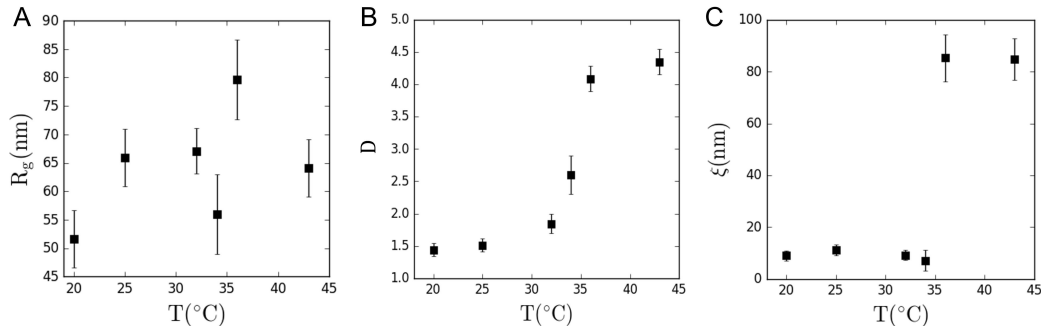


Figure 7.15: Fitting results of the gel under increasing temperatures. A: The radius of gyration R_g is plotted with respect to temperature. B: The dimensions D are plotted with respect to the temperature.

The change in parameters as the gel is heated gradually is shown in more detail in Fig.7.14. The model describes the data well at all temperatures. For small T , the upturn in the low- q range is due to large features, having length scales described by the radius of gyration R_g , as shown by the Guinier plot in Fig.7.13A. At higher T , the scattering intensity shows an asymptotic behavior characterized by the Lorentzian with correlation length ξ and fractal dimension D , as shown by the Lorentzian plot in Fig.7.13B. We have observed that the dimension D , and the correlation length ξ increase dramatically near the volume phase transition temperature $T_{\text{LCST}} \approx 33^{\circ}\text{C}$. The largest q that can be included in the Guinier region is $qR_g = 1.0$, which gives $q \approx 0.03 \text{ nm}^{-1}$. This indicates that the Guinier regime is nearly inaccessible with the smallest available q . As a result, the radius of gyration R_g does not show a strong temperature dependence, as shown in Fig.7.15A. The dimension D_m increases from $D_m \sim 1.5$ at 20°C to $D_m \approx 2.0$ near the transition temperature, indicating the change from a good solvent to a Θ solvent. At even higher T , the D_m increases further to $D_m \approx 3.0$ at $T \approx 35^{\circ}\text{C}$, suggesting the formation of the clustered network in a bad solvent. Lastly, at the highest temperatures, the asymptotic behavior follows the Porod law with $I(q) \sim q^{-4}$. The correlation length ξ remains nearly constant below the phase transition temperature and is comparable to that of microgels in similar conditions. Above the transition temperature, ξ increases dramatically. For the hydrogel, the increase in ξ indicates the formation of structures with a large correlation length, possibly reflecting the inhomogeneities due to the distribution of crosslinkers [33, 32]. The result also indicates that the behavior of the deswollen gel is comparable to that of the gel that is swollen with the skin. Lastly, the scattering intensity of the deswollen gel is comparable to that of the swollen gel with

the skin. The larger ξ of the deswollen polymer chain indicates the formation of objects ordered over a large distance, which can have a larger volume V compared to that of the swollen gel. Since the intensity of the scatter $I(q)$ is proportional to V^2 , $I(q)$ increases dramatically compared to swollen chains, again indicating that the characteristics of the polymer skin are similar to those of the deswollen gel.

7.5 Neutron imaging: direct visualization of the polymer skin

To directly visualize and capture the change in the hydrogel in response to rapid temperature changes, neutron imaging techniques are used to monitor the hydrogel. The neutron imaging experiment is performed at NEUTRA at the neutron spallation source SINQ, Paul Scherrer Insitut. NEUTRA uses thermal neutrons with an energy of 25 meV to perform radiography. The detector is a CMOS digital camera system that detects on a neutron scintillator screen. The maximum field of view is $(30 \times 30) \text{ cm}^2$, in our measurement, the field of view $(15 \times 15) \text{ cm}^2$ with a pixel resolution of $50 \mu\text{m}$ is applied. The sample environment is shown in Fig.7.16. An aluminum holder is mounted on top of a heat plate as a heat reservoir and a quartz glass container is inserted inside the holder, with the gel standing at the center, as shown in Fig.7.16A.

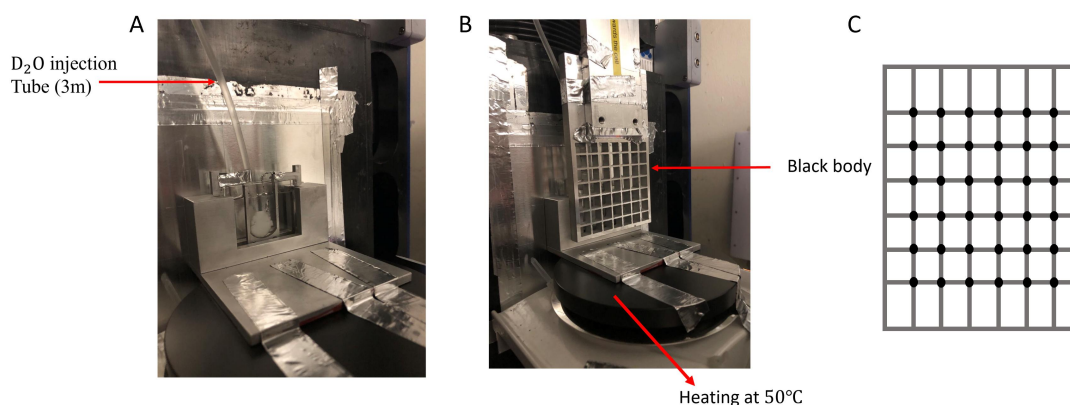


Figure 7.16: Sample environment used for hydrogel measurement at NEUTRA. A: hydrogel swollen with H_2O is placed in the quartz glass container placed in front of the neutron scintillator screen. The glass container is mounted on an aluminum holder placed on top of a heat plate. A tube is used for injection of D_2O . B: The black body grid is placed in front of the glass container. The temperature is set to 50°C during the measurement. C: Schematic of the black body grid.

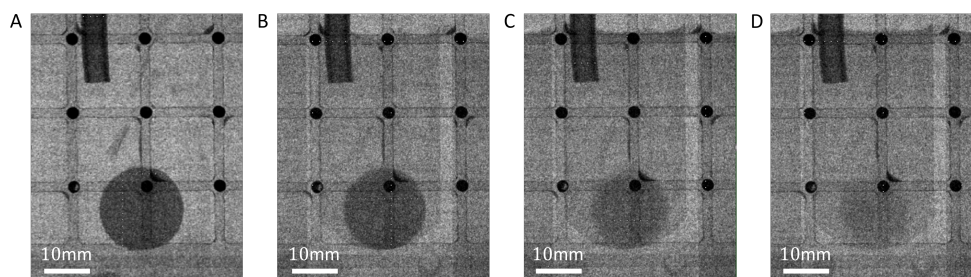


Figure 7.17: The raw images of the hydrogel contain H_2O with 1s exposure time. The large, dark circular object is the macrogel and the smaller black dots are the absorbing points on the grid. The dark tube in the upper left corner is used for the injection of D_2O . A: Hydrogel in an empty glass container at $t = 0$ min. B: Immediately after hot injection of D_2O . C: 5 min after injection. D: 10 min after injection.

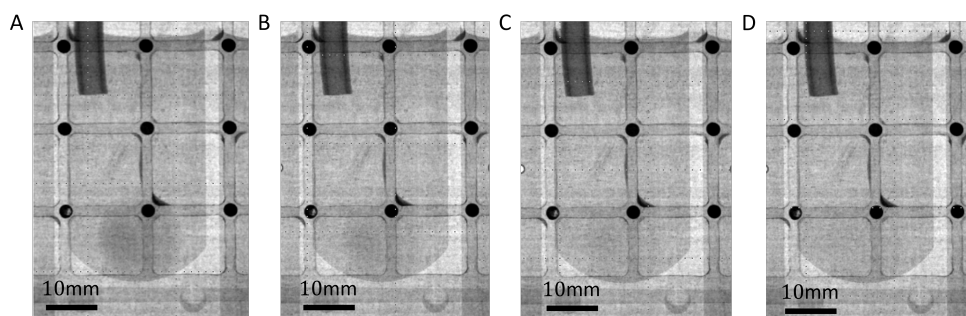


Figure 7.18: The raw images of the hydrogel contain H_2O with 30s exposure time. A: 15 min after injection. B: 30 min after injection. C: 45 min after injection. D: 60 min after injection.

The hydrogel is swollen with H_2O , while hot D_2O is used to achieve a rapid temperature change. As the skin evolves in a matter of seconds, it is important to capture the gel transition immediately after the rapid temperature increase. This is achieved by injecting D_2O during image acquisition. First, the swollen gel sample containing H_2O is placed in the empty glass container at room temperature. Subsequently, we mount the glass container on the preheated aluminum holder at 50°C in front of the scintillator and begin to acquire images. After a few seconds, hot D_2O at 80°C is injected through a three-meter long tube into the glass container. Due to heat dissipation within the tube, D_2O cools down to 45°C when it reaches the sample container. This results in the desired rapid temperature increase. The temperature is maintained by the heat plate underneath the aluminum holder. During the measurements, a black body grid is placed in front of the sample facing the incident neutrons, as shown in Fig.7.16B. The black body grid is made of aluminum and has a neutron-absorbing gadolinium dot at each of the grid points, as shown

in Fig.7.16C. It helps to correct the images from the sample scattering intensity to obtain intensities only due to linear attenuation by the samples. This will be discussed in more detail in the next section. The sample was measured for one hour, and two exposure times are used. The exposure time of the image describes the measurement time where the intensities are accumulated. As the gel evolves rapidly immediately after the temperature change, the exposure time is 1 s for the first ten minutes of measurement. After that, the exposure time is 30 s to achieve better image quality. As the gel is swollen with H₂O, incoherent scattering is significant and the gel appears dark, while the D₂O bath appears nearly transparent. The strong contrast between H₂O and D₂O allows monitoring the diffusion of water in or out of the gel network. It also makes it possible to identify the water-poor regime inside the gel and possibly detect the skin directly. The raw images of the hydrogel are shown in Fig.7.17 and in Fig.7.18. After injection of D₂O, the contrast between the gel and the solvent background diminishes. Especially for images with an exposure time of 30 s, there is no contrast between the gel and the solvent bath 45 min after injection, as shown in Fig.7.18. This is due to the exchange of H₂O within the gel and the D₂O in the bath. As the brightness of the solvent remains about the same, there is no external change in the solvent; therefore, it must be a mixing of the D₂O injected and the D₂O inside the macrogel. However, this suggests the possibility that the skin is still permeable to solvent exchange, despite preventing the gel from reaching the deswollen state.

7.5.1 Data reduction

The image correction using a black body grid is based on the conventional open beam method to normalize the raw images. The procedure requires the dark current image I_{DC} , and the raw image I^* , which is related to the sample image I and the dark current I_{DC} as $I^* = I + I_{DC}$. The raw open beam image I_{OB}^* is the reference image taken with sample without D₂O. I_{OB}^* relates to the open beam image I_{OB} and the dark current image as $I_{OB}^* = I_{OB} + I_{DC}$. The sample image normalized by the open beam image is obtained according to [24, 15] as:

$$\frac{\tilde{I}}{\tilde{I}_{OB}} = \frac{I}{I_{OB}} \cdot \frac{D(I_{OB})}{D(I)} = \frac{(I^* - I_{DC})}{(I_{OB}^* - I_{DC})} \cdot \frac{D(I_{OB}^* - I_{DC})}{D(I^* - I_{DC})} \quad (7.10)$$

where $\tilde{I} = I/D(I)$ and $\tilde{I}_{OB} = I_{OB}/D(I_{OB})$ are the normalized images. The operator D calculates the average pixel intensity in the region of interest. Dividing the intensity I by $D(I)$ allows correcting for possible fluctuation of the neutron beam due

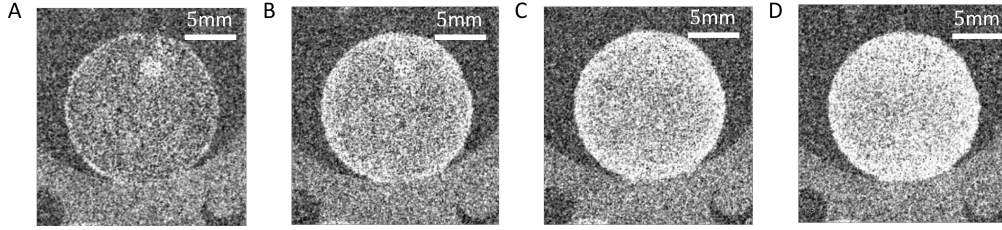


Figure 7.19: The processed image normalized with the open beam image. A: Immediately after hot injection of D_2O . B: 3 min after injection. C: 7 min after injection. D: 10 min after injection. The dot on the gel is due to the black body.

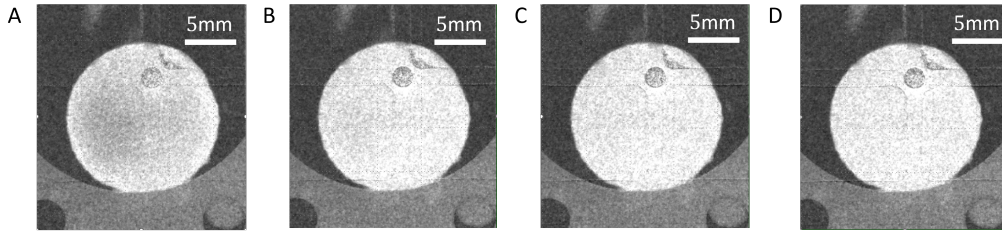


Figure 7.20: The processed images of the hydrogel contain H_2O with 30 s exposure time. A: 15 min after injection. B: 30 min after injection. C: 45 min after injection. D: 60 min after injection. The dot on the gel is due to the black body.

to the spallation source. To account for the scattering originating from the sample and sample environment, the black body grid (BB) is placed close to the sample facing the incoming beam. The grid is made of aluminum with black bodies at the junction of the grid that absorb neutrons. The signal detected at the corresponding black dots on the scintillator is essentially due to scattered neutrons. Considering this, the raw image intensity becomes $I^* = I + I^s + I_{DC}$, and the raw open beam intensity becomes $I_{OB}^* = I_{OB} + I_{BG}^s + I_{DC}$. Here, the open beam image is taken with sample and BB without D_2O . I_{BG}^s and I^s are the backgrounds containing the scattering intensity of the sample, which are measured in pixels covered by the black bodies. These measurements are then subtracted from the raw image I to obtain a full image of the scattering background. The sample intensity normalized by the open beam intensity can now be obtained as

$$\frac{\tilde{I}}{\tilde{I}_{OB}} = \frac{I}{I_{OB}} \cdot \frac{D(I_{OB})}{D(I)} = \frac{(I^* - I_{DC}) - I^s}{(I_{OB}^* - I_{DC}) - I_{BG}^s} \cdot \frac{D(I_{OB}^* - I_{DC} - I_{BG}^s)}{D(I^* - I_{DC} - I^s)} \quad (7.11)$$

Following the procedure defined in Eq.7.11, we obtain the processed images and are shown in Fig.7.19. The open beam image used to normalize the raw image is shown in Fig.7.17A. In the processed images, the difference is highlighted by the lighter color, while the darker color emphasizes the similarities. As shown in Fig.7.19A, a

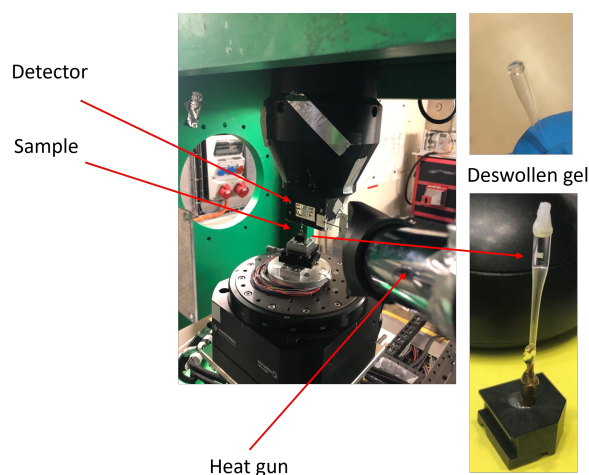


Figure 7.21: The sample environment of BOA. The capillary is mounted in front of the scintillator. The heat gun is pointing to the sample to perform the rapid heating. The inserts show the fully swollen gel inside the capillary and the deswollen gel after the experiment.

white ring appears right after injection. This might be caused by the shrinking of the gel upon heating, corresponding to the decrease in gel radius shown in Fig.7.1. As the gel evolves over time, the darker region inside the sample reduces to the center area of the gel, indicating the H_2O -rich regime, while the D_2O - H_2O exchange reducing the overall contrast of the gel with respect to the background. From the images processed with an exposure time of 30 s, the region to the left of the gel contains a higher amount of H_2O . The H_2O -rich region becomes less obvious as the experiment progresses. Eventually, there is almost no contrast change between the gel and the solvent background. Despite that, the gel still maintains its swollen size at the end of the experiment, as shown in Fig.7.20D. At this stage, the composition of the solvent inside the gel is very similar to that of the solvent bath.

In addition to the NEUTRA beamline, we also used the imaging beamline BOA at the Paul Scherrer Institut. BOA uses the SINQ cold source and the Micro-setup of the CCD camera box, in which a sensitive microstructured scintillator and magnifying optics are used for data acquisition. The Micro-setup provides a field of view of $(27.5 \times 27.5) \text{ mm}^2$ with a pixel size of $13.5 \mu\text{m}$, which is nearly five times better than that of the NEUTRA beamline[184]. The experimental setup is shown in Fig.7.21. The sample container is a quartz glass capillary. The capillary is filled with D_2O and the cylindrical gel, prepared also in D_2O , is cut from the bulk sample using the open end of the capillary. The capillary is sealed with parafilm to prevent evaporation. The cylindrical gel has a dimension of $(2 \pm 0.2) \text{ mm}$ in diameter and

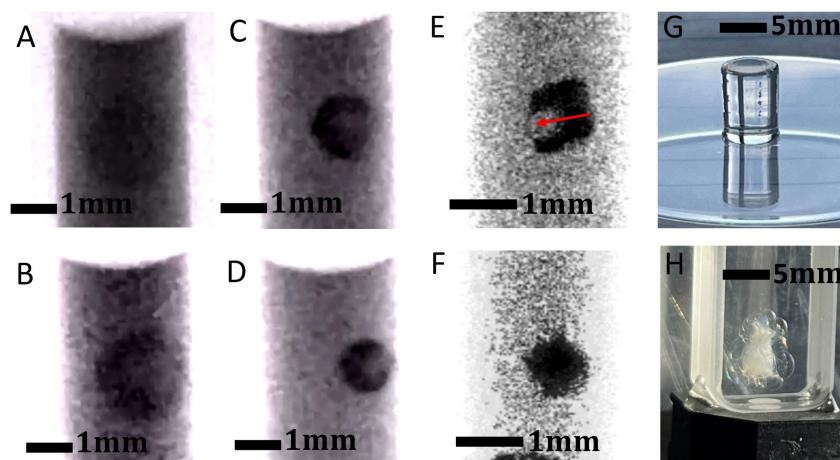


Figure 7.22: Hydrogel images taken at BOA with 30 s exposure time. A: Fully swollen gel with circular face facing out. B: 1 min after rapidly applying heat. C: 2 min later. D: 3 min after rapid heating. E: gel sample with rectangular side facing out, 1 min after rapid heating. A visible boundary between the gel and the solvent bath is detected (red arrow), highlighting the ballooning of the gel upon rapid heating. F: gel in the deswollen state 4 min after rapid heating, corresponding to the deswollen gel shown in the insert of Fig.7.21. G: A cylindrical gel in the swollen state with diameter of 5.0 mm and height of 6.5 mm. H: A cylindrical gel under rapid heating at 45°C. The center of the gel tends to deswell, expelling the solvent to the gel surface. The surface skin traps the solvent from escaping and ballooning pattern is observed.

(3 ± 0.3) mm in height. As shown in Fig.7.21, the capillary is mounted on a stand that is magnetically attached in front of the scintillator. Rapid heating is achieved with a heat gun. The hot air blows directly to the sample cell, and images are acquired to capture the behavior of the gel upon heating. In Fig.7.22, the images with 30 s exposure time are shown. Upon rapid heating with the heat gun, the gel shrunk and did not remain at its swollen size. However, we notice that, when viewing from the circular side of the gel, it becomes "donut-shaped" during shrinking, where the center appears to be more transparent compared to the edge of the gel. Since both the solvent bath and the gel contain D_2O , the darker areas in the image are due to neutron incoherent scattering by the protonated polymer chains. As shown in Fig.7.22A-D, the darker regions indicate a higher polymer concentration. More interestingly, the dark region becomes discontinuous on the right side of the gel, and the gel appears to bulge out toward the capillary wall. This behavior is better captured by measuring the rectangular side of the gel, where the gel shows a balloon filled with D_2O before reaching the deswollen state, as shown in 7.22E-

F. This balloon-forming behavior is demonstrated in Fig.7.22G-H, and has been reported in previous works [19, 36]. The boundary shown in Fig.7.22E contains 2-3 pixels corresponding to $25\ \mu\text{m}$ to $40\ \mu\text{m}$ in thickness. Eventually, the gel reaches the deswollen state. This could be due to how we heat; we blow hot air on the sample, which may cause a large temperature gradient and uneven heating of the gel. Ultimately, this may result in poor skin formation. However, for the gel to exhibit ballooning, the skin has to present, indicating that the characteristic of the skin is nevertheless captured in this measurement.

7.6 Summary

In this chapter, we have demonstrated that the skin formation of the gel can be triggered by rapid heating, whereas the gel reaches the deswollen state by heating progressively. We performed uniaxial compression experiments of a disk-shaped gel in swollen and deswollen phases, as well as in conditions for it to form a deswollen skin. By treating the gel with skin as a three-layered composite material, we are able to estimate the skin thickness using the Modified Rule of mixture (MRM) model. The thickness of the skin is in the range of $50\ \mu\text{m}$. We also studied the internal structure of the gel in these states via SANS. We extracted the correlation length corresponding to the skin, as well as the fractal dimension D , which reveals the mass fractal dimensions of the scatterers. Lastly, neutron imaging techniques were used to study the diffusion of water in and out of the gel and directly image the skin. Small cylindrical gels are found to exhibit ballooning behavior with a visible boundary between the gel and the solvent interface. The results indicate that the dense skin does prevent the gel from reaching the deswollen state. However, water can nevertheless diffuse through the skin. This suggests that the two-phase state with skin and a swollen interior is not only stabilized by the skin trapping the solvent in the interior but also by the rigid structure of the skin.

Chapter 8

Conclusion and Outlook

The work presented in this thesis was originally inspired by experimental observations in which a large microgel introduced in a sea of smaller, but otherwise identical ones, was found to shrink to the size of the smaller microgels. This results in an overall reduction of the suspension polydispersity (PD), rendering the suspension susceptible to crystallization, despite having an initially high polydispersity (PD). This was an unexpected finding that clearly reflected the difference between soft and hard colloids, as crystallization of hard-sphere colloidal suspensions is suppressed at $PD \geq 12\%$. This spontaneous deswelling behavior of pNIPAM microgels was further investigated in subsequent works [150, 149]. The structure of the monodisperse and bidisperse suspensions was studied by Small-angle Neutron Scattering (SANS) and Small-angle X-ray Scattering (SAXS). It was been observed that the microgel suspension can crystallize up to $PD \sim 19\%$ [150]. The freezing and melting point of the suspension is largely dependent on the deswelling mechanism of the large particles, which are usually the softest. Furthermore, SANS measurements, together with osmotic pressure measurements, revealed that spontaneous deswelling is triggered by an increase in the osmotic pressure of the suspension due to the ions. pNIPAM is uncharged, but because of the ionic initiator used in its synthesis, almost all microgels carry charged groups in their periphery and are expected to be surrounded by counterion clouds. Together, these results lead to the theory that spontaneous deswelling is caused by the percolation of counterion clouds at high particle concentrations. When percolation of the clouds occurs, the suspension osmotic pressure increases and, if it is comparable to or greater than the microgel bulk modulus, deswelling occurs. However, a detailed study of the deswelling mechanism over the concentration range for particles with different softness, as well as the direct characterization of the counterion cloud, was missing.

The internal structure, shape, and size of the microgel from $\zeta \sim 0.02$ to $\zeta \sim 1.2$ have been extracted by SANS. Our results indicate that the microgels remain in their swollen size at low concentrations and begin to deswell isotropically above a critical concentration ζ_c . The theory suggests that the deswelling should be triggered by counterion cloud percolation, which occurs when microgels, including their surface counterion cloud of width ΔR occupy the entire suspension volume. By rescaling the volume fraction ϕ to obtain a ϕ_{eff} , defined in terms of an effective particle radius $R_{\text{SANS}} + \Delta R$, and considering that spontaneous deswelling occurs at $\phi_{\text{eff}} = 1$, we can extract the width of the counterion cloud ΔR . This indirect method produces a cloud width on the order of 45nm, which is in good agreement with prior results [150, 204]. In addition, the polydispersity of the microgel core decreases with increasing ζ due to compression of the largest microgels, which are usually the softest. Importantly, polydispersity plays a different role for soft particles, as polydispersity is not fixed but can vary with concentration. Therefore, polydispersity must be taken into account for both the form factor $P(q)$ and the structure factor $S(q)$ to obtain reliable results.

Despite all of the evidence that points to the fact that there is a counterion cloud at the microgel periphery, a direct measurement of the cloud was never obtained. Several methods have been applied to determine the distribution of chemical elements in a material; however, because the ion density in the cloud is low, none of them work for our purposes. Through dialysis, microgels are forced to have either Na^+ or NH_4^+ . Taking advantage of their large difference in scattering length density, SANS with contrast variation enables extracting an amplified counterion cloud signal by directly subtracting the scattering intensities in the presence of either ion, $I^{\text{NH}_4^+}(q) - I^{\text{Na}^+}(q)$. The cloud signal can be fitted to a spherical shell model, and the results clearly indicate that counterion clouds are located in the microgel periphery. The width of the cloud is on the order of 45 nm, which is in agreement with the result obtained with the indirect method by rescaling ϕ mentioned above. Our findings are important input for the development of models to describe the suspension phase transition of soft colloids, such as microgels.

The deswelling mechanism is further investigated with an increasing particle stiffness controlled by the cross-link density. Our results show that microgels begin to deswell at a higher ζ with increasing stiffness, indicating that higher osmotic pressure is required to compress stiffer particles. In addition, the balance between the osmotic pressure and the elastic properties of the microgel is an important factor in the development of a model for the behavior of microgel suspensions, which can

predict microgel deswelling with increasing concentration. Our work is the first direct measurement of the dilute ion cloud with ion density that is nearly four orders of magnitude smaller than that of micelles or DNA. The contrast variation method with ion species has been proven to be robust and can be useful in the investigation of the structures of both soft and hard colloids. By varying the cross-link density, microgels with different softness, charge distribution in the fuzzy shell, and counterion cloud width can be synthesized such that the microgel deswelling mechanism can be tailored for applications such as biological sensors and drug delivery vehicles.

Counterion clouds clearly have an effect on the swelling behavior and the crystallization of polydisperse suspensions, and because of this, it is of interest to learn about the effect of the counterion cloud on the microgel-microgel interaction. The nature of this interaction can be studied in microgel crystals using confocal microscopy. Microgels used in this work are pNIPAM copolymerized with acrylic acid (AAc) with a fluorescent core. Measurements are carried out at $\text{pH} \sim 3.5$ and $\text{pH} \sim 7.0$, which corresponds to the AAc being uncharged and charged, respectively. Our results show that microgels crystallize as random stacking of face-centered cubic (fcc) and hexagonal close-packed (hcp) crystals, which agrees with the structure expected for hard colloidal crystals. This work is also inspired by the study of crystals of charged hard colloids, where the macroions are surrounded by much smaller microions. The strong screening resulting from the microions causes a noncentral interaction among the macroions, and the simple addition of pairwise radially symmetric interaction potentials, such as the DLVO potential, become insufficient to describe such systems. In this study, normal modes, the basic lattice excitations in a crystal, are obtained from confocal images that allow tracking of all observed microgels. The observed deviations of the microgels from their lattice sites show that the colloidal crystal essentially behaves as a harmonic crystal and the equipartition theorem can be applied to study the measured normal modes. This allows extraction of the force constants. The observation of non-central forces highlights the importance of counterion clouds, which control the microgel swelling and also have an important impact on the interaction in concentrated (crystalline) suspensions. The force constants and elastic constants obtained indicate that the interaction is non-central regardless of pH. It is reasonable to assume that the noncentral force is a direct consequence of the counterions, and the non-pairwise interaction should be considered when modeling the behavior of microgels that are charged or peripherally charged. Our work highlights the need to develop an interaction model that takes deswelling and non-central forces into account. Further experiments can be

performed for a series of concentrations, and it would be interesting to investigate whether the non-centrality appears with microgel deswelling or if it is also present at lower concentrations. In addition, crystals consisting of truly neutral microgels synthesized without ionic initiators are of interest, as the effects of charges would not be present, enabling the effect of particle softness to be characterized more rigorously.

The volume phase transition of microgels is well described by the Flory-Rehner model. Although there are many similarities between micro and macrogels, this model may be insufficient to describe the macrogel in phase coexistence states. It has been demonstrated that when the first-order transition temperature is rapidly approached, macrogel deswelling is arrested, and both the deswollen and swollen states coexist at a constant volume for a prolonged time period. The coexistent phases are located in a polymer-dense skin at the gel periphery and a solvent-rich interior; the skin is what helps maintain a constant volume of the gel. Furthermore, it is reported that the skin grows inward and eventually allows the gel to reach the deswollen state. In previous work [36], shear rigidity has been reported to provide a stabilizing effect on the gel above the phase transition temperature T_{LCST} . As a result, the free energy of the macrogel is assumed to be a function of the shear modulus of the gel, the volume fractions of the skin and the swollen interior, and the energy resulting from the polymer-solvent mixing. Since the shear rigidity is coupled with shape, various morphologies, such as bamboo-like and balloon-like structures, are observed for cylindrical and toroidal gels, respectively. For the study of the state with phase coexistence, the skin thickness and its internal structure are key parameters, since these parameters are needed to calculate the free energy and determine the diffusion rate of the solvent molecules from the gel. In this work, a disk-shaped gel is brought to the coexistent phase by rapid heating, where the gel remains at its swollen size and shape above T_{LCST} . Via SANS, the internal structure of the gel is extracted in the swollen, deswollen, and coexistent states. The result shows an increase in the high- q exponent related to the fractal dimension of the gel and the correlation length for the deswollen and coexistent states, indicating the formation of fractal structures due to a collapsed polymer network, respectively. Furthermore, using rheology and neutron imaging measurement, the average skin thickness is obtained on the order of $(45 \pm 6) \mu\text{m}$. For future development of this work, AFM and other indentation equipment can be applied to analyze the skin thickness; by probing the same region over time after rapid heating, the growth of the skin could be monitored. Moreover, the low- q upturn is not fully observed and, therefore, it would be good to measure the gel at lower q using USANS or light

scattering. Neutron tomography can be applied to carefully monitor the diffusion of water molecules and the growth of the skin. Different observed behaviors such as skin formation and ballooning suggest that it is of interest to study the crosslink distribution from the surface toward the interior of the gel. Additionally, macrogels with tailored internal structures, such as the distribution of cross-linkers, can be explored to understand how the internal inhomogeneities alter the coexistent phases of the macrogel under rapid heating. The development of this work can be used to synthesize macrogels with desired properties, where the thermodynamic instabilities can be utilized to achieve dramatic shape actuation for various applications, such as smart sensors and smart braille devices in haptic technology.

Bibliography

- [1] Rupal Agrawal and David A Kofke. Thermodynamic and structural properties of model systems at solid-fluid coexistence: I. fcc and bcc soft spheres. *Molecular physics*, 85(1):23–24, 1995.
- [2] S. Alexander, P. M. Chaikin, P. Grant, G. J. Morales, P. Pincus, and D. Hone. Charge renormalization, osmotic pressure, and bulk modulus of colloidal crystals: Theory. *J. Chem. Phys.*, 80(11):5776–5781, 1984.
- [3] JI Amalvy, EJ Wanless, Y Li, V Michailidou, SP Armes, and Y Duccini. Synthesis and characterization of novel ph-responsive microgels based on tertiary amine methacrylates. *Langmuir*, 20(21):8992–8999, 2004.
- [4] T. Amiya, Y. Hirokawa, Y. Hirose, Y. Li, and T. Tanaka. Re-entrant phase-transition of n-isopropylacrylamide gels in mixed solvents. *J. Chem. Phys.*, 86:2375, 1987.
- [5] M. Andersson and S. L. Maunu. Structural studies of poly(n-isopropylacrylamide) microgels: Effect of sds surfactant concentration in the microgel synthesis. *Journal of Polymer Science: Part B: Polymer Physics*, 44:3305–3314, 2006.
- [6] Neil W Ashcroft and N David Mermin. *Solid state physics*. Cengage Learning, 2022.
- [7] NW Ashcroft and David C Langreth. Structure of binary liquid mixtures. i. *Physical Review*, 156(3):685, 1967.
- [8] Sajjad Ashraf, Hun-Kuk Park, Hansoo Park, and Soo-Hong Lee. Snapshot of phase transition in thermoresponsive hydrogel pnipam: Role in drug delivery and tissue engineering. *Macromolecular Research*, 24:297–304, 2016.
- [9] V.K. Aswal, P.S. Goyal, S. De, S. Bhattacharya, H. Amenitsch, and S. Bernstorff. Small-angle x-ray scattering from micellar solutions of gemini surfactants. *Chemical Physics Letters*, 329(5):336–340, 2000.
- [10] Takuya Azuma and Takayuki Kei. Super-resolution spinning-disk confocal microscopy using optical photon reassignment. *Optics Express*, 23(11):15003–15011, 2015.
- [11] GK Batchelor. The effect of brownian motion on the bulk stress in a suspension of spherical particles. *Journal of fluid mechanics*, 83(1):97–117, 1977.

- [12] Yuxing Ben, Ian Robb, Peng Tonmukayakul, and Qiang Wang. Microgels for oil recovery. *Microgel suspensions: fundamentals and applications*, pages 407–422, 2011.
- [13] Maxime J. Bergman, Nicoletta Gnan, Marc Obiols-Rabasa, Janne-Mieke Meijer, Lorenzo Rovigatti, Emanuela Zaccarelli, and Peter Schurtenberger. A new look at effective interactions between microgel particles. *Nature Communications*, 9(1):5039, 2018.
- [14] Bertrand Blau, Kurt N Clausen, S Gvasaliya, M Janoschek, S Janssen, L Keller, B Roessli, J Schefer, Ph Tregenna-Piggott, W Wagner, et al. The swiss spallation neutron source sinq at paul scherrer institut. 2009.
- [15] P Boillat, C Carminati, F Schmid, C Grünzweig, J Hovind, A Kaestner, D Mannes, M Morgano, M Siegwart, P Trtik, et al. Chasing quantitative biases in neutron imaging with scintillator-camera detectors: a practical method with black body grids. *Optics Express*, 26(12):15769–15784, 2018.
- [16] Giulia Bonacucina, Marco Cespi, Monica Misici-Falzi, and Giovanni F Palmieri. Colloidal soft matter as drug delivery system. *Journal of pharmaceutical sciences*, 98(1):1–42, 2009.
- [17] R Borrega, M Cloitre, I Betremieux, B Ernst, and L Leibler. Concentration dependence of the low-shear viscosity of polyelectrolyte micro-networks: From hard spheres to soft microgels. *EPL (Europhysics Letters)*, 47(6):729, 1999.
- [18] Redouane Borsali and Robert Pecora. *Soft-matter characterization*. Springer Science & Business Media, 2008.
- [19] Arezki Boudaoud and Sahraoui Chaieb. Mechanical phase diagram of shrinking cylindrical gels. *Physical Review E*, 68(2):021801, 2003.
- [20] Joseph M Brader, Robert Evans, and Matthias Schmidt. Statistical mechanics of inhomogeneous model colloid—polymer mixtures. *Molecular Physics*, 101(23-24):3349–3384, 2003.
- [21] J. Brijitta and P. Schurtenberger. Responsive hydrogel colloids: Structure, interactions, phase behavior, and equilibrium and nonequilibrium transitions of microgel dispersions. *Curr. Op. in Colloid & Interface Sci.*, 40:87–103, 2019.
- [22] M. Brunner, C. Bechinger, W. Strepp, V. Lobaskin, and H.H. von Gruenberg. Density-dependent pair interactions in 2d colloidal suspensions. *Europhys. Lett.*, 58(6):926–932, 2002.
- [23] M. Brunner, J. Dobnikar, H.-H. von Gruenberg, and C. Bechinger. Direct measurement of three - body interactions amongst charged colloids. *Phys. Rev. Lett.*, 92(7):078301, 2004.
- [24] Chiara Carminati, Pierre Boillat, Florian Schmid, Peter Vontobel, Jan Hovind, Manuel Morgano, Marc Raventos, Muriel Siegwart, David Mannes, Christian Gruenzweig, et al. Implementation and assessment of the black body bias correction in quantitative neutron imaging. *PLoS One*, 14(1):e0210300, 2019.

- [25] Ya-Wen Chang, Michael S Dimitriyev, Anton Souslov, Svetoslav V Nikolov, Samantha M Marquez, Alexander Alexeev, Paul M Goldbart, and Alberto Fernández-Nieves. Extreme thermodynamics with polymer gel tori: Harnessing thermodynamic instabilities to induce large-scale deformations. *Physical Review E*, 98(2):020501, 2018.
- [26] Guoping Chen, Yukio Imanishi, and Yoshihiro Ito. pH-sensitive thin hydrogel microfabricated by photolithography. *Langmuir*, 14(22):6610–6612, 1998.
- [27] Sow-Hsin Chen. Small angle neutron scattering studies of the structure and interaction in micellar and microemulsion systems. *Annual Review of Physical Chemistry*, 37(1):351–399, 1986.
- [28] J. Clark. Reactions of alkenes with sulfuric acid. <https://chem.libretexts.org>, 2020.
- [29] G. M. Conley, P. Aebischer, Nöjd, S., P. Schurtenberger, and F. Scheffold. Jamming and overpacking fuzzy microgels: Deformation, interpenetration, and compression. *Sci. Adv.*, 3:e1700969, 2017.
- [30] J. C. Crocker and D. G. Grier. Methods of digital video microscopy for colloidal studies. *J. Colloid Interface Sci.*, 179:298–310, 1996.
- [31] S. B. Debord and L. A. Lyon. Influence of particle volume fraction on packing in responsive hydrogel colloidal crystals. *J. Phys. Chem. B*, 107(13):2927–2932, 2003.
- [32] P. Debye, H.R. Anderson, and H. Brumberger. Scattering by an inhomogeneous solid. ii. the correlation function and its application. *J. Appl. Phys.*, 28(6):679–683, 1957.
- [33] P. Debye and A.M. Bruce. Scattering by an inhomogeneous solid. *J. Appl. Phys.*, 20:518–525, 1949.
- [34] G. Del Monte, D. Truzzolillo, F. Camerin, A. Ninarello, E. Chauveau, L. Tavagnacco, N. Gnan, L. Rovigatti, S. Sennato, and E. Zaccarelli. Two-step deswelling in the volume phase transition of thermoresponsive microgels. *Proc. Natl. Acad. Sci. USA*, 117(37):e2109560118, 2021.
- [35] J. K. G. Dhont. *An Introduction to Dynamics of Colloids*. Elsevier, 1996.
- [36] Michael S Dimitriyev, Ya-Wen Chang, Paul M Goldbart, and Alberto Fernández-Nieves. Swelling thermodynamics and phase transitions of polymer gels. *Nano Futures*, 3(4):042001, 2019.
- [37] Peter J Dowding and Brian Vincent. Suspension polymerisation to form polymer beads. *Colloids and Surfaces A: Physicochemical and Engineering Aspects*, 161(2):259–269, 2000.
- [38] K Dušek and Donald Patterson. Transition in swollen polymer networks induced by intramolecular condensation. *Journal of Polymer Science Part A-2: Polymer Physics*, 6(7):1209–1216, 1968.

- [39] T. Eckert and W. Richtering. Thermodynamic and hydrodynamic interaction in concentrated microgel suspensions: Hard or soft sphere behavior? *J. Chem. Phys.*, 129(12):124902, 2008.
- [40] Andreas Erbe, Klaus Tauer, and Reinhard Sigel. Ion distribution around electrostatically stabilized polystyrene latex particles studied by ellipsometric light scattering. *Langmuir*, 23(2):452–459, 2007. PMID: 17209593.
- [41] L. A. Fernández, V. Martín-Mayor, and P. Verrocchio. Phase diagram of a polydisperse soft-spheres model for liquids and colloids. *Phys. Rev. Lett.*, 98(8):085702, 2007.
- [42] A Fernandez-Barbero, A Fernandez-Nieves, I Grillo, and E Lopez-Cabarcos. Structural modifications in the swelling of inhomogeneous microgels by light and neutron scattering. *Physical Review E*, 66(5):051803, 2002.
- [43] Alberto Fernandez-Nieves, H Wyss, Johan Mattsson, and David A Weitz. *Microgel suspensions*. Wiley Online Library, 2011.
- [44] M Finot, S Suresh, C Bull, and S Sampath. Curvature changes during thermal cycling of a compositionally graded ni al₂o₃ multi-layered material. *Materials Science and Engineering: A*, 205(1-2):59–71, 1996.
- [45] Michael E Fisher. Correlation functions and the critical region of simple fluids. *Journal of Mathematical Physics*, 5(7):944–962, 1964.
- [46] P. J. Flory. *Principles of Polymer Chemistry*. Cornell University Press, Ithaca NY, 1953.
- [47] Paul J Flory and John Rehner Jr. Statistical mechanics of cross-linked polymer networks ii. swelling. *The journal of chemical physics*, 11(11):521–526, 1943.
- [48] Daan Frenkel. Soft particles feel the squeeze. *Nature*, 460(7254):465–466, 2009.
- [49] Daan Frenkel, RJ Vos, CG De Kruif, and A Vrij. Structure factors of polydisperse systems of hard spheres: A comparison of monte carlo simulations and percus–yevick theory. *The Journal of chemical physics*, 84(8):4625–4630, 1986.
- [50] J. Gao and Z. B. Hu. Optical properties of n-isopropylacrylamide microgel spheres in water. *Langmuir*, 18:1360, 2002.
- [51] U. Gasser and A. Fernandez-Nieves. Crystal structure of highly concentrated, ionic microgel suspensions studied by small-angle x-ray scattering. *Phys. Rev. E*, 81(5):052401, 2010.
- [52] U. Gasser, J. S. Hyatt, J.-J. Lietor-Santos, E. S. Herman, L. A. Lyon, and A. Fernandez-Nieves. Form factor of pnipam microgels in overpacked states. *J. Chem. Phys.*, 141(3):034901, 2014.
- [53] U. Gasser, J.-J. Lietor-Santos, A. Scotti, O. Bunk, A. Menzel, and A. Fernandez-Nieves. Transient formation of bcc crystals in suspensions of pNIPAM-based microgels. *Phys. Rev. E*, 88(5):052308, 2013.

- [54] U. Gasser, A. Scotti, and Alberto Fernandez-Nieves. Spontaneous deswelling of microgels controlled by counterion clouds. *Phys. Rev. E*, 99(4):042602, 2019.
- [55] Urs Gasser and Boyang Zhou. Accurate detection of spherical objects in a complex background. *Optics Express*, 29(23):37048–37065, 2021.
- [56] Urs Gasser, Florian Ziese, and Georg Maret. Characterization of local structures with bond-order parameters and graphs of the nearest neighbors, a comparison. *The European Physical Journal Special Topics*, 223(3):455–467, 2014.
- [57] Shivkumar V Ghugare, Ester Chiessi, Rainer Fink, Yuri Gerelli, Andrea Scotti, Antonio Deriu, Geraldine Carrot, and Gaio Paradossi. Structural investigation on thermoresponsive pva/poly (methacrylate-co-n-isopropylacrylamide) microgels across the volume phase transition. *Macromolecules*, 44(11):4470–4478, 2011.
- [58] Mitsuaki Ginoza and Makoto Yasutomi. Measurable structure factor of a multi-species polydisperse percus-yevick fluid with schulz distributed diameters. *Journal of the Physical Society of Japan*, 68(7):2292–2297, 1999.
- [59] D. Gottwald, C. N. Likos, G. Kahl, and H. Löwen. Phase behavior of ionic microgels. *Phys. Rev. Lett.*, 92(6):068301, 2004.
- [60] James M Griffin, Ian Robb, and Alexander Bismarck. Preparation and characterization of surfactant-free stimuli-sensitive microgel dispersions. *Journal of applied polymer science*, 104(3):1912–1919, 2007.
- [61] W. Groenewegen, A. Lapp, S. U. Egelhaaf, and J. R. C. van der Maarel. Counterion distribution in the coronal layer of polyelectrolyte diblock copolymer micelles. *Macromolecules*, 33(11):4080–4086, 2000.
- [62] Yu Gu, Toshio Nakamura, Lubos Prchlik, Sanjay Sampath, and Jay Wallace. Micro-indentation and inverse analysis to characterize elastic–plastic graded materials. *Materials Science and Engineering: A*, 345(1-2):223–233, 2003.
- [63] J.-P. Hansen and J.B. Hayter. A rescaled msa structure factor for dilute charged colloidal dispersions. *Molecular Physics*, 46(3):651–656, 1982.
- [64] J.B. Hayter and J. Penfold. An analytic structure factor for macroion solutions. *Molecular Physics*, 42(1):109–118, 1981.
- [65] Pascale Hazot, Thierry Delair, Christian Pichot, Jean-Paul Chapel, and Abdelhamid Elaissari. Poly (n-ethylmethacrylamide) thermally-sensitive microgel latexes: effect of the nature of the crosslinker on the polymerization kinetics and physicochemical properties. *Comptes Rendus Chimie*, 6(11-12):1417–1424, 2003.
- [66] T. Hellweg, C. D. Dewhurst, E. Brueckner, K. Kratz, and W. Eimer. Colloidal crystals made of poly(n-isopropylacrylamide) microgel particles. *Colloid Polym. Sci.*, 278:972–978, 2000.

- [67] Michael Heskins and James E Guillet. Solution properties of poly (n-isopropylacrylamide). *Journal of Macromolecular Science—Chemistry*, 2(8):1441–1455, 1968.
- [68] D. M. Heyes and A. C. Branka. Interactions between microgel particles. *Soft Matter*, 5(14):2681–2685, 2009.
- [69] J. S. Higgins and H. C. Benoît. *Polymers and Neutron Scattering*. Oxford University Press Inc., New York, 1994.
- [70] Rodney Hill. A self-consistent mechanics of composite materials. *Journal of the Mechanics and Physics of Solids*, 13(4):213–222, 1965.
- [71] Terrell L Hill. *An introduction to statistical thermodynamics*. Courier Corporation, 1986.
- [72] T. Hoare and R. Pelton. Highly ph and temperature responsive microgels functionalized with vinylacetic acid. *Macromolecules*, 37(7):2544–2550, 2004.
- [73] P. Holmqvist, P. S. Mohanty, G. Nägele, P. Schurtenberger, and M. Heinen. Structure and dynamics of loosely cross-linked ionic microgel dispersions in the fluid regime. *Phys. Rev. Lett.*, 109(4):048302, 2012.
- [74] W. G. Hoover and F. H. Ree. Melting transition and communal entropy for hard spheres. *Journal of Chemical Physics*, 49(8):3609, 1968.
- [75] William G. Hoover, Steven G. Gray, and Keith W. Johnson. Thermodynamic properties of the fluid and solid phases for inverse power potentials. *J. Chem. Phys.*, 55(3):1128–1136, 1971.
- [76] Sawyer S Hopkins, Amitabha Chakrabarti, and Jeremy D Schmit. Effects of non-pairwise repulsion on nanoparticle assembly. *The Journal of Chemical Physics*, 151(3), 2019.
- [77] Tom Hofken, Christian Strauch, Stefanie Schneider, and Andrea Scotti. Changes in the form factor and size distribution of nanogels in crowded environments. *Nano Letters*, 22(6):2412–2418, 2022.
- [78] A.-P. Hynninen and M. Dijkstra. Phase diagrams of hard-core repulsive yukawa particles. *Phys. Rev. E*, 68:021407, 2003.
- [79] Jacob N Israelachvili. *Intermolecular and surface forces*. Academic press, 2011.
- [80] A. St. J. Iyer and L. A. Lyon. Self-healing colloidal crystals. *Angew. Chem. Int. Ed.*, 48:4562–4566, 2009.
- [81] Shan Jiang, Antony Van Dyk, Alvin Maurice, James Bohling, David Fasano, and Stan Brownell. Design colloidal particle morphology and self-assembly for coating applications. *Chemical Society Reviews*, 46(12):3792–3807, 2017.
- [82] Crocker John and Weeks Eric. Particle tracking tutorial, <http://www.physics.emory.edu/faculty/weeks//idl/tracking.html>, 2006.

- [83] C. Jones and A Lyon. Synthesis and characterization of multiresponsive core-shell microgels. *Macromolecules*, 33(22):8301–8306, 2000.
- [84] B. Kang, H. Tang, Z. Zhao, and S. Song. Hofmeister series: Insights of ion specificity from amphiphilic assembly and interface property. *ACS Omega*, 5:6229–6239, 2020.
- [85] K. Kassapidou, W. Jesse, M. E. Kuil, A. Lapp, S. Egelhaaf, and J. R. C. van der Maarel. Structure and charge distribution in dna and poly(styrenesulfonate) aqueous solutions. *Macromolecules*, 30(9):2671–2684, 1997.
- [86] U. Keiderling. The new ‘bersans-pc’ software for reduction and treatment of small angle neutron scattering data. *Applied Physics A*, 74(1):s1455–s1457, 2002.
- [87] O Kesler, M Finot, S Suresh, and S Sampath. Determination of processing-induced stresses and properties of layered and graded coatings: Experimental method and results for plasma-sprayed ni al₂o₃. *Acta materialia*, 45(8):3123–3134, 1997.
- [88] RJ Ketz, RK Prud’homme, and WW Graessley. Rheology of concentrated microgel solutions. *Rheologica acta*, 27:531–539, 1988.
- [89] Steven R Kline. Reduction and analysis of sans and usans data using igor pro. *Journal of applied crystallography*, 39(6):895–900, 2006.
- [90] Daniel Klinger and Katharina Landfester. Photo-sensitive pmma microgels: light-triggered swelling and degradation. *Soft Matter*, 7(4):1426–1440, 2011.
- [91] J. Kohlbrecher and W. Wagner. The new SANS instrument at the Swiss spallation source SINQ. *J. Appl. Cryst.*, 33(1):804–806, 2000.
- [92] D. E. Koppel. Analysis of macromolecular polydispersity in intensity correlation spectroscopy - method of cumulants. *Journal of Chemical Physics*, 57(11):4814–4820, 1972.
- [93] M. Kotlarchyk and Chen Sow-Hsin. Analysis of small angle neutron scattering spectra from polydisperse interacting colloids. *J. Chem. Phys.*, 79(5):2461–2469, 1983.
- [94] Karl Kratz, Thomas Hellweg, and Wolfgang Eimer. Structural changes in pnipam microgel particles as seen by sans, dls, and em techniques. *Polymer*, 42(15):6631–6639, 2001.
- [95] P. Kujawa and F. M. Winnik. Volumetric Studies of Aqueous Polymer Solutions Using Pressure Perturbation Calorimetry: A New Look at the Temperature-Induced Phase Transition of Poly(*N*-isopropylacrylamide) in Water and D₂O. *Macromolecules*, 34:4130–4135, 2001.
- [96] Tetyana Kyrey, Judith Witte, Jana Lutzki, Michaela Zamponi, Stefan Wellert, and Olaf Holderer. Mobility of bound water in pnipam microgels. *Phys. Chem. Chem. Phys.*, 23:14252–14259, 2021.
- [97] Katharina Landfester, Mirjam Willert, and Markus Antonietti. Preparation of polymer particles in nonaqueous direct and inverse miniemulsions. *Macromolecules*, 33(7):2370–2376, 2000.

- [98] LX Li and TJ Wang. A unified approach to predict overall properties of composite materials. *Materials Characterization*, 54(1):49–62, 2005.
- [99] J. J. Lieter-Santos, U. Gasser, R. Vavrin, Z. Hu, and A. Fernandez-Nieves. Structural changes of poly(n-isopropylacrylamide)-based microgels induced by hydrostatic pressure and temperature studied by small angle neutron scattering. *J. Chem. Phys.*, 133(3):034901, 2010.
- [100] J. J. Lieter-Santos, B. Sierra-Martin, U. Gasser, and A. Fernandez-Nieves. The effect of hydrostatic pressure over the swelling of microgel particles. *Soft Matter*, 7:6370–6374, 2011.
- [101] J. J. Lieter-Santos, B. Sierra-Martin, R. Vavrin, Z. Hu, U. Gasser, and A. Fernandez-Nieves. Deswelling microgel particles using hydrostatic pressure. *Macromolecules*, 42(16):6225–6230, 2009.
- [102] Juan José Liétor-Santos, Benjamín Sierra-Martín, and Alberto Fernández-Nieves. Bulk and shear moduli of compressed microgel suspensions. *Physical Review E*, 84(6):060402, 2011.
- [103] Shaojian Lin, Philipp Schattling, and Patrick Theato. Thermo- and CO₂-responsive linear polymers and hydrogels as CO₂ capturing materials. *Science of Advanced Materials*, 7(5):948–955, 2015.
- [104] P. Lindner. Scattering experiments: experimental aspects, initial data reduction absolute calibration. In P. Lindner and Th. Zemb, editors, *Neutrons, X-Rays and Light: Scattering methods applied to soft condensed matter*. Elsevier, Amsterdam, 2002.
- [105] T. Lopez-Leon and A. Fernandez-Nieves. Macroscopically probing the entropic influence of ions: Deswelling neutral microgels with salt. *Phys. Rev. E*, 75(1):011801, 2007.
- [106] H. Löwen and G. Krampphuber. Optimal effective pair potential for charged colloids. *Europhys. Lett.*, 23(9):673–678, 1993.
- [107] Yunhua Luo. Improved Voigt and Reuss formulas with the Poisson effect. *Materials*, 15(16):5656, 2022.
- [108] Johannes Lyklema. *Fundamentals of interface and colloid science: soft colloids*, volume 5. Elsevier, 2005.
- [109] Rosemary A MacDonald. Cauchy relations for second- and third-order elastic constants. *Physical Review B*, 5(10):4139, 1972.
- [110] Prashant S Malpure, Shital S Patil, Yashpal M More, and Priti P Nikam. A review on hydrogel. *Am J PharmTech Res*, 8(3):42–60, 2018.
- [111] JW Martin. Many-body forces in metals and the Brugger elastic constants. *Journal of Physics C: Solid State Physics*, 8(18):2837, 1975.
- [112] Wayne McPhee, Kam Chiu Tam, and Robert Pelton. Poly (n-isopropylacrylamide) lattices prepared with sodium dodecyl sulfate. *Journal of colloid and interface science*, 156(1):24–30, 1993.

- [113] Donald Allan McQuarrie. *Mathematical methods for scientists and engineers*. University science books, 2003.
- [114] Chuanwei Miao, Xiaonong Chen, and Robert Pelton. Adhesion of poly (vinylamine) microgels to wet cellulose. *Industrial & engineering chemistry research*, 46(20):6486–6493, 2007.
- [115] P. S. Mohanty, D. Paloli, J. J. Crassous, E. Zaccarelli, and P. Schurtenberger. Effective interactions between soft-repulsive colloids: Experiments, theory, and simulations. *J. Chem. Phys.*, 140(9):094901, 2014.
- [116] P. S. Mohanty and W. Richtering. Structural ordering and phase behavior of charged microgels. *J. Phys. Chem. B*, 112(47):14692–14697, 2008.
- [117] A. Moncho-Jorda. Effective charge of ionic microgel particles in the swollen and collapsed states: The role of the steric microgel-ion repulsion. *J. Chem. Phys.*, 139(6):064906, 2013.
- [118] G. E. Morris, B. Vincent, and M. J. Snowden. Adsorption of lead ions onto n-isopropylacrylamide and acrylic acid copolymer microgels. *J. Colloid Interface Sci.*, 190:198, 1997.
- [119] A. Munter. Scattering length density calculator, <http://www.ncnr.nist.gov/resources/sldcalc.html>, 2012.
- [120] N. Murthy, Y. X. Thng, S. Schuck, M. C. Xu, and J. M. J. Frechet. A novel strategy for encapsulation and release of proteins: Hydrogels and microgels with acid-labile acetal cross-linkers. *J. Am. Chem. Soc.*, 124(42):12398–12399, 2002.
- [121] T Nakamura, T Wang, and S Sampath. Determination of properties of graded materials by inverse analysis and instrumented indentation. *Acta Materialia*, 48(17):4293–4306, 2000.
- [122] John Nicholson. *The chemistry of polymers*. Royal Society of Chemistry, 2017.
- [123] KARL J NIKLAS. Voigt and reuss models for predicting changes in young’s modulus of dehydrating plant organs. *Annals of Botany*, 70(4):347–355, 1992.
- [124] S Nikolov, A Fernandez-Nieves, and A Alexeev. Mesoscale modeling of microgel mechanics and kinetics through the swelling transition. *Applied Mathematics and Mechanics*, 39(1):47–62, 2018.
- [125] Nöjd, S., P. Holmqvist, N. Boon, Marc Obiols-Rabasa, P. S. Mohanty, R. Schweins, and P. Schurtenberger. Deswelling behaviour of ionic microgel particles from low to ultra-high densities. *Soft Matter*, 14:4150–4159, 2018.
- [126] Yoshihito Osada, Hidenori Okuzaki, and Hirofumi Hori. A polymer gel with electrically driven motility. *Nature*, 355(6357):242–244, 1992.
- [127] D. Paloli, P. S. Mohanty, J. J. Crassous, E. Zaccarelli, and P. Schurtenberger. Fluid-solid transitions in soft-repulsive colloids. *Soft Matter*, 9(11):3000–3004, 2013.

- [128] Josep C Pàmies, Angelo Cacciuto, and Daan Frenkel. Phase diagram of hertzian spheres. *The Journal of chemical physics*, 131(4):044514, 2009.
- [129] J. S. Pedersen. Analysis of small-angle scattering data from colloids and polymer solutions: modeling and least-squares fitting. *Advances in Colloid and Interface Science*, 70:171–210, 1997.
- [130] J Skov Pedersen, Dorte Posselt, and Kell Mortensen. Analytical treatment of the resolution function for small-angle scattering. *Journal of Applied Crystallography*, 23(4):321–333, 1990.
- [131] M. Pelaez-Fernandez, A. Souslov, L. A. Lyon, P. M. Goldbart, and A. Fernandez-Nieves. Impact of single-particle compressibility on the fluid-solid phase transition for ionic microgel suspensions. *Phys. Rev. Lett.*, 114(9):098303, 2015.
- [132] R. Pelton. Temperature-sensitive aqueous microgels. *Advances in Colloid and Interface Science*, 85(1):1–33, 2000.
- [133] R. Pelton and T. Hoare. Microgels and their synthesis: An introduction. In Alberto Fernandez-Nieves, H. M. Wyss, J. Mattsson, and D. A. Weitz, editors, *Microgel Suspensions: Fundamentals and Applications*, chapter 1. WILEY-VCH Verlag GmbH & CO. KGaA, 2011.
- [134] J. K. Percus and G. J. Yevick. Analysis of classical statistical mechanics by means of collective coordinates. *Physical Review*, 110(1):1–13, 1958.
- [135] Alexander V Petrunin, Maximilian M Schmidt, Ralf Schweins, Judith E Houston, and Andrea Scotti. Self-healing of charged microgels in neutral and charged environments. *Langmuir*, 2023.
- [136] Ekaterina Ponomareva, Ben Tadgell, Marco Hildebrandt, Marcel Krüsmann, Sylvain Prévost, Paul Mulvaney, and Matthias Karg. The fuzzy sphere morphology is responsible for the increase in light scattering during the shrinkage of thermoresponsive microgels. *Soft Matter*, 18(4):807–825, 2022.
- [137] P. N. Pusey and W. van Megen. Phase behaviour of concentrated suspensions of nearly hard colloidal spheres. *Nature*, 320:340–342, 1986.
- [138] Daniel Pussak, Daniela Ponader, Simone Mosca, Salomé Vargas Ruiz, Laura Hartmann, and Stephan Schmidt. Mechanical carbohydrate sensors based on soft hydrogel particles. *Angewandte Chemie (International ed. in English)*, 52(23):6084–6087, 2013.
- [139] D. Reinke. *Elastische Eigenschaften von Kolloidkristallen*. Phd thesis, University of Konstanz, 2006.
- [140] Daniel Reinke, Holger Stark, H-H von Grünberg, Andrew B Schofield, Georg Maret, and Urs Gasser. Noncentral forces in crystals of charged colloids. *Physical review letters*, 98(3):038301, 2007.
- [141] Ferdinand Rodriguez, Ferdinand Cohen, Christopher K Ober, and Lynden Archer. *Principles of polymer systems*. CRC Press, 2003.

- [142] G. Romeo, L. Imperiali, J.-W. Kim, A. Fernandez-Nieves, and D. A. Weitz. Origin of deswelling and dynamics of dense ionic microgel suspension. *J. Chem. Phys.*, 136(12):124905, 2012.
- [143] Michael Rubinstein, Ralph H Colby, et al. *Polymer physics*, volume 23. Oxford university press New York, 2003.
- [144] Carsten Russ, Matthias Brunner, Clemens Bechinger, and Hans-Hennig von Grünberg. Three-body forces at work: Three-body potentials derived from triplet correlations in colloidal suspensions. *Europhysics Letters*, 69(3):468, 2004.
- [145] (Jun John) Sakurai Sakurai and Jim J Napolitano. *Modern Quantum Mechanics*. Pearson, 2014.
- [146] Andrés Santos, Mariano Lopez de Haro, Giacomo Fiumara, and Franz Saija. The effective colloid interaction in the asakura–oosawa model. assessment of non-pairwise terms from the virial expansion. *The Journal of chemical physics*, 142(22), 2015.
- [147] F. Scheffold, P. Diaz-Leyva, M. Reufer, N. Ben Braham, I. Lynch, and J. L. Harden. Brush-like interactions between thermoresponsive microgel particles. *Phys. Rev. Lett.*, 104(12):128304, 2010.
- [148] Stephan Schmidt, Michael Zeiser, Thomas Hellweg, Claus Duschl, Andreas Fery, and Helmut Möhwald. Adhesion and mechanical properties of pnipam microgel films and their potential use as switchable cell culture substrates. *Advanced Functional Materials*, 20(19):3235–3243, 2010.
- [149] A. Scotti, U. Gasser, E. S. Herman, Jun Han, A. Menzel, L. A. Lyon, and A. Fernandez-Nieves. Phase behavior of binary and polydisperse suspensions of compressible microgels controlled by selective particle deswelling. *Phys. Rev. E*, 96(3):032609, 2017.
- [150] A. Scotti, U. Gasser, E. S. Herman, M. Pelaez-Fernandez, L. A. Lyon, and A. Fernandez-Nieves. The role of ions in the self-healing behavior of soft particle suspensions. *Proc. Natl. Acad. Sci. USA*, 113:5576–5581, 2016.
- [151] A Scotti, U Gasser, B Zhou, A Arenas-Gullo, A de la Cotte, J Rojo González, and A Fernandez-Nieves. Compressible microgels in concentrated suspensions: Phase behavior, flow properties, and scattering techniques to probe their structure and dynamics. *Smart Stimuli-Responsive Polymers, Films, and Gels*, pages 203–240, 2022.
- [152] A Scotti, W Liu, JS Hyatt, ES Herman, HS Choi, JW Kim, LA Lyon, U Gasser, and A Fernandez-Nieves. The contin algorithm and its application to determine the size distribution of microgel suspensions. *The Journal of chemical physics*, 142(23), 2015.
- [153] A. Scotti, M. Pelaez-Fernandez, U. Gasser, and A. Fernandez-Nieves. Osmotic pressure of suspensions comprised of charged microgels. *Phys. Rev. E*, 103(1):012609, 2021.

- [154] Andrea Scotti. *Phase behavior of binary mixtures and polydisperse suspensions of compressible spheres*. Doctoral thesis, ETH Zurich, Zürich, 2015. Dissertation. ETH-Zürich. 2016. No. 22806.
- [155] Andrea Scotti. Characterization of the volume fraction of soft deformable microgels by means of small-angle neutron scattering with contrast variation. *Soft Matter*, 17(22):5548–5559, 2021.
- [156] Andrea Scotti, Alan R Denton, Monia Brugnoli, Judith E Houston, Ralf Schweins, Igor I Potemkin, and Walter Richtering. Deswelling of microgels in crowded suspensions depends on cross-link density and architecture. *Macromolecules*, 52(11):3995–4007, 2019.
- [157] Dror Seliktar. Designing Cell-Compatible Hydrogels for Biomedical Applications. *Science*, 336(6085):1124–1128, 2012.
- [158] H. Senff and W. Richtering. Temperature sensitive microgel suspensions: Colloidal phase behavior and rheology of soft spheres. *The Journal of Chemical Physics*, 111(4):1705–1711, 1999.
- [159] H. Senff and W. Richtering. Influence of cross-link density on rheological properties of temperature-sensitive microgel suspensions. *Colloid Polym. Sci.*, 278(9):830–840, 2000.
- [160] PK Sharma and RK Awasthi. Noncentral force model for the lattice dynamics of cubic metals. *Physical Review B*, 19(4):1963, 1979.
- [161] M. Shibayama. *Small Angle Neutron Scattering on Gels*, pages 783–832. Springer Netherlands, Dordrecht, 2008.
- [162] M. Shibayama, T. Tanaka, and C. C. Han. Small angle neutron scattering study on poly(nisopropyl acrylamide) gels near their volume phase transition temperature. *J. Chem. Phys.*, 97(9):6829–6841, 1992.
- [163] Mitsuhiro Shibayama. Small-angle neutron scattering on polymer gels: phase behavior, inhomogeneities and deformation mechanisms. *Polymer journal*, 43(1):18–34, 2011.
- [164] Mitsuhiro Shibayama, Masato Morimoto, and Shunji Nomura. Phase separation induced mechanical transition of poly (n-isopropylacrylamide)/water isochore gels. *Macromolecules*, 27(18):5060–5066, 1994.
- [165] Mitsuhiro Shibayama and Toyochi Tanaka. Volume phase transition and related phenomena of polymer gels. *Responsive gels: volume transitions I*, pages 1–62, 2005.
- [166] B Sierra-Martin, MS Romero-Cano, A Fernandez-Nieves, and A Fernandez-Barbero. Thermal control over the electrophoresis of soft colloidal particles. *Langmuir*, 22(8):3586–3590, 2006.
- [167] Benjamin Sierra-Martin, Juan Jose Lietor-Santos, Antonio Fernandez-Barbero, Toan T Nguyen, and Alberto Fernandez-Nieves. Swelling thermodynamics of microgel particles. *Microgel suspensions: fundamentals and applications*, pages 71–116, 2011.

- [168] P. J. Steinhardt, D. R. Nelson, and M. Ronchetti. Bond-orientational order in liquids and glasses. *Phys. Rev. B*, 28(2):784–805, 1983.
- [169] M. Stieger, J.S. Pedersen, P. Lindner, and W. Richtering. Are thermoresponsive microgels model systems for concentrated colloidal suspensions? a rheology and small-angle neutron scattering study. *Langmuir*, 20(17):7283–7292, 2004.
- [170] M. Stieger, W. Richtering, J.S. Pedersen, and P. Lindner. Small-angle neutron scattering study of structural changes in temperature sensitive microgel colloids. *J. Chem. Phys.*, 120(13):6197–6206, 2004.
- [171] A. N. St. John, V. Breedveld, and L. A. Lyon. Phase behavior in highly concentrated assemblies of microgels with soft repulsive interaction potentials. *Journal of Physical Chemistry B*, 111(27):7796–7801, 2007.
- [172] J. R. Stokes. *Microgel Suspensions*, chapter Rheology of Industrially Relevant Microgels, pages 327–353. WILEY-VCH Verlag GmbH and Co. KGaA, 69469 Weinheim, Germany, 2011.
- [173] P. Strunz, K. Mortensen, and S. Janssen. SANS-II at SINQ: installation of the former Risø-SANS facility. *Physica B*, 350(1-3):e783–e786, 2004.
- [174] Kimio Sumaru, Hideki Matsuoka, and Hitoshi Yamaoka. Evaluation of the counterion distribution around spherical micelles in solution by small-angle neutron scattering. *Phys. Rev. E*, 53(2):1744–1752, 1996.
- [175] Salvatore P. Sutera and Richard Skalak. The history of poiseuille’s law. *Annual review of fluid mechanics*, 25(1):1–20, 1993.
- [176] T. Takigawa, T. Yamawaki, K. Takahashi, and T. Masuda. Change in young’s modulus of poly (n-isopropylacrylamide) gels by volume phase transition. *Polymer Gels and Networks*, 5(6):585–589, 1998.
- [177] T. Tanaka. Collapse of gels and critical endpoint. *Phys. Rev. Lett.*, 40:820, 1978.
- [178] Toyochi Tanaka. Kinetics of phase transition in polymer gels. *Physica A: Statistical Mechanics and its Applications*, 140(1-2):261–268, 1986.
- [179] Toyochi Tanaka, Izumi Nishio, Shao-Tang Sun, and Shizue Ueno-Nishio. Collapse of gels in an electric field. *Science*, 218(4571):467–469, 1982.
- [180] Toyochi Tanaka, Shao-Tang Sun, Yoshitsugu Hirokawa, Seiji Katayama, John Kucera, Yoshiharu Hirose, and Takayuki Amiya. Mechanical instability of gels at the phase transition. *Nature*, 325(6107):796–798, 1987.
- [181] John Robert Taylor and William Thompson. *An introduction to error analysis: the study of uncertainties in physical measurements*, volume 2. Springer, 1982.
- [182] IWAO TERAOKA. An introduction to physical properties. *Polymer Solutions*, 2002.

- [183] Y Tomota, K Kuroki, T Mori, and I Tamura. Tensile deformation of two-ductile-phase alloys: Flow curves of α - γ Fe-Cr-Ni alloys. *Materials Science and Engineering*, 24(1):85–94, 1976.
- [184] P. Trtik, J. Hovind, C. Grünzweig, A. Bollhalder, V. Thominet, C. David, A. Kaestner, and E. Lehmann. Improving the spatial resolution of neutron imaging at Paul Scherrer Institut—the neutron microscope project. *Physics Procedia*, 69:169–176, 2015.
- [185] M. Urich and A. R. Denton. Swelling, structure, and phase stability of compressible microgels. *Soft Matter*, 12:9086–9094, 2016.
- [186] J. R. C. van der Maarel, W. Groenewegen, S. U. Egelhaaf, and A. Lapp. Salt-induced contraction of polyelectrolyte diblock copolymer micelles. *Langmuir*, 16(19):7510–7519, 2000.
- [187] S. van Kesteren, L. Alvarez, S. Arrese-Igor, A. Alegria, and L. Isa. Self-propelling colloids with finite state dynamics. *Proceedings of the National Academy of Sciences*, 120(11):e2213481120, 2023.
- [188] W. van Meegen and I. Snook. Statistical mechanical approach to phase transitions in colloids. *Faraday Discussions of the Chemical Society*, 65:92–100, 1978.
- [189] P. Voudouris, D. Florea, P. van der Schoot, and H. Wyss. Micromechanics of temperature sensitive microgels: dip in the Poisson ratio near the LCST. *Soft Matter*, 9(29):7158–7166, 2013.
- [190] D. Wallace. Thermoelastic theory of stressed crystals and higher-order elastic constants. In *Solid state physics*, volume 25, pages 301–404. Elsevier, 1970.
- [191] T. Wang, P. Colver, S. Bon, and J. Keddie. Soft polymer and nano-clay supracolloidal particles in adhesives: synergistic effects on mechanical properties. *Soft Matter*, 5(20):3842–3849, 2009.
- [192] G. Wick. The evaluation of the collision matrix. *Physical review*, 80(2):268, 1950.
- [193] R. Williamson, B. Rabin, and J. Drake. Finite element analysis of thermal residual stresses at graded ceramic-metal interfaces. part i. model description and geometrical effects. *Journal of Applied Physics*, 74(2):1310–1320, 1993.
- [194] J. Wu, B. Zhou, and Z. Hu. Phase behavior of thermally responsive microgel colloids. *Phys. Rev. Lett.*, 90(4):048304, 2003.
- [195] X. Wu, R.H. Pelton, A.E. Hamielec, D.R. Woods, and W. McPhee. The kinetics of poly(*n*-isopropylacrylamide) microgel latex formation. *Colloid and Polymer Science*, 272(4):467–477, 1994.
- [196] X. Xu, N. Bizmark, K. Christie, S. Datta, Z. Ren, and R. Priestley. Thermoresponsive polymers for water treatment and collection. *Macromolecules*, 55(6):1894–1909, 2022.
- [197] Mengchen Yue, Yu Hoshino, Yukinori Ohshiro, Kazushi Imamura, and Yoshiko Miura. Temperature-responsive microgel films as reversible carbon dioxide absorbents in wet environment. *Angewandte Chemie International Edition*, 53(10):2654–2657, 2014.

- [198] Mark W Zemansky and Richard H Dittman. Heat and thermodynamics, 1998.
- [199] L. Zhang, E. Daniels, V. Dimonie, and A. Klein. Synthesis and characterization of pnipam/ps core/shell particles. *Journal of applied polymer science*, 118(5):2502–2511, 2010.
- [200] B. Zhou, A. Fernandez-Nieves, W. Chen, T. Kim, and C. Do. Complexation of pluronic l62 (eo 6)–(po 34)–(eo 6)/aerosol-ot (sodium bis (2-ethylhexyl) sulfosuccinate) in aqueous solutions investigated by small angle neutron scattering. *Physical Chemistry Chemical Physics*, 22(22):12524–12531, 2020.
- [201] B. Zhou, U. Gasser, and A. Fernandez-Nieves. Measuring the counterion cloud of soft microgels using sans with contrast variation. *Nature Communications*, 14(1):3827, 2023.
- [202] B. Zhou, U. Gasser, and A. Fernandez-Nieves. Poly(*n*-isopropylacrylamide) microgel swelling behavior and suspension structure studied with small-angle neutron scattering. *Phys. Rev. E*, 108:054604, Nov 2023.
- [203] B. Zhou, U. Gasser, and A. Fernandez-Nieves. Supplementary information: Measuring the counterion cloud of soft microgels using sans with contrast variation. *Nature Communications*, 2023.
- [204] J. Zhou, J. Wei, T. Ngai, L. Wang, D. Zhu, and J. Shen. Correlation between dielectric/electric properties and cross-linking/ charge density distributions of thermally sensitive spherical pnipam microgels. *Macromolecules*, 45:6158–6167, 2012.
- [205] P. Zihlerl and R. D. Kamien. Soap froths and crystal structures. *Phys. Rev. Lett.*, 85(16):3528–3531, 2000.
- [206] P. Zihlerl and R. D. Kamien. Maximizing entropy by minimizing area: Towards a new principle of self-organization. *J. Phys. Chem. B*, 105(42):10147–10158, 2001.

Curriculum Vitae

Personal data

Name: Boyang Zhou
Date of Birth: April 25, 1995
Place of Birth: Taiyuan, China
Citizenship: Chinese

Academic Appointments

PhD Student at: ETH of Zurich and Paul Scherrer Insitut (March 2020 - Jan 2024)

Education and Academic Training

Hercules European School

February 26, 2021 - March 28, 2021.

A five-weeks course coordinated by the Universite Grenoble Alpes (UGA).

The school provides training in neutron/X-ray scattering for studies of condensed matter (biology, chemistry, physics, materials science, geosciences, industrial applications).

Georgia Institute of Technology - Master degree in Materials Science and Engineering (2 years)

August 23, 2017 - August 28, 2019.

Dissertation: Micellar and Liquid crystalline phases of surfactant/Pluronic mixtures studied by SANS

Advisors: Prof. Alberto Fernandez Nieves, Dr. Changwoo Do

Oak Ridge National Laboratory (2 years)

July 21, 2018 - February 28, 2020.

Worked as a full-time student researcher, conducting Neutron scattering and Neutron imaging experiments on surfactants, microgels, and hydrogels, as part of the Master's degree.

Illinois Wesleyan University - Bachelor of Science (3 years)

August 23, 2014 - May 26, 2017.

Advisor: Prof. Gabriel C. Spalding

List of Publications

Research articles:

1. **Zhou, B.**, Gasser, U. and Fernandez-Nieves, A. "Measuring the counterion cloud of soft microgels using SANS with contrast variation." *Nature Communications* 14, no. 1 (2023): 3827.
2. **Zhou, B.**, Gasser, U. and Fernandez-Nieves, A. "Poly (N-isopropylacrylamide) microgel swelling behavior and suspension structure studied with small-angle neutron scattering." *Physical Review E* 108, no. 5 (2023): 054604.
3. Scotti, A., Gasser, U., **Zhou, B.**, A. Arenas-Gullo, A. de la Cotte, J. Rojo Gonzalez, and A. Fernandez-Nieves. "Compressible Microgels in Concentrated Suspensions: Phase Behavior, Flow Properties, and Scattering Techniques to Probe Their Structure and Dynamics." *Smart Stimuli-Responsive Polymers, Films, and Gels* (2022): 203-240.
4. Gasser, U., and **Zhou, B.** "Accurate detection of spherical objects in a complex background." *Optics Express* 29, no. 23 (2021): 37048-37065.

Works in preparation:

1. **Zhou, B.**, Gasser, U., Fernandez-Nieves, A. Counterion sea in microgel fcc crystals, non-central interactions, and the stiffening of the crystal.
2. **Zhou, B.**, Gasser, U., Fernandez-Nieves, A. Halting deswelling: Skin formation in pNIPAM hydrogels subjected to fast temperature changes.

Selected Conferences:

1. **Zhou, B.**, pNIPAM microgel deswelling and suspension structure in crowded suspensions studied with SANS: Swiss Soft Days (31th). 13.04.2023: Fribourg, Switzerland.

2. **Zhou, B.**, Concentration dependence of the microgel Counter-ion Cloud configuration with increasing particle stiffness studied with Small-Angle Neutron Scattering (SANS), 06.03.2023: APS March meeting. Las Vegas, USA.
3. **Zhou, B.**, Particle Deswelling below Random close packing density. Swiss Soft Days (29th). 05.04.2022: Villigen, Switzerland.
4. **Zhou, B.**, Small-Angle Neutron Scattering Tutorial: instrumental detail, data reduction, data analysis. (teaching) 23.03.2022: Hercules European School. Villigen, Switzerland.
5. **Zhou, B.**, Direct measurements of the pNipam Microgel Counter-ion Cloud via SANS. 06.03.2022: APS March meeting (Virtual). Chicago, USA.
6. **Zhou, B.**, Directly measuring the counterion cloud of soft microgels using SANS with contrast variation by ion species. 03.02.2022: Strasbourg, France.
7. **Zhou, B.**, Directly measuring the counterion cloud of soft microgels using SANS with contrast variation. 08.06.2021: Swiss Soft Days (27th), (Virtual).
8. **Zhou, B.**, Characterization of the counter-ion cloud of pNipam microgel via Small Angle Neutron scattering (SANS) (Poster), 03.06.2021: APS March meeting. Nashville, USA.

Acknowledgements

First of all, I would like to thank my advisors and mentors, Urs and Alberto, for always being supportive, responsible, and passionate. I have learned a lot from them, especially on how to conduct research and the attitude towards science. I also express my gratitude to Prof. Lucio Isa for his continuing support, comments, and scientific contributions.

I want to thank my parents for always trying their best to help, guide, and support my decisions, and for their unconditional love. They will always be my role models, showing me the importance of being diligent, strong, and considerate. Additionally, I extend my thanks to Tiantian Wang for being my companion, sharing laughs, and helping me through times of stress and unhappiness.

I also would like to thank all the friends I met at PSI: Zheyu, Dongyang, Longdi, Xiaoyang, Matt, and more to count for all the fun we had! Special thanks to my office mates Victor, Marnik, Mohammad, Ashley, and Wouter for the joy and support they bring.

Finally, to myself: keep motivated, be genuine, think straight and positive, act fast, work hard and everything will fall into the right place.